Wideband Dual-Circular-Polarization Antennas for Millimetre-Wave Wireless Communications

by

Chao Shu

A thesis submitted in partial fulfilment of the requirements for the degree of Doctor of Philosophy

School of Electronic Engineering and Computer Science
Queen Mary University of London
United Kingdom

November 2020

Declaration

I, Chao Shu, confirm that the research included within this thesis is my own work or that where it has been carried out in collaboration with, or supported by others, that this is duly acknowledged below and my contribution indicated. Previously published material is also acknowledged below.

I attest that I have exercised reasonable care to ensure that the work is original, and does not to the best of my knowledge break any UK law, infringe any third party's copyright or other Intellectual Property Right, or contain any confidential material.

I accept that the College has the right to use plagiarism detection software to check the electronic version of the thesis.

I confirm that this thesis has not been previously submitted for the award of a degree by this or any other university.

Signature: Chao Shu

Date: 8th November 2020

TO MY FAMILY

Abstract

Millimetre-wave (mmWave) wireless communications has attracted great interest in recent years as a promising technology that can provide high data rate beyond 5G. Circular Polarization (CP) radiation is preferable to Linear Polarization (LP) in mmWave wireless communications, owing to the reliability of the wireless link it provides to suppress multi-path fading and polarization misalignment. Apart from the link robustness, high link capacity is also desirable by introducing technologies such as Polarization Division Multiplexing (PDM) or In-Band Full-Duplex (IBFD). Therefore, this research aims to design dual-circular-polarization (dual-CP) antennas with wide bandwidth and high port isolation to enable PDM or IBFD for mmWave wireless communications thereby achieving twofold spectral efficiency. The research work has been conducted in the following four parts.

Firstly, a dual-CP horn antenna based on a stepped septum polarizer is designed in the W-band. By optimising the horn profile, a wide bandwidth with good isolation is achieved in simulation and verified in experiment.

Secondly, to further push the limits of the dual-CP antenna based on the stepped septum polarizer, a grooved-wall septum polarizer is proposed for the first time with a 2-step design method to realize a dual-CP antenna with wider operating bandwidth and higher port isolation.

Thirdly, in order to ease the fabrication difficulty and further improve the antenna performance, a novel grooved-wall CP horn antenna is designed in simulation and verified in experiment in the W-band. The dual CP performance can be generated when used with an Orthomode Transducer (OMT), instead of a septum.

Finally, this septum-free approach has been generalised to design a multi-section grooved-

wall CP horn antenna with a low reflection coefficient over a wide bandwidth in the W-band. This horn antenna is demonstrated to be capable of achieving dual-CP with high isolation over a wide bandwidth when used together with an OMT.

Acknowledgments

First and foremost, I would like to express my deepest gratitude to my supervisor, Prof. Xiaodong Chen, for his patient guidance, insightful comments, and his generous and continuous support throughout my research work, especially during the period of unprecedented uncertainty caused by the COVID-19 outbreak in the last year of my research. I am also grateful to my second supervisor Dr Yasir Alfadhl, independent assessor Dr Robert Donnan and Prof. Yuan Yao at Beijing University of Posts and Telecommunications (BUPT), for valuable suggestions on my research. Additionally, I appreciate the scholarship provided by the China Scholarship Council (CSC).

I would like to express my sincere appreciation to Dr Shaoqing Hu for the work we did together and fruitful discussions we had. I would also like to thank Dr Xiaohe Cheng, Dr Junbo Wang and Dr Caixia Wang for their help with the measurement at BUPT. I am particularly grateful for the assistance provided by Dr Andre Sarker Andy with the measurement in the Antenna Lab. The expertise on CATR shared by Dr Max Munoz Torrico are greatly appreciated. My appreciation also goes to Dr Qiao Cheng, who kindly spared me part of his experiment time slot for my last experiment. My thanks are extended to Dr Jin Zhang, Prof. Bin Deng, Dr Tianzhong Zhang, Wanlin Li, Wei Su, Zihang Song, Xiaolan Liu, Dr Min Zhou, Dr Liang Yang, Dr Rui Zhang, Dr Qianyun Zhang, for sharing valuable research experience with me and offering kind help to me.

Finally, I would like to express my gratitude to my parents, my brothers-in-law and sister-in-law, especially my wife, Lei, for their tremendous support throughout my PhD. I am grateful to my lifelong friends, Dr Tong Wu and Yi Wang, for being a great source of encouragement and inspiration. My little daughter, Frances, also deserves many thanks. This thesis has been written along with her giggles, cries and mumbles during a period of much difficulty, but her sweet kiss is always a miraculous cure for my anxiety.

Table of Contents

List of Figures

List of Tables

List of Abbreviations

4G	Fourth-Generation
5G	Fifth-Generation
ADE	Axial Displaced Ellipse
AR	Axial Ratio
BW	Bandwidth
B5G	Beyond 5G
AUT	Antenna Under Test
CATR	Compact Antenna Test Range
CMA-ES	Covariance Matrix Adaptation Evolution Strategy
CP	Circular-Polarization
DNNs	Deep Neural Networks
Dual-CP	Dual-Circular-Polarization
EAs	Evolutionary Algorithms
EDM	Electrical Discharge Machining
EM	Electromagnetic
FSPL	Free-Space Path-Loss
GAs	Genetic Algorithms

GNSS	Global Navigation Satellite System
GO	Geometrical Optics
GPR	Gaussian Process Regression
HPC	High Performance Computing
IBFD	In-Band Full Duplex
ITS	Intelligent Transport Systems
LHCP	Left-Hand Circular Polarization
LOS	Line-of-Sight
LP	Linear Polarization
LTE	Long Term Evolution
MAE	Mean Absolute Error
MIMO	Multiple-Input Multiple-Output
MLFMM	Multilevel Fast Multipole Method
mmWave	millimetre Wave
MSE	Mean Square Error
NN	Neural Network
NR	New Radio
OMT	Orthomode Transducer
PCB	Printed Circuit Board
PDM	Polarization Division Multiplexing
PO	Physical Optics
PSO	Particle Swarm Optimization
PtP	Point-to-Point
PtMP	Point-to-MultiPoint
RHCP	Right-Hand Circular Polarization

SIW	Substrate Integrated Waveguide
SLL	Sidelobe Level
SLM	Selective Laser Melting
SPAA	Spherical Phased-Array Antenna
THz	Terahertz
UE	User Equipment
UHD	Ultra-High-Definition
VR	Virtual Realities

Chapter 1

Introduction

1.1 Background of Millimetre-Wave Communications

Wireless communications has fundamentally revolutionized the way people live and work in the past two decades. Data traffic over wireless channels has been increasing dramatically after the deployment of the fourth-generation Long Term Evolution mobile communication (4G LTE) network, and this trend is expected to accelerate exponentially over the coming decade, as the high-quality low-latency multimedia services continue to gain in popularity on the wireless devices. However, the wireless network nowadays is operating in the spectrum below 5 GHz with only small slices of frequency bands available. In order to deliver a higher data rate, a number of enabling technologies have been explored to increase spectral efficiency after 4G LTE, such as massive MIMO [1], new waveforms, and advanced modulation and coding schemes [2]. Nevertheless, achieving an ultra-high data rate at the level of several tens of Gigabit-per-second is still quite challenging in the crowded sub-6 GHz spectrum. Another key technology that can alleviate this spectrum shortage is to operate in millimetre wave (mmWave) band between 30 and 300 GHz, within which larger amounts of spectral bandwidths have been identified [3, 4]. Furthermore, a successful marriage of millimetre waves and the aforementioned spectral-efficiency-enhancing technologies may push the wireless link capacity to

a new level [5]. To meet the rapidly growing demand, the wireless industry is developing fifth-generation (5G) technology that will use mmWave bands to provide multi-Gigabit-per-second (Gbps) data rates [6–8].

Currently, 5G mmWave research and development mainly focuses on the lower end of the mmWave band, such as 28 GHz band and 38 GHz band [7], which is used for the radio access links (the links between base station and user equipment (UE)). An mm-wave adaptive beamforming prototype is developed in [9]. With a bandwidth of 520 MHz at 28GHz, a peak data rate of 1.056 Gbps was achieved in the laboratory, supporting two stationary mobile stations with 528 Mb/s each. An outdoor scenario with more than 500 Mb/s data rate at a speed of 8 km/h within a radius of a few hundred metres was also demonstrated. However, the data rate and bandwidth of this type of wireless link can not support some applications which require a data rate up to several tens of Gbps and transmission distance up to several kilometres, such as wireless backhaul and fronthaul of 5G base stations.

Furthermore, it is envisaged that the capacity of wireless links will increase up to 100 Gbps to meet the requirement of the market [10], as some emerging technologies which demand ultra-high data rate with ultra-low latency, such as cloud computing, ultra-high-definition (UHD) video, augmented reality (AR) and virtual reality (VR), vehicular communication, show promising applications on the wireless devices. Hence, it is anticipated that wireless communications should move to higher frequencies in the mmWave band or even terahertz (THz) band where larger continuous bandwidth is available, so that mmWave wireless links can offer ultra-high data rate that is comparable to the data rate of fibre-optic communications. In fact, some efforts have been made to investigate the wireless systems in these bands, which aim to realize data rate of several tens of Gbps or even 100 Gbps over a long transmission distance.

The following section provides an overview of the most representative state-of-the-art mmWave wireless communication systems and the technologies they used to increase the reliability and capacity of the wireless links, from which the requirement on the antenna

side can be derived. The research motivation and objectives are then presented accordingly in Section 1.3, followed by the key contributions of this research work. Finally, the outline of this thesis is given in Section 1.5.

1.2 Overview of mmWave Wireless Communication Systems with High-Data-Rate over a Long Distance

1.2.1 Channel Characteristics

According to the discussion in Section 1.1, mmWave communications is considered as a promising technology that can provide ultra-high data rate for wireless communication systems Beyond 5G (B5G). On the other hand, mmWave wireless communications is still facing several challenges. One of the biggest concern for the mmWave wireless link is its propagation characteristics.

Figure 1.1 depicts the atmospheric attenuation of the electromagnetic wave within the mmWave band ranging from 1 GHz to 300 GHz. The figure shows that there are several peaks of attenuation in the mmWave band, which divide the mmWave band into several windows with relatively low attenuations. It can be observed that W-band ranging from 75 to 110 GHz is located in a window with low attenuation in both dry air and wet air cases, and the attenuation is only 0.4 - 0.6 dB/km even in wet air case. According to the Friis equation, the free-space path-loss (FSPL) L_{FS} is given by

$$L_{FS}(dB/km) = 32.4 + 20log(f) + 20log(d) \tag{1.1}$$

where f is the frequency in MHz, d is the distance between transmitter and receiver in kilometres (km). It can be derived that the FSPL of signal transmission over 1 km in the mmWave band between 30 - 300 GHz is from 122 dB to 142 dB, which indicates that the total loss is mainly determined by the FSPL rather than the atmospheric attenuation. However, compared with the FSPL of LTE 2.5 GHz band in the same condition, which is only 100 dB, the FSPL is much higher. Consequently, it is imperative to use the

high-gain antenna to compensate for the higher path loss for the mmWave link.

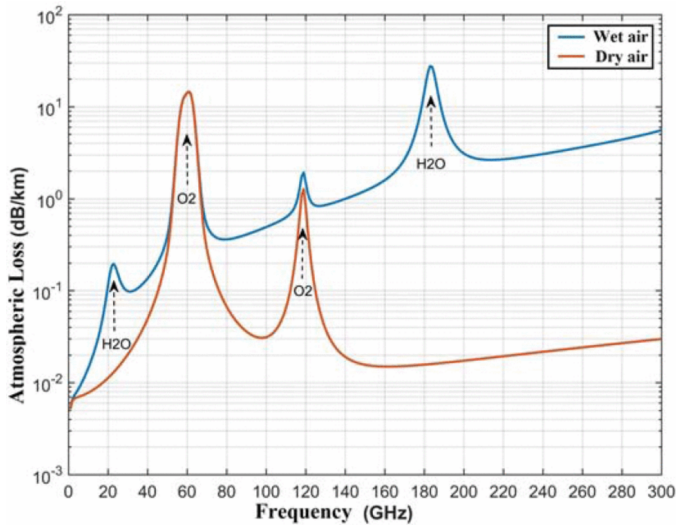

Figure 1.1: Atmospheric attenuation from 1 GHz to 300 GHz [11]

Besides FSPL and atmospheric attenuation, penetration losses and blockage also pose a significant challenge for mmWave communication. The measured results of the penetration losses through common building materials at 28 GHz are presented in [7]. It shows that outdoor tinted glass and brick pillars have high penetration losses of 40.1 dB and 28.3 dB, respectively. This means building penetration of mmWaves will be difficult for outdoor transmitters. The measurements carried out in [12] show that the average power can change by 25 dB when the receiver moves around a building corner from non-line-of-sight (NLOS) to line-of-sight LOS in an urban microcell (UMi) environment. Furthermore, human body blockage can cause more than 40 dB of fading.

1.2.2 High-data-rate mmWave Wireless Communication Systems with High-Data-Rate over a Long Distance

Since the mmWave band provides a large amount of bandwidth, the mmWave wireless communication system is designed to offer high data rate of several tens of Gbps or even up to 100 Gbps. In this section, we present several most representative state-of-the-art mmWave wireless communication systems with high data rate.

In 2012, a system working in 120 GHz band is demonstrated to be able to deliver 10 Gbps over up to 5.8 km in fine weather [13]. The bandwidth used in this system is 17 GHz. A pair of Cassegrain reflector antennas with gain up to 52 dBi is applied at the transmitting and receiving sides. The schematic of the system and the antenna used in this system are shown in Figure 1.2.

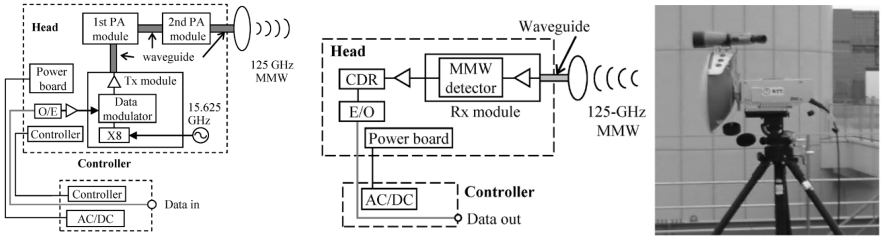

Figure 1.2: System schematic and the antenna used in the system [13]

In 2013, a wireless communication system at 237.5 GHz for data transmission over 20 m with a data rate of 100 Gpbs is reported in [14]. This system covers a large bandwidth of 35 GHz, and a pair of horn-fed lens antennas with a combined gain of 86 dBi is used in this system, as shown in Figure 1.3.

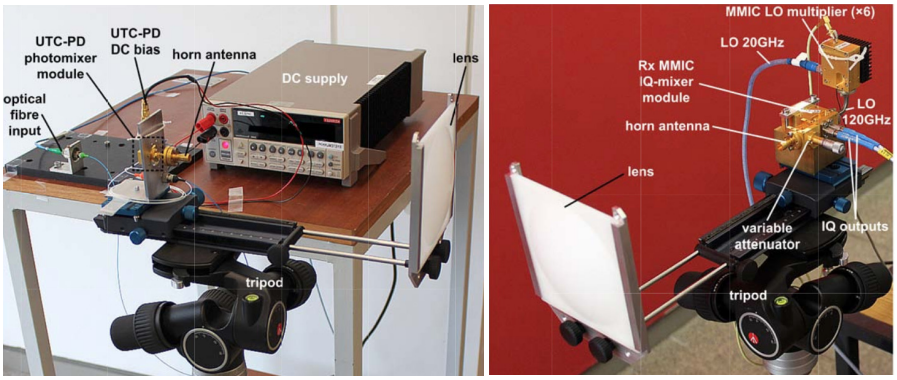

Figure 1.3: System schematic and the antenna used in the system [14]

Over the past few years, besides long transmission distance, much effort has been devoted to improving the spectrum efficiency for mmWave wireless links by introducing Polarization-Division-Multiplexing (PDM) technology, which is currently widely used in satellite broadcasting downlinks [15] and Point-to-Point (PtP) microwave links such as wireless backhaul links [16]. This technology allows two channels of information to

be transmitted on electromagnetic waves of two orthogonal polarizations at the same carrier frequency, thereby achieving twofold data rate without increasing the working bandwidth.

In 2016, a wireless transmission link at 85.5 GHz realizing 20 Gbps data rate over 1.7 km is demonstrated with 10.5-GHz bandwidth [17]. In this system, PDM is applied by using two pairs of 45-dBi Cassegrain reflector antenna to transmit and receive vertical and horizontal polarized signal, respectively. The schematic of the system and the antenna used in this system are shown in Figure 1.4. The same research group further demonstrates a 54-Gbps W-band signal transmission over a distance of 2.5 km using a similar system with 19-GHz bandwidth [18]. However, the antennas of these systems have a very large footprint because two pairs of Cassegrain reflectors are used.

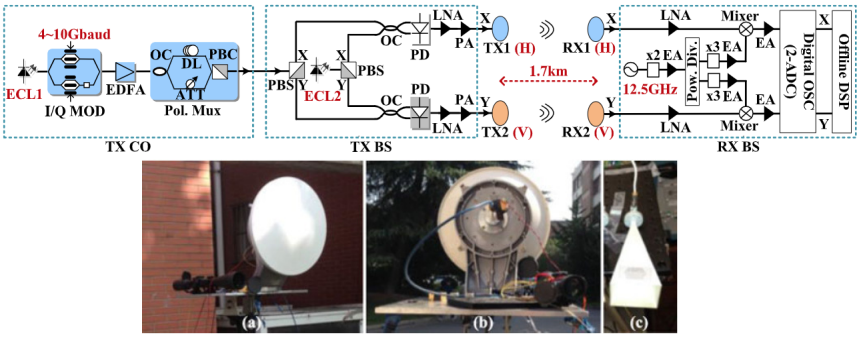

Figure 1.4: System schematic and the antenna used in the system [17]

In 2017, a wireless link of 38.1 Gbps over a distance of 16 km at E-band (60 - 90 GHz) is reported using a bandwidth of 8 GHz [19]. In this system, only one pair of Axial Displaced Ellipse (ADE) reflector antennas is employed as the vertical- and horizontal-polarized signals are multiplexed using an OMT before radiated by the horn-fed reflector antenna. The schematic of the system and the antenna used in this system are shown in Figure 1.5.

In-Band Full Duplex (IBFD) is also a promising technology that can increase the spectral efficiency. This technology allows the wireless communication system to transmit and receive signals at the same frequency at the same time so that spectral efficiency

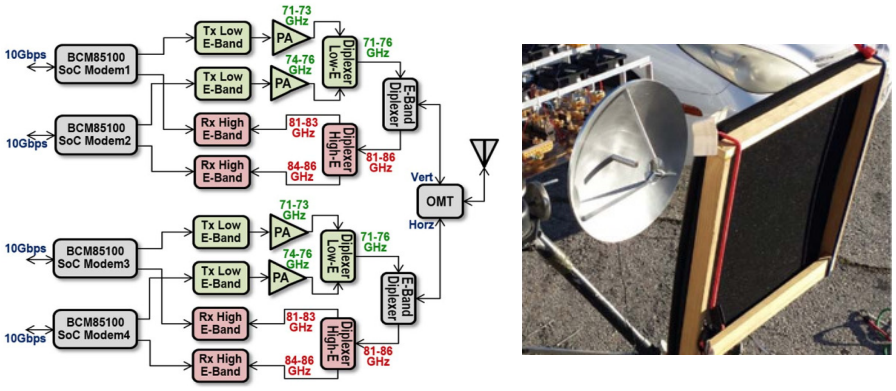

Figure 1.5: System schematic and the antenna used in the system [19]

can be doubled. Although currently this technology is proposed for 5G New Radio (NR) and most demonstrations are at the frequencies below 6 GHz [20], it is also applicable to mmWave wireless communication systems. In 2014, a W-band (75 - 110 GHz) full-duplex transmission is demonstrated by using two pairs of 25-dBi horn antenna which are vertically and horizontally polarized, respectively, as shown in Figure 1.6. A high data rate of 60 Gbps is achieved for both uplink and downlink channels over 1 m [21].

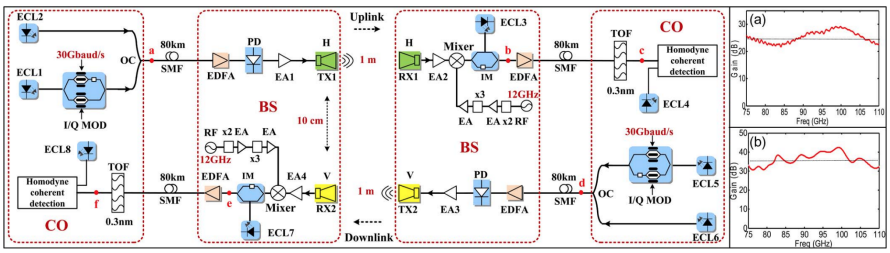

Figure 1.6: System schematic and the antenna used in the system [21]

The ultra-high-data-rate mmWave wireless link for long-haul applications has also attracted great interest of leading telecommunications equipment vendors, such as Huawei and Ericsson. Point-to-Point (PtP) links in the mmWave band with more than 100-Gbps capacity are envisaged to be commercially available before 2027 in a report from Ericsson [22]. Spectrum-efficient technologies, such as dual polarization and even Line-of-Sight (LOS) multiple-input multiple-output (MIMO), are also identified as key solutions toward 100-Gbps links [16], as shown in Figure 1.7. In 2019, Ericsson conducted a trial that successfully achieved error-free data rate up to 126 Gbps over 1.5 km in E-band

by using dual polarization and 4x4 LOS MIMO together. Four 0.6-m parabolic reflector antennas are used at both transmitting and receiving side to form a 4x4 LOS MIMO link with each antenna transmitting 2-channel signal on two orthogonal linear polarization. The antenna arrangement is shown in Figure 1.8. Recently, Huawei released its E-band solution that offers a single-link with 50 Gbps by using 2x2 LOS MIMO [23]. Additionally, a D-band (110 – 170 GHz) prototype is also under development in Huawei [24].

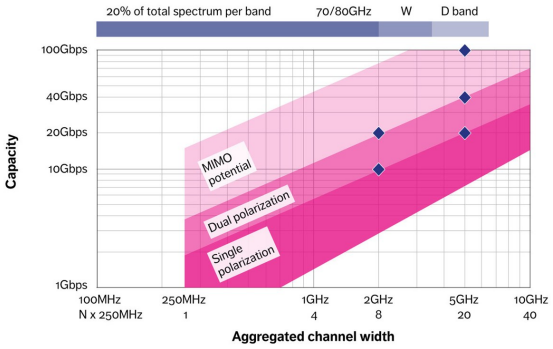

Figure 1.7: Realistic capacity versus channel bandwidth with single polarization, dual polarization and MIMO [16]

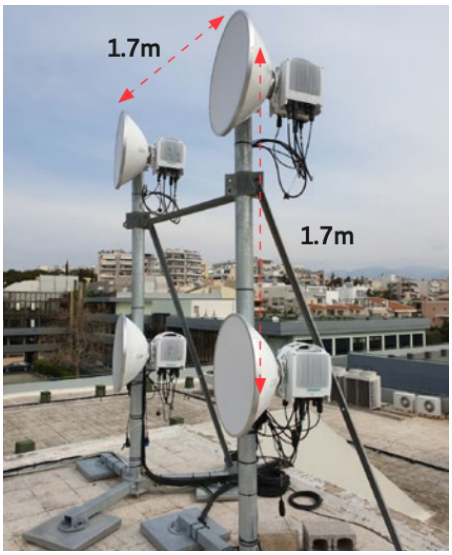

Figure 1.8: Antenna arrangement for the 100-Gbps link [22]

1.3 Research Motivation and Objectives

According to the channel characteristics and the mmWave wireless communication systems presented in Section 1.2, the requirement of the antenna that can be applied in the mmWave wireless communication system with an ultra-high data rate is derived in this section. In order to exploit the enormous bandwidth available in the mmWave band which is essential to achieve a high data rate as discussed in Section 1.1, the antenna of the mmWave wireless communication system should cover a wide bandwidth. Moreover, since the free space path loss is very high in the mmWave band, it is imperative to use a high-gain antenna to achieve acceptable transmission distance. The systems mentioned in Section 1.2.2 either use horn-fed reflector or horn-fed lens to achieve antenna gain from 43 to 52 dBi. It is well known that high reliability and spectral efficiency are the two uttermost challenges that all technologies involved in wireless communications are designed to address. Since the antenna plays an important role in the ultra-high-data-rate wireless system, it is anticipated that the antenna should have some features that would benefit the system in terms of reliability and spectral efficiency besides the essential characteristic of wide bandwidth and high gain.

According to Section 1.2.2, Polarization Division Multiplexing (PDM) are used in several systems to achieve twofold data rate without increasing the working bandwidth [17–19]. The antennas used in [17–19] are one or two pairs of horn-fed Cassegrain antennas with two orthogonal linear polarization. However, these systems are susceptible to polarization mismatch, which will lead to crosstalk between the two multiplexed wireless channels and degrade the reliability of the link.

For certain applications, Circular-Polarization (CP) antennas are preferable to Linear-Polarization (LP) antennas, such as radar [25], Global Navigation Satellite System (GNSS) [26–28], RFID [29] and satellite communications [30, 31], because it is able to suppress multipath fading and polarization misalignment thereby improving the reliability of the wireless link [32]. Millimetre-Wave (mmWave) wireless communications for point-to-point (PtP) and point-to-multipoint (PtMP) high-data-rate transmission could

also benefit from CP wireless links by using CP antennas [33].

The dual-circular-polarization (dual-CP) antenna, which is capable of simultaneously transmitting and receiving two orthogonal CP signals [left-hand circular polarization (LHCP) and right-hand circular polarization (RHCP)], will not only mitigate the cross-polarization interference resulted from propagation impairments and antenna misalignment but also enable PDM technology. Additionally, it is worth mentioning that the dual-CP antenna can also be used to realize In-Band Full Duplex (IBFD) [34] by using only one pair of antennas rather than two pairs like what is used in [21].

However, a significant level of isolation between the transmit (Tx) and receive (Rx) chains is required for the practical application of these systems. For example, a simple link budget calculation shows that total isolation levels higher than 100 dB between the Tx and Rx chains is required in the IBFD system [35, 36], and it is anticipated that isolation at least $>$ 20 dB should be provided at the antenna stage. A port isolation $>$ 30 dB is highly desirable in the mmWave wireless communication system offering high wireless link capacity, especially when IBFD is introduced.

Taking the characteristics of the high-data-rate mmWave wireless communications with long transmission distance and the requirement of PDM/IBFD technologies into account, the aim of this research is to design wideband dual-CP antennas with high isolation in a shared aperture, thereby realizing higher reliability and spectral efficiency for the mmWave wireless communication systems. The designed antennas should also have high gain or be able to achieve high gain when used as a feed to a reflector. The objectives of this research were as follows:

1. **To optimize the dual-CP antenna design that is based on the conventional stepped septum polarizer.**

   Since we identified dual-CP antenna based on waveguide structure could be a better candidate that is able to achieve a wide bandwidth $>$ 20% with isolation $>$ 20% in the mmWave band after review on all types of dual-CP antenna (see Chapter 2

for details), the stepped septum polarizer is used to design a wideband dual-CP antenna. The design of this type of dual-CP antenna needs to be optimized as a whole to achieve a wide bandwidth $> 20\%$ with isolation $> 20\%$.

2. **To further improve the performance of septum-polarizer-based dual-CP antenna in terms of port isolation and bandwidth.**
   After the optimization of dual-CP antenna that is based on the conventional stepped septum polarizer, the barrier that prevents this type of dual-CP antenna from achieving higher isolation over a wider bandwidth should be identified. Then the issue identified should be addressed by introducing necessary modification to the structures, so that the bandwidth and port isolation can be improved to be better than the best performance ever reported, which is isolation > 30 dB over 10% bandwidth.

3. **To propose and verify a new design of dual-CP antenna that can achieve higher isolation over wider bandwidth beyond the performance limitation of dual-CP antenna based on septum polarizer.**
   To further push the performance limit of dual-CP antenna to a new level in terms of isolation and bandwidth, a new type of dual-CP antenna needs to be designed to achieve results better than that of the dual-CP antenna based-on improved septum polarizer. The target is isolation > 30 dB over 25% bandwidth.

1.4 Key Contributions

The key contributions made in this work can be summarized as:

1. A wideband dual-CP antenna based on the stepped septum polarizer is designed in the W-band by applying a smooth-wall horn with a specific profile optimized to exploit the bandwidth and isolation potential of the septum polarizer, so that it can be employed in mmWave wireless communication systems to make use of the rich spectrum in the mmWave band.

2. An improved stepped septum polarizer with a 2-step design method is proposed to realize a dual-CP antenna.

   (a) This dual-CP antenna achieves higher isolation over a wider bandwidth than those based on the conventional septum polarizer.

   (b) The number of steps of the septum is also reduced in this design in comparison with the reported conventional septum polarizers that have similar performance, which will benefit the fabrication of dual-CP antennas based on the septum polarizer in the mmWave or even sub-THz band.

3. A novel wideband grooved-wall CP horn antenna with a septum-free structure is proposed, which is capable of generating dual CP when it is used together with an Orthomode Transducer (OMT).

   (a) To the best of the authors' knowledge, this new type of dual-CP antenna we proposed is demonstrated to achieve the highest isolation over the widest bandwidth among all types of dual-CP antennas ever reported. Besides high isolation and wide bandwidth, this new type of CP/dual-CP antenna can also achieve rotationally symmetric radiation patterns and low SLL.

   (b) With the septum-free structure, this new type of CP/dual-CP antenna can be easily scaled up to terahertz (THz) band, not like the CP/dual-CP antennas based on the septum structure whose working frequency is limited by the thickness of the septum.

4. Several state-of-the-art optimization techniques are explored and developed for the electromagnetic (EM) device design.

   (a) A Python-based software is developed to launch and control CST Microwave Studio full-wave simulations and analyze the result data exported during the simulation automatically, in which advanced algorithms, such as Covariance Matrix Adaptation Evolution Strategy (CMA-ES) algorithm, can easily be

integrated. This software facilitates the automatic optimization of complex EM devices with the state-of-the-art optimization algorithms, and has been applied in the antenna design in this research.

(b) A novel design method for EM devices is proposed. In this method, a deep-learning-based inverse modelling is introduced to generate candidate design which is further optimized in a limited solution space using CMA-ES. This method is suitable for generating new designs for complex EM devices with many design parameters and multiple objectives at a reduced computational cost base on the historical design data. This method is applied and verified in the design of a W-band septum polarizer.

1.5 Outline of the thesis

The outline of this thesis is summarized as follows.

Chapter 2 provides theoretical background of circular polarization and a review on a variety types of dual-CP antenna which could meet the requirement. Additionally, antenna design/optimization techniques and measurement method for CP antennas is also covered.

Chapter 3 presents a wideband dual-CP antenna based on the stepped septum polarizer. A smooth-wall horn with a specific profile is designed and optimized, and then applied to the optimized stepped septum polarizer.

Chapter 4 delivers a novel design of a grooved-wall septum polarizer to improve the bandwidth and isolation performance of the conventional septum polarizer. A dual-CP antenna is also designed based on the proposed grooved-wall septum polarizer.

Chapter 5 proposes a novel type of CP horn and a dual-CP antenna based on it. This antenna is designed to have a septum-free structure by introducing a pair of grooves on the wall of a conical horn to serve as an inbuilt polarize.

Chapter 6 generalizes the approach in Chapter 5 and designs a novel dual-CP antenna based on a multi-section grooved-wall CP horn, which introduces grooves with various widths and depths for each section.

Chapter 7 summarises the outcomes achieved in this work and presents some thoughts for future work.

References

[1] F. Boccardi, R. W. Heath, A. Lozano, T. L. Marzetta, and P. Popovski, "Five disruptive technology directions for 5G," *IEEE Communications Magazine*, vol. 52, no. 2, pp. 74–80, 2014.

[2] N. Maziar, W. Yue, T. Milos, W. Shangbin, Q. Yinan, and A.-I. Mohammed, "Overview of 5G modulation and waveforms candidates," *Journal of Communications and Information Networks*, vol. 1, no. 1, pp. 44–60, 2016. [Online]. Available: https://doi.org/10.1007/BF03391545

[3] M. R. Akdeniz, Y. Liu, M. K. Samimi, S. Sun, S. Rangan, T. S. Rappaport, and E. Erkip, "Millimeter Wave Channel Modeling and Cellular Capacity Evaluation," *IEEE Journal on Selected Areas in Communications*, vol. 32, no. 6, pp. 1164–1179, 2014.

[4] I. A. Hemadeh, K. Satyanarayana, M. El-Hajjar, and L. Hanzo, "Millimeter-Wave Communications: Physical Channel Models, Design Considerations, Antenna Constructions, and Link-Budget," *IEEE Communications Surveys Tutorials*, vol. 20, no. 2, pp. 870–913, 2018.

[5] W. Hong, Z. H. Jiang, C. Yu, D. Hou, H. Wang, C. Guo, Y. Hu, L. Kuai, Y. Yu, Z. Jiang, Z. Chen, J. Chen, Z. Yu, J. Zhai, N. Zhang, L. Tian, F. Wu, G. Yang, Z. C. Hao, and J. Y. Zhou, "The Role of Millimeter-Wave Technologies in 5G/6G Wireless Communications," *IEEE Journal of Microwaves*, vol. 1, no. 1, pp. 101–122, 2021.

[6] T. S. Rappaport, Y. Xing, G. R. MacCartney, A. F. Molisch, E. Mellios, and J. Zhang, "Overview of Millimeter Wave Communications for Fifth-Generation (5G)

Wireless Networks—With a Focus on Propagation Models," *IEEE Transactions on Antennas and Propagation*, vol. 65, no. 12, pp. 6213–6230, 2017.

[7] T. S. Rappaport, S. Sun, R. Mayzus, H. Zhao, Y. Azar, K. Wang, G. N. Wong, J. K. Schulz, M. Samimi, and F. Gutierrez, "Millimeter Wave Mobile Communications for 5G Cellular: It Will Work!" *IEEE Access*, vol. 1, pp. 335–349, 2013.

[8] A. N. Uwaechia and N. M. Mahyuddin, "A Comprehensive Survey on Millimeter Wave Communications for Fifth-Generation Wireless Networks: Feasibility and Challenges," *IEEE Access*, vol. 8, pp. 62 367–62 414, 2020.

[9] W. Roh, J. Y. Seol, J. Park, B. Lee, J. Lee, Y. Kim, J. Cho, K. Cheun, and F. Aryanfar, "Millimeter-wave beamforming as an enabling technology for 5G cellular communications: theoretical feasibility and prototype results," pp. 106–113, 2014.

[10] T. Kürner and S. Priebe, "Towards THz Communications - Status in Research, Standardization and Regulation," *Journal of Infrared, Millimeter, and Terahertz Waves*, vol. 35, no. 1, pp. 53–62, 2014. [Online]. Available: http://dx.doi.org/10.1007/s10762-013-0014-3

[11] X. Li, J. Yu, and G. Chang, "Photonics-Assisted Technologies for Extreme Broadband 5G Wireless Communications," *Journal of Lightwave Technology*, vol. 37, no. 12, pp. 2851–2865, 2019.

[12] T. S. Rappaport, G. R. MacCartney, S. Sun, H. Yan, and S. Deng, "Small-Scale, Local Area, and Transitional Millimeter Wave Propagation for 5G Communications," *IEEE Transactions on Antennas and Propagation*, vol. 65, no. 12, pp. 6474–6490, 2017.

[13] A. Hirata, T. Kosugi, H. Takahashi, J. Takeuchi, H. Togo, M. Yaita, N. Kukutsu, K. Aihara, K. Murata, Y. Sato, T. Nagatsuma, and Y. Kado, "120-GHz-Band Wireless Link Technologies for Outdoor 10-Gbit/s Data Transmission," pp. 881–895, 2012.

[14] KoenigS., Lopez-DiazD., AntesJ., BoesF., HennebergerR., LeutherA., TessmannA., SchmogrowR., HillerkussD., PalmerR., ZwickT., KoosC., FreudeW., AmbacherO., LeutholdJ., and KallfassI., "Wireless sub-THz communication system with high

data rate," *Nat Photon*, vol. 7, no. 12, pp. 977–981, 12 2013. [Online]. Available: http://dx.doi.org/10.1038/nphoton.2013.275http://10.0.4.14/nphoton.2013.275http://www.nature.com/nphoton/journal/v7/n12/abs/nphoton.2013.275.html#supplementary-information

[15] H. Vasseur, "Degradation of availability performance in dual-polarized satellite communications systems," *IEEE Transactions on Communications*, vol. 48, no. 3, pp. 465–472, 2000.

[16] J. Edstam, J. Hansryd, S. Carpenter, T. Emanuelsson, Y. Li, and H. Zirath. (2017, Feb.) Microwave backhaul evolution – reaching beyond 100ghz. Tech. Review Article. [Online]. Available: https://www.ericsson.com/en/reports-and-papers/ericsson-technology-review/articles/microwave-backhaul-evolution-reaching-beyond-100ghz

[17] X. Li, J. Xiao, and J. Yu, "Long-Distance Wireless mm-Wave Signal Delivery at W-Band," *Journal of Lightwave Technology*, vol. 34, no. 2, pp. 661–668, 2016.

[18] X. Li, J. Yu, K. Wang, Y. Xu, L. Chen, L. Zhao, and W. Zhou, "Delivery of 54-Gb/s 8QAM W-Band Signal and 32-Gb/s 16QAM K -Band Signal Over 20-km SMF-28 and 2500-m Wireless Distance," *Journal of Lightwave Technology*, vol. 36, no. 1, pp. 50–56, 2018.

[19] K. Brown, A. Brown, T. Feenstra, D. Gritters, E. Ko, S. O'Connor, M. Sotelo, and Raytheon, "Long-range wireless link with fiber-equivalent data rate," in *2017 IEEE MTT-S International Microwave Symposium (IMS)*, 2017, pp. 809–811.

[20] K. E. Kolodziej, B. T. Perry, and J. S. Herd, "In-Band Full-Duplex Technology: Techniques and Systems Survey," *IEEE Transactions on Microwave Theory and Techniques*, vol. 67, no. 7, pp. 3025–3041, 2019.

[21] Y. Xu, Z. Zhang, X. Li, J. Xiao, and J. Yu, "Demonstration of 60 Gb/s W-Band Optical mm-wave Signal Full-Duplex Transmission Over Fiber-Wireless-Fiber Network," *IEEE Communications Letters*, vol. 18, no. 12, pp. 2105–2108, 2014.

[22] Ericsson. (2019, Oct.) Breaking the 100 gbps barrier. [Online]. Available: https://www.ericsson.com/4aedf7/assets/local/reports-papers/microwave-outlook/2019/breaking-the-100-gbps-barrier-article-co-screen.pdf

[23] Huawei. (2020, Feb.) Huawei released innovative 5g microwave 50 gbps solution to continuously build a simplified, ultra-broadband, and easy-to-deploy 5g transport network. [Online]. Available: https://www.huawei.com/en/news/2020/2/innovative-5g-microwave-50gbps-solution

[24] G. Roveda and M. Costa, "Flexible Use of D Band Spectrum for 5G Transport: a Research Field Trial as Input to Standardization," in *2018 IEEE 29th Annual International Symposium on Personal, Indoor and Mobile Radio Communications (PIMRC)*, 2018, pp. 800–804.

[25] Y. He, C. Gu, H. Ma, J. Zhu, and G. V. Eleftheriades, "Miniaturized Circularly Polarized Doppler Radar for Human Vital Sign Detection," *IEEE Transactions on Antennas and Propagation*, vol. 67, no. 11, pp. 7022–7030, 2019.

[26] Z. Wang, S. Fang, S. Fu, and S. Lu, "Dual-Band Probe-Fed Stacked Patch Antenna for GNSS Applications," *IEEE Antennas and Wireless Propagation Letters*, vol. 8, pp. 100–103, 2009.

[27] M. Maqsood, S. Gao, T. W. C. Brown, M. Unwin, R. de vos Van Steenwijk, J. D. Xu, and C. I. Underwood, "Low-Cost Dual-Band Circularly Polarized Switched-Beam Array for Global Navigation Satellite System," *IEEE Transactions on Antennas and Propagation*, vol. 62, no. 4, pp. 1975–1982, 2014.

[28] R. Xu, S. S. Gao, J. Li, K. Wei, and Q. Luo, "A Reconfigurable Dual-Band Dual-Circularly Polarized Antenna for Vehicle Global Navigation Satellite System Application," *IEEE Transactions on Vehicular Technology*, vol. 69, no. 10, pp. 11 857–11 867, 2020.

[29] Y. Yao, X. Ren, Y. Liang, J. Yu, and X. Chen, "Multipolarized Reader Antenna With Periodic Units Based on Electric Field Coupling for UHF RFID Near-Field Applications," *IEEE Transactions on Antennas and Propagation*, vol. 67, no. 8, pp. 5265–5271, 2019.

[30] C. Mao, S. Gao, Y. Wang, Q. Chu, and X. Yang, "Dual-Band Circularly Polarized Shared-Aperture Array for C -/ X -Band Satellite Communications," *IEEE Transactions on Antennas and Propagation*, vol. 65, no. 10, pp. 5171–5178, 2017.

[31] G. Mishra, S. K. Sharma, and J. S. Chieh, "A Circular Polarized Feed Horn With

Inbuilt Polarizer for Offset Reflector Antenna for W-Band CubeSat Applications," *IEEE Transactions on Antennas and Propagation*, vol. 67, no. 3, pp. 1904–1909, 2019.

[32] S. Gao, Q. Luo, and F. Zhu, *Circularly Polarized Antennas*. Chichester, UK: John Wiley & Sons, Ltd, 1 2014.

[33] Y. Yao, X. Cheng, C. Wang, J. Yu, and X. Chen, "Wideband Circularly Polarized Antipodal Curvedly Tapered Slot Antenna Array for 5G Applications," *IEEE Journal on Selected Areas in Communications*, vol. 35, no. 7, pp. 1539–1549, 2017.

[34] A. Sabharwal, P. Schniter, D. Guo, D. W. Bliss, S. Rangarajan, and R. Wichman, "In-Band Full-Duplex Wireless: Challenges and Opportunities," *IEEE Journal on Selected Areas in Communications*, vol. 32, no. 9, pp. 1637–1652, 2014.

[35] J. Wu, M. Li, and N. Behdad, "A Wideband, Unidirectional Circularly Polarized Antenna for Full-Duplex Applications," *IEEE Transactions on Antennas and Propagation*, vol. 66, no. 3, pp. 1559–1563, 2018.

[36] H. Nawaz, A. U. Niazi, M. Abdul Basit, and M. Usman, "Single Layer, Differentially Driven, LHCP Antenna With Improved Isolation for Full Duplex Wireless Applications," *IEEE Access*, vol. 7, pp. 169 796–169 806, 2019.

Chapter 2

Circularly-Polarized Antenna Fundamentals, Review, Design Optimization and Measurement

In Chapter 1, we proposed to design wideband dual-circular-polarization (dual-CP) antennas for ultra-high-data-rate mmWave wireless systems with long-distance applications, such as backhaul and fronthaul links of 5G or Beyond-5G (B5G) networks, as CP antennas have a number of advantages compared with linearly polarized (LP) antennas, especially for long-distance transmission.

In this Chapter, the fundamentals of CP antenna is presented in Section 2.1. Section 2.2 gives a review on dual-CP antennas. The antenna design/optimization approaches and CP antenna measurement method we used or proposed in this research is provided in Section 2.3 and Section 2.4, respectively. Section 2.5 concludes this chapter.

2.1 Circular-Polarization Antenna Fundamentals

2.1.1 Polarization and Axial Ratio

A radio wave propagating over a long distance, as in the mmWave wireless links presented in Chapter 1, is always in the form of a plane wave, which has no field components in the propagation direction (z direction). The instantaneous field of a plane wave travelling in the z direction, can be written as

$$\boldsymbol{E} = \boldsymbol{e_x} E_x + \boldsymbol{e_y} E_y \tag{2.1}$$

where E_x and E_y are the components in x and y direction, respectively, and is given by

$$E_x = E_{xm} cos(\omega t - kz + \phi_x) \tag{2.2a}$$

$$E_y = E_{ym} cos(\omega t - kz + \phi_y) \tag{2.2b}$$

where E_{xm} and E_{ym} are, respectively, the maximum magnitudes of the x and y components. $k = 2\pi/\lambda$ is the wavenumber.

Polarization can be categorized as linear, circular, or elliptical, according to the direction of its electric field vector $\boldsymbol{E}$. Without loss of generality, we assume $z = 0$ in the following discussion, so equation (2.2) can be written as

$$E_x = E_{xm} cos(\omega t + \phi_x) \tag{2.3a}$$

$$E_y = E_{ym} cos(\omega t + \phi_y) \tag{2.3b}$$

2.1.1.1 Linear Polarization

If the phase difference between the two components satisfies

$$\Delta\phi = \phi_y - \phi_x = n\pi, \quad n = 0, \pm 1, \pm 2, ... \tag{2.4}$$

the magnitude of electric field vector $\boldsymbol{E}$ can be derived as

$$E = \sqrt{E_x^2 + E_y^2} = \sqrt{E_{xm}^2 + E_{ym}^2} cos(\omega t + \phi_x) \tag{2.5}$$

The tilt of the direction of the electric field vector, relative to the x axis, is represented by the angle α given by

$$\alpha = arctan\left(\frac{E_y}{E_x}\right) = arctan\left(\frac{E_{ym}}{E_{xm}}\right) \tag{2.6}$$

It can be found from equation (2.5) and equation (2.6) that, the magnitude of electric field vector will vary as a function of time while the direction of the electric field vector is always directed along a line, as shown in Figure 2.1. For this reason, this field is characterized as linearly polarized.

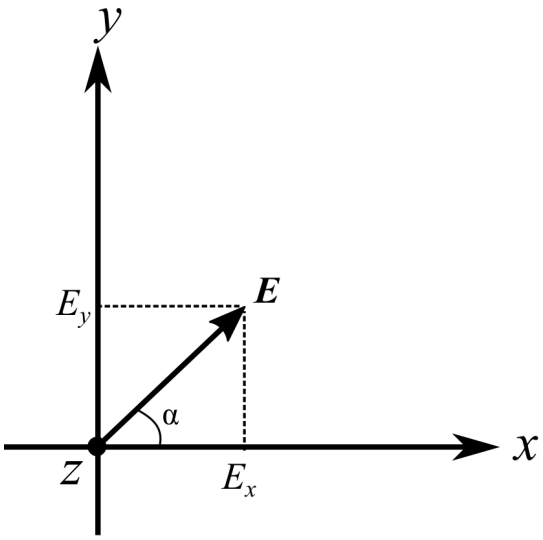

Figure 2.1: E-field vector of linear polarization

2.1.1.2 Circular Polarization

Circular Polarization can be achieved only if the magnitudes of the x and y components are the same and the phase difference between them is odd multiples of $\pi/2$, that is

$$E_{xm} = E_{ym} = E_m \tag{2.7}$$

$$\Delta\phi = \phi_y - \phi_x = \pm\frac{\pi}{2} + 2n\pi, \quad n = 0, 1, 2, ... \tag{2.8}$$

Suppose $\phi_y - \phi_x = \pi/2$, it can be derived from equation (2.3) that

$$E_x = E_m cos(\omega t + \phi_x) \tag{2.9a}$$

$$E_y = E_m cos(\omega t + \phi_x + \pi/2) = -E_m sin(\omega t + \phi_x) \tag{2.9b}$$

hence the magnitude of $\boldsymbol{E}$ and α can be obtained as

$$E = \sqrt{E_x^2 + E_y^2} = E_m \tag{2.10}$$

$$\alpha = arctan\left(\frac{E_y}{E_x}\right) = -(\omega t + \phi_x) \tag{2.11}$$

It can be found that the magnitude of the electric field vector is a constant, while the direction varies as a function of time. This means the electric field vector rotates along the propagation direction – tracing a circle on the xy plane, as indicated in Figure 2.2. For this reason, the electric field is said to be circularly polarized. In this case, i.e., when $\phi_y - \phi_x = \pi/2$, the electric field vector rotates in a counterclockwise sense as the wave is viewed along the direction of wave propagation, which is designated as Left-Hand Circular Polarization (LHCP), as indicated in Figure 2.2(a). In case that $\phi_y - \phi_x = -\pi/2$, it can be derived that

$$\alpha = arctan\left(\frac{E_y}{E_x}\right) = \omega t + \phi_x \tag{2.12}$$

This implies that the electric field vector rotates in a clockwise sense as the wave is viewed along the direction of propagation, and the wave is designated as Right-Hand Circular Polarization (RHCP), as indicated in Figure 2.2(b).

2.1.1.3 Elliptical Polarization

In reality, however, the phase difference between x and y components is not equal to multiples of $\pi/2$ or their magnitudes are not the same.

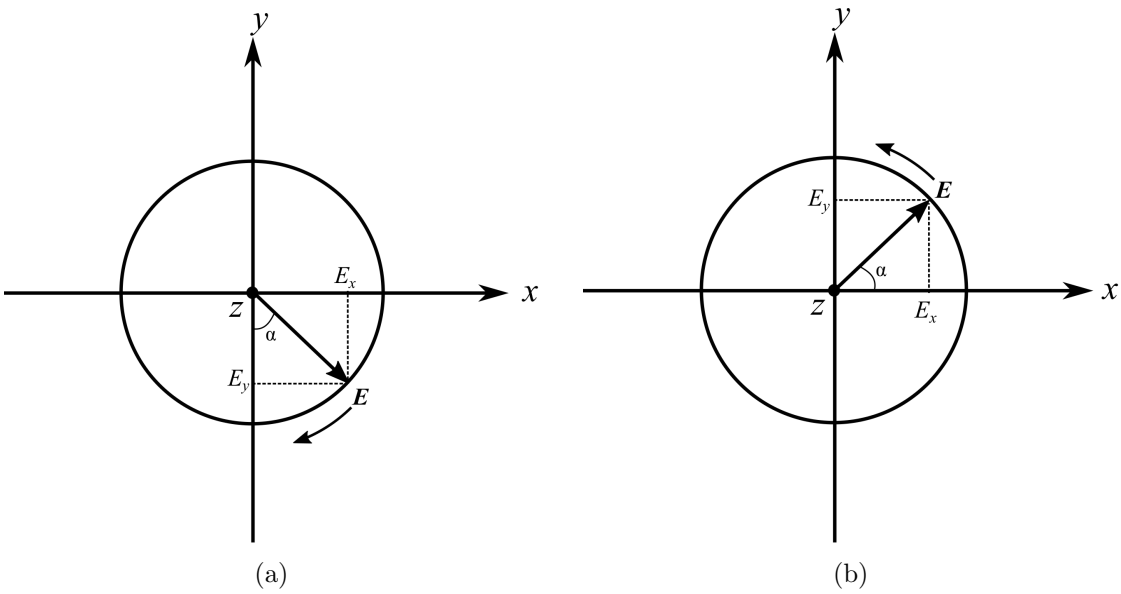

(a) (b)

Figure 2.2: E-field vector of circular polarization (a) LHCP and (b) RHCP.

For simplicity, let $\phi_x = 0$, $\phi_y = \phi$, then we have

$$E_x = E_{xm}cos(\omega t) \tag{2.13a}$$

$$E_y = E_{ym}cos(\omega t + \phi) \tag{2.13b}$$

It can be derived from equation (2.13) that

$$\frac{E_x^2}{E_{xm}^2} + \frac{E_y^2}{E_{ym}^2} - \frac{2E_x^2E_y^2}{E_{xm}^2E_{ym}^2}cos\phi = sin^2\phi \tag{2.14}$$

which is an ellipse equation. This means the figure that the electric field traces is an ellipse, as shown in Figure 2.3, and the field is said to be elliptically polarized. Linear and circular polarizations can be considered as special cases of elliptical. The tilt of the direction of the electric field vector relative to the x axis is

$$\alpha = arctan\left[\frac{E_{ym}}{E_{xm}}(cos\phi - sin\phi tan(\omega t))\right] \tag{2.15}$$

Left-hand polarization and right-hand polarization are also applicable to elliptical polarization. When $0 < \phi < \pi$, the electric field vector rotates in a counterclockwise sense as

observed along the direction of wave propagation hence left-hand elliptical polarization. When $0 < \phi < \pi$, the electric field vector rotates in a clockwise sense as observed along the direction of wave propagation hence right-hand elliptical polarization.

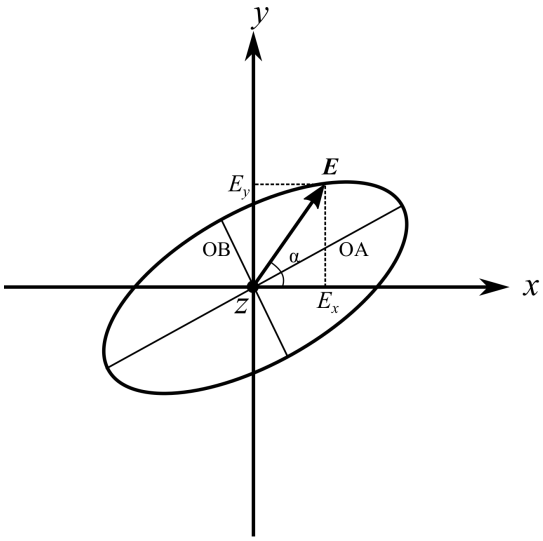

Figure 2.3: E-field vector of elliptical polarization

The ratio of the major axis to the minor axis of the ellipse shown in Figure 2.3 is referred to as the axial ratio (AR), and it is equal to

$$ar = \frac{major\ axis}{minor\ axis} = \frac{OA}{OB}, \qquad 1 \leq ar \leq \infty \tag{2.16a}$$

$$AR[dB] = 20log(ar) \tag{2.16b}$$

The polarization of an antenna can be defined by the polarization of the radiated fields produced by an antenna, evaluated in the far-field. Consequently, antennas can be classified as: linearly polarized (LP), circularly polarized (CP) and elliptically polarized (EP). For an elliptically polarized antenna, if its AR is 0 dB, it is a perfect CP antenna. In practice, when the axial ratio is less than 3 dB, the antenna is usually accepted as a CP antenna [1, 2].

2.1.2 Bandwidth of CP Antennas

Since AR is a key parameter of a CP antenna, the CP antenna should be designed to have AR lower than a certain value within the expected operating frequency range. The 3-dB AR bandwidth, which is determined by the frequency range within which the AR of the antenna keeps under 3 dB, is usually used to evaluate the bandwidth of a CP antenna together with the impedance bandwidth because 3-dB AR is required for a CP antenna. Therefore, usually the bandwidth of a CP antenna is no larger than the overlapping frequency range of the impedance bandwidth and 3-dB AR bandwidth.

2.1.3 Advantages of CP Radiation

There are several key advantages for circular polarization over linear polarization.

Firstly, wireless links using CP antennas are not susceptible to the polarization mismatch losses compared with those using LP antennas, especially in the applications where the alignment between transmitting and receiving antennas is difficult to maintain, such as mobile satellite communications. Strict antenna alignment between the transmitter and receiver is not required when CP antennas are used, and the receiving signal level can be relatively stable regardless of the antenna orientation.

Secondly, the CP antenna is able to suppress multipath fading or interference. Because the reflection of a CP wave will be in an opposite sense of rotation, the reflected signal will not be received by the receiving CP antenna. For example, the signal transmitting from an RHCP antenna will become LHCP after it is reflected from ground or other surfaces, and an RHCP receiving antenna would reject these reflected signals, thereby reducing the multipath fading or interference from the reflected signals.

Thirdly, CP signals are not subject to the Faraday rotation effect in the ionosphere [3]. This effect occurs as a wave passes through the ionosphere and undergoes a rotation of its polarization orientation angle, which causes the depolarization of linearly polarized signals. For this reason, again, the polarization match between the antennas can be

maintained without the use of complex tracking systems.

2.2 Review on Dual-CP Antennas

According to the discussion in Chapter 1, the mmWave wireless communication systems can benefit from employing dual-CP antennas, and we aim to design wideband dual-CP antennas with high isolation. In this section, we present a review on a variety of antennas and components proposed to realize dual CP from microwave band to mmWave band.

2.2.1 Dipole/Monopole, Patch and Slot Dual-CP Antennas

Dipole/monopole, patch and slot antennas are widely used in the lower microwave band below 5 GHz, which have low cost and are smaller in size. A number of dual-CP antennas based on these types are also developed to achieve wideband for various applications [4–10]. The highest port isolation over the widest bandwidth reported for this type of dual-CP antenna is isolation $>$ 20 dB over 80.7% bandwidth from 3.74 to 8.8 GHz [10]. The schematic and prototype of this antenna is shown in Figure 2.4. This planar monopole antenna is fed by dual orthogonal microstrip lines, and circular polarization is achieved with a modified ground-plane structure. The high isolation between the ports is realized by placing a diagonally protruded strip of from the lower edge of the monopole between the feed lines to form an isolation network. The combination of L-shaped strips (LSSs) and inverted LSSs are designed along the radiating edges of the monopole, in order to maximize the AR bandwidth, when they are placed $\lambda_g/4$ apart at centre frequency of the CP band. However, this antenna shows different maximum radiation directions for LHCP and RHCP at the same frequency, and unstable radiation patterns across the operating bandwidth, which is not desirable for wireless communication. In [5], a wideband dual-CP antenna is proposed to address this issue and achieves a bandwidth of 53.4% from 1.07 to 1.85 GHz for Intelligent Transport Systems (ITS), as shown in Figure 2.5. In this antenna design, an integrated feed network consisting of an orthogonal power divider (OPD) and four phase shifters is designed to provide two sets

of equal magnitude and quadrature phase to the crossed dipoles for dual-CP radiation. By designing a symmetrical radiator backed by a square copper sheet as the antenna reflector, this dipole-based antenna achieves wide bandwidth for DCP radiation with unidirectional and symmetrical radiation patterns. However, the isolation is limited to 15.2 dB, and a reflector used to achieve unidirectional radiation pattern increases the size and profile.

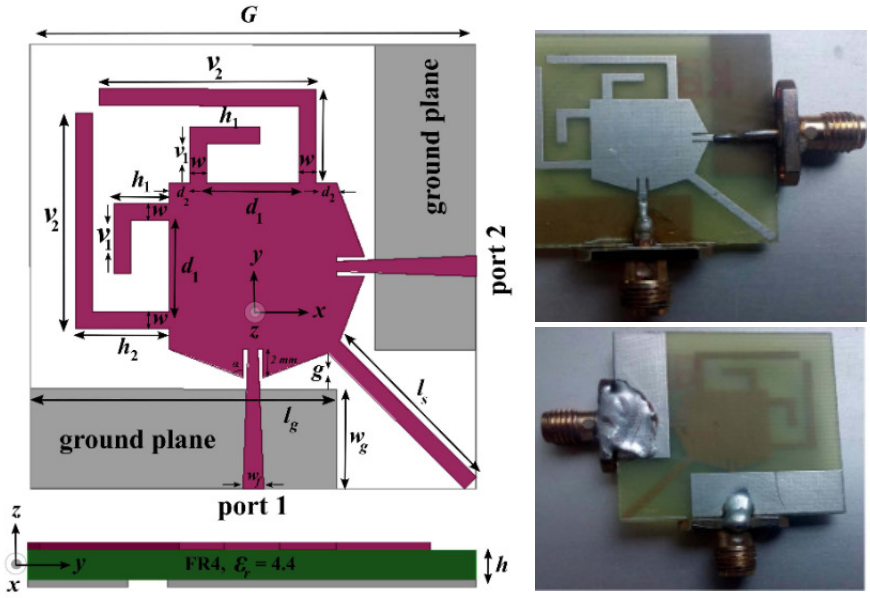

Figure 2.4: Schematic and prototype of the dual-CP antenna proposed in [10]

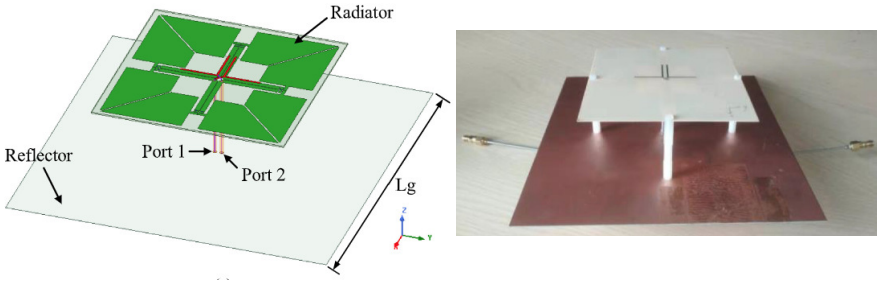

Figure 2.5: Schematic and prototype of the dual-CP antenna proposed in [5]

All of these types of antenna show low gains and will face the loss issue of feeding network if they are scaled to arrays in the mmWave band.

2.2.2 Dual-CP Microstrip antenna array

Microstrip antenna array is an attractive candidate in the microwave band below 30 GHz as they can offer low profile and acceptable gain, and is widely investigated [11–16]. The highest port isolation over the widest bandwidth reported for this type of dual-CP antenna is isolation > 20 dB over 14.7% bandwidth in the X-band [13]. The radiating element and the prototype of the array are shown in Figure 2.6. This antenna array uses double-stacked microstrip patches as radiation elements. Each element is fed by two via holes and a hybrid circuit to create two orthogonal modes in the microstrip patch and the dual circular polarization.

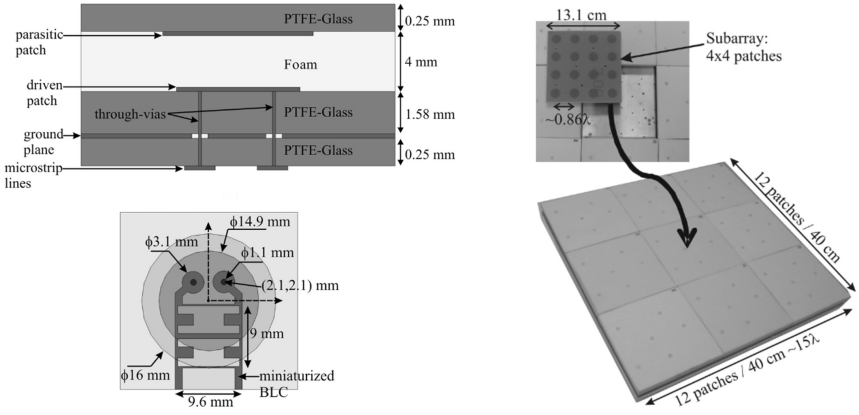

Figure 2.6: Radiating element and prototype of the dual-CP antenna array proposed in [13]

The technique of sequentially rotating each patch element together with an appropriate offset in the feed excitation phase, which is described in [17] and used to increase both the impedance and AR bandwidths of CP microstrip arrays consisting of relatively narrowband radiating elements, has also been applied to the dual-CP microstrip array design [11, 18]. This technique enables errors in the radiated polarisation of each element to be cancelled by the adjacent element, and reflections from the mismatched elements off resonance add destructively at the corporate feed input terminal. The analysis in [18] shows the port isolation is not improved by applying this technique, and the feeding phase shifts are introduced to cancel the coupled signals within the feed networks hence achieving isolation > 30 dB over 9% bandwidth with AR < 4 dB. However, main lobes

are squinted, and sidelobe levels are significantly increased. A more recent work using interlaced sequentially rotated feed (see Figure 2.7) to suppress the sidelobes and reduced the number of radiating elements in a dual-CP microstrip array shows port isolation > 12 dB over 10.5% bandwidth (5.05 - 5.61 GHz) with AR < 3 dB [11].

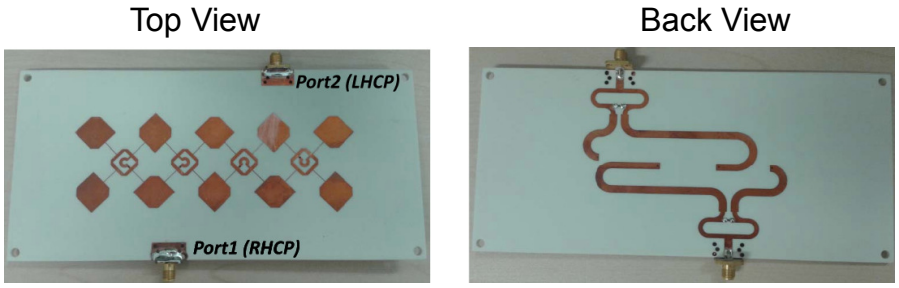

Figure 2.7: Prototype of the dual-CP microstrip array proposed in [11]

Dual-CP antenna arrays with elements and/or feeding networks based on Substrate Integrated Waveguide (SIW) are proposed to overcome the high-loss issue of the microstrip antenna array in the mmWave band up to 69 GHz [19–23]. The antenna array proposed in [22] consists of cross-slot-coupled cavity-backed square patch antenna elements fed by a SIW network where parallel structure is applied to achieve wide bandwidth. The CP is achieved by equally separate the signals into two components propagating orthogonally along the SIW paths with a path difference of a quarter wavelength using the 45° slanted crossed slot. Although this antenna array (see Figure 2.8) shows a wide bandwidth of 23% in the 60 GHz band and has the advantages of low cost and light in weight, the port isolation is only higher than 14 dB over the operating bandwidth. In [23], a SIW-based parallel-plate long-slot array antenna is reported to work in the W-band with low sidelobe level (SLL). However, it shows a port isolation is still limited to 15 dB, and the bandwidth is limited to 1%.

2.2.3 Dual-CP Metasurface Antenna

Metasurface (MTS) antenna is demonstrated to be another option to realize dual-CP with high gain and low profile in [24]. The dual-CP generation of this antenna is based on the interaction of two cylindrical-wavefront surface wave (SW) modes of trans-

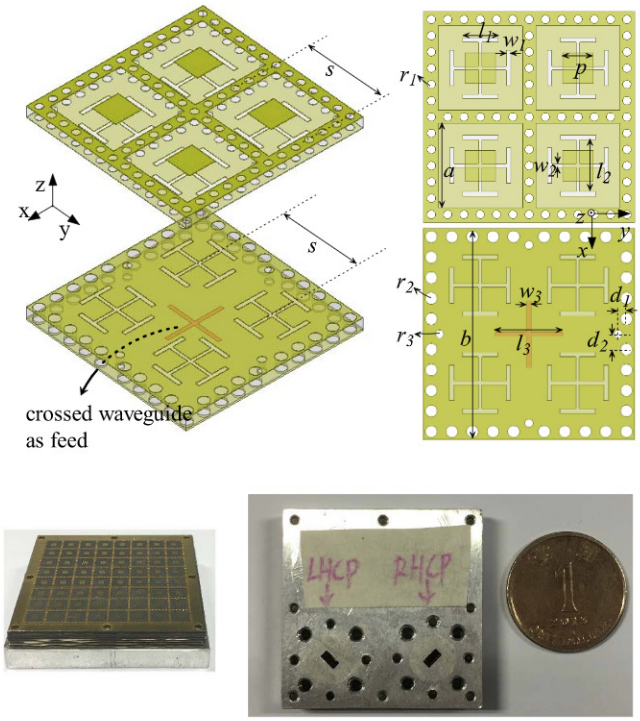

Figure 2.8: Radiating element and prototype of the dual-CP antenna array proposed in [22]

verse electric (TE) and transverse magnetic (TM) types with a rotationally symmetric, anisotropic-modulated MTS placed on top of a grounded slab. Nevertheless, the working frequency reported currently is in the microwave band (Ku-band), the bandwidth is narrow (around 0.5%), and the port isolation of the feed is only around 11 dB. The prototypes of the feed and metasurface antenna are shown in Figure 2.9.

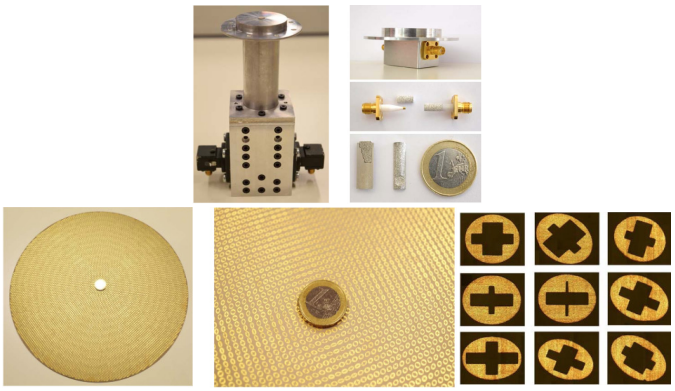

Figure 2.9: Prototypes of the feed and metasurface antenna proposed in [24]

2.2.4 Dual-CP Antennas Based on the Septum Polarizer

Another widely used type of dual-CP antenna is based on the waveguide septum polarizer which can generate dual CP with a compact size. The operating principle of the septum polarizer is illustrated in [25] and will be revisited later in Chapter 3 by full-wave simulation. A horn antenna or a waveguide array is usually connected to the septum polarizer to achieve good dual-CP radiation performance. This structure can be applied both in the microwave band [26–30] and mmWave band [31].

In [29], a feed horn with integrated septum polarizer working in Ka-band (28.5 - 31.2 GHz) is designed and fabricated as one piece using selective laser melting (SLM) technology. The measured results show a high isolation $>$ 27 dB is achieved over a bandwidth of 9% with AR $<$ 0.7 dB. The septum polarizer used in this antenna has a 4-step septum. The feed horn is a smooth-wall horn whose profile is divided into 15 linear sections and then optimized. The geometric structure of the septum polarizer and feed horn profile as well as a photo of the prototype are shown in Figure 2.10

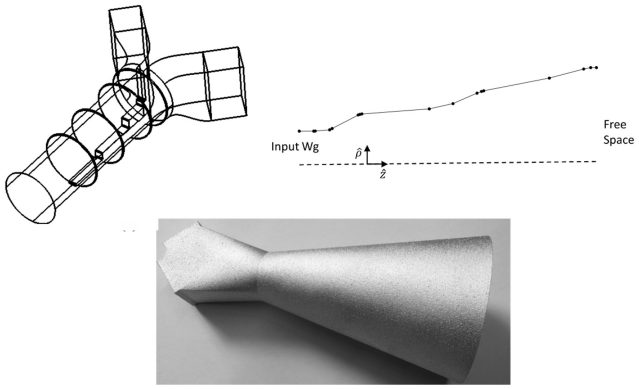

Figure 2.10: Geometric structure of the septum polarizer and feed horn profile as well as a photo of the prototype proposed in [29]

Another dual-CP antenna that is also comprised of a smooth-wall horn and a septum polarizer is reported in [31], whose working frequency is at the top end of the mmWave band. This dual-CP antenna achieves port isolation $>$ 30 dB over a bandwidth 10% in the frequency range between 213 GHz and 237 GHz, which is the highest port isolation over widest bandwidth ever reported for this type of structure. In order to achieve this result,

the number of septum steps is increased to 5 to improve the impedance performance. Figure 2.11 presents the photo of the prototype along with the geometry of the septum polarizer and the smooth-wall horn.

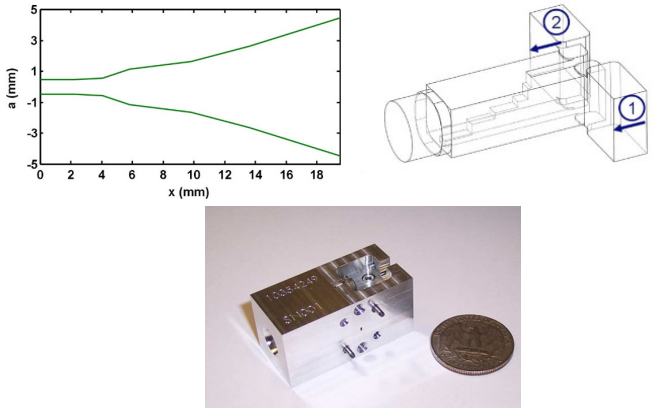

Figure 2.11: Geometry of the septum polarizer and feed horn profile as well as a photo of the prototype proposed in [31]

The septum polarizer can also be used as an element of array. In [28], a septum polarizer with 4-step septum is designed to be the element of a spherical phased-array antenna (SPAA), as shown in Figure 2.12. The element has a reflection coefficient $<$ -15 dB and isolation $>$ 20 dB over 13% bandwidth ranging from 8 - 8.5 GHz with AR $<$ 0.7 dB. A Ka-band dual circularly polarized (CP) waveguide array antenna is presented in [30], using integrated septum polarizers to generate dual-CP. The measured results of a 16x16 array show that a bandwidth of 16% from 27.6 GHz to 32.4 GHz is achieved with reflection coefficient $<$ -10 dB, isolation $>$ 13 dB and AR $<$ 3 dB. A maximum gain of 32.8 dBic is realized. The antenna configuration, integrated septum polarizer and the prototype are shown in Figure 2.13.

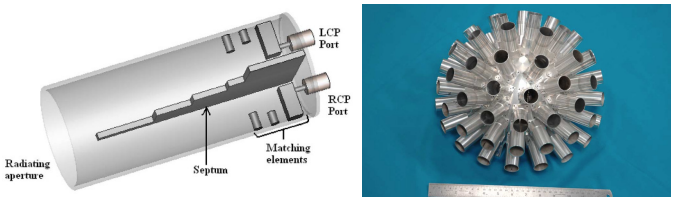

Figure 2.12: The radiating element and prototype of the array proposed in [28]

In fact, because the dimension of the square (circular) waveguide in septum polarizer

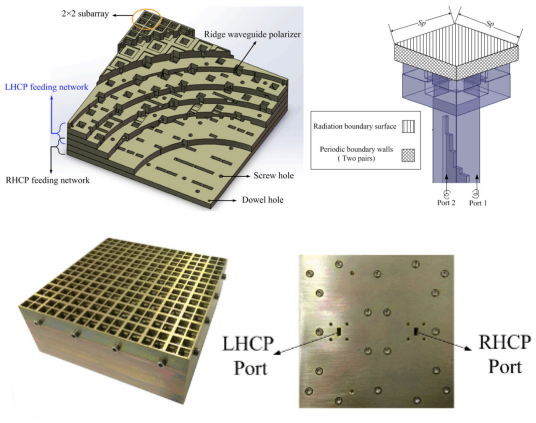

Figure 2.13: The antenna configuration, integrated septum polarizer and the array prototype proposed in [30]

should be designed in such a way that only TE_{10}/TE_{01} (TE_{11}) modes can propagate in the square waveguide, the square (circular) waveguide of the septum polarizer has a fractional bandwidth of 1:1.4 (1:1.3) so that all higher modes are below their cutoff frequencies. For this reason, the maximum bandwidth of the septum polarizer with square (circular) waveguide is about 34% (26%). Moreover, it is revealed in [25] that 12% at the lower edge and 2% at the upper edge of the operating bandwidth should be left as guard for good matching, as the polarizer performance is difficult to control in these parts, which leads to only 20% (12%) bandwidth for use. It is believed that the maximum practical operating bandwidth for the septum polarizer is about 25% (15%) even with further optimization.

Consequently, further improvement for this type of dual-CP antenna to achieve bandwidth $> 20\%$, or high isolation at the level of 30 dB over a bandwidth wider than 10% is quite challenging since there is also a trade-off between impedance bandwidth and AR bandwidth of the stepped septum polarizer.

In [32], a novel septum polarizer using a waveguide common port with triangular cross-section is proposed to cover a bandwidth of 37.8% in the W-band and K-band, respectively, as shown in Figure 2.14. This design breaks the bandwidth limit of the conventional septum polarizer with a square- or circular-waveguide common port. Nev-

ertheless, the port isolation is only > 17 dB over the operating bandwidth.

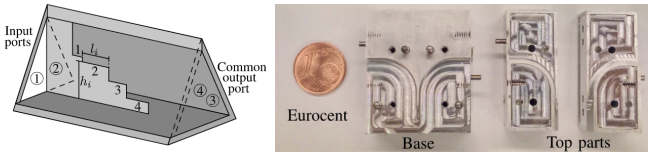

Figure 2.14: Geometry of the septum polarizer with triangular waveguide common port and the prototype in W-band proposed in [32]

The dual-CP antennas mentioned in this section are summarized in Table 2-A.

From the literature review on all types of dual-CP antenna reported, it can be found that dual-CP antenna based on waveguide structure will be a better choice if a wide bandwidth > 20% with isolation > 20% is required in the mmWave band.

2.3 Antenna Design/Optimzation

2.3.1 EM device optimization using Covariance Matrix Adaptation Evolution Strategy (CMA-ES)

Electromagnetic (EM) device designs, especially those who have complex structures, can be optimized to achieve better performance by using optimization algorithms. Evolutionary algorithms (EAs) such as Genetic algorithms (GAs) and Particle Swarm Optimization (PSO) have been extensively investigated and widely applied in antenna designs to find the globally optimized solutions [33, 34]. Although these optimization algorithms have been demonstrated in a wide variety of electromagnetic device design problems, including antennas, antenna arrays and filters, the difficulty in successfully applying the aforementioned algorithms is that the optimization result relies heavily on the evolutionary settings of the algorithms selected by the users, such as mutation rate, mutation range, and number of crossovers. For instance, the researchers may experience quite different outcomes if different crossover and mutation probabilities are used in GAs [35]. The research in [36] even reveals that optimal genetic algorithm parameters vary not only from problem to problem but also from stage to stage during the optimization pro-

Table 2-A: Summary of reported dual-CP antennas.

Ref	Frequency (GHz)	Type	Reflection Coefficient (dB)	Isolation (dB)	AR (dB)	Overall Band-width	Max Gain (dBic)	Year
[4]	0.864 - 0.929	Patch	<-18	>25	<2	7%	6	2013
[5]	1.07 - 1.85	Dipole	<-10	>15.2	<1.7	53.4%	8.8	2020
[6]	1.43–2.11	Dipole	<-10	>15	<3	38.4%	9.9	2020
[7]	1.83 - 6.35	Slot	<-10	>14.8	<3	110.5%	4.5	2017
[8]	2 - 3.7	CPW-fed slot	<-10	>15	<3	60%	4	2016
[9]	3.5 - 4	Patch	<-10	>10	<3	16%	9.6	2014
[10]	3.74 - 8.8	Monopole	<-10	>20	<3	80.7%	3.8	2017
[11]	5.05 - 5.61	Microstrip antenna array	<-10	>12	<3	10.5%	10.7	2016
[12]	4.9 - 5.5	Microstrip antenna array	<-10	>19	<3	11.5%	11.2	2017
[13]	7.25 - 8.4	Microstrip patch array	<-10	>20	<1.9	14.7%	26.2	2012
[14]	9.48 - 10.8	Patch array	<-10	>15	<3	13%	11.1	2019
[15]	10.35 - 10.75	Patch array	<-10	>20	<3	3.8%	9.3	2016
[16]	29.13 - 31.1	Microstrip antenna array	<-19	>20	<3	6.6%	11.8	2019
[19]	17.6 - 19.8	SIW septum polarizer and horn	<-15	>15	<3	11.8%	10.3	2016
[20]	33.5 - 42	SIW-based stepped slot array	<-10	>15	<3	22.5%	12.8	2018
[21]	40 - 43.75	Patch array fed by SIW	<-10	>19	<2	8.9%	19.35	2017
[22]	55 - 69	SIW-fed patch array	<-9.5	>14	<3	23.0%	25.5	2018
[23]	93.5 - 94.5	SIW parallel-plate long-slot array	<-10	>15	<3	1.0%	26	2017
[24]	13.05 - 13.11	Metasurface	<-10	>11	<3	0.5%	23.8	2018
[26]	1.27 - 1.32	Waveguide septum polarizer + Horn	<-25	>30	<1*	3.9%	-	2011
[27]	1.57542	Waveguide septum polarizer + Horn	<-29.3	>23	<0.023	1.0%	16.2	2016
[28]	8 - 8.5	Waveguide septum polarizer array	<-15	>20	<0.7	13.0%	8	2009
[29]	28.5 - 31.2	Waveguide septum polarizer + Horn	<-25	>27	<0.7	9.0%	-	2018
[30]	27.6 - 32.4	Waveguide array + Septum polarizer	<-10	>13	<3	16.0%	32.8	2017
[31]	213 - 237	Waveguide septum polarizer + Horn	<-21	>30	<1.5	10.0%	22**	2013
[32]	75 - 110	Septum Polarizer with triangular common port	<-15	>17	<1.3	37.8%	NA	2019

* Simulated results.
** Simulated results of the linearly-polarized horn.

cess for a given problem. The cost of determining the exact optimal genetic algorithm parameters sometimes may exceed the cost of solving the original problem [37].

On the other hand, the Covariance Matrix Adaptation Evolution Strategy (CMA-ES), which is a relatively new algorithm, operates in a self-adaptive way [38, 39]. Only an initial solution, an initial standard deviation, and possibly the termination criteria is left for the user to decide. Finding good strategy parameters is considered as part of the algorithm‘s job, by constantly re-shaping the search distribution while moving it around the search space, which is the difference between CMA-ES and other normal distribution-based algorithms.

The CMA-ES has been demonstrated to work well in different types of EM design problems [40, 41], and a comprehensive comparison between CMA-ES and PSO when they are applied to the design of a wideband stacked-patch antenna can be found in [42].

A complete survey of the CMA-ES is beyond the scope of this thesis; the reader can refer to [43] for further details.

2.3.2 Deep-Learning-based Inverse Modelling with CMA-ES

Although the optimization techniques mentioned in the previous section enjoy great success in EM device designs, it could be extremely computationally expensive to achieve an optimized design through EAs, since full-wave Electromagnetic (EM) simulation is required to obtain results for each evaluation and it usually takes at least several thousand evaluations to converge. The number of evaluations can even go up to tens of thousands if many geometrical parameters of the antenna needs to be optimized due to the large population size.

In recent years, much effort has been devoted to developing efficient optimization methods by introducing Gaussian Process Regression (GPR) based surrogate models that are constructed by using limited simulation results to replace full-wave EM simulation in optimization, which shows promising results in reducing computational cost [44].

However, these approaches still suffer from several major issues. Firstly, the workflow still completely relies on the optimization algorithm to search for the optimum solution, which means even for the same antenna structure, it will have to start optimization from scratch to obtain a new design that is able to meet the new requirement. Secondly, the GPR will lose efficiency in high dimensional spaces (so called "curse of dimensionality"), which limits its application to simple structure with small number of design parameters (mostly less than 10) [45]. Thirdly, multi-objective optimization is still quite challenging for these methods. Although an approach has been proposed in [46] for multi-objective modelling, it can be found that multiple models will have to be trained, one for each objective, which will increase the complexity of the model and workflow considerably.

In this section, a multi-objective inverse model based on deep neural networks (DNNs) working in conjunction with CMA-ES is proposed. This method is also applied to obtain a septum polarizer design with high-isolation over a wide bandwidth based on the data saved during the optimization of a septum polarizer to achieve moderate isolation. In this method, the aforementioned 3 issues of GPR surrogate model can be addressed. Once the training is completed, the model can be reused with new designs without optimization from scratch again, because the DNNs model can generate the candidate design directly, and the optimal design can be found by searching a limited solution space using CMA-ES, which significantly reduce the computational cost associated with optimization. Unlike GPR model, there is no limitation on the dimensions of input to the DNNs model. Furthermore, tensor/vector-based input of a DNNs model allows multi-objective modelling as an intrinsic feature in just one model. The septum polarizer design obtained by this method achieved isolation $>$ 40 dB over 15.8% bandwidth.

2.3.2.1 DNNs-based Inverse Modelling with CMA-ES

Design methods based on forward modelling are commonly used when neural networks are introduced in EM design. Shallow neural networks (NNs) was applied to optimize patch antennas in [47] with forward modelling. The concept of inverse modelling was

proposed in [48] using shallow NNs to design microwave filters. This method has also been applied to the design of single-feed circularly-polarized square microstrip antenna with truncated corners [49]. However, the complexity of these EM problems is small due to the limit learning capacity of shallow NNs. DNNs are considered to be more suitable for complex EM modelling as it can learn the meaningful representations of the training data and unfold complex relationships with successive layers. DNNs are particularly a better choice for inverse EM modelling because the input could contain dozens of data points extracted from performance characteristics, such as S-parameters over a wide bandwidth.

In this section, we propose a design method that combines the inverse modelling and DNNs. In this method, the DNNs model is trained in a reverse manner, i.e., single/multiple performance characteristics (reflection coefficient, isolation, etc.) of the samples are used as the train data while geometric parameters of the samples are used as the train targets for the supervised training, as illustrated in Figure 2.15, so that it is able to generate geometric parameters for new design requirement directly.

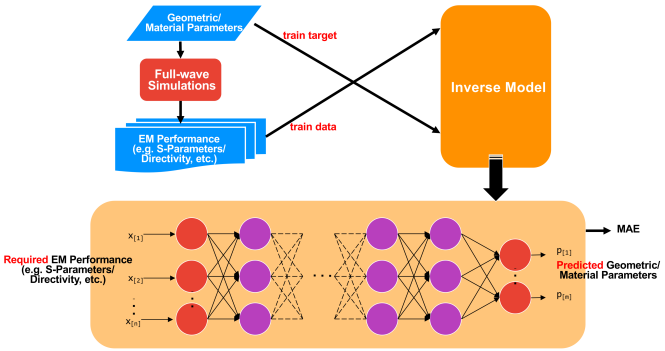

Figure 2.15: Illustration of proposed Deep-Learning-Based Inverse Modelling.

In order to determine the structure of the DNNs model, the hyperparameters of the DNNs model should be obtained during the training, such as the number of hidden layers and the number of nodes in each hidden layer, the learning rate. To evaluate the DNNs while its hyperparameters are tuned during the training, the data is typically split into a training set and a validation set. However, the validation scores may change

a lot depending on how the data is split if the number of samples is small, which will cause the evaluation less precise. For this reason, the iterated K-fold cross-validation with shuffling can be used during training to evaluate the model. The available data is split into K partitions, and the DNNs model is trained on $K-1$ partitions while evaluating on the remaining partition. Additionally, the data is shuffled every time it is split into K partitions. The final score is the average of the scores at each run of the K-fold validation. In our training, $K = 4$ is used. The process of the iterated K-fold cross-validation with shuffling is illustrated in Figure 2.16.

At the beginning of the training, when the DNNs model has not adequately captured the underlying structure of the data, the model is said to be underfit. After a certain number of iterations on the training data, the DNNs model starts to learn patterns that are specific to the training data but fail to predict future observations reliably when it comes to new data; in other words, overfitting occurs. The aim of adjusting the hyperparameters is to achieve good balance between underfitting and overfitting [50]. When the training of the model with tuned hyperparameters is completed, the saved model is evaluated using a test dataset, which is set aside from the original data, as shown in Figure 2.16. The mean absolute error (MAE) between the predictions and the test targets will be calculated automatically, which will be used to determine the limited solution space for CMA-ES optimization.

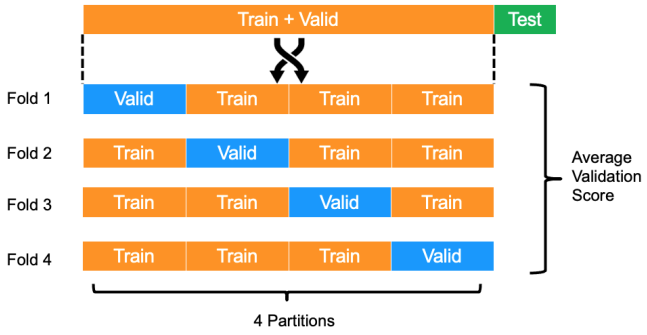

Figure 2.16: The iterated K-fold cross-validation with shuffling.

The workflow to obtain a new design using the deep-learning-based inverse model and CMA-ES is illustrated in Figure 2.17. Firstly, the trained DNNs model, which

contains the knowledge of the device learned by historical design data, is loaded. The desired performance characteristics for the new design such as expected S-parameters can be fed into the model as the input. Then the model will predict a geometric design immediately. This initial design predicted by DNNs model will be verified by a full-wave EM simulation with user-defined cost function. If the initial design does not meet the requirement, an optimization will be performed to search the optimal solution against the cost function within a limited solution space around the initial solution. The range of the searching space is determined by the initial solution and MAE obtained from DNNs model evaluation process mentioned above.

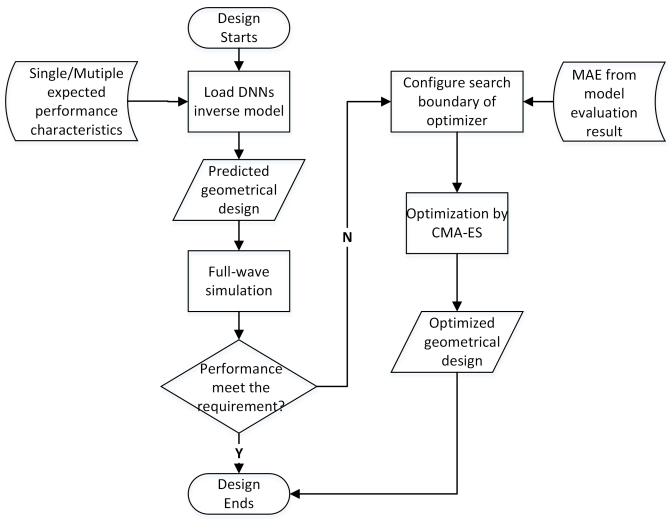

Figure 2.17: Flow diagram of proposed DNNs inverse model assisted design with CMA-ES.

The DNNs model is built by using Google TensorFlow 2.0 (an end-to-end open source machine learning platform [51]), and the complete project is developed using Python, which is able to optimize EM designs by integrating CST Microwave Studio with a python implementation of CMA-ES called pycma [52].

2.3.2.2 Deep-Learning-Based High-Isolation Septum Polarizer Design

A septum polarizer which can generate dual circular polarization is a complex waveguide device having dozens of parameters that need to be optimised to achieve multiple objec-

tives including reflection coefficient, isolation and axial ratio (AR) [25]. For this reason, the design of septum optimizer relies heavily on optimization algorithms to meet the performance requirement such as high isolation which is critical when it is used in wireless communication and radar application. Even in the paper where the septum polarizer was proposed, the authors stated that the complete field solutions for the septum polarizer are very difficult to arrive at and they achieved a successful design by trial and error experimental methods [25]. To the best of the author's knowledge, all the reported designs of septum polarizer over the past two decades are obtained by optimization. The simulation results of highest isolation with widest bandwidth ever reported is $>$ 37 dB over 10% bandwidth in [31].

The dataset saved during an optimization of a W-band septum polarizer that achieved 35-dB isolation is used to train the DNNs model in a reverse manner, as explained in Section 2.3.2.1. The new design aims to achieve isolation $>$ 40 dB and moderate reflection coefficient over a wide bandwidth with acceptable AR. According to [25], these characteristics are more critically dependent on septum geometry than AR. For this reason, only $|S_{11}|$ and $|S_{21}|$ are used as the two objectives to train the model. The linear values of $|S_{11}|$ and $|S_{21}|$ are extracted within the expected working bandwidth from 87 GHz to 110 GHz with the interval of 1 GHz. To realize the multi-objective prediction, vectors of $|S_{11}|$ and $|S_{21}|$ are concatenated to form an input vector of length 48, which is used as the training data. Geometric parameters of the septum polarizer shown in Figure 2.18 is used as the training target with a length of 12. A 5-layer DNNs model is built and trained after the hyperparameters tuned from aforementioned iterated 4-fold cross-validation with shuffling, each layer has 256 nodes, and a drop-out rate of 0.2 is applied to each layer. The mean square error (MSE) and MAE obtained from the final evaluation of the model on the test dataset is 0.0107 and 0.0214, respectively.

Then $|S_{11}|$ of 0.1 (-20 dB) and $|S_{21}|$ of 0.00708 (-43 dB) is vectorized over the desired bandwidth to form the input vector. After the input vector is fed into the model, the model predicts a set of geometric parameters, which is considered to be the initial

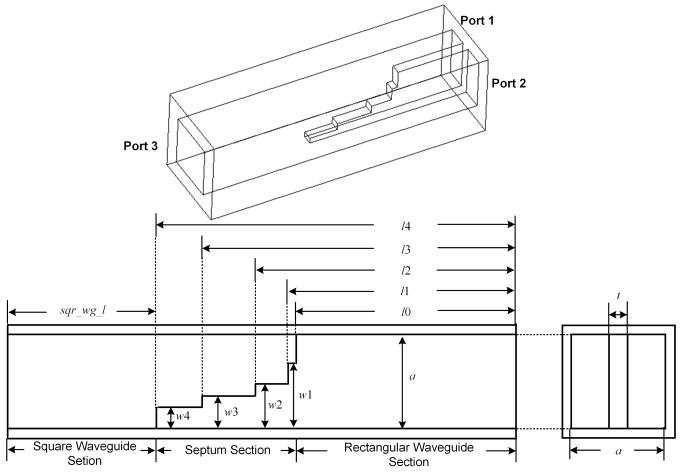

Figure 2.18: Geometry of the septum polarizer.

candidate solution. With this initial solution and MAE, the optimization is conducted within a limited solution space using CMA-ES and full-wave EM simulation to evaluate each candidate solution. After less than 150 evaluations, a suitable solution is found, whose $|S_{11}|$ and $|S_{21}|$ are close to the expectation. The best solution in the training dataset and the initial prediction from the DNNs model are shown in Figure 2.19. A suitable solution after 132 evaluations during the search in the limited solution space are also shown in Figure 2.19. It can be observed that the initial predication from the DNNs model has already achieved expected $|S_{11}|$ and a better $|S_{21}|$ than the best result in the training dataset. The final result after limited search achieves isolation $>$ 40 dB over 15.8% bandwidth with AR $<$ 2.4 dB, which to the best of the authors' knowledge, is the highest isolation over widest bandwidth of the stepped septum polarizer ever reported in terms of simulation results.

In order to verify the effectiveness of this deep-learning-based method, we compared the best result achieved by proposed deep-learning-based method with that from a conventional optimization using CMA-ES, as shown in Figure 2.20. The cost function of the conventional optimization is designed to achieve the same two objectives with an emphasis on isolation. The best result of the conventional optimization using CMA-ES appears at the 2682^{nd} evaluation after 3653 evaluations. It can be found that the result obtained

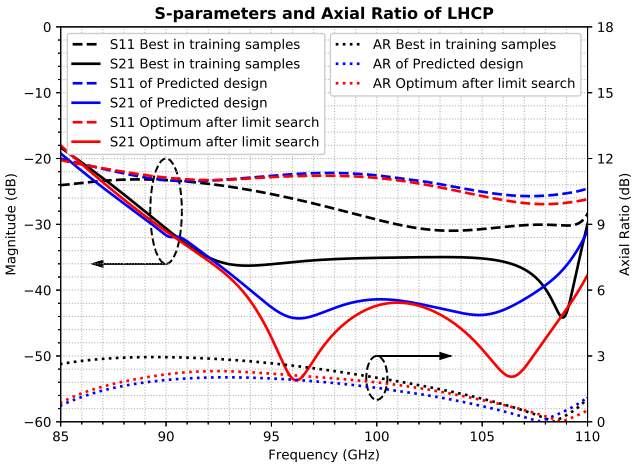

Figure 2.19: Simulation results of the septum polarizer design using proposed method.

by the proposed method after only 132 evaluations is comparable to that achieved by conventional optimization by CMA-ES.

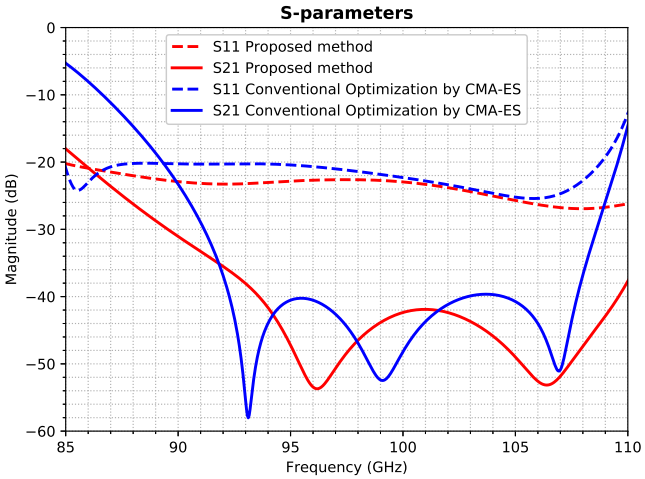

Figure 2.20: Comparison between results between proposed method and conventional optimization by CMA-ES.

2.4 Circular-Polarization Antenna Measurement

The radiation patterns and axial ratio (AR) of a CP antenna can be measured either directly or indirectly. If the antenna under test (AUT) is measured by using a circularly-polarized reference antenna with very small axial ratio, the co-polar and cross-polar

radiation patterns can be obtained directly. However, to the best of the author's knowledge, there is no circularly-polarized reference antenna in the W-band due to the difficulty in designing and fabricating a CP antenna with extremely low AR (extremely low cross polarization) covering a wide bandwidth in the W-band band. Moreover, no manufacturer ever claimed they could provide such a CP antenna in the W-band and the frequency bands above the W-band. Consequently, the radiation patterns and AR should be obtained indirectly by using a linearly-polarized antenna as the reference antenna in the measurement.

In this research, mmWave Compact Antenna Test Range (CATR) in the Antenna Lab at Queen Mary University of London is used to measure radiation characteristics of the antenna prototype. The schematic of the CATR measurement setup is shown in Figure 2.21. A W-band linearly-polarized corrugated horn is connected to a motor and installed in the CATR as a reference feed antenna, which can be rotated to an arbitrary angle within 360° along its centre axis, so that the magnitudes of different polarization components of Antenna Under Test (AUT) can be measured. In our measurement, the angle of the reference antenna is set from 0° to 150° with a step of 30°. For each angle, the AUT mounted on a positioner is scanned horizontally to measure the magnitudes with respect to azimuth (θ) for this polarization components. After that, the polarization components with maximum and minimum magnitudes at $\theta = 0°$ (boresight) are considered as the major and minor axes of the polarization ellipse, respectively. The ratio of the maximum to minimum magnitude defines the AR at the boresight of the AUT. By calculating the difference between these two selected curves, AR with respect to θ can also be obtained.

After AR is calculated, radiation patterns of co-polar and cross-polar can be derived. The total radiation pattern with respect to azimuth (θ) can be derived from the equation

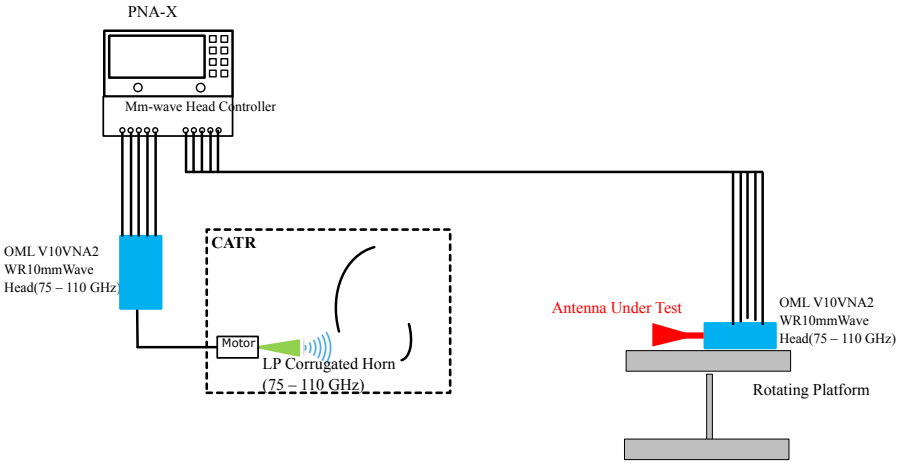

Figure 2.21: Schematic of the CATR measurement setup

below.

$$P_{tot\_dB} = 10log_{10}(M_{major}^2 + M_{minor}^2) \tag{2.17a}$$

$$P_{tot\_lin} = M_{major}^2 + M_{minor}^2 \tag{2.17b}$$

where M_{major} and M_{minor} are the linear values of the magnitudes of the two polarization components representing the major and minor axes of the polarization ellipse.

In order to get the radiation pattern for co-polar component and cross-polar components, XPD with respect to azimuth (θ) will be derived from AR firstly by using the equation below.

$$XPD_{dB} = 20log_{10}\left(\frac{ar+1}{ar-1}\right) \tag{2.18a}$$

$$XPD_{lin} = \left(\frac{ar+1}{ar-1}\right)^2 \tag{2.18b}$$

where ar is the linear value of AR.

Finally, radiation patterns for co-polar and cross-polar can be calculated as

$$P_{cx\_dB} = 10log_{10}\left(\frac{P_{tot\_lin}}{XPD_{lin}+1}\right) \tag{2.19}$$

$$\begin{aligned} P_{co\_dB} &= 10log_{10}\left(P_{tot\_lin} - P_{cx\_lin}\right) \\ &= 10log_{10}\left(\frac{XPD_{lin}P_{tot\_lin}}{XPD_{lin}+1}\right). \end{aligned} \tag{2.20}$$

2.5 Summary

In this chapter, an overview of the most representative state-of-the-art mmWave wireless communication systems and the antennas used in these systems are presented, which reveals the requirement of the antennas that could enable high capacity for mmWave wireless links. A comprehensive literature review on all types of dual-CP antenna is introduced, followed by antenna design/optimization and CP antenna measurement approaches used in the research work. Additionally, a design method using deep-learning-based inverse modelling and CMA-ES is proposed and applied to the design of a wideband high-isolation septum polarizer, which is an attempt to develop a new multi-objective design/optimization method for complex EM devices by introducing machine learning.

References

[1] X. Chen, C. G. Parini, B. Collins, Y. Yao, and M. Ur Rehman, *Antennas for Global Navigation Satellite Systems*. Chichester, UK: John Wiley & Sons, Ltd, 3 2012.

[2] S. Gao, Q. Luo, and F. Zhu, *Circularly Polarized Antennas*. Chichester, UK: John Wiley & Sons, Ltd, 1 2014.

[3] J. L. Volakis, *Antenna Engineering Handbook, Fourth Edition*, 4th ed. New York: McGraw-Hill Education, 2007. [Online]. Available: https://www.accessengineeringlibrary.com/content/book/9780071475747

[4] X. Lai, Z. Xie, Q. Xie, and X. Cen, "A Dual Circularly Polarized RFID Reader Antenna With Wideband Isolation," *IEEE Antennas and Wireless Propagation Letters*, vol. 12, pp. 1630–1633, 2013.

[5] L. Wen, S. Gao, Q. Luo, W. Hu, and Y. Yin, "Wideband Dual Circularly Polarized Antenna for Intelligent Transport Systems," *IEEE Transactions on Vehicular Technology*, vol. 69, no. 5, pp. 5193–5202, 2020.

[6] H. D. Li, X. Y. Du, J. Y. Yin, J. Ren, and Y. Yin, "Differentially Fed Dual-Circularly Polarized Antenna With Slow Wave Delay Lines," *IEEE Transactions on Antennas and Propagation*, vol. 68, no. 5, pp. 4066–4071, 2020.

[7] R. Xu, J. Li, J. Yang, K. Wei, and Y. Qi, "A Design of U-Shaped Slot Antenna With Broadband Dual Circularly Polarized Radiation," *IEEE Transactions on Antennas and Propagation*, vol. 65, no. 6, pp. 3217–3220, 2017.

[8] R. K. Saini and S. Dwari, "A Broadband Dual Circularly Polarized Square Slot Antenna," *IEEE Transactions on Antennas and Propagation*, vol. 64, no. 1, pp. 290–294, 2016.

[9] C. Zhang, X. Liang, X. Bai, J. Geng, and R. Jin, "A Broadband Dual Circularly Polarized Patch Antenna With Wide Beamwidth," *IEEE Antennas and Wireless Propagation Letters*, vol. 13, pp. 1457–1460, 2014.

[10] C. D.S. and S. S. Karthikeyan, "A Novel Broadband Dual Circularly Polarized Microstrip-Fed Monopole Antenna," *IEEE Transactions on Antennas and Propagation*, vol. 65, no. 3, pp. 1410–1415, 2017.

[11] Y. Shen, S. Zhou, G. Huang, and T. Chio, "A Compact Dual Circularly Polarized Microstrip Patch Array With Interlaced Sequentially Rotated Feed," *IEEE Transactions on Antennas and Propagation*, vol. 64, no. 11, pp. 4933–4936, 2016.

[12] C. Mao, S. S. Gao, Y. Wang, and J. T. Sri Sumantyo, "Compact Broadband Dual-Sense Circularly Polarized Microstrip Antenna/Array With Enhanced Isolation," *IEEE Transactions on Antennas and Propagation*, vol. 65, no. 12, pp. 7073–7082, 2017.

[13] A. Garcia-Aguilar, J. Inclan-Alonso, L. Vigil-Herrero, J. Fernandez-Gonzalez, and M. Sierra-Perez, "Low-Profile Dual Circularly Polarized Antenna Array for Satellite Communications in the X Band," *IEEE Transactions on Antennas and Propagation*, vol. 60, no. 5, pp. 2276–2284, 2012.

[14] Y. Yang, J. Guo, B. Sun, Y. Cai, and G. Zhou, "The Design of Dual Circularly Polarized Series-Fed Arrays," *IEEE Transactions on Antennas and Propagation*, vol. 67, no. 1, pp. 574–579, 2019.

[15] Q. Luo, S. Gao, M. Sobhy, J. T. Sri Sumantyo, J. Li, G. Wei, J. Xu, and C. Wu,

"Dual Circularly Polarized Equilateral Triangular Patch Array," *IEEE Transactions on Antennas and Propagation*, vol. 64, no. 6, pp. 2255–2262, 2016.

[16] Y. Yang, B. Sun, and J. Guo, "A Low-Cost, Single-Layer, Dual Circularly Polarized Antenna for Millimeter-Wave Applications," *IEEE Antennas and Wireless Propagation Letters*, vol. 18, no. 4, pp. 651–655, 2019.

[17] P. Hall, J. Dahele, and J. James, "Design principles of sequentially fed, wide bandwidth, circularly polarised microstrip antennas," *IEE Proceedings H Microwaves, Antennas and Propagation*, vol. 136, no. 5, 1989.

[18] P. S. Hall, "Dual circularly polarized sequentially rotated microstrip array with high isolation," *Microwave and Optical Technology Letters*, vol. 5, no. 5, 5 1992.

[19] Y. Cai, Y. Zhang, Z. Qian, W. Cao, and S. Shi, "Compact Wideband Dual Circularly Polarized Substrate Integrated Waveguide Horn Antenna," *IEEE Transactions on Antennas and Propagation*, vol. 64, no. 7, pp. 3184–3189, 2016.

[20] Q. Wu, J. Hirokawa, J. Yin, C. Yu, H. Wang, and W. Hong, "Millimeter-Wave Multibeam Endfire Dual-Circularly Polarized Antenna Array for 5G Wireless Applications," *IEEE Transactions on Antennas and Propagation*, vol. 66, no. 9, pp. 4930–4935, 2018.

[21] J. Xu, W. Hong, Z. H. Jiang, J. Chen, and H. Zhang, "A Q-Band Low-Profile Dual Circularly Polarized Array Antenna Incorporating Linearly Polarized Substrate Integrated Waveguide-Fed Patch Subarrays," *IEEE Transactions on Antennas and Propagation*, vol. 65, no. 10, pp. 5200–5210, 2017.

[22] Y. Zhao and K. Luk, "Dual Circular-Polarized SIW-Fed High-Gain Scalable Antenna Array for 60 GHz Applications," *IEEE Transactions on Antennas and Propagation*, vol. 66, no. 3, pp. 1288–1298, 2018.

[23] Y. J. Cheng, J. Wang, and X. L. Liu, "94 GHz Substrate Integrated Waveguide Dual-Circular-Polarization Shared-Aperture Parallel-Plate Long-Slot Array Antenna With Low Sidelobe Level," *IEEE Transactions on Antennas and Propagation*, vol. 65, no. 11, pp. 5855–5861, 2017.

[24] A. T. Pereda, F. Caminita, E. Martini, I. Ederra, J. Teniente, J. C. Iriarte, R. Gonzalo, and S. Maci, "Experimental Validation of a Ku-Band Dual-Circularly Polarized

Metasurface Antenna," *IEEE Transactions on Antennas and Propagation*, vol. 66, no. 3, pp. 1153–1159, 2018.

[25] M. Chen and G. Tsandoulas, "A wide-band square-waveguide array polarizer," *IEEE Transactions on Antennas and Propagation*, vol. 21, no. 3, pp. 389–391, 1973.

[26] M. J. Franco, "A High-Performance Dual-Mode Feed Horn for Parabolic Reflectors with a Stepped-Septum Polarizer in a Circular Waveguide [Antenna Designer's Notebook]," *IEEE Antennas and Propagation Magazine*, vol. 53, no. 3, pp. 142–146, 2011.

[27] M. Mrnka, M. Pavlovic, and Z. Raida, "Antenna Range Illuminator Based on a Septum Polarizer and a Dual-Mode Horn [Measurements Corner]," *IEEE Antennas and Propagation Magazine*, vol. 58, no. 4, pp. 82–86, 2016.

[28] C. Kumar, V. V. Srinivasan, V. K. Lakshmeesha, and S. Pal, "Novel Dual Circularly Polarized Radiating Element for Spherical Phased-Array Application," *IEEE Antennas and Wireless Propagation Letters*, vol. 8, pp. 826–829, 2009.

[29] G. Addamo, O. A. Peverini, D. Manfredi, F. Calignano, F. Paonessa, G. Virone, R. Tascone, and G. Dassano, "Additive Manufacturing of Ka-Band Dual-Polarization Waveguide Components," *IEEE Transactions on Microwave Theory and Techniques*, vol. 66, no. 8, pp. 3589–3596, 2018.

[30] J. Wu, Y. J. Cheng, H. B. Wang, Y. C. Zhong, D. Ma, and Y. Fan, "A Wideband Dual Circularly Polarized Full-Corporate Waveguide Array Antenna Fed by Triple-Resonant Cavities," *IEEE Transactions on Antennas and Propagation*, vol. 65, no. 4, pp. 2135–2139, 4 2017.

[31] C. A. Leal-Sevillano, K. B. Cooper, J. A. Ruiz-Cruz, J. R. Montejo-Garai, and J. M. Rebollar, "A 225 GHz Circular Polarization Waveguide Duplexer Based on a Septum Orthomode Transducer Polarizer," *IEEE Transactions on Terahertz Science and Technology*, vol. 3, no. 5, pp. 574–583, 2013.

[32] B. Deutschmann and A. F. Jacob, "Broadband Septum Polarizer With Triangular Common Port," *IEEE Transactions on Microwave Theory and Techniques*, pp. 1–8, 2019.

[33] J. Leech, B. K. Tan, G. Yassin, P. Kittara, and S. Wangsuya, "Experimental Investigation of a Low-Cost, High Performance Focal-Plane Horn Array," *IEEE Transactions on Terahertz Science and Technology*, vol. 2, no. 1, pp. 61–70, 2012.

[34] J. Robinson and Y. Rahmat-Samii, "Particle swarm optimization in electromagnetics," *IEEE Transactions on Antennas and Propagation*, vol. 52, no. 2, pp. 397–407, 2004.

[35] D. W. Boeringer, D. H. Werner, and D. W. Machuga, "A simultaneous parameter adaptation scheme for genetic algorithms with application to phased array synthesis," *IEEE Transactions on Antennas and Propagation*, vol. 53, no. 1, pp. 356–371, 2005.

[36] A. E. Eiben, R. Hinterding, and Z. Michalewicz, "Parameter control in evolutionary algorithms," *IEEE Transactions on Evolutionary Computation*, vol. 3, no. 2, pp. 124–141, 1999.

[37] J. Lis, "Parallel genetic algorithm with the dynamic control parameter," in *Proceedings of IEEE International Conference on Evolutionary Computation*, 1996, pp. 324–329.

[38] N. Hansen and A. Ostermeier, "Completely Derandomized Self-Adaptation in Evolution Strategies," *Evolutionary Computation*, vol. 9, no. 2, pp. 159–195, 2001.

[39] N. Hansen, "The CMA Evolution Strategy: A Comparing Review," in *Towards a New Evolutionary Computation.* Berlin, Heidelberg: Springer Berlin Heidelberg.

[40] M. D. Gregory, X. Wang, and D. H. Werner, "Flexible design of doubly periodic frequency selective surfaces with a prismatic mesh based FEBI simulation tool and CMA-ES," in *2011 IEEE International Symposium on Antennas and Propagation (APSURSI)*, 2011, pp. 1867–1870.

[41] M. D. Gregory and D. H. Werner, "Multi-band and wideband antenna design using port substitution and CMA-ES," in *2013 IEEE Antennas and Propagation Society International Symposium (APSURSI)*, 2013, pp. 598–599.

[42] M. D. Gregory, Z. Bayraktar, and D. H. Werner, "Fast Optimization of Electromagnetic Design Problems Using the Covariance Matrix Adaptation Evolutionary Strategy," *IEEE Transactions on Antennas and Propagation*, vol. 59, no. 4, pp.

1275–1285, 2011.

[43] N. Hansen, "The CMA Evolution Strategy: A Tutorial," Tech. Rep., 2016.

[44] B. Liu, H. Aliakbarian, Z. Ma, G. A. E. Vandenbosch, G. Gielen, and P. Excell, "An Efficient Method for Antenna Design Optimization Based on Evolutionary Computation and Machine Learning Techniques," *IEEE Transactions on Antennas and Propagation*, vol. 62, no. 1, pp. 7–18, 2014.

[45] S. Koziel and S. Ogurtsov, "Multi-Objective Design of Antennas Using Variable-Fidelity Simulations and Surrogate Models," *IEEE Transactions on Antennas and Propagation*, vol. 61, no. 12, pp. 5931–5939, 2013.

[46] Q. Wu, J. Yin, C. Yu, H. Wang, and W. Hong, "Machine-Learning-Assisted Two-Step Antenna Modelling Method," in *2019 IEEE International Symposium on Antennas and Propagation and USNC-URSI Radio Science Meeting*, 2019, pp. 1043–1044.

[47] N. P. Somasiri, X. Chen, and A. A. Rezazadeh, "Neural network modeller for design optimisation of multilayer patch antennas," *IEE Proceedings: Microwaves, Antennas and Propagation*, vol. 151, no. 6, pp. 514–518, 12 2004.

[48] H. Kabir, Y. Wang, M. Yu, and Q. Zhang, "Neural Network Inverse Modeling and Applications to Microwave Filter Design," *IEEE Transactions on Microwave Theory and Techniques*, vol. 56, no. 4, pp. 867–879, 2008.

[49] Z. Wang, S. Fang, Q. Wang, and H. Liu, "An ANN-Based Synthesis Model for the Single-Feed Circularly-Polarized Square Microstrip Antenna With Truncated Corners," *IEEE Transactions on Antennas and Propagation*, vol. 60, no. 12, pp. 5989–5992, 2012.

[50] I. Goodfellow, Y. Bengio, and A. Courville, *Deep Learning*. MIT Press, 2016.

[51] Google. (2019, Sep.) Tensorflow: An end-to-end open source machine learning platform. [Online]. Available: https://www.tensorflow.org/

[52] Y. A. Nikolaus Hansen and P. Baudis, "pycma version 2.7.0," 2019. [Online]. Available: https://github.com/CMA-ES/pycma

Chapter 3

Design of Wideband Dual-Circular-Polarization Antenna Based on the Septum Polarizer

3.1 Introduction

According to Chapter 1, wireless communication systems could benefit from employing dual-circular-polarization (dual-CP) antennas. From the literature review in Chapter 2, it can be found that an attractive method to achieve dual circular polarization with wide bandwidth and good isolation in mmWave band is to employ a stepped septum polarizer. However, the bandwidths of most dual-CP antennas reported based on septum polarizers are in the range from 9% - 16% [1–4].

For this reason, we propose to design a dual CP antenna with wider bandwidth and better isolation for mmWave communications in W-band. This chapter presents our design and experimental verification of a compact feed antenna with dual CP working in

W-band based on a stepped septum polarizer, by applying a smooth-wall horn with an optimized profile and a wideband waveguide transformer. This antenna is optimized to exhibit a wide bandwidth with good isolation, rotationally symmetric radiation patterns, full-duplex capability, as well as the high gain when used as a feed to a reflector antenna.

The remainder of this chapter is organized as follows. The operating principles of the septum polarizer is described in Section 3.2. Section 3.3 presents the design of the dual-CP horn antenna consisting of a stepped septum polarizer, a profiled smooth-wall horn and an octagonal square-to-circular waveguide transformer. The simulated and measured results of the dual-CP horn are also presented and discussed in this section. In Section 3.4, an axially displaced ellipse (ADE) reflector antenna is designed and simulated to demonstrate a high-gain dual-CP antenna when the dual-CP horn is used as the feed. Section 3.5 gives the summary of this chapter.

3.2 Operating Principles of the Septum Polarizer

A septum polarizer is a waveguide device which has three physical ports and can operate as a polarization converter. With two rectangular waveguide ports and one square or circular waveguide port, it is capable of generating both senses of CP when used as a transmitter. A schematic of a stepped septum polarizer with square waveguide port as the common port is depicted in Figure 3.1. When one of the two rectangular waveguide ports is excited with its dominant TE_{10} mode, a TE_{01} mode and a TE_{10} mode can be generated within the septum section, which can be regarded as two orthogonal linear polarization components of the CP. With well-optimized dimensions of the stepped septum, the same amplitude and a phase difference of $\pm 90°$ between the two orthogonal linear polarization components can be achieved and thus a CP is obtained in the square waveguide after the septum section. The sense of the CP generated depends on which rectangular waveguide port is excited. In Figure 3.1, when port 1 is excited, LHCP will be generated, while RHCP will be generated if port 2 is excited. From an electrical point of view, this septum polarizer can be considered as a four-port device since two degener-

ate modes can propagate in the square waveguide section, as shown in Figure 3.1. The CP generation principle can be explained using even- and odd-mode excitations at the rectangular waveguide section as described in [5]. In this section, we revisit the principle of operation with full-wave simulation.

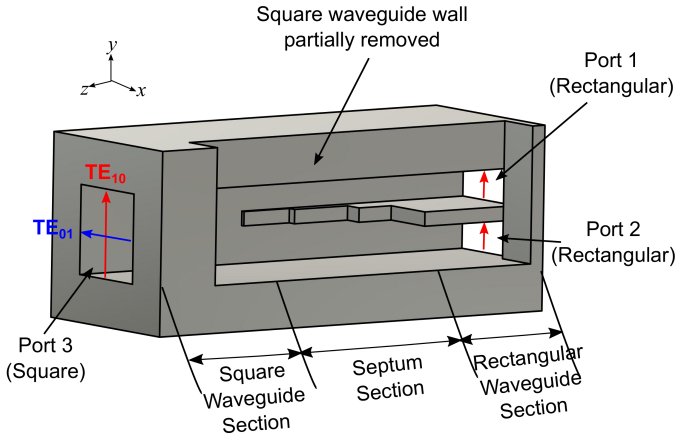

Figure 3.1: Schematic of a septum polarizer.

The excitation of port 1 and port 2 can both be regarded as the superposition of even- and odd-mode excitations, as depicted in Figure 3.2. The simulated E-field response to the even-mode and odd-mode excitations decomposed from port 1 excitation are shown in Figure 3.3(a). It can be found that propagation of the even-mode wave is unaffected by the septum and the E-field distributions remain unchanged within and after the septum section, which results in the TE_{10} mode in the square waveguide. On the other hand, when the odd mode shown in Figure 3.3(a) is excited, horizontal E-field is gradually created within the septum section between the septum and the side wall of the waveguide, as shown in Figure 3.3(a). Finally, horizontal E-field is generated after the septum section, leading to the TE_{01} mode in the square waveguide. Since port 1 excitation is equivalent to the superposition of even- and odd-mode excitation shown in Figure 3.3(a), the E-field generated in the square waveguide section will be the superposition of the corresponding TE_{10} mode and TE_{01} mode. With well-optimized dimensions of the septum polarizer, a phase difference of 90° of these two modes can be achieved, thereby realizing CP. The reason why the even mode is unaffected by the

septum and leads to a TE_{10} mode whereas the odd mode leads to a TE_{01} mode is elaborated in [5].

Figure 3.3(b) shows the simulated E-field response for the even-mode and odd-mode excitations decomposed from port 2 excitation, and results similar to that when port 1 is exicited can be found. It can also be observed that the TE_{01} mode resulted from the odd-mode excitation shown in Figure 3.3(b) and the TE_{01} mode resulted from the odd-mode excitation shown in Figure 3.3(a) are 180° out of phase. For this reason, the sense of CP obtained by port 1 and port 2 excitation will be opposite to each other, leading to dual CP generation.

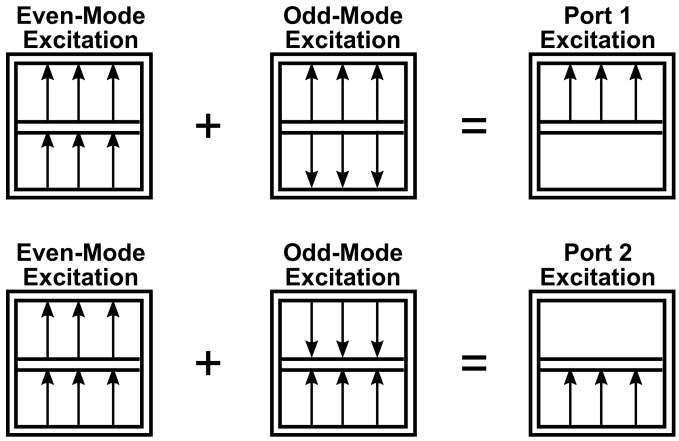

Figure 3.2: Excitation decomposition of port 1 and port 2.

3.3 Feed Antenna Design

The structure of the complete antenna is shown in Figure 3.4, consisting of three sections. The LHCP and RHCP signals generated by the stepped septum polarizer in a square waveguide will propagate through a square-to-circular waveguide transformer into a profiled smooth-wall horn. A pair of waveguide transformers with 90° E-plane bends is used to convert the input ports of the septum polarizer into standard WR-10 rectangular waveguides. When port 1 is excited, LHCP will be generated; while port 2 is excited, RHCP will be generated. A circular horn is selected as opposed to a square horn because it is generally observed that the circular horns have better cross-polar performance than

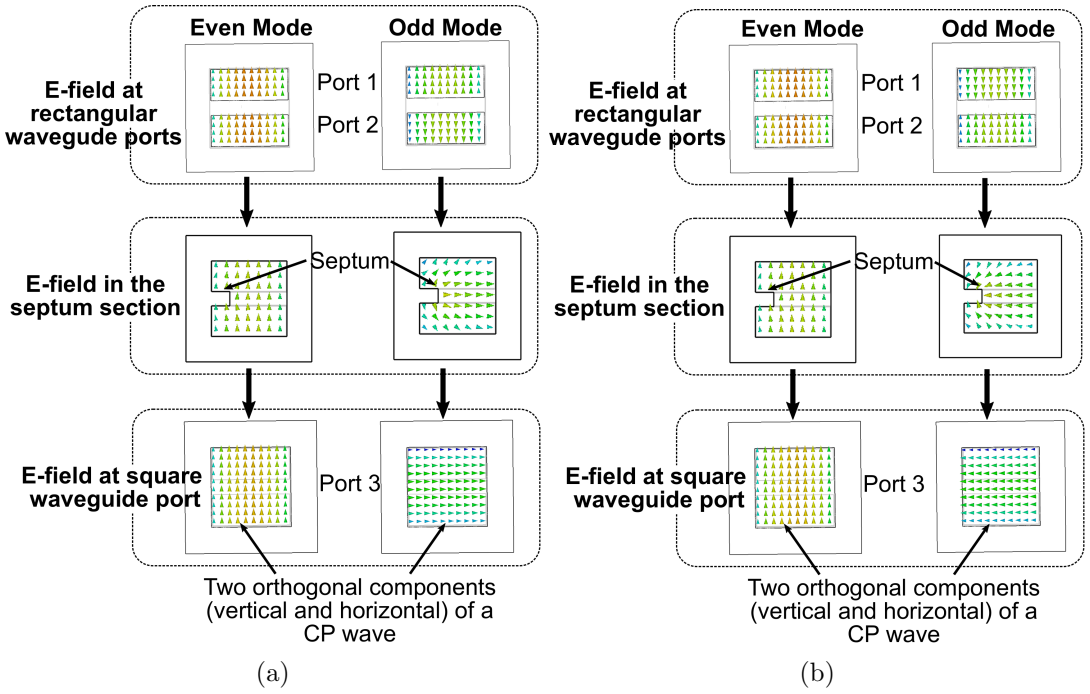

Figure 3.3: Simulated E-fields in septum polarizer when even-mode and odd-mode decomposed from (a) port 1 and (b) port 2 excitation.

that of a square horn, and the circular horns are easier to realize rotationally symmetric radiation patterns compared with the square ones. A square-to-circular waveguide transformer is therefore required to connect the square port of the septum polarizer to the circular port of the circular horn.

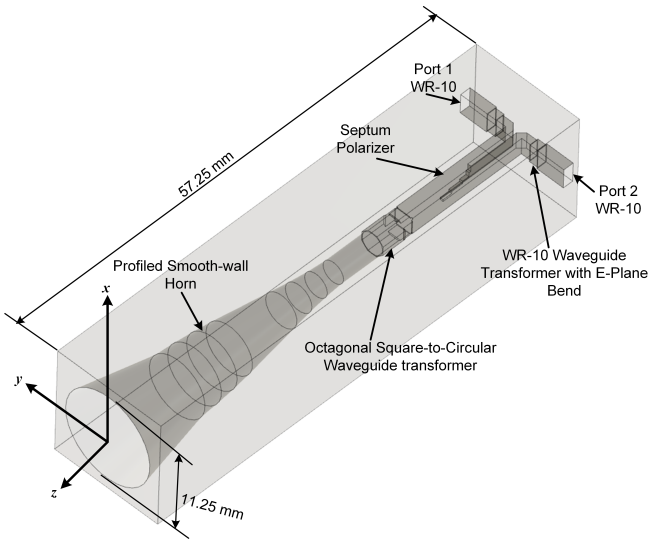

Figure 3.4: Structure of the complete antenna.

3.3.1 Stepped Septum Polarizer

The geometry of the septum polarizer with a 4-step septum placing in the centre of a square waveguide is shown in Figure 3.5. The dimensions of the square waveguide is designed so that only TE_{10} and TE_{01} mode can propagate through it within the working frequency range. The two rectangular ports of the polarizer are converted into two standard WR-10 rectangular waveguides (2.54 mm x 1.27 mm) by using a pair of 90° E-plane bends and transformers. The dimensions of the septum polarizer are optimised by using Nelder Mead Simplex and Particle Swarm Optimisation (PSO) Algorithm provided by CST Microwave Studio, and are listed in Figure 3.5.

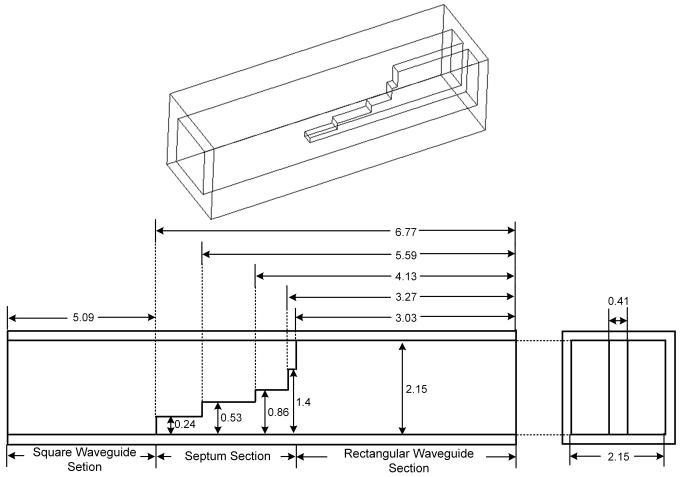

Figure 3.5: Geometry of the septum polarizer.

3.3.2 Profiled Smooth-wall Horn

The whole profile of the smooth-wall horn is divided into two sections, as shown in Figure 3.6. A sinusoid profile which is one of the empirical profiles [6] is selected for profile of the first section:

$$R(z) = sin^p(z), \tag{3.1}$$

where $R(z)$ is the radius and z is axial distance. The value of p is optimised to be 2.5 to achieve low reflection coefficient over wide bandwidth and rotationally symmetric radiation pattern. This section is discretized into seven linear segments for the ease of

fabrication. A conical section is cascaded to add a degree of freedom in order to optimise further the overall performance of the antenna. The second section is optimised to follow a linear-tapered circular conical profile with radius changing from 3.72 mm to 5.625 mm in a length of 9.5mm.

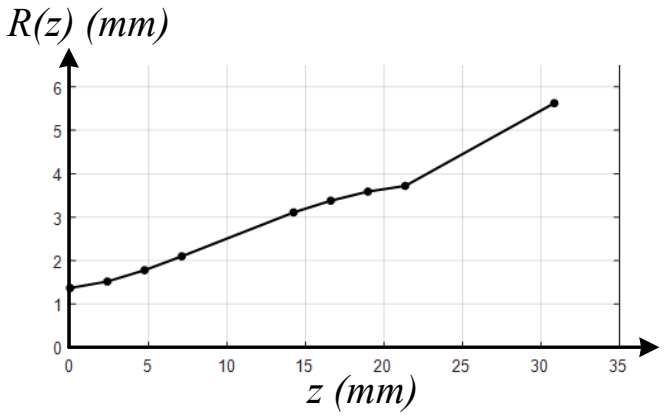

Figure 3.6: Profile of the smooth-wall horn.

3.3.3 Octagonal Square-to-Circular Waveguide Transformer

A multi-section octagonal waveguide transformer [7] is applied to connect circular horn and the septum polarizer for ease of fabrication at the high frequency with wide bandwidth and a compact size. The reflection coefficient of this transformer is optimised to be lower than -30 dB across the entire bandwidth ranging from 75 GHz to 95 GHz.

3.3.4 Simulation and Measurement Results

After the design of the complete antenna is optimised through simulation in CST Microwave Studio, a prototype of the proposed antenna is fabricated and measured. The proposed antenna is split into two block halves in the fabrication, as shown in Figure 3.7. The fabricated antenna is shown in Figure 3.8.

The scattering parameters of the proposed dual-CP antenna are measured using a Keysight PNA-X network analyzer with two OML WR-10 extension heads. The simulated and measured reflection coefficient as well as the isolation are illustrated in Figure 3.9. As can be seen from the result, the measured reflection coefficient for both

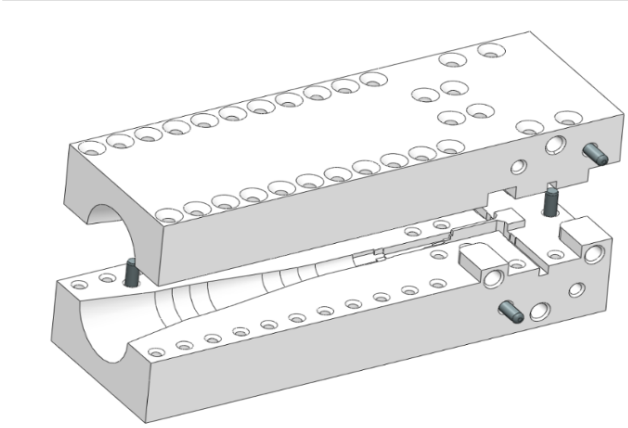

Figure 3.7: Mechanical design and assembly of the dual-CP antenna.

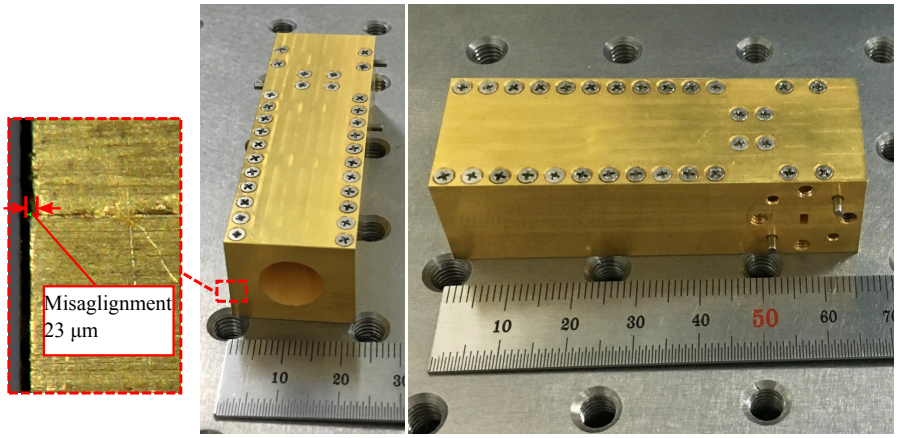

Figure 3.8: Photo of the fabricated antenna.

port 1 and port 2 are lower than -15 dB over the bandwidth from 75 GHz to 95 GHz, which agrees well with the simulated result. It can be observed that the measured isolation deteriorates at the edges of the band compared with the simulated result. This minor discrepancy is caused by the fabrication tolerance of $5-10\ \mu m$, and the scattering parameters are sensitive to the dimensions of the septum polarizer, especially the tiny septum steps at high frequencies. But an isolation higher than 20 dB is still met within 76.8 - 94.7 GHz.

The radiation characteristics are measured in a mmWave compact antenna test range (CATR) in the Antenna Lab at Queen Mary University of London. The measurement follows the CP measurement method described in Section 2.4. In this measurement, the

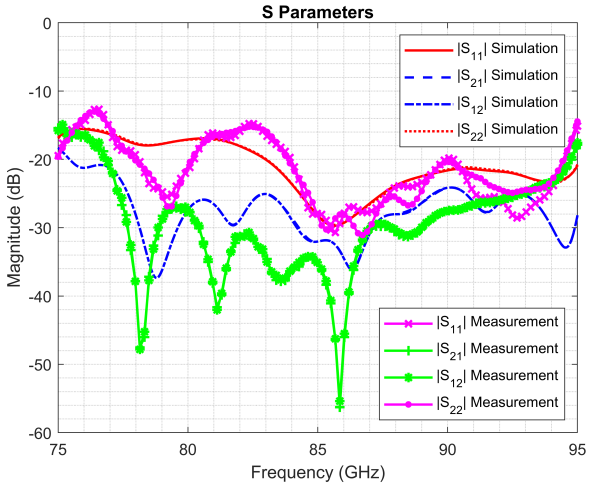

Figure 3.9: Simulated and measured S parameters of the proposed antenna.

angle of the reference antenna is set from 0° to 150° with a step of 30° to measure each polarization component at these angles, which is proved to be sufficient to find the major and minor axes of the polarization ellipse of our antenna.

Figure 3.10 depicts the simulated and measured AR for both LHCP and RHCP at boresight, and the inset of Figure 3.10 shows an arc of the polarization ellipse measured in $YZ-$plane at 85 GHz as an example, whose polarization angle ranges from 0° to 150° with a step of 30°, and major and minor axes appear at 60° and 150° respectively. It can be found that the simulated AR is below 2 dB. However, the measured AR ranges from 2.4 dB to 5.8 dB, much worse than the simulated results. The cause of this large discrepancy is mostly due to misalignment between the fabricated block halves. The fabricated antenna then has been investigated under a microscope and the approximate misalignment has been measured to be around 23 μm, which is shown in the inset of Figure 3.8. To verify this, simulations were also conducted by introducing misalignments in the fabrication model deliberately. The dot lines in Figure 3.10 depict the effect of misalignments of 20 and 24 μm on the AR, which agrees better with the measured results, and is consistent with the hypothesis and aforementioned measurement under a microscope.

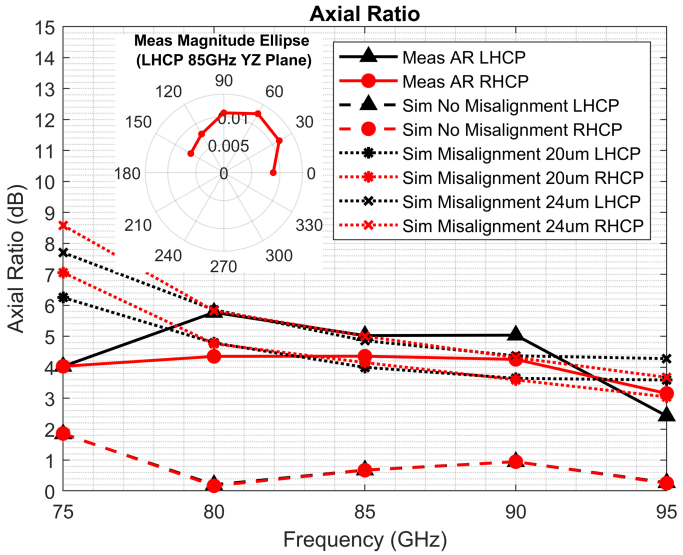

Figure 3.10: Simulated and measured Axial Ratio of the proposed antenna.

The normalized radiation patterns in XZ, YZ and 45° (with respect to XZ or YZ plane) plane at 85 GHz for RHCP and LHCP are shown in Figure 3.11 and Figure 3.12. The peaks located on either side of the main beam are caused by the rise in the cross-polarization on the two sides of the main beam. The method to obtain the measured AR with respect to azimuth angle (θ) and the relationship between AR and cross-polarization have been illustrated in Section 2.4. It can be observed that there is a good agreement between the measured and simulated results. It can also be found that a good rotational symmetry is achieved, allowing this antenna to be used as a feed for reflector antennas. The normalized radiation patterns for LHCP and RHCP in XZ, YZ plane and 45° plane at 75 and 95 GHz are presented in Figure 3.13 - Figure 3.16, which shows a good agreement between simulated and measured results as well as the stable radiation patterns across the band.

The antenna gain over the entire working bandwidth are shown in Figure 3.17. The measured antenna gain is 18.3 ± 2 dBic from 75 GHz to 95 GHz, which agrees with simulated one, the drop at 75 GHz and 95 GHz is probably due to the deterioration of $|S_{11}|$ at the edges of the band which can be observed in Figure 3.9.

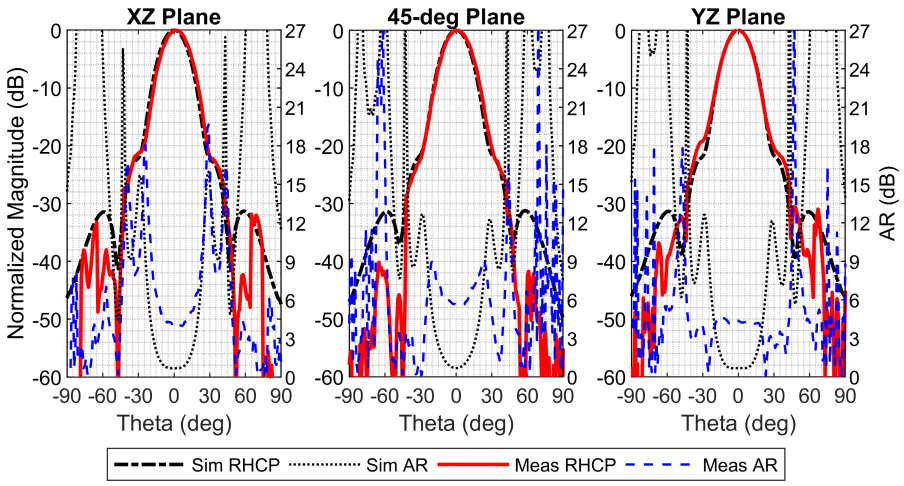

Figure 3.11: Simulated and measured radiation pattern for RHCP at 85 GHz.

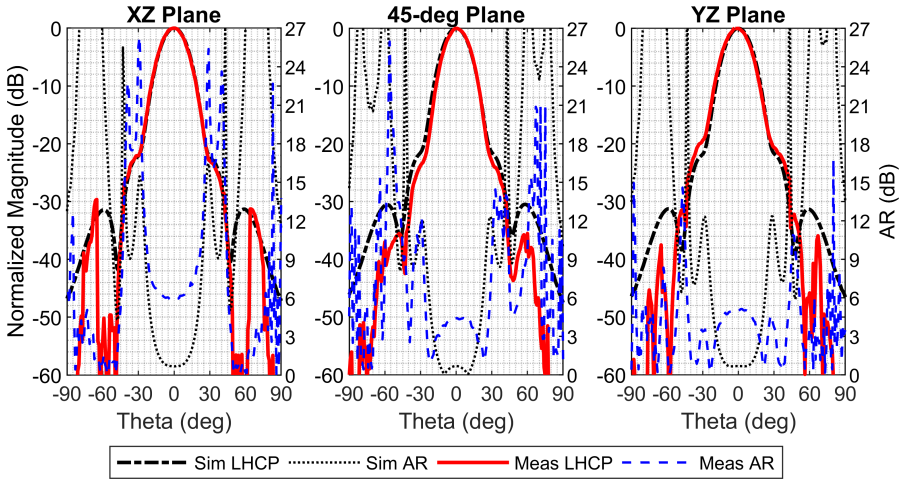

Figure 3.12: Simulated and measured radiation pattern for LHCP at 85 GHz.

3.4 Reflector Antenna Design

In this section, a reflector antenna is designed in order to demonstrate that a high gain can be achieved when the dual-CP horn designed in Section 3.3 is used together with a reflector antenna.

3.4.1 Axially Displaced Ellipse Reflector Antenna

Axially-symmetric Cassegrain and Gregorian reflector antennas have been widely used in radio astronomy and satellite communications. The dual-reflector configurations of the Cassegrain and Gregorian reflector antenna have been proven to be capable of achieving

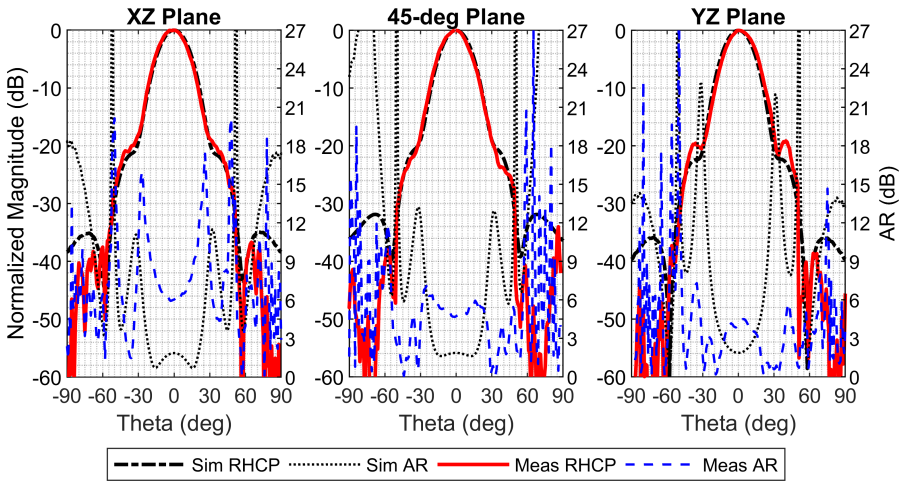

Figure 3.13: Simulated and measured radiation pattern for RHCP at 75 GHz.

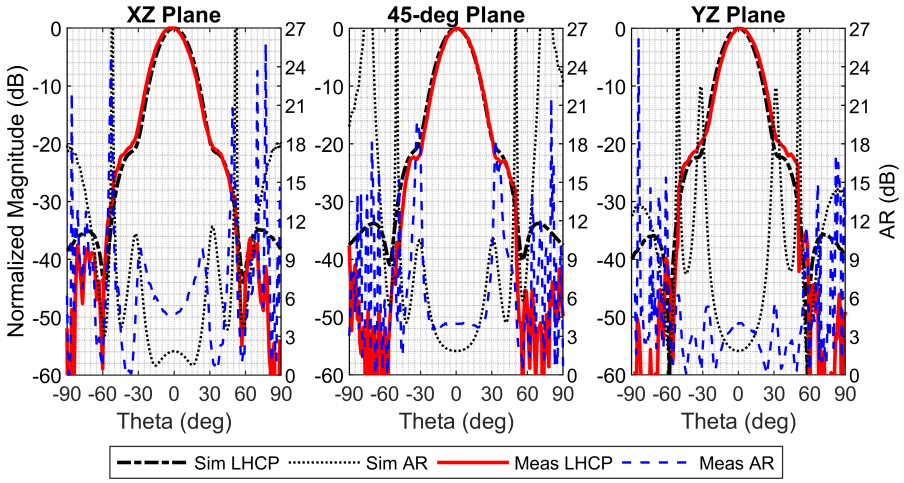

Figure 3.14: Simulated and measured radiation pattern for LHCP at 75 GHz.

high gain with a short focal length and allow a convenient rear location for the feed [8]. The main disadvantage of these configurations is the sub-reflector blockage, which causes performance degradation like high sidelobes and poor return loss [9]. Particularly, when the dual-CP antenna is used as the feed in a dual-reflector configuration, the reflection from the reflector back into the feed will degrade the isolation of the entire antenna because the reflection of a CP wave will be in an opposite sense of rotation. For example, when port 1 of the dual-CP feed is excited, the LHCP wave will be generated. The LHCP wave will be in the opposite sense of rotation, i.e., RHCP wave, after it is reflected by the sub-reflector. Part of the RHCP wave will go back into the dual-CP feed in the

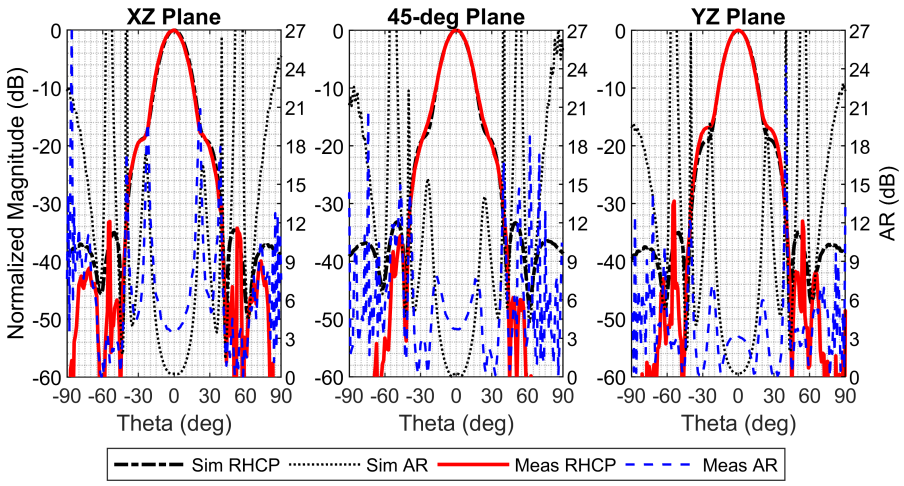

Figure 3.15: Simulated and measured radiation pattern for RHCP at 95 GHz.

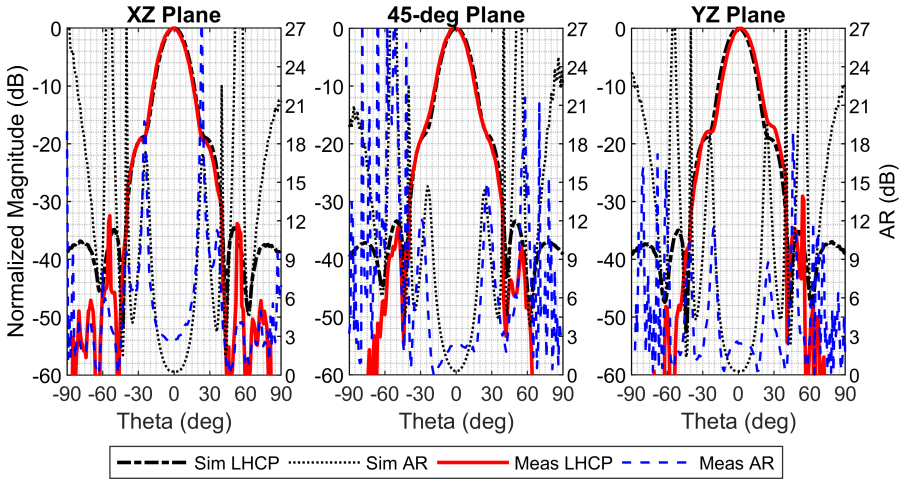

Figure 3.16: Simulated and measured radiation pattern for LHCP at 95 GHz.

traditional Cassegrain/Gregorian configurations and be guided to port 2 of the dual-CP feed, which implies that the $|S_{21}|$ (port isolation) will be degraded due to the presence of the sub-reflector. In order to minimize the degradation of the port isolation (minimize the reflection from the sub-reflector into the dual-CP feed), the Axially Displaced Ellipse (ADE) reflector antenna is selected to be used together with the dual-CP feed.

The ADE reflector antenna [10] has the advantage of low reflections into the feeds when compared with the traditional Cassegrain and Gregorian configurations due to its unique geometry. The geometry of the ADE reflector antenna with some relevant rays is depicted in Figure 3.18. The profile of the main reflector is a parabola whose axis is

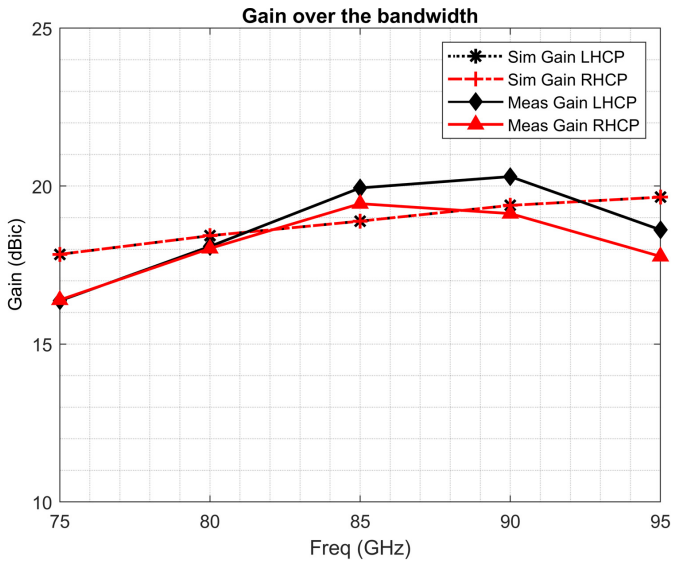

Figure 3.17: Simulated and measured gains of the proposed antenna.

displaced from the antenna axis of symmetry. The profile of the sub-reflector is an arc of an ellipse with a tilted axis. One of the focal points (O_1) of the ellipse coincides with that of the parabola, while the other focal point of the ellipse (O_2) is located on the antenna axis of symmetry where the phase centre of the feed is placed. When the two profiles are rotated along the symmetric axis, the surface of the main and sub-reflector is produced. According to the geometrical property of the ellipse, the rays radiated from the phase centre of the feed at O_2 will converge at O_1. The converged rays at O_1 will act like a point source at the focal point of the parabolic reflector (main reflector) because O_1 coincides with the focal point of the parabolic reflector. Consequently, the rays will then be reflected into a collimated plane wave beam by the main reflector, thereby achieving a high directivity and a narrow beamwidth. Additionally, it can be seen from Figure 3.18 that the inner-most ray radiating from O_2 is redirected to the outer edge of the main reflector by the sub-reflector, while the outer-most ray radiating from O_2 to the outer edge of the sub-reflector is redirected to the most inward radius of the main reflector. The ray plot of ADE reflector antenna is shown in Figure 3.19 [11]. It can be found that the rays reflected by the main reflector will not go back into the sub-reflector, leading to low sub-reflector blockage loss. It can also be observed that most of the rays reflected by the sub-reflector will not go back into the feed, thereby reducing the reflection into

the feed significantly.

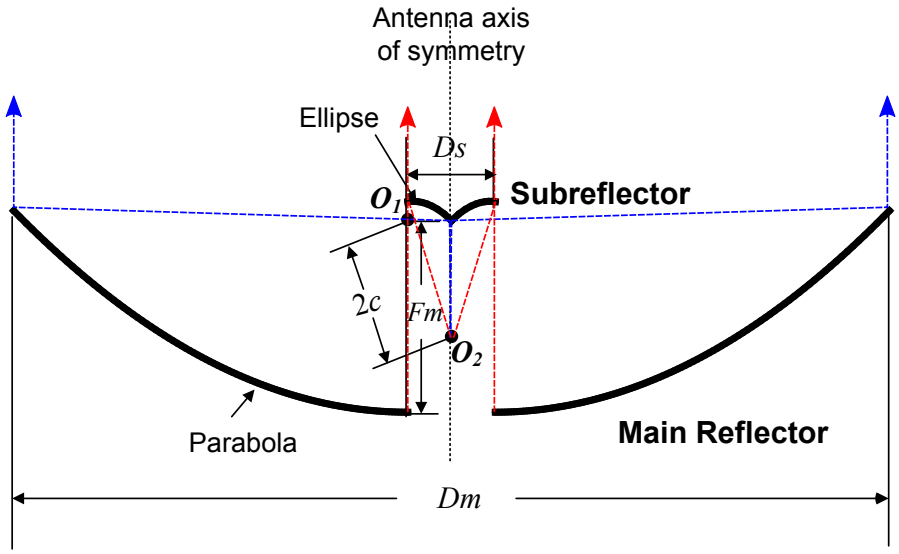

Figure 3.18: Geometry of the ADE reflector antenna.

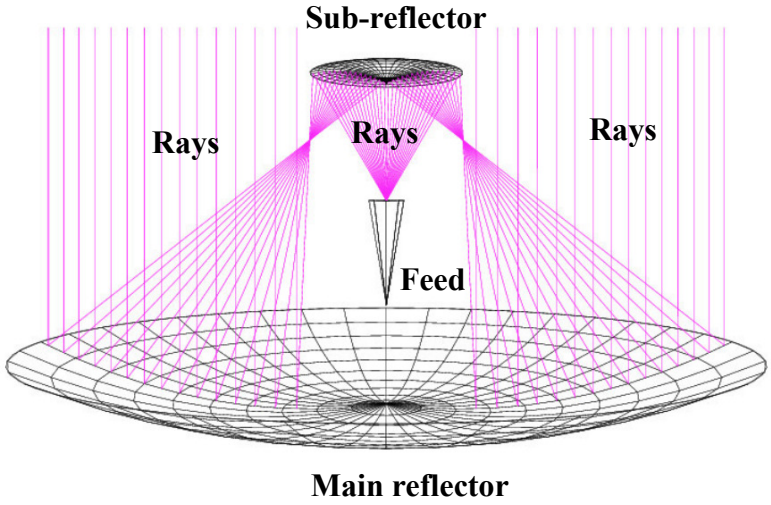

Figure 3.19: Geometric ray plot of the ADE reflector antenna [11].

The configuration of ADE reflector antenna is analyzed in a generalized study in [12]. In [13], a prototype of X-band ADE with an aperture diameter of 1250 mm is fabricated and measured as part of the NASA's Mars Surveyor 2001 Program, which shows a high gain up to 39.3 dBi and SLL of about -15 dB. Another ADE antenna realizing LHCP at X-band with an aperture diameter of 0.7 m is reported in [14], which achieves an antenna gain of 33.3 dBic and SLL of about -18 dB. This design has been successfully implemented in India's first mission to the Moon, Chandrayaan-1. In [15], a monopulse

dual-reflector antenna operating at W-band with an aperture diameter of 180 mm is proposed based on the ADE structure, which shows a measured gain of 40.1 dBi with SLL < -19.7 dB.

3.4.2 Design of the ADE Antenna

The complete antenna system consisting of an ADE reflector antenna and the dual-CP antenna designed in Section 3.3 as a feed is presented in Figure 3.20.

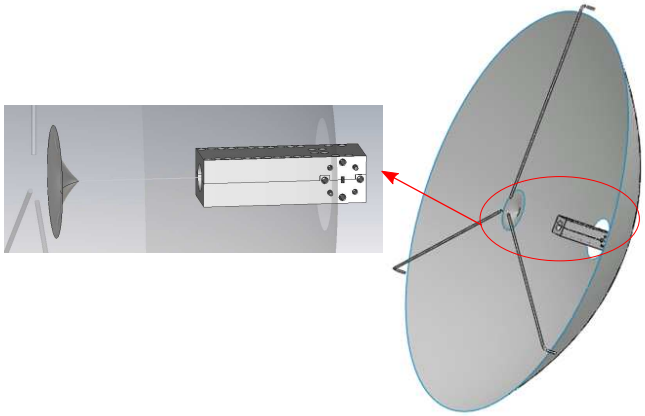

Figure 3.20: The complete ADE antenna system.

To illustrate the design procedure of the ADE reflector antenna, the geometry of the main reflector and sub-reflector and relevant parameters are depicted in Figure 3.21. The three-dimensional reflector surfaces can be generated by rotating the curves around antenna axis of symmetry.

Initially, the diametre of the main reflector (D_m) and sub-reflector (D_s) as well as the focal length of the main reflector should be decided. Given expected antenna gain of G_0 (dB) at the centre frequency of f_c with an aperture efficiency of η_0, which can be written as

$$G_0[dB] = 10log\left[4\pi\frac{\pi(D_m/2)^2}{\lambda_c^2}\eta_0\right], \qquad (0 < \eta_0 \leq 1) \tag{3.2}$$

so we can have

$$D_m = (c/f_c)10^{(G_0-9.94-10log\eta_0)/20} \qquad (0 < \eta_0 \leq 1) \tag{3.3}$$

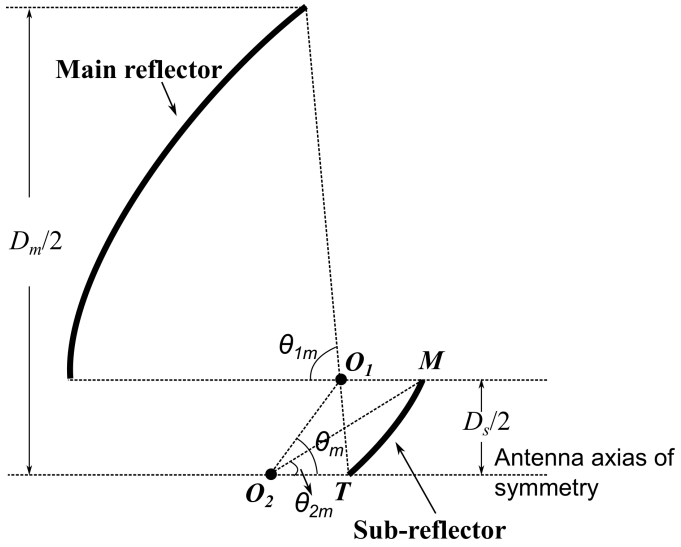

Figure 3.21: Geometry of the ADE configuration.

where c is the speed of light.

The focal length of the main reflector (F_m) can be decided by choosing a suitable focal length over diameter ratio (τ), and $\tau \leq 0.25$ is normally used for a low-profile ADE reflector antenna used in wireless communication applications [14]. So the focal length of the main reflector can be decided as

$$F_m = \tau D_m \tag{3.4}$$

The diameter of sub-reflector can be decided as

$$D_s = \alpha D_m \tag{3.5}$$

where $\alpha = D_s/D_m$. Normally, $\alpha \approx 0.1$ is considered to be the best choice for ADE structure [14].

After D_m, D_s and F_m is obtained, the geometry of the main reflector is determined. Because we design the dual-CP feed first, the reflector antenna should be designed to match the radiation characteristics of the feed. Since 10-dB or 12-dB taper angle of the feed is normally used to illuminate the sub-reflector to achieve best aperture efficiency,

the half-illuminating angle of the sub-reflector (θ_{2m} in Figure 3.21) should be decided by the taper angle of the feed. With θ_{2m} obtained from the radiation characteristics of the feed, as well as D_m, D_s, F_m, the geometry of sub-reflector and the configuration of the complete reflector antenna can be obtained as follows.

Firstly, the half-illuminating angle of the main reflector is derived. According to the parabola equation in polar coordinates, we have

$$\frac{2F_m}{1+cos\theta_{1m}}sin\theta_{1m} = \frac{D_m - D_s}{2} \tag{3.6}$$

It can be derived that

$$tan\left(\frac{\theta_{1m}}{2}\right) = \frac{D_m - D_s}{4F_m} \tag{3.7}$$

Thus the half illuminating angle of main reflector can be obtained by

$$\theta_{1m} = 2arctan\left(\frac{D_m - D_s}{4F_m}\right) \tag{3.8}$$

According to the geometry configuration, we have

$$O_2Msin(\theta_m - \theta_{2m}) = O_1Msin\theta_m \tag{3.9a}$$

$$O_1M = 2a - O_2M \tag{3.9b}$$

$$O_2M = \frac{D_s}{2sin\theta_{2m}} \tag{3.9c}$$

where a is the semi-major axis of the ellipse that the profile of sub-reflector follows. It can be derived from equation (3.9) that

$$\frac{D_s}{2}\left(\frac{1}{tan\frac{\theta_{2m}}{2}} - \frac{1}{tan\theta_m}\right) = 2a \tag{3.10}$$

From the geometry configuration, we can also obtain that

$$O_1T = \frac{D_s}{2sin\theta_{1m}} \tag{3.11a}$$

$$O_2T = \frac{D_s}{2}(\frac{1}{tan\theta_m} + \frac{1}{tan\theta_{1m}}) \tag{3.11b}$$

$$2a = O_1T + O_2T \tag{3.11c}$$

It can be derived from equation (3.11) that

$$\frac{D_s}{2}(\frac{1}{tan\theta_m} + \frac{1}{tan\frac{\theta_{1m}}{2}}) = 2a \tag{3.12}$$

By using equation (3.10) and equation (3.12), we can get

$$\frac{D_s}{2}\left(\frac{1}{tan\frac{\theta_{2m}}{2}} - \frac{1}{tan\theta_m}\right) = 2a = \frac{D_s}{2}(\frac{1}{tan\theta_m} + \frac{1}{tan\frac{\theta_{1m}}{2}}) \tag{3.13}$$

Then it can be obtained that

$$\theta_m = arctan\left(\frac{2tan\frac{\theta_{1m}}{2}tan\frac{\theta_{2m}}{2}}{tan\frac{\theta_{1m}}{2} - tan\frac{\theta_{2m}}{2}}\right) \tag{3.14}$$

With θ_m obtained, the semi-major axis a can be given from equation (3.12) as

$$a = \frac{D_s}{4}(\frac{1}{tan\theta_m} + \frac{1}{tan\frac{\theta_{1m}}{2}}) \tag{3.15}$$

The focal distance c can be derived from the geometry that

$$c = \frac{D_s}{4sin\theta_m} \tag{3.16}$$

The eccentricity of the ellipse that the profile of sub-reflector follows can then be obtained as

$$e = \frac{c}{a} \tag{3.17}$$

Finally, let O_1 be the origin in the global polar coordinates, the equation of the profile for the main reflector can be expressed as

$$\rho_{main} = \frac{2F_m}{1 + cos\theta_{main}}, \quad \theta_{main} \in [0, \theta_{1m}] \tag{3.18}$$

while the equation of the profile for the sub-reflector can be expressed as

$$\rho_{sub} = \frac{a(1-e^2)}{1 - ecos\theta_{sub}}, \quad \theta_{sub} \in [\pi - \theta_m, \pi - (\theta_m + \theta_{1m})] \tag{3.19}$$

The profile obtained from the aforementioned design principles can then be evaluated in simulation and used as a start point of optimization. The design parameters, such as D_m, F_m, D_s and half-illuminating angle (θ_{2m}), can be tuned to achieve expected performance.

In our design, we start with an expected gain of 51 dBic with an aperture efficiency of 78% at centre frequency of 85 GHz, which leads to a diameter of 450 mm for the main reflector. Then the design parameters are optimized to achieve the SLL < -20 dB when keep the directivity higher than 50 dBic at the centre frequency in full-wave simulations using CST Microwave Studio. The optimized design parameters are listed in Table 3-A.

Table 3-A: Optimized design parameters of the ADE reflector antenna.

Parameters	$D_m(mm)$	$F_m(mm)$	$D_s(mm)$	$\theta_{2m}(deg)$
Values	450	108	40	16°

3.4.3 Simulation Considerations of the ADE reflecctor with the dual-CP feed

The dual-CP antenna based on the septum polarizer is simulated using the transient solver in CST Microwave Studio as mentioned in Section 3.3.4. However, the transient solver is not suitable anymore when it comes to the simulation of the ADE reflector together with the dual-CP antenna used as a feed. The reason is that the size of the whole antenna system (ADE reflector antenna and the dual-CP feed) is much larger than

the working wavelength of the antenna (a so-called electrically large object), which leads to a huge number of mesh elements in the simulation thereby unacceptable computational cost if transient solver is used. An alternative technique should therefore be employed for simulating the ADE reflector antenna illuminated by the dual-CP feed.

Fortunately, there are a variety of numerical analysis techniques available nowadays, each of which is tailored to solve EM problems in specific scenarios. The comprehensive computational electromagnetics (CEM) software products, such as CST Microwave Studio and Feko, are both powerful tools featuring a pack of different numerical analysis techniques to cover solutions to EM problems in different scenarios. The application scenarios for most of the available numerical analysis techniques are illustrated in Figure 3.22, which can be found at the beginning of the Feko user guide. The principles of these techniques are beyond the scope of this thesis. The basics and further readings on these techniques can be found in the user guides of these CEM software products.

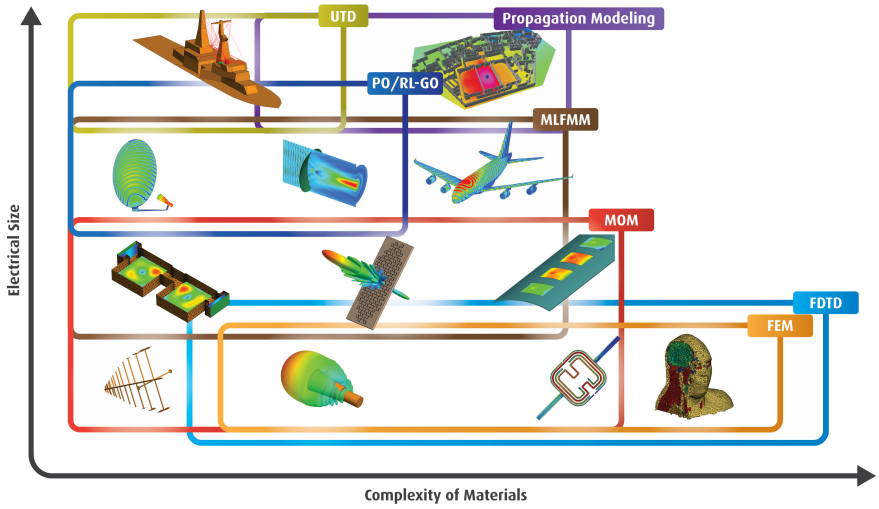

Figure 3.22: Application scenarios for most of the EM numerical analysis techniques [16].

It can be found from Figure 3.22 that Physical Optics (PO) and Multilevel Fast Multipole Method (MLFMM) are suitable for simulating reflector antennas. The MLFMM is an accelerated formulation of the Method of Moments (MoM, a full-wave solution of Maxwell's integral equations in the frequency domain) with an extreme reduction in the

required computational resources [17]. For this reason, the MLFMM has been considered as an efficient and accurate method for the full-wave analysis of electrically large structures like reflector antennas [18], and provided in Feko and the integral equation solver in CST Microwave Studio. The PO approximation, which is based on the calculation of induced surface current on a scatterer's surface [19], is an intermediate method between geometric optics, which ignores wave effects, and full-wave electromagnetism, which is a precise theory. The PO method is designed to solve EM problems where electrically very large metallic or dielectric structures are modelled. In some cases, despite the reduced computational cost of the MLFMM, the scatterers are still too electrically large to be solved by full-wave methods like the MLFMM. Under these circumstances, if the scatters are relatively smooth, the PO approximation might be an alternative solution. Although the PO is an approximation that assumes the scatterer can locally be approximated by an infinite tangent plane, it is usually considered to be a sufficiently accurate approximation for electrically large reflectors.

From the introduction mentioned above, we can find that either PO or MLFMM can be applied to the analysis of reflector antennas. The PO approximation typically requires fewer computational resources than the MLFMM. In Feko's example guide [20], an example project of a parabolic reflector fed by a conical horn is used to demonstrate the required computational resources and differences in radiation pattern results of several numerical analysis techniques. The results obtained by MLFMM are used as a benchmark since MLFMM is the most reliable approach for electrically large models. The results of this example show that the memory requirement and solution time can be significantly reduced by replacing the horn with the equivalent source and applying the PO to the parabolic reflector. However, because Feko does not support PO for two objects, for dual-reflector configuration like the ADE reflector antenna, MLFMM have to be applied to the sub-reflector, the PO can only be applied to the main reflector, so the simulation speed will be much slower than that in TICRA GRASP (a software dedicated to the design of reflector antenna systems) where PO can be applied to both sub-reflector

and main reflector. The PO approximation also has some drawbacks. The PO approximation is less accurate than the MLFMM, as we explained before, although for most reflector antenna the accuracy is sufficient. It can be found from the results that the SLL obtained from the PO approximation is about 2 dB lower than that obtained from the MLFMM. The PO approximation has limited application scenarios. For instance, for the reflector antenna system designed in this chapter which includes the ADE reflectors and the dual-CP antenna as the feed, the PO can only be used to calculate radiation patterns of the ADE reflector antenna with the equivalent farfield/nearfield source of the dual-CP feed obtained by full-wave simulation, while the MLFMM not only can be used to calculate the radiation patterns of the ADE reflector antenna but also can be used to simulate the dual-CP feed just like other full-wave numerical analysis techniques. The MLFMM can even be used to simulate the ADE reflector antenna together with the dual-CP feed without using an equivalent farfield/nearfield source of the dual-CP feed if the size of the whole antenna system is not too large. With this configuration, the reflection coefficient and port isolation of the whole antenna system, i.e., the reflection coefficient and port isolation at port 1 and 2 of the dual-CP antenna with the presence of the ADE reflector, can be obtained.

Another consideration is the CEM software. For reflector antenna designs, TICRA GRASP could be another choice besides CST Microwave Studio and Feko because it is dedicated to reflector antenna designs. The PO method in TICRA GRASP is much faster than the MLFMM. It is worth pointing out that TICRA has also developed the MLFMM and integrated it into GRASP since a very recent version (v10.4). However, the antenna group at Queen Mary University of London only has GRASP 9.6 with only one dongle licence, which was released about ten years ago and does not have technical support now. The 3-D modelling of the ADE reflector antenna is difficult in GRASP 9.6 because it is not a typical Cassegrain or Gregorian structure (ADE structure has been introduced in TICRA GRASP in a newer version, but we don't have licence), not to mention carrying out a parameter sweep and optimizing the reflector structure. By contrast, we have

the latest version of CST Microwave Studio with full licence and technical support. Moreover, 3-D modelling of the ADE reflector is much easier in CST Microwave Studio in a programmatical way, and we have developed a Matlab program to create and run CST projects of the ADE reflector, including building the reflector's 3-D model from scratch. This program facilitates automatic parameter sweep and optimization of the ADE reflector antenna design.

In Table 3-B, we compare the different solutions for computing radiation patterns of the ADE reflector antenna system designed in section x. It can be found that MLFMM (integral equation solver) in CST Microwave Studio can provide the best accuracy and gratifying simulation speed with the support of GPU acceleration. Moreover, the 3-D modelling and automatic optimization/parameter sweep of the ADE reflector antenna system is much easier in CST Microwave Studio with the Matlab interface it provides and the Matlab program we have developed. Considering the fact that the aim of this research is not to design reflectors but to design the feed, the reflector design is only a one-time demonstration to show the high gain can be realized when the dual-CP antennas we designed are used to feed the reflectors. For this reason, using MLFMM (integral equation solver) in CST Microwave Studio is considered to be the best choice in our case. It should be pointed out that the simulation time of each software in Table 3-B was measured using the best computational resources we could offer for each software, respectively. The TICRA GRASP was not available on any of our workstations, so it was running on a personal desktop. The FEKO did not support GPU acceleration at the time of this research and was not available on the High Performance Compouting (HPC) cluster at QMUL, so we ran it on the most powerful workstation we had. Most of the solvers in CST Microwave Studio support GPU acceleration, and CST Microwave Studio has been installed on the HPC at QMUL, so we ran CST Microwave Studio on the GPU nodes of the HPC cluster with NVIDIA Tesla V100 GPU cards.

The co-polar radiation patterns obtained by these three CEM software with different numerical analysis techniques are shown in Figure 3.23. It can be observed that there

Table 3-B: Comparison of the different solutions for computing radiation patterns of the ADE reflector antenna system in Section 3.4.2

Software	TICRA GRASP	Feko	CST Microwave Studio
Configuration	equivalent source of the dual-CP feed + ADE reflector antenna		
Solver	PO	sub-reflector: MLFMM; main reflector: PO	MLFMM (I-Solver)
Simulation Time	< 10 s*	243 min**	28 min***
Peak Memory	< 10 GByte	15.386 GByte	18.472 GByte
Accuracy	medium	good	good

* PC, Intel i7-6700@3.40 GHz, 16 GB RAM.
** Workstation, Intel Xeon CPU E5-4620@2.20 GHz (2 processors), 512 GB RAM.
*** HPC, Intel Xeon Gold 6142 (Skylake), 384 GB RAM, GPU: 1 x NVIDIA Tesla V100.

is good agreement among these three radiation patterns, although the first SLL of the result obtained from TICRA GRASP is 1 dB lower than those from Feko and CST Microwave Studio.

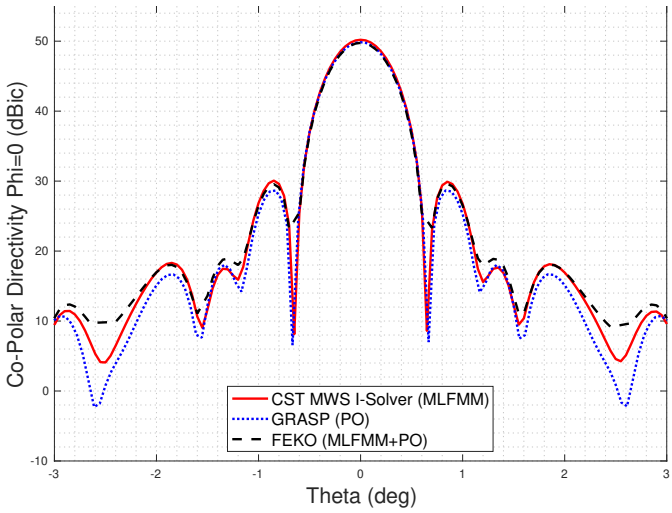

Figure 3.23: Radiation patterns of the ADE reflector antenna obtained from different CEM software listed in Table 3-B.

However, when it comes to computing the reflection coefficient and port isolation of the entire ADE reflector antenna system, i.e., computing the reflection coefficient and port isolation of the dual-CP antenna at port 1 and port 2 (see Figure 3.4) with the presence of the ADE reflector antenna, the dual-CP feed cannot be replaced with the equivalent source to reduce the computational cost. For this reason, using TICRA GRASP

was not an option because the dual-CP feed based on the septum polarizer cannot be modelled in TICRA GRASP (TICRA GRASP cannot model waveguide structure). The options left for us was to use Feko or CST to simulate the ADE reflector antenna together with the dual-CP feed, and it can be found from Figure 3.22 that the MLFMM would be the most suitable choice because this configuration exhibits structure characteristics of both complexity (due to the small stepped septum in the septum polarizer) and electrical large size (due to the main reflector). However, this configuration would increase the computational cost considerably. The GPU acceleration for MFLMM in CST failed to solve this configuration because the size of the data required to be exported to the GPU exceeded the RAM size on the best GPU we could use. Consequently, the only option was to run the simulation on the most powerful workstation we had. Nevertheless, we found that it took about 2 days to calculate the result for only one frequency sample. It means it would take several months to obtain sufficient samples of the S-parameters covering the expected working bandwidth from 75 - 95 GHz, which is unacceptable. According to the geometry of the ADE reflector antenna, the reflection coefficient and port isolation of the dual-CP feed will largely be affected by the scattered energy from sub-reflector that is just in front of the aperture of the dual-CP horn. For this reason, it is reasonable to obtain approximate reflection coefficient and port isolation of the entire ADE reflector antenna system by computing the reflection coefficient and port isolation of the dual-CP antenna at port 1 and port 2 with the presence of only the sub-reflector. For this model, the transient solver in CST Microwave Studio with GPU acceleration can then be used to perform this simulation efficiently since the size of the sub-reflector and the dual-CP feed is not large.

3.4.4 Simulated Results of the Complete High-Gain Dual-CP Antenna

In this section, the simulated results of the complete high-gain dual-CP antenna shown in Figure 3.20 are presented. The simulation is performed using CST Microwave Studio. The simulation results of the feed horn at different frequencies are exported as nearfield sources, and used to excite the ADE reflector antenna in the simulation of the complete

antenna system. Only simulation results of LHCP are shown here, because all results of RHCP are identical to those of LHCP in the simulation due to the symmetry of structures of the feed and the ADE reflector antenna.

The radiation patterns of LHCP at 75 GHz, 85 GHz and 95 GHz are presented in Figure 3.24. It can be seen from the results that directivities of 48.29 dBic, 50.2 dBic and 50.94 dBic are achieved at 75 GHz, 85 GHz and 95 GHz, respectively. It can also be observed that rotationally symmetric radiation patterns are achieved at all frequencies.

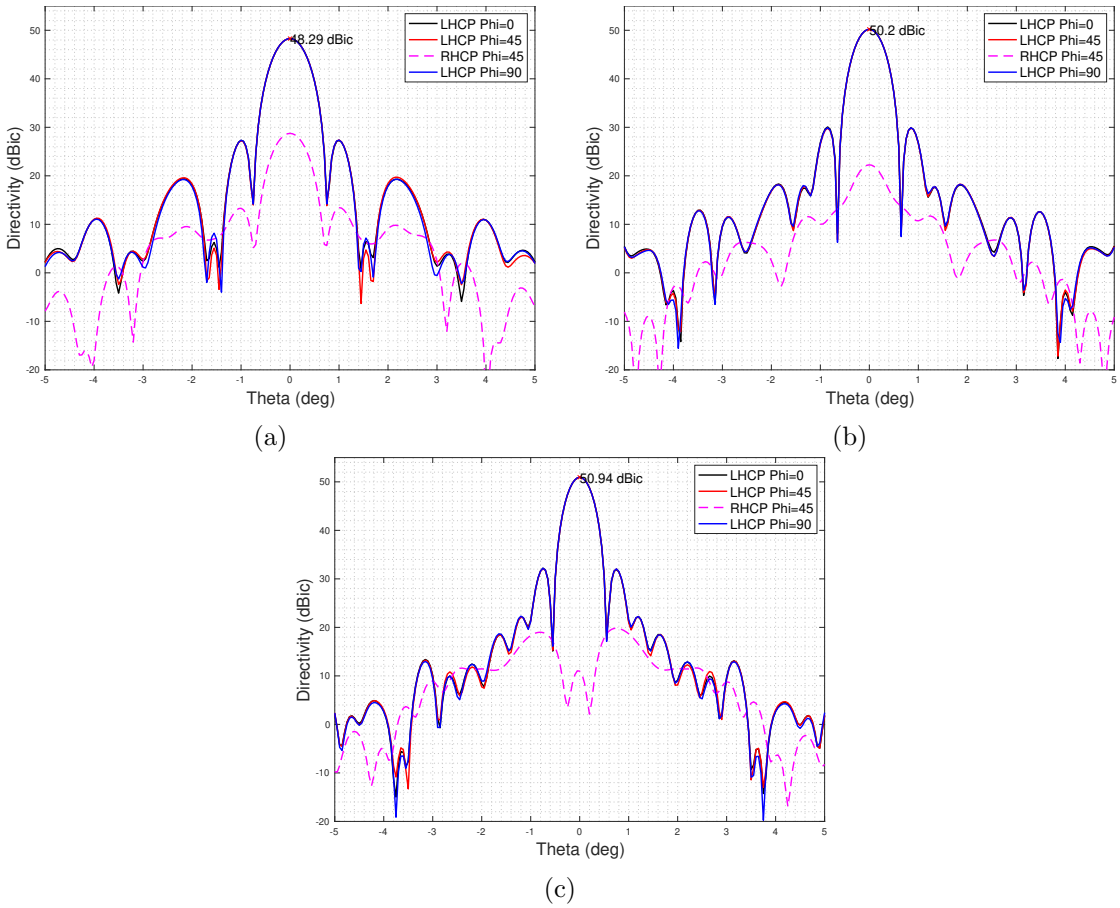

Figure 3.24: Simulated radiation patterns of the complete high-gain dual-CP antenna at (a) 75 GHz, (b) 85 GHz and (c) 95 GHz.

The simulated AR results at boresight over the working bandwidth for LHCP are shown in Figure 3.25. The result shows that the AR is below 1.9 dB and is close to the simulated AR of the feed antenna, which means the CP characteristics of the feed are

well maintained in the ADE reflector antenna.

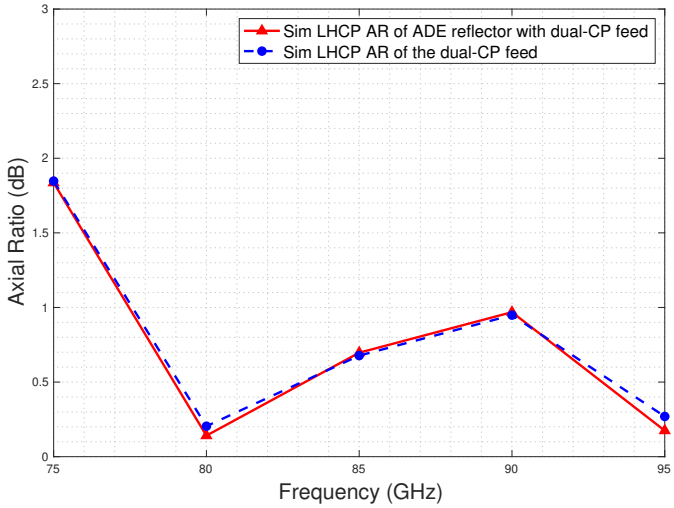

Figure 3.25: Simulated LHCP AR of the ADE reflector with the dual-CP feed and the dual-CP feed.

Figure 3.26 depicts the directivity of co-polar (LHCP) and cross-polar level at boresight as well as sidelobe level (SLL) over the entire working bandwidth. The result shows that directivity of co-polar (LHCP) is 49.6 ± 1.3 dBic. The best cross-polarization isolation (XPD) of 42 dB is found at 80 GHz, while the worst case is 20 dB at 75 GHz. The SLL is -20 ± 0.9 dB.

In order to investigate the reflection coefficient and port isolation of the complete antenna system, i.e., the reflection coefficient and port isolation of the dual-CP horn antenna at port 1 and port 2 (see Figure 3.4) with the presence of the ADE reflector antenna, a full-wave simulation which only includes the dual-CP feed antenna and the sub-reflector as shown in Figure 3.27 is carried out using the transient solver in CST Microwave Studio. The reason for using this approach has been elaborated at the end of Section 3.4.3. To verify that this approach is a reasonable approximation to simulate the dual-CP feed with the presence of both the sub-reflectors and main reflector, we also simulated the complete antenna system at 21 frequency samples within the 20-GHz operating bandwidth using MLFMM in CST Microwave Studio.

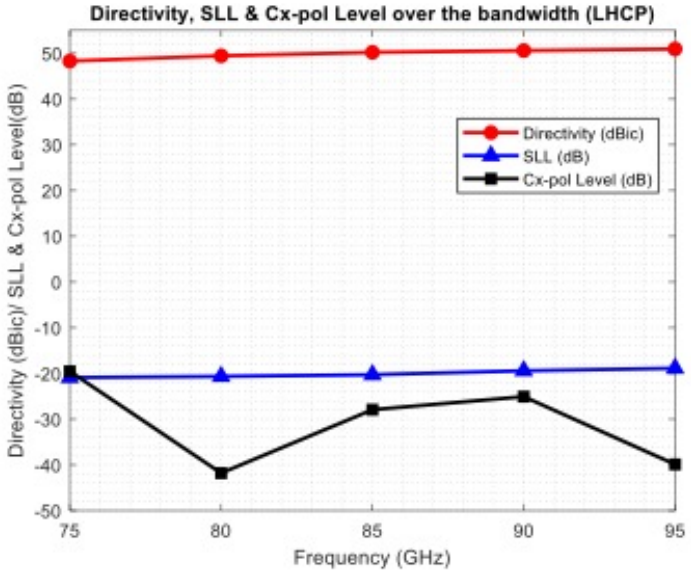

Figure 3.26: Simulated directivity, cross-polar level at boresight and SLL over the working bandwidth.

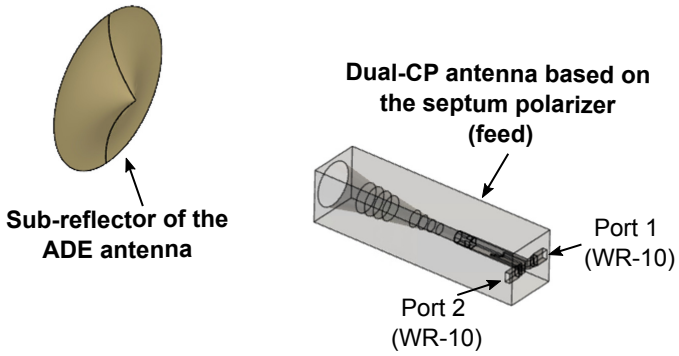

Figure 3.27: Simulation model for computing S-parameters of the dual-CP feed with the presence of the sub-reflector.

The simulated reflection coefficient and isolation of port 1 of the dual-CP feed horn are shown in Figure 3.28. It can be found that the results from the simulation in which only sub-reflector is included agree well with those from the simulation in which both reflectors are included, which proves the former is a reasonable approximation of the latter. The results show that the reflection coefficient when the feed works with the sub-reflector does not change too much. However, it can be observed that the isolation is degraded by about 5 dB even though the ADE structure has a relatively low reflection into the feed.

The reasons for the degradation of the port isolation are listed as follows. Firstly, the centre tip of the sub-reflector will reflect a small amount of energy back into the dual-CP feed. Secondly, the dual-CP antenna is not an ideal point source (in practice, no antenna is [21]); the position of its phase centre cannot be accurately calculated and placed at the focal point O_2 in Figure 3.18. Moreover, the position of its phase centre varies from frequency to frequency. Consequently, the EM wave radiated from the dual-CP feed will not exactly follow the geometric optics (GO) path described in Section 3.4.1 thereby causing unexpected reflection back into the dual-CP feed. Despite the degradation, the isolation is still higher than 20 dB over most of the working bandwidth. According to the results, it can be derived that 5 - 10 dB margin should be reserved for the isolation in the design of the feed, which means a dual-CP horn with high isolation is strongly desirable.

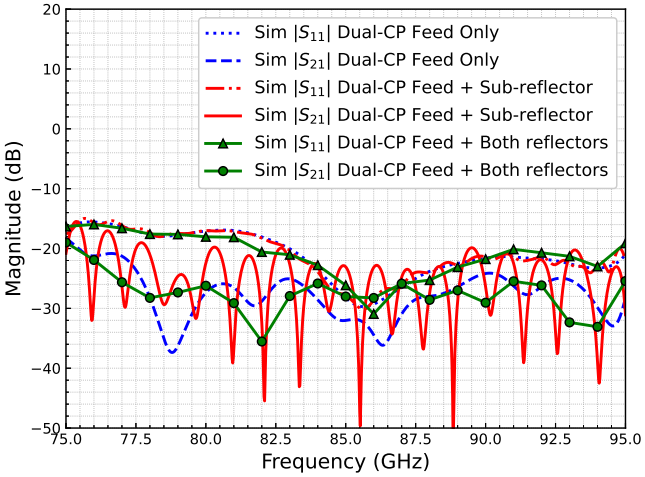

Figure 3.28: Simulated reflection coefficient and port isolation when the feed horn works with the sub-reflector.

3.5 Summary

A wideband horn antenna with dual circular polarization is proposed and investigated in this chapter. This antenna is designed based on a stepped septum polarizer and a profiled smooth-wall circular horn. A prototype is fabricated and measured, and the experimental results show that 21% relative bandwidth ranging from 76.8 GHz to 94.7

GHz is achieved with reflection coefficient $|S_{11}| < -15$ dB and isolation > 20 dB as well as AR < 5.8 dB for both LHCP and RHCP. The discrepancy between simulated and measured AR has been found to be mostly caused by the misalignment of the fabrication. Furthermore, an ADE reflector antenna is designed based on the radiation characteristics of the dual-CP horn. The simulated results show that directivity of 49.6 ± 1.3 dBic with AR < 1.9 dB is achieved over the entire working bandwidth, which demonstrates that both high gain and dual-CP for mmWave communications can be realized when the dual-CP horn is used as a feed to reflector antennas.

References

[1] C. Kumar, V. V. Srinivasan, V. K. Lakshmeesha, and S. Pal, "Novel Dual Circularly Polarized Radiating Element for Spherical Phased-Array Application," *IEEE Antennas and Wireless Propagation Letters*, vol. 8, pp. 826–829, 2009.

[2] U. P. Hong, M. Schneider, and R. Gehring, "Slim Ka-band triple band polariser network for user and gateway antenna feed application," in *2017 47th European Microwave Conference (EuMC)*, 2017, pp. 1163–1166.

[3] G. Addamo, O. A. Peverini, D. Manfredi, F. Calignano, F. Paonessa, G. Virone, R. Tascone, and G. Dassano, "Additive Manufacturing of Ka-Band Dual-Polarization Waveguide Components," *IEEE Transactions on Microwave Theory and Techniques*, vol. 66, no. 8, pp. 3589–3596, 2018.

[4] C. A. Leal-Sevillano, K. B. Cooper, J. A. Ruiz-Cruz, J. R. Montejo-Garai, and J. M. Rebollar, "A 225 GHz Circular Polarization Waveguide Duplexer Based on a Septum Orthomode Transducer Polarizer," *IEEE Transactions on Terahertz Science and Technology*, vol. 3, no. 5, pp. 574–583, 2013.

[5] M. Chen and G. Tsandoulas, "A wide-band square-waveguide array polarizer," *IEEE Transactions on Antennas and Propagation*, vol. 21, no. 3, pp. 389–391, 1973.

[6] C. Granet, "Profile options for feed horn design," in *2000 Asia-Pacific Microwave Conference. Proceedings (Cat. No.00TH8522)*, 2000, pp. 1448–1451.

[7] A. Mediavilla, J. L. Cano, and K. Cepero, "On the Octave Bandwidth Properties of Octagonal-Shaped Waveguide Mode Transformers," *IEEE Transactions on Microwave Theory and Techniques*, vol. 59, no. 10, pp. 2447–2451, 2011.

[8] P. Hannan, "Microwave antennas derived from the cassegrain telescope," *IRE Transactions on Antennas and Propagation*, vol. 9, no. 2, pp. 140–153, 1961.

[9] S. K. Sharma, S. Rao, and L. Shafai, *Handbook of Reflector Antennas and Feed Systems Volume I: Theory and Design of Reflectors*, ser. Antennas and Propagation. Artech House, 2013.

[10] W. Rotman and J. Lee, "Compact dual frequency reflector antennas for EHF mobile satellite communication terminals," in *1984 Antennas and Propagation Society International Symposium*, vol. 22, 1984, pp. 771–774.

[11] M. Schneider and M. Rayner, "Design of a shipborne dual-band reflector antenna," in *51st Internationales Wissenschaftliches Kolloquium*, 2006.

[12] F. J. S. Moreira and A. Prata, "Generalized classical axially symmetric dual-reflector antennas," *IEEE Transactions on Antennas and Propagation*, vol. 49, no. 4, pp. 547–554, 2001.

[13] A. Prata, F. J. S. Moreira, and L. R. Amaro, "Displaced-axis-ellipse reflector antenna for spacecraft communications," in *Proceedings of the 2003 SBMO/IEEE MTT-S International Microwave and Optoelectronics Conference - IMOC 2003. (Cat. No.03TH8678)*, vol. 1, 2003, pp. 391–395.

[14] C. Kumar, V. V. Srinivasan, V. K. Lakshmeesha, and S. Pal, "Performance of an Electrically Small Aperture, Axially Displaced Ellipse Reflector Antenna," *IEEE Antennas and Wireless Propagation Letters*, vol. 8, pp. 903–904, 2009.

[15] Y. Wang, W. Dou, and B. Bi, "W band axially displaced monopulse dual-reflector antenna for inter-satellite communications," *IET Microwaves, Antennas & Propagation*, vol. 10, no. 7, pp. 742–747, 2016.

[16] *Altair Feko User Guide (Altair Feko)*, Altair Engineering Inc., 2020.

[17] W. C. Chew, E. Michielssen, J. M. Song, and J. M. Jin, *Fast and Efficient Algorithms in Computational Electromagnetics*. USA: Artech House, Inc., 2001.

[18] Altair Engineering Inc. (2016, Dec.) Numerical methods in feko. [Online].

Available: https://www.altair.com/resource/numerical-methods-in-feko

[19] J. S. Asvestas, "The physical optics method in electromagnetic scattering," *Journal of Mathematical Physics*, vol. 21, no. 2, 2 1980.

[20] *Altair Feko Example Guide (Altair Feko)*, Altair Engineering Inc., 2020.

[21] C. A. Balanis, *Antenna Theory: Analysis and Design*, 4th ed. Hoboken, New Jersey: John Wiley & Sons, Inc., 2016.

Chapter 4

Design of Wideband Dual-Circular-Polarization Antenna with High Isolation Based on the Grooved-Wall Septum Polarizer

4.1 Introduction

In Chapter 3, a dual-CP antenna based on a 4-step septum polarizer and a profiled smooth-wall horn is designed. The measured results show a bandwidth of 21% from 76.8 to 94.7 GHz with isolation higher than 20 dB. However, as discussed in Chapter 1, antenna port isolation higher than 30 dB is preferable if Polarization Division Multiplexing (PDM) or In-Band Full Duplex (IBFD) is employed in the wireless communication system, in order to achieve proper performance [1, 2].

According to the literature review in Chapter 2, a variety of Dual-Circular-Polarization (Dual-CP) antennas have been investigated in the frequency bands below 60 GHz, based on waveguide septum polarizer with horn antenna, microstrip patch array, and Substrate Integrated Waveguide (SIW). However, most of them show the port isolations at the level of 15 dB or 20 dB. The highest port isolations are reported in [3] and [4], which are both based on a waveguide septum polarizer with a horn antenna. They achieve port isolations higher than 30 dB and 27 dB respectively. Nevertheless, their overall bandwidths with the high isolations are limited to 3.86% and 9% respectively.

On the other hand, there are only a few dual-CP antennas reported in the frequency bands above 60 GHz [5–7], where wider continuous spectrum for point-to-point (PtP) and point-to-multi-point (PtMP) wireless communications with ultra-high data rate is available. According to the literature review in Chapter 2, the dual-CP antenna reported in [7], which consists of a 5-step septum polarizer and a smooth-wall horn, shows a port isolation higher than 30 dB over 10% bandwidth from 213 to 237 GHz, which is the highest isolation over widest bandwidth ever reported. It can be found from the performance of dual-CP antennas reported in the frequency bands above 60 GHz that, dual-CP antennas based on septum polarizer with horn still appear to be an attractive choice in the frequency bands above 60 GHz when high isolation over a wide bandwidth is required. However, the design of conventional septum polarizers like that reported in Chapter 3 mainly relies on adjusting the dimensions of the stepped septum to achieve both desired impedance bandwidth and AR bandwidth. Further improvement for the dual-CP antenna based on the conventional septum polarizer to achieve high isolation > 30 dB over a bandwidth $> 10\%$ is quite challenging, due to the bandwidth limitation up to 25% and the trade-off between impedance bandwidth and AR bandwidth of the stepped septum polarizer, as discussed in Chapter 2.

In this chapter, a grooved-wall septum polarizer is proposed for the first time to realize a wideband dual-CP antenna with high port isolation in conjunction with a conical horn. By introducing a pair of grooves to the walls of the conventional stepped septum

polarizer to improve the phase orthogonality of the CP wave, it allows optimization of the septum polarizer to focus on the impedance performance, thereby alleviating the trade-off between impedance performance and AR performance and achieving both high port isolation and good AR over a wide bandwidth. Additionally, the number of steps of the septum can be reduced with this design hence ease for fabrication in the mmWave band. The operating principle of the proposed dual-CP antenna has been analyzed, and a prototype has been fabricated to verify the design in the W-band. The measured results show the proposed dual-CP antenna has a port isolation higher than 30 dB and AR $<$ 3 dB over a bandwidth of 15.8% from 93 to 109 GHz while the reflection coefficient lower than -17 dB. To the best of the author's knowledge, this is the dual-CP antenna with the highest isolation over widest bandwidth ever reported. A high antenna gain above 25 dBic is achieved with rotationally symmetric radiation patterns over the entire operating bandwidth. With a high isolation over a wide bandwidth as well as good AR and radiation characteristics, this dual-CP antenna is able to offer polarization diversity/multiplexing or Full-Duplex capability for high-data-rate mmWave wireless communication systems with good performance.

The remainder of this chapter is organized as follows. An overview of the entire antenna configuration is described in Section 4.2. In Section 4.3, the operating principles of the proposed grooved-wall stepped septum polarizer is analyzed. Section 4.4 presents the designs of the grooved-wall stepped septum polarizer and the horn in W-band. In Section 4.5, simulated and measured results are presented and discussed, followed by summary in Section 4.6.

4.2 Antenna Overview

The structure of the complete dual-CP antenna is presented in Figure 4.1, which is comprised of three sections. A conical horn is connected to a stepped septum polarizer by a smooth square-to-circular waveguide transformer. A pair of grooves is introduced on the wall of the square waveguide of the septum polarizer to improve the phase orthogonality

of the CP wave, and a pair of 90° E-plane bends with waveguide transformers is used to transform the input ports of the septum polarizer into standard WR-10 rectangular waveguides. When port 1 is excited, LHCP will be generated; while port 2 is excited, RHCP will be generated. The LHCP and RHCP signals generated by the stepped septum polarizer in a square waveguide will propagate through the square-to-circular waveguide transformer into the conical horn and radiate into the free space.

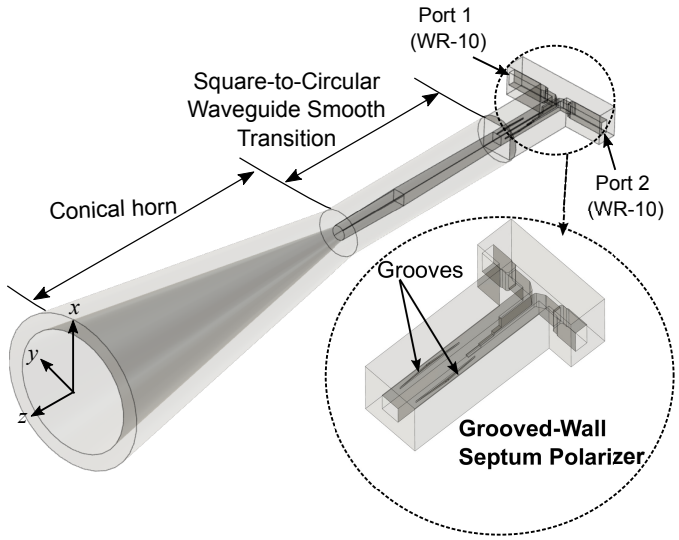

Figure 4.1: Structure of the complete dual-CP antenna.

4.3 Operating Principles of the Grooved-Wall Septum Polarizer

According to section 3.2, with well-optimized dimensions of the stepped septum, the same amplitude and a phase difference of ±90° between the TE_{10} mode and TE_{01} mode can be achieved hence a CP wave in the square waveguide after the septum section. Apart from obtaining approximately equal amplitudes and orthogonal phase between the TE_{10} and TE_{01} mode, i.e. low axial ratio (AR) for the CP propagating in the square waveguide, the septum dimensions should also be optimized to achieve an acceptable reflection coefficient, and particularly a high isolation between the two input rectangular ports

which is critical to some applications such as wireless communication and radar. Since the septum polarizer plays a critical role in our dual-CP antenna design, it is desirable to achieve high electromagnetic (EM) performance over a wide bandwidth. However, it is very challenging to achieve high isolation and low axial ratio over a wide bandwidth at the same time since there is a trade-off between them by only using the stepped septum. An equilateral triangular common port waveguide is introduced to replace the square waveguide in [8] in order to reach a relative bandwidth (BW) of 37.8% covering the W-band, but the isolation is only more than 17 dB within the bandwidth. A thin dielectric slab is inserted in the square waveguide following the septum in [9] to achieve good phase orthogonality, which leads to 26 dB isolation over 20% bandwidth around 2.9 GHz. Nevertheless, this method is not suitable for mmWave applications considering the fabrication complexity and insertion loss introduced by the dielectric slab in the high frequency. An increase in the number of steps may introduce extra degrees of freedom, but it will also increase the difficulty in fabrication as the dimensions of the square waveguide is too small in the mmWave band. According to the review on all reported dual-CP antennas based on the septum polarizer in Section 2.2.4, it can be found that using at least 4 steps is essential to achieve bandwidth larger than 10% with acceptable EM performance. The step number of reported septum polarizers both in the microwave bands and the mmWave bands are also summarized in Table 4-C.

In order to achieve high isolation better than 30 dB over a wide bandwidth of 20% from 90 GHz to 110 GHz with low AR, we propose a grooved-wall septum polarizer and a 2-step design method described as follows.

1. We firstly optimize the dimensions of the stepped septum polarizer only to achieve goals of impedance performance, i.e. reflection coefficient and isolation, thereby avoiding the trade-off between impedance performance and AR performance during optimization. It is also proved that the number of steps of the septum can be reduced, which will be beneficial to the fabrication in mmWave band.

2. After a wideband septum polarizer with a high isolation is obtained, a pair of

grooves is introduced on the walls of the square waveguide section to tune the phase difference between TE_{10} and TE_{01} modes without degrading the impedance performance too much thus improving the phase orthogonality.

In the rest of this section (Section 4.3), the operating principle of the grooved-wall square waveguide will be investigated in the first place to prove the feasibility that it can be used to adjust the phase difference between TE_{10} and TE_{01} modes in the square waveguide.

4.3.1 Mode Analysis of the Grooved-Wall Square Waveguide

Firstly, mode analysis for the cross-section of the grooved-wall square waveguide is carried out using CST Microwave Studio. The cross-section geometry of grooved-wall square waveguide is shown in the inset of Figure 4.2, where the width of the square waveguide (a) is 1.887 mm, depth (dw) and height (h) of the grooves are 0.2 mm and 0.4 mm respectively. The result shows that two orthogonal modes can propagate in the grooved-wall square waveguide. Figure 4.2 depicts the propagation constants and E-field profiles of these two modes. It can be found that the propagation constants of these two orthogonal modes are different, which means an extra phase difference between them can be introduced after propagating over a certain distance in the grooved-wall square waveguide.

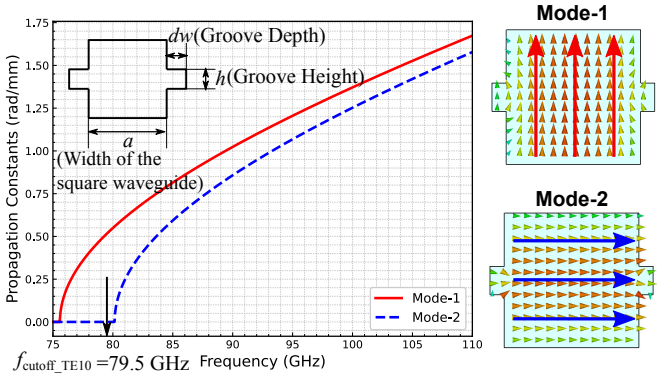

Figure 4.2: Mode analysis for the grooved-wall square waveguide.

Given the initial phases of the vertical and horizontal polarization components are

φ_y^0 and φ_x^0 respectively, their phases after they propagate through a grooved-wall square waveguide with a length of l will be

$$\varphi_y = \varphi_y^0 - \beta_y l \tag{4.1a}$$

$$\varphi_x = \varphi_x^0 - \beta_x l \tag{4.1b}$$

where β_y and β_x are the propagation constants of the vertical and horizontal polarization components respectively, which are different in the grooved-wall square waveguide owing to the existence of the grooves as shown in Figure 4.2. The phase difference of the two orthogonal polarization components at the output of the grooved-wall square waveguide can be calculated as

$$\begin{aligned} \Delta\varphi = \varphi_y - \varphi_x &= \varphi_y^0 - \varphi_x^0 - (\beta_y - \beta_x)l \\ &= \Delta\varphi_0 - (\beta_y - \beta_x)l \end{aligned} \tag{4.2}$$

where $\Delta\varphi_0$ is the initial phase difference. If the propagation constant difference between the vertical and horizontal polarization components is defined as

$$\Delta\beta = \beta_{m1} - \beta_{m2} > 0 \tag{4.3}$$

where β_{m1} and β_{m2} are the propagation constants of mode-1 and mode-2 shown in Figure 4.2 respectively, $\Delta\varphi$ can be written as

$$\Delta\varphi = \Delta\varphi_0 \pm \Delta\beta l \tag{4.4}$$

where the sign before $\Delta\beta$ depends on which pair of walls the grooves exist. It can be seen from the analysis that the phase orthogonality of the CP wave generated in the septum section of the septum polarizer can be improved by applying this grooved-wall square waveguide following the septum section.

It can also be observed that the grooves lower the cutoff frequency of TE_{10} mode

in the square waveguide (mode-1 in the grooved-wall square waveguide), while the cut-off frequency of the horizontal mode (mode-2) in the grooved-wall square waveguide is slightly higher than that of the TE_{01} mode in the square waveguide.

Based on the mode analysis, a 6-mm grooved-wall square waveguide with the same cross-section dimensions in Figure 4.2 is used to demonstrate the phase difference tuning effect at 100 GHz. The grooved-wall square waveguide is connected to two square waveguides acting as input and output waveguide, respectively, as shown in the upper part of Figure 4.3. E-fields along the centre axis through the whole waveguide (see the upper part of Figure 4.3) are monitored in the full-wave simulation. The maginitude ratio and phase difference between y and x components of E-fields along the centre axis of the waveguide is shown in Figure 4.3. It can be observed that the phase difference between y and x components of the E-fields is changing within the grooved-wall square waveguide section. The phase difference gradually changes from 180° at the beginning of the grooved-wall section to 140° at the end of the grooved-wall section. The result demonstrates that phase difference of around 40° has been introduced by the end of the 6-mm grooved-wall square waveguide section while their magnitudes almost keep the same.

4.3.2 Parametric Study And Analysis

In this section, a parametric analysis is carried out to find out the impact of groove height and depth (see Figure 4.2) on the phase difference tuning effect.

The impact of the groove height (h) and depth (dw) on the propagation constant difference ($\Delta\beta$) between the two orthogonal modes are shown in Figure 4.4(a) and Figure 4.4(b), respectively. It can be found that larger h or dw leads to larger $\Delta\beta$, which means the same phase difference shift can be achieved with shorter waveguide using larger groove dimensions. However, the result also shows $\Delta\beta$ increases as frequency goes down given the same groove dimensions, and the larger the groove dimensions are, the more significant variation of $\Delta\beta$ with respect to the frequency will be. It means the

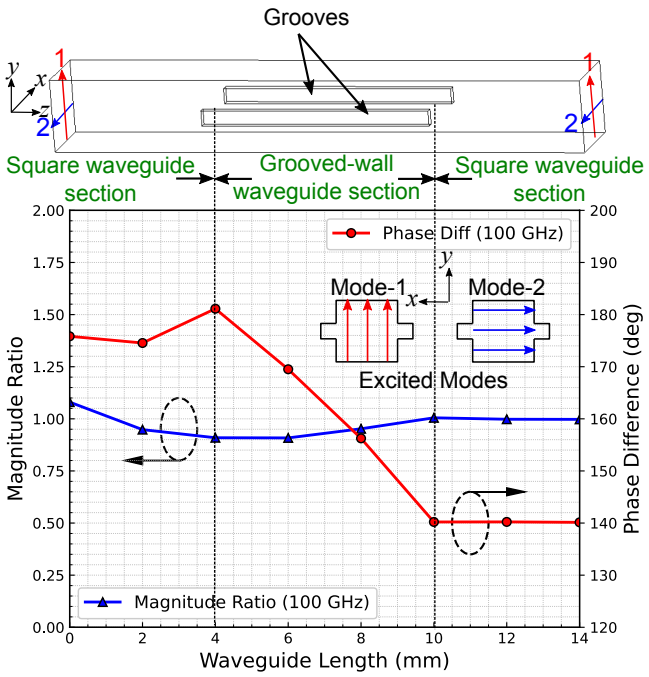

Figure 4.3: Magnitude ratio and phase difference between y and x components of the E-fields along the centre axis of the waveguide. The magnitude ratio is $|E_y|/|E_x|$.

phase difference over a wide bandwidth will be tuned unequally, which should be taken into account when design. It should also be noted that the increment of $\Delta\beta$ is becoming smaller as h or dw increases, which indicates the effect of increasing $\Delta\beta$ by increasing h or dw is limited when h or dw becomes large.

4.3.3 Grooved-Wall Square Waveguide with Gradient Depth

Since the grooved-wall square waveguide section after the septum section can be regarded as a load to a septum polarizer, it is desirable to achieve a low reflection coefficient when designing the grooved-wall square waveguide with high isolation. In order to achieve a lower reflection coefficient, grooved-wall square waveguide with gradient depth is proposed, as shown in the inset of Figure 4.5(a). The depth of the groove increases linearly from 0 to dw, after keeping this depth for a length of l_0, it decreases from dw to 0. The height of the groove keeps h over the total length of l_1.

A grooved-wall square waveguide with the same dw, h and total length ($l_1 = 6\ mm$)

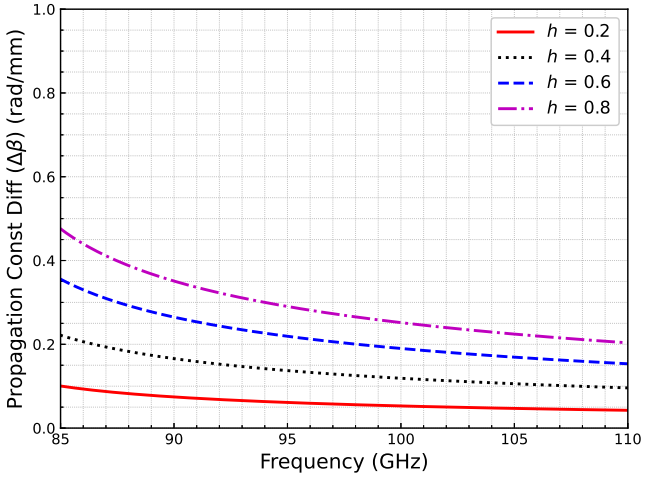

(a)

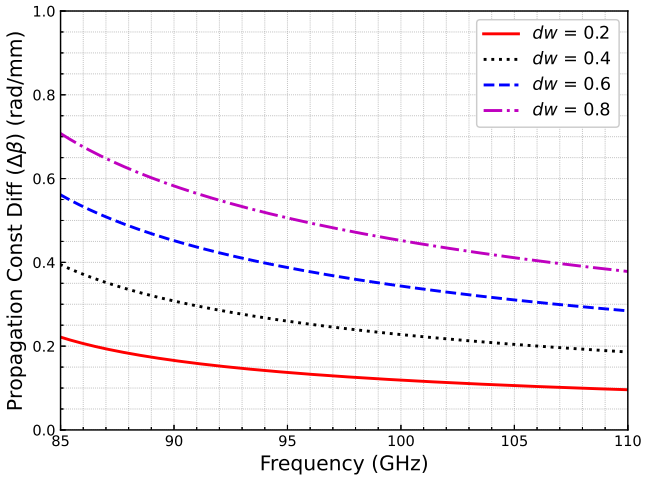

(b)

Figure 4.4: Effect of (a) groove height (h) and (b) groove depth (dw) on the propagation constant difference ($\Delta\beta$) between the two orthogonal TE modes.

as the dimensions in Figure 4.3 but with a gradient depth is used to investigate the reflection improvement. The reflection coefficients for TE_{10} (mode-1) or TE_{01} (mode-2) are shown in Figure 4.5(a) and Figure 4.5(b) respectively. The results show that the grooved-wall waveguide with gradient depth has better reflection coefficients than that without gradient depth over the operating bandwidth. It can also be found that, given fixed groove depth (dw) and groove length (l_1), longer slope section (i.e., shorter l_0) will lead to better reflection coefficient. On the other hand, because $\Delta\beta$ will be smaller when

grooves has smaller dw (Figure 4.4(b)), the longer slope section will lead to a smaller phase difference shift ($\Delta\varphi - \Delta\varphi_0$) given a fixed total groove length (l_1), as illustrated in Figure 4.6. In other words, a longer waveguide is required to achieve the same phase difference shift given a fixed dw if grooves with gradient depth is used.

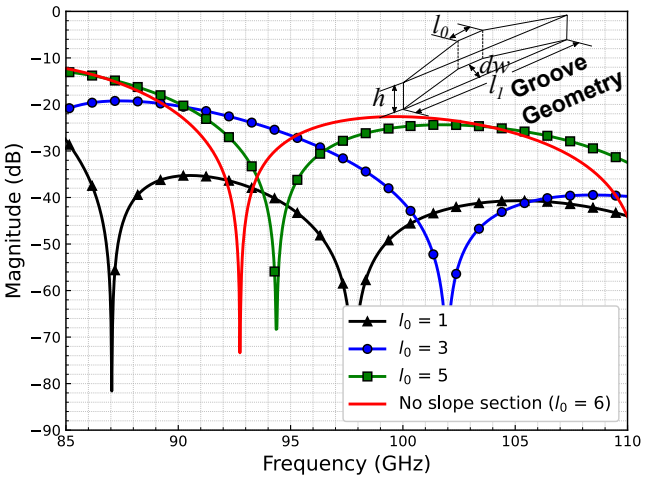

(a)

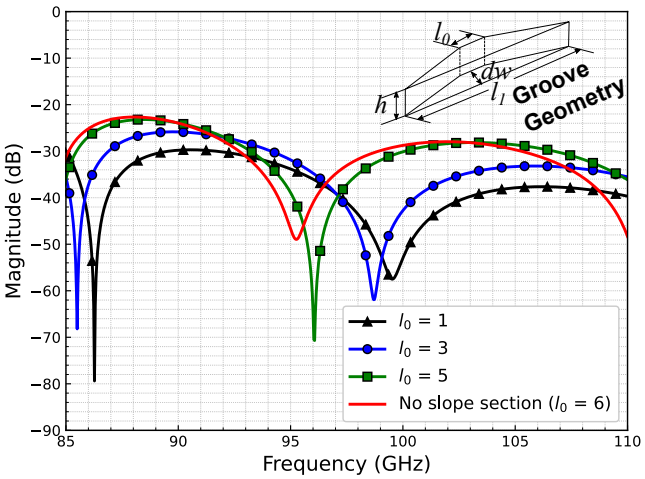

(b)

Figure 4.5: Reflection Coefficient for (a) TE_{10} mode and (b) TE_{01} mode.

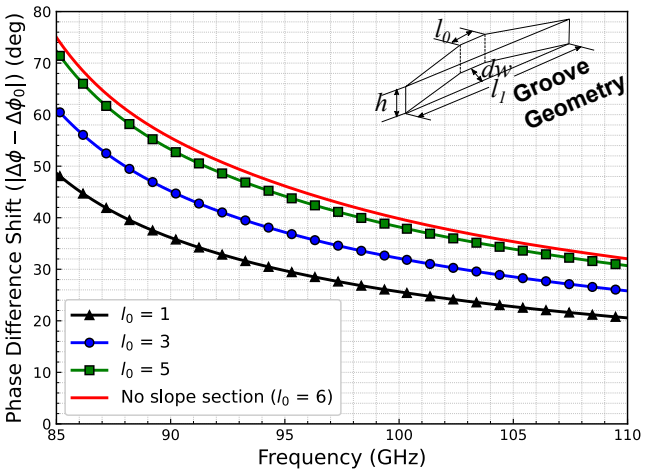

Figure 4.6: Effect of the length of the gradient section on phase difference shift.

4.4 Dual-CP Antenna Design

4.4.1 Grooved-Wall Septum Polarizer Design

The geometrical parameters of the septum polarizer under optimization are illustrated in Figure 4.7. The dimension of the square waveguide is optimized within the range that

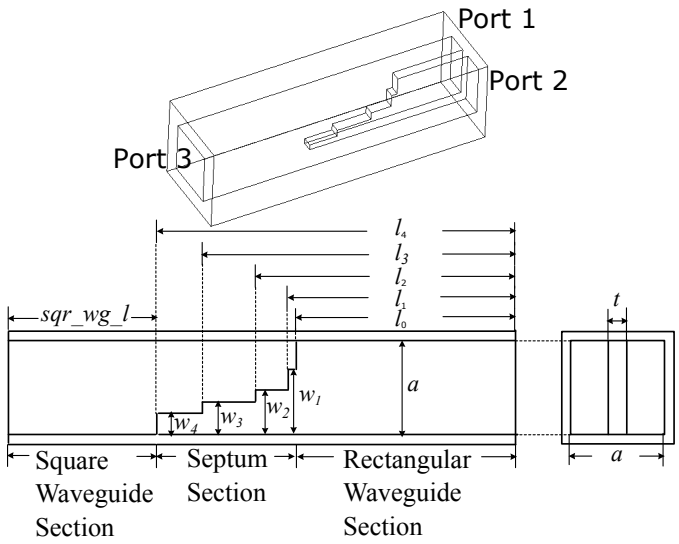

Figure 4.7: Geometrical parameters of the septum polarizer.

allows only TE_{10} and TE_{01} mode to propagate through it within the operating bandwidth from 90 GHz to 110 GHz, which means the cutoff frequencies of the dominant modes

(TE_{10} and TE_{10}) should be lower than 90 GHz while the first higher-order modes (TE_{11} and TM_{11}) should be larger than 110 GHz. Since the cutoff frequency of the square waveguide is given by

$$\begin{aligned} f_{c_{mn}} &= \frac{c}{2\pi}\sqrt{\left(\frac{m\pi}{a}\right)^2 + \left(\frac{n\pi}{a}\right)^2} \\ &= \frac{c}{2a}\sqrt{m^2+n^2} \end{aligned} \tag{4.5}$$

the cutoff frequencies of the dominant modes and the first higher-order modes should satisfy

$$f_{c_{TE_{10}}} = f_{c_{TE_{01}}} = \frac{c}{2a} < 90\ GHz \tag{4.6a}$$

$$f_{c_{TM_{11}}} = f_{c_{TE_{11}}} = \sqrt{2}\frac{c}{2a} > 110\ GHz \tag{4.6b}$$

Thus we have

$$1.667\ mm < a < 1.928\ mm \tag{4.7}$$

Then the step widths and lengths of the septum can be set taking this constraint into account. The minimal thickness of the septum is set to be 0.3 mm for the consideration of fabrication. It should be pointed out that although a conventional 4-step septum is used as the initial configuration for optimization, as shown in Figure 4.7, the number of steps could be equal or less than 4 during optimization, e.g. when $w_n = w_{n-1}$ or $l_n = l_{n-1}$. Finally, because the stepped septum may excite higher-order modes inside the waveguide, which may affect the overall performance, including the reflection and isolation as well as the radiation patterns [7], it is desirable to suppress the higher-order modes. Since the dimensions of the square waveguide are designed to only allow TE_{10} and TE_{01} mode to propagate as described above, the higher-order modes are all evanescent modes. For this reason, the easiest and most common approach in waveguide design to suppress the higher-order modes is to increase the length of the waveguide to let them attenuated to a certain level according to their attenuation constants. The attenuation constants (α) of the first higher-order modes in the square waveguide of the septum polarizer, which

are TE_{11} and TM_{11} modes in our case, is given by

$$\begin{aligned} \alpha_{TE11} = \alpha_{TM11} = \alpha[Np/m] &= \sqrt{k_c^2 - k^2} \\ &= \sqrt{2\left(\frac{\pi}{a}\right)^2 - \left(\frac{2\pi f}{c}\right)^2} \end{aligned} \tag{4.8}$$

where k_c and k are the cutoff wavenumber and wavenumber at the frequency of f. In our design, the length of the square waveguide section (including the waveguide transition) following the septum section is designed to give at least 40 dB attenuation for the first higher-order modes, which can be calculated as

$$l_{ext} = \frac{40}{(20/ln(10))\alpha} \tag{4.9}$$

The geometry of the septum polarizer is optimized using a Matlab implementation of Covariance Matrix Adaptation Evolution Strategy (CMA-ES) algorithm [10] which is introduced in Chapter 2 with a Matlab program developed to launch and control CST Microwave Studio full-wave simulations [11]. Each set of geometrical parameters generated by CMA-ES will be used to update the model in CST Microwave Studio, and the reflection coefficient and isolation will be evaluated by the full-wave simulation. A cost function[1] described below will then be calculated, and CMA-ES will be used to minimize the value of the cost function to find the optimal design after a sufficient number of iterations.

Since we aim to achieve high impedance performance over a wide bandwidth at this step, a cost function is defined only including reflection coefficient and isolation. The cost function at a frequency sample f_n is written as

$$F = \sum_{n=1}^{N} [w_R R(f_n) + w_I I(f_n)] \tag{4.10}$$

[1]In optimization, a cost function is used to evaluate how close the results being optimized are to the desired results. The optimization algorithm attempts to minimize the value of the cost function during the optimization.

where N is the number of frequency samples within the frequency range from 90 GHz to 110 GHz in the simulation. w_R and w_I are the weighting factors. $R(f_n)$ and $I(f_n)$ are objective functions for reflection coefficient and isolation, respectively, which are defined as follows.

$$R(f_n) = max(r(f_n) - r_{target},\ 0) \tag{4.11a}$$

$$I(f_n) = max(i(f_i) - i_{target},\ 0) \tag{4.11b}$$

where $r(f_n)$ is the simulated reflection coefficient at frequency f_n, $i(f_n)$ is the simulated isolation at frequency f_n. r_{target} and i_{target} are the target reflection coefficient and isolation in dB, which are set to -25 dB and -40 dB, respectively. $w_R = 1$ and $w_I = 2$ are applied in the optimization because a high isolation is more desirable in our design, and $N = 626$ is used in the simulation. Interestingly, isolation larger than 30dB over the expected operating bandwidth is found using CMA-ES with only 3 steps, where $w_4 = w_3$, although we started the optimization with 4 steps. The optimized dimensions of septum polarizer are listed in Table 4-A.

Table 4-A: Optimized dimensions of the grooved-wall septum polarizer.

Parameters	l_0	l_1	l_2	l_3	w_1	w_2	w_3
Values (mm)	2.71	3.532	4.988	6.415	0.682	0.296	0.1
Parameters	a	t	sqr_wg_l				
Values (mm)	1.887	0.3	8.65				

After a septum polarizer with expected impedance performance is obtained, a pair of WR-10 waveguide transformers with E-plane bends is optimized and added to port 1 and 2 to form a complete septum polarizer. Then a pair of grooves is introduced on the walls of its square waveguide section. The dimensions of the grooves can be initially calculated based on the simulated phase difference between vertical and horizontal E-field components of the CP wave at port 3 of the optimized septum polarizer, and the analysis in Section 4.3.1. Then the dimensions of the grooves are optimized to improve AR of the septum polarizer without affecting the impedance performance too much. The

optimized structure of the grooved-wall septum polarizer is shown in Figure 4.8. The optimized dimensions of the grooves are listed in Table 4-B.

Table 4-B: Optimized dimensions of the grooves.

Parameters	dw	h	l_0	l_1
Values (mm)	0.2	0.2	0.25	6.65

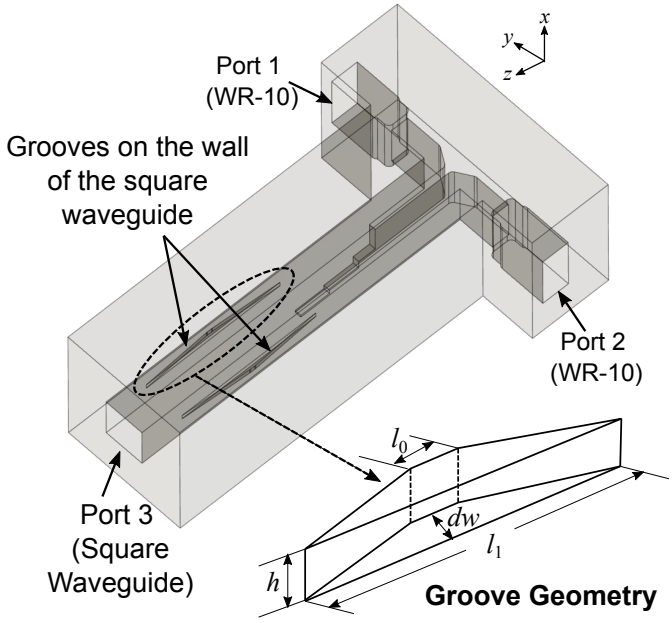

Figure 4.8: Structure of the grooved-wall septum polarizer.

The simulated $|S_{11}|$ and $|S_{21}|$ of the complete septum polarizers with and without grooves are shown in Figure 4.9. The reflection coefficient of the grooved-wall septum polarizer is lower than -20 dB, and the isolation is better than 30 dB from 89.1 GHz to 109.5 GHz. It can also be observed that the grooves introduced have no noticeable impact on the reflection coefficient, and only degrade the isolation a little at the lower end of the expected operating bandwidth. The simulated results when port 2 is excited are not shown here because, due to the symmetry of the polarizer structure, they are identical to those when port 1 is excited.

Figure 4.10 depicts the phase difference ($\Delta\varphi$) and magnitude ratio ($|E_y|/|E_x|$) between the vertical (y-axis) and horizontal components (x-axis) of the E-field at the centre of port 3. The results show that the magnitude ratio stays very close to 1 after adding

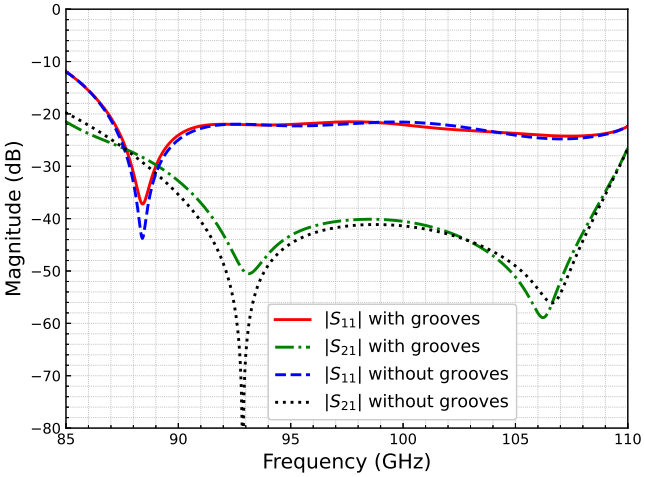

Figure 4.9: Simulated reflection coefficient and isolation of the septum polarizer with and without grooves.

the grooves while the phase difference ($\Delta\varphi$) is shifted to around 90°. It is worth noting that, for the septum polarizer without grooves, its phase difference (shown as the dashed blue line) at the higher end of the band is closer to 90° than that at the lower end of the band. By contrast, for the septum polarizer with grooves, its phase difference (shown as the solid red line) is more balanced around 90° over the entire band, which introduces further improvement for the phase orthogonality and AR. This improvement is attributed to the unequal frequency response of $\Delta\beta$ as illustrated in Section 4.3.2. To demonstrate this conclusion, the normalized distribution of phase difference values at all frequency samples between 90 GHz and 110 GHz for the septum polarizers with and without grooves is presented in the inset of Figure 4.10. It can be found that the grooves introduced not only shift $\Delta\varphi$ to 90°, but also allow $\Delta\varphi$ at more frequencies close to 90°, thereby improving the phase orthogonality significantly.

The axial ratio of CP wave generated by the septum polarizer with and without the grooves are shown in Figure 4.11. It can be seen that AR is lower than 2.5 dB from 90 GHz to 110 GHz and the CP purity of the grooved-wall septum polarizer is higher than that of the septum polarizer without grooves since 80% of the AR from 90 GHz to 110 GHz is lower than 0.8 dB for the grooved-wall septum polarizer. In contrast, the same

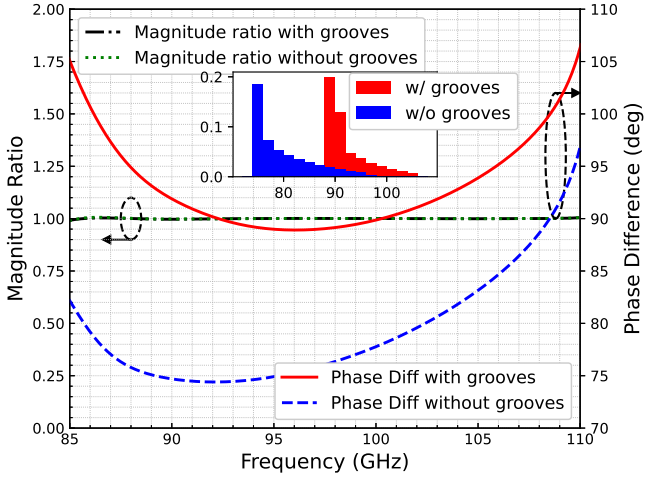

Figure 4.10: Simulated phase difference ($\Delta\varphi$) and magnitude difference ($|E_y|/|E_x|$) between the vertical (y-axis) and horizontal components (x-axis) of the E-field at the centre of port 3.

portion of AR is larger than 0.8 dB for the septum polarizer without grooves.

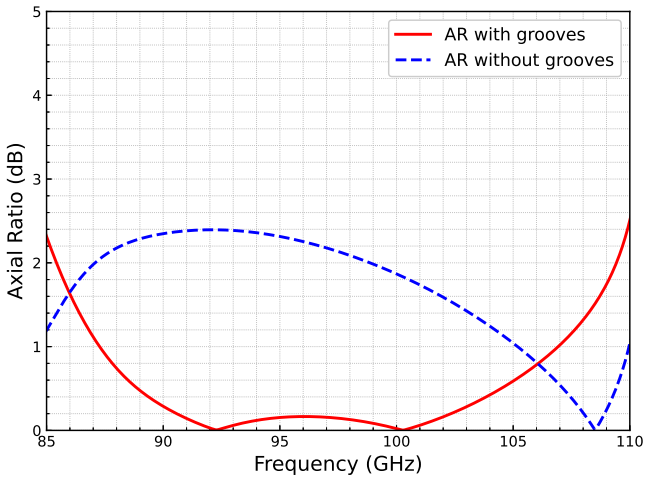

Figure 4.11: Simulated axial ratio of the septum polarizers with and without grooves.

Figure 4.12 shows the transmission coefficients of the optimized grooved-wall septum polarizer. It can be seen that transmission coefficients for both TE_{10} and TE_{01} modes are very close to -3 dB. The result also shows that the higher-order modes (TM_{11} and TE_{11}) are well suppressed under -40 dB in the operating bandwidth.

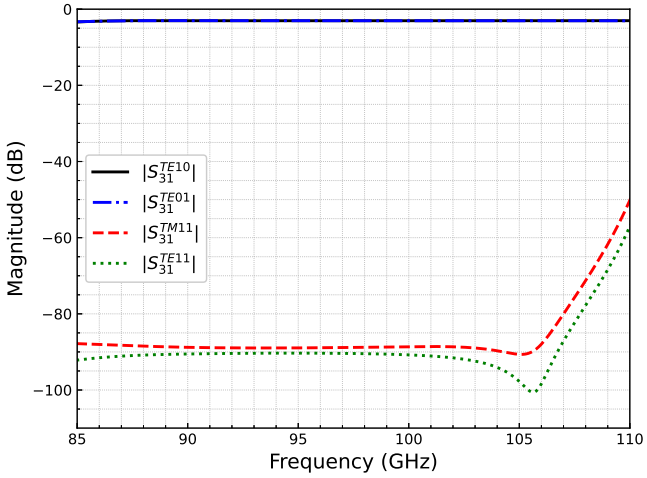

Figure 4.12: Simulated transmission coefficient of the septum polarizer with and without grooves.

4.4.2 Horn Design

A horn is used to radiate the CP wave generated in the grooved-wall septum polarizer. However, when the CP wave generated by the septum polarizer arrives at the input port of the horn, part of the energy will be reflected. Since the reflection of the CP wave will be in an opposite sense of rotation, it will be guided to the other port of the septum polarizer rather than the excited port, which leads to increased $|S_{21}|/|S_{12}|$ (degraded isolation). For this reason, the reflection coefficient of the horn will affect the isolation of the entire dual-CP antenna significantly. Thus it is highly desirable to design a horn with a low reflection coefficient. In order to achieve an isolation better than 30 dB for the entire dual-CP antenna, it is anticipated to keep the reflection coefficient of the horn below -35 dB. Besides a low reflection coefficient, we aim to achieve rotationally symmetric and stable radiation patterns over the entire operating bandwidth from 90 GHz to 110 GHz with a directivity higher than 25 dBi.

A simple conical horn antenna with only one flare section is selected for the ease of fabrication in the mmWave band. The geometry of the horn is shown in the inset of Figure 4.13, where $r_i = 1.364$ mm and $r_o = 11.567$ mm are the radii of the input and output aperture, $l_{horn} = 66.396$ mm is the length of the flare section. The conical horn is

connected to a smooth square-to-circular waveguide transformer which is used to convert the TE_{10}/TE_{01} mode in the square waveguide into TE_{11} mode in the circular waveguide as shown in Figure 4.1. The cross-section of this waveguide transformer smoothly changes from a circular with a radius of 1.364 mm to a square with a width of 1.887 mm, in order to match the dimension of the common port of the septum polarizer listed in Table 4-A. The smooth waveguide transition is chosen instead of the stepped waveguide transition because it can achieve a low reflection over a wider bandwidth at the expense of longer length [12].

It can be seen in Figure 4.13 that the optimized conical horn can achieve a reflection coefficient lower than -40 dB from 90 GHz to 110 GHz in simulation, while a reflection coefficient of -35 dB is achieved after the smooth square-to-circular waveguide transformer is added.

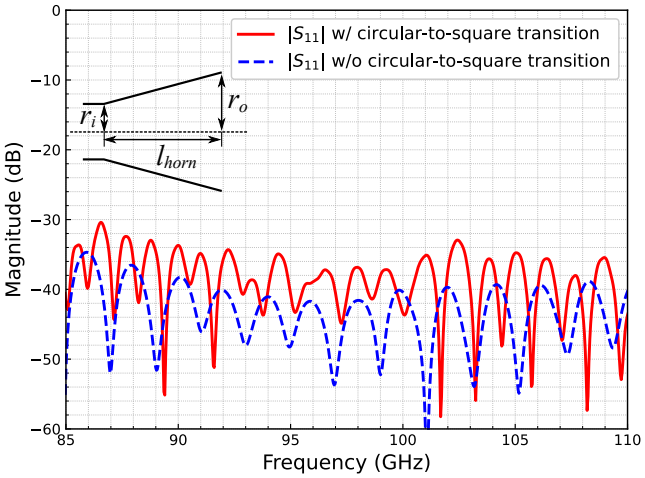

Figure 4.13: Simulated reflection coefficient of the horn with and without square-to-circular waveguide transformer.

The simulated radiation patterns at 90/100/110 GHz are presented in Figure 4.14, which correspond to linear polarizations, as only one of the TE_{11} modes is excited during the optimization of the horn. The results obtained when the horn is excited by the other orthogonal TE_{11} will be the same owing to the symmetry of revolution of the horn. It can be observed that radiation patterns are rotationally symmetric within -12 dB taper

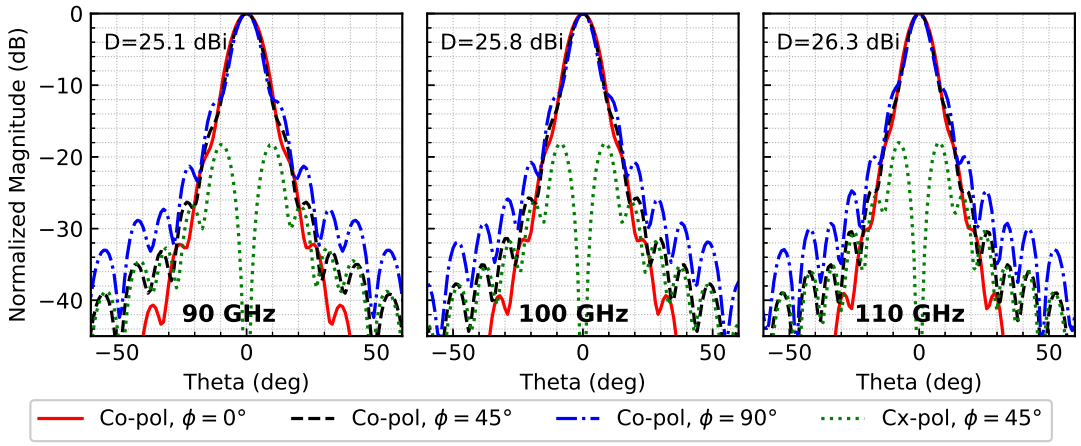

Figure 4.14: Simulated normalized radiation patterns of the designed horn for linear polarization at 90/100/110 GHz.

angle with directivity of 25.7 ± 0.6 dBi. The -12 dB taper angles are only $9.15 \pm 0.45°$, which shows the stability of the radiation patterns over the entire operating bandwidth.

4.4.3 Fabrication of the Prototype

The grooved-wall stepped septum polarizer is split into two blocks to allow endmill machining of the septum and the grooves. It is worth noting that the septum polarizer should be split along the top of the square waveguide to avoid degradation of AR as discussed in [7, 13] and Chapter 3. The fabrication tolerance of the endmill machining we used for this septum polarizer is about 5 μm. Furthermore, the horn and the square-to-circular waveguide transformer should be fabricated as one piece rather than two splitting blocks, because the misalignment of two splitting blocks during the assembling will affect the AR significantly as discussed in [14]. The horn with the square-to-circular waveguide transformer is then assembled with the grooved-wall stepped septum polarizer via flanges, as shown in Figure 4.15. Figure 4.16 shows a photograph of the prototype. Both the grooved-wall stepped septum polarizer and the horn are fabricated from brass and electroplated with gold.

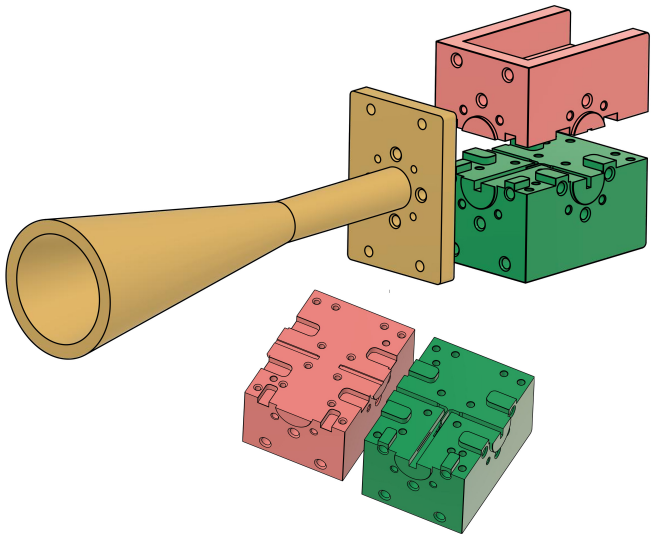

Figure 4.15: Mechanical design and assembly of the dual-CP antenna.

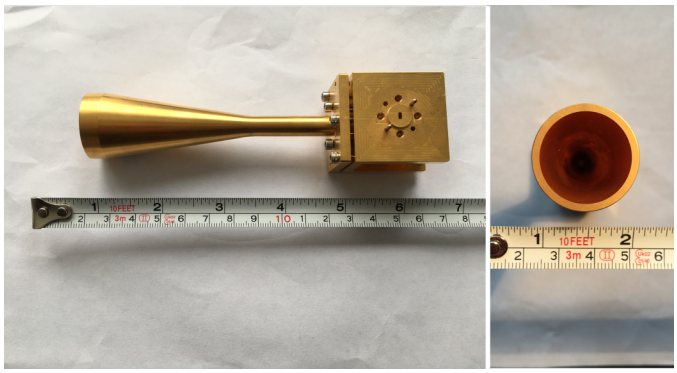

Figure 4.16: Photograph of the fabricated dual-CP antenna.

4.5 Measurement Results and Discussion

4.5.1 Simulation and Measurement Results

Full-wave simulation of the complete dual-CP antenna shown in Figure 4.1 is carried out using CST Microwave Studio, and the prototype working in the W-band shown in Figure 4.16 is also measured.

The scattering parameters of the proposed dual-CP antenna are measured using a Keysight PNA-X network analyzer with two OML WR-10 extension heads. The simulated and measured reflection coefficient and port isolation are shown in Figure 4.17. The reflection coefficient and isolation of port 2 is the same as those of port 1 because the

structure is symmetric for port 1 and 2 in the simulation. For this reason, only simulated $|S_{11}|$ and $|S_{21}|$ are shown for the clarity of the figure. The simulation predicts a reflection coefficient lower than -20 dB and an isolation higher than 30 dB over the expected operating bandwidth from 90 - 110 GHz. It can been seen that measured $|S_{11}|$ and $|S_{22}|$ are lower than -17 dB and is close to the simulated reflection coefficient. The measured $|S_{21}|$ and $|S_{12}|$ deteriorate at the two ends of the expected operating bandwidth, so the frequency range within which the isolation $>$ 30 dB is from 93 -109 GHz, which means 30 dB port isolation is achieved over a relative bandwidth of 15.8%. It can also be observed that measured $|S_{21}|$ overlaps with $|S_{12}|$, which implies that a good symmetry of stepped septum and the square waveguide section is achieved during the fabrication of the septum polarizer. The deterioration of reflection coefficient and isolation observed in measured results is probably resulted from the flange misalignment between the horn and the septum polarizer and the dimension error introduced in the fabrication.

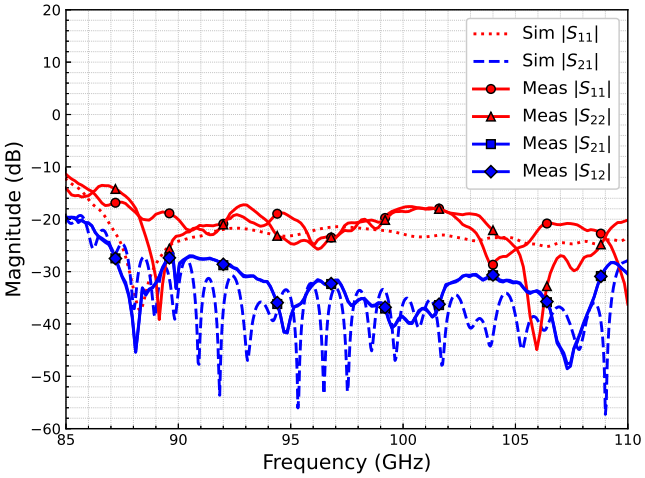

Figure 4.17: Simulated and measured scattering parameters of the proposed dual-CP antenna.

The radiation characteristics are measured in a mmWave compact antenna test range (CATR) in the Antenna Lab at Queen Mary University of London. The photograph of the CATR measurement setup is shown in Figure 4.18. The measurement follows the CP measurement method described in Section 2.4. In this measurement, the rotation angle of the reference antenna is set from 0° to 150° with a step of 30° to measure each

polarization component at these angles, which is proved to be sufficient to find the major and minor axes of the polarization ellipse of our antenna.

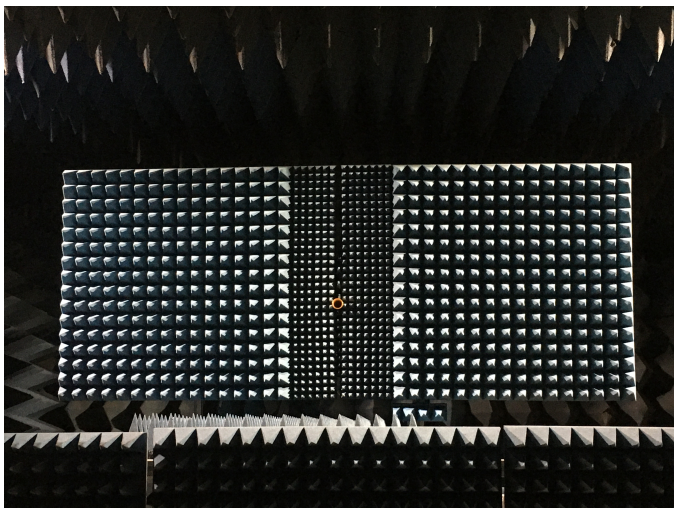

Figure 4.18: Photograph of the CATR measurement setup.

Figure 4.19 depicts the measured and simulated AR over the frequency range from 90 GHz to 110 GHz. It can be observed that the measured AR is close to the simulated AR above 105 GHz, but worse than the simulated ones at the rest of the frequencies. This degradation might be attributed to the dimension discrepancy of the fabricated stepped septum polarizer. Since the symmetry of the square waveguide section of the septum polarizer is derived from the measured results in Figure 4.17, the discrepancy between the AR of LHCP (port 1) and RHCP (port 2) is probably because of the flange misalignment between the horn and the septum polarizer, as they were fabricated by two manufacturers with different fabrication tolerances. Despite the discrepancies, the measured AR of both LHCP and RHCP can be kept below 3 dB from 90 GHz to 109 GHz, which means a 3-dB AR bandwidth of 19% is realized. Thus the overall operating bandwidth with port isolation $>$ 30 dB is 15.8% (93 - 109 GHz), which is limited by the impedance bandwidth.

The normalized measured polarization patterns [15] of the proposed dual-CP antenna at several frequencies across the frequency range from 90 GHz to 110 GHz are illustrated in Figure 4.20 which are used to calculate the AR shown in Figure 4.19 and reveals the CP

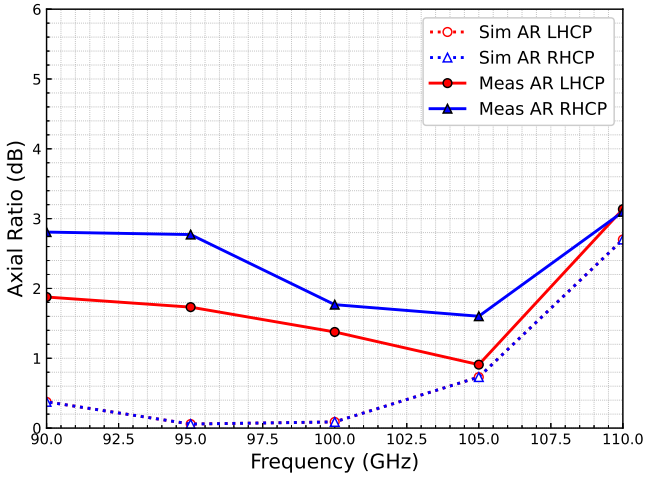

Figure 4.19: Measured and simulated AR of the proposed dual-CP antenna.

characteristics of the proposed dual-CP antenna. The results show that the polarization patterns at the middle frequencies are closer to circles than those at the edge frequencies, which is consistent with the measured AR result. It can also be observed that the major axes of the polarization ellipses deviate from $x-$ and $y-$axis (0° and 90°), which means more accurate ARs are obtained by using this measuring approach than the approach in which only 0° and 90° polarization components are measured.

The normalized simulated and measured radiation patterns of both LHCP and RHCP in $yz-$ and $xz-$plane (see Figure 4.1) at 90 GHz, 100 GHz and 110 GHz are presented in Figure 4.21 and Figure 4.22. The measured radiation patterns agree well with the simulated ones. It can also be found that a good rotational symmetry is achieved for the main lobes at all frequencies, allowing this dual-CP antenna to be used as a feed to a reflector antenna to achieve high gain.

Figure 4.23(a) and Figure 4.23(b) depict the measured and simulated co-polar gain for LHCP (port 1 excitation) and RHCP (port 2 excitation) at boresight over the frequency range from 90 GHz to 110 GHz, respectively. The maximum SLLs of co-polar radiation patterns are also shown in these figures. The result shows the proposed dual-CP antenna has an LHCP gain from 22.7 dBic to 25.6 dBic, and a RHCP gain from 23.1 dBic to

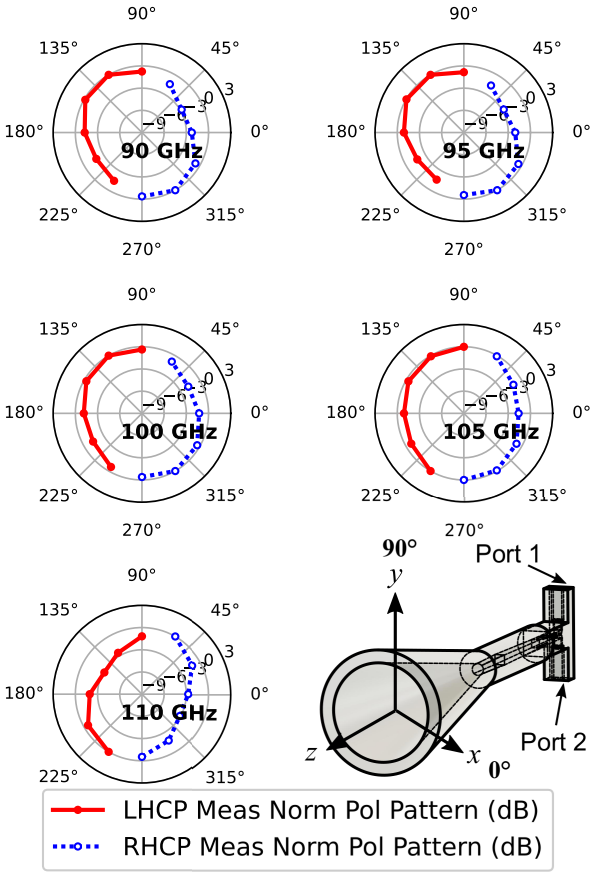

Figure 4.20: Normalized measured polarization patterns of the proposed dual-CP antenna.

25.4 dBic, which agree well with the simulated results. It can also be found that the SLLs of both LHCP and RHCP are all below -21.5 dB, which also agrees with the simulated ones.

4.5.2 Comparison and Discussion

The performance of the reported dual-CP antennas based on the septum polarizer both in microwave and mmWave band are summarized in Table 4-C in comparison with the results of the proposed antenna. The overall bandwidth in Table 4-C describes the overlapped bandwidth for the impedance and AR. It can be seen that our design achieves higher isolation over wider bandwidth with even fewer septum steps. Most septum polarizer designs use 4-step septum to achieve proper performance; a 5-step septum is

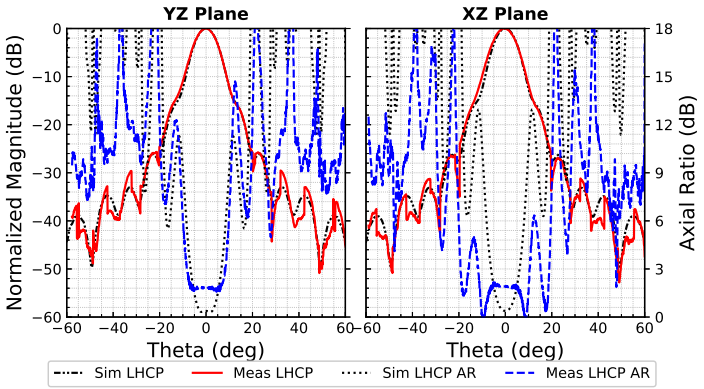

(a)

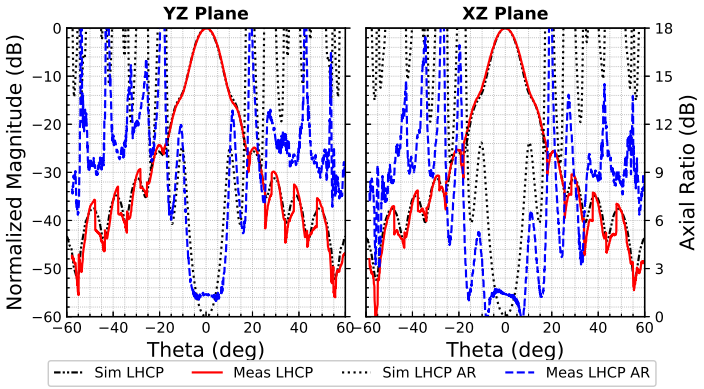

(b)

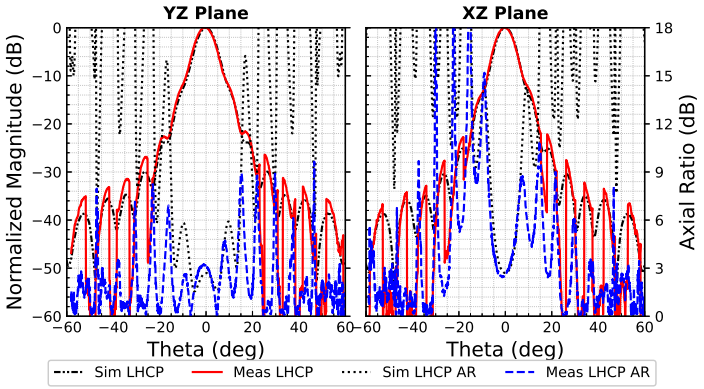

(c)

Figure 4.21: Measured and simulated LHCP (port 1 excited) radiation patterns of the proposed dual-CP antenna at (a) 90 GHz, (b) 100 GHz and (c) 110 GHz.

used to realize isolation $>$ 30 dB over 10% bandwidth in [7]; while in our design the septum only has 3 steps, which eases the most challenging part of the fabrication for

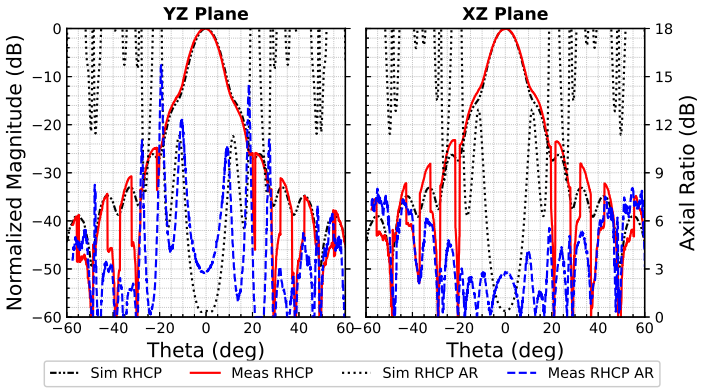

(a)

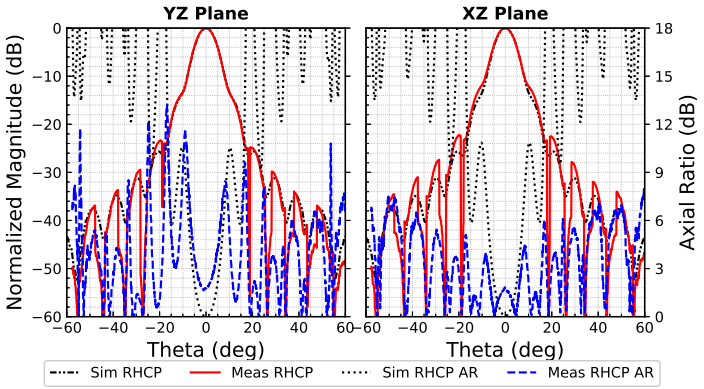

(b)

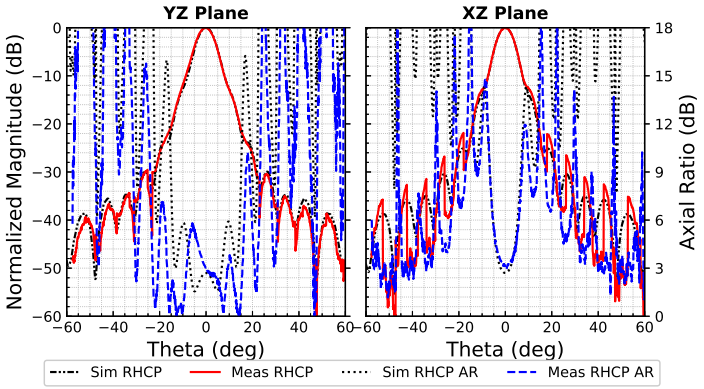

(c)

Figure 4.22: Measured and simulated RHCP (port 2 excited) radiation patterns of the proposed dual-CP antenna at (a) 90 GHz, (b) 100 GHz and (c) 110 GHz.

the septum polarizer at higher frequencies. Furthermore, it also means the proposed grooved-wall septum polarizer with the 2-step design method still has the potential for

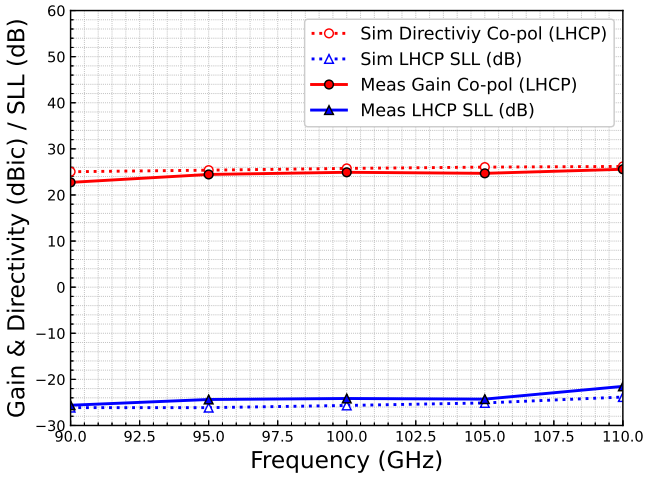

(a)

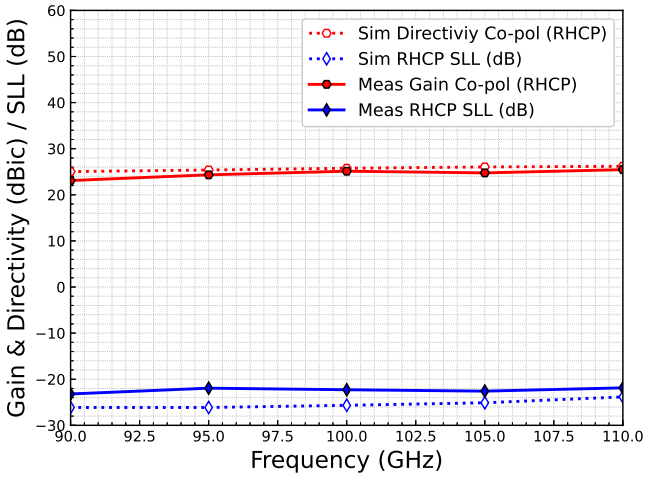

(b)

Figure 4.23: Measured and simulated co-polar gain and maximum SLL of (a) LHCP (port 1 excitation) and (b) RHCP (port 2 excitation).

better performance.

4.6 Summary

In this chapter, a wideband dual-CP antenna based on a grooved-wall septum polarizer is designed, fabricated and verified by experimental measurement. The proposed septum polarizer has a pair of grooves with gradient depth on the walls of the square waveguide section, which is used to improve the phase orthogonality of the CP wave when the design

Table 4-C: Comparison with other dual-CP antennas based on the septum polarizer.

Ref	Frequency (GHz)	Type	Reflection Coefficient (dB)	Isolation (dB)	AR (dB)	Overall Band-width	Max Gain (dBic)	Num of Septum Steps
[3]	1.27 - 1.32	Waveguide septum polarizer + Horn	<-25	>30	<1*	3.9%	-	5
[16]	1.57542	Waveguide septum polarizer + Horn	<-29.3	>23	<0.023	1.0%	16.2	2
[17]	8 - 8.5	Waveguide septum polarizer array	<-15	>20	<0.7	13.0%	8	4
[4]	28.5 - 31.2	Waveguide septum polarizer + Horn	<-25	>27	<0.7	9.0%	-	4
[18]	27.6 - 32.4	Waveguide array + Septum polarizer	<-10	>13	<3	16.0%	32.8	4
[7]	213 - 237	Waveguide septum polarizer + Horn	<-21	>30	<1.5	10.0%	22**	5
This work	93 - 109	Waveguide septum polarizer + Horn	<-17	>30	<3	15.8%	25.6	3

* Simulated results of the linearly-polarized horn.

and optimization of the septum structure focus only on achieving high isolation over a wide bandwidth. The operating principle of the grooved-wall septum polarizer is also illustrated. With a proposed 2-step design method, we aim to push further the limits of the dual-CP antenna based on the stepped septum polarizer to realize a dual-CP antenna with wider operating bandwidth and higher port isolation. A prototype of the proposed dual-CP antenna is fabricated and measured, and the experimental results show that 15.8% bandwidth ranging from 93 to 109 GHz is achieved with reflection coefficient $<$ -17 dB and port isolation $>$ 30 dB as well as AR $<$ 3 dB for both LHCP and RHCP. A high gain within the range of 22.7 - 25.6 dBic is realized for both LHCP and RHCP over the entire operating bandwidth with the SLL lower than -21.5 dB. Rotationally symmetric radiation patterns are also observed. Compared with other dual-CP antennas, the proposed antenna has higher isolation over a wide bandwidth while the number of steps of the septum has also been reduced for the ease of fabrication in the mmWave band.

References

[1] J. Wu, M. Li, and N. Behdad, "A Wideband, Unidirectional Circularly Polarized Antenna for Full-Duplex Applications," *IEEE Transactions on Antennas and Propagation*, vol. 66, no. 3, pp. 1559–1563, 2018.

[2] H. Nawaz, A. U. Niazi, M. Abdul Basit, and M. Usman, "Single Layer, Differentially Driven, LHCP Antenna With Improved Isolation for Full Duplex Wireless Applications," *IEEE Access*, vol. 7, pp. 169 796–169 806, 2019.

[3] M. J. Franco, "A High-Performance Dual-Mode Feed Horn for Parabolic Reflectors with a Stepped-Septum Polarizer in a Circular Waveguide [Antenna Designer's Notebook]," *IEEE Antennas and Propagation Magazine*, vol. 53, no. 3, pp. 142–146, 2011.

[4] G. Addamo, O. A. Peverini, D. Manfredi, F. Calignano, F. Paonessa, G. Virone, R. Tascone, and G. Dassano, "Additive Manufacturing of Ka-Band Dual-Polarization Waveguide Components," *IEEE Transactions on Microwave Theory and Techniques*, vol. 66, no. 8, pp. 3589–3596, 2018.

[5] Y. Zhao and K. Luk, "Dual Circular-Polarized SIW-Fed High-Gain Scalable Antenna Array for 60 GHz Applications," *IEEE Transactions on Antennas and Propagation*, vol. 66, no. 3, pp. 1288–1298, 2018.

[6] Y. J. Cheng, J. Wang, and X. L. Liu, "94 GHz Substrate Integrated Waveguide Dual-Circular-Polarization Shared-Aperture Parallel-Plate Long-Slot Array Antenna With Low Sidelobe Level," *IEEE Transactions on Antennas and Propagation*, vol. 65, no. 11, pp. 5855–5861, 2017.

[7] C. A. Leal-Sevillano, K. B. Cooper, J. A. Ruiz-Cruz, J. R. Montejo-Garai, and J. M. Rebollar, "A 225 GHz Circular Polarization Waveguide Duplexer Based on a Septum Orthomode Transducer Polarizer," *IEEE Transactions on Terahertz Science and Technology*, vol. 3, no. 5, pp. 574–583, 2013.

[8] B. Deutschmann and A. F. Jacob, "Broadband Septum Polarizer With Triangular Common Port," *IEEE Transactions on Microwave Theory and Techniques*, pp. 1–8, 2019.

[9] M. Chen and G. Tsandoulas, "A wide-band square-waveguide array polarizer," *IEEE Transactions on Antennas and Propagation*, vol. 21, no. 3, pp. 389–391, 1973.

[10] N. Hansen, "CMA-ES Source Code," 2012. [Online]. Available: http://cma.gforge.inria.fr/cmaes_sourcecode_page.html

[11] H. Giddens and C. Shu, "CST_App," 2021. [Online]. Available: https://github.com/chaoshu1201/CST_App

[12] A. D. Olver, P. J. B. Clarricoats, L. Shafai, and A. A. Kishk, *Microwave Horns and Feeds*, ser. IEE electromagnetic waves series, P. J. B. Clarricoats, Ed. London, United Kingdom: IEE, 1994, vol. 39.

[13] A. Dunning, S. Srikanth, and A. R. Kerr, "A simple orthomode transducer for centimeter to submillimeter wavelengths," in *20th International Symposium on Space Terahertz Technology*, Charlottesville, USA, 2009, pp. 191–193.

[14] C. Shu, J. Wang, S. Hu, Y. Yao, J. Yu, Y. Alfadhl, and X. Chen, "A Wideband Dual-Circular-Polarization Horn Antenna for mmWave Wireless Communications," *IEEE Antennas and Wireless Propagation Letters*, vol. 18, no. 9, pp. 1726–1730, 9 2019.

[15] C. A. Balanis, "Polarization Measurements," in *Antenna Theory: Analysis and Design, 4th Edition.* Hoboken, New Jersey: John Wiley & Sons, 2016, ch. 17, p. 1017.

[16] M. Mrnka, M. Pavlovic, and Z. Raida, "Antenna Range Illuminator Based on a Septum Polarizer and a Dual-Mode Horn [Measurements Corner]," *IEEE Antennas and Propagation Magazine*, vol. 58, no. 4, pp. 82–86, 2016.

[17] C. Kumar, V. V. Srinivasan, V. K. Lakshmeesha, and S. Pal, "Novel Dual Circularly Polarized Radiating Element for Spherical Phased-Array Application," *IEEE Antennas and Wireless Propagation Letters*, vol. 8, pp. 826–829, 2009.

[18] J. Wu, Y. J. Cheng, H. B. Wang, Y. C. Zhong, D. Ma, and Y. Fan, "A Wideband Dual Circularly Polarized Full-Corporate Waveguide Array Antenna Fed by Triple-Resonant Cavities," *IEEE Transactions on Antennas and Propagation*, vol. 65, no. 4, pp. 2135–2139, 4 2017.

Chapter 5

Design of Wideband Grooved-Wall Circularly Polarized Horn Antenna for Dual-Circular-Polarization Application

5.1 Introduction

In Chapter 3, we designed a dual-CP antenna based on the conventional septum polarizer, which achieves 21% bandwidth with isolation $>$ 20%. In Chapter 4, we proposed a grooved-wall septum polarizer in order to improve the bandwidth and isolation performance, and a dual-CP antenna based on the grooved-wall septum polarizer and a conical horn is proposed and studied, which shows a working bandwidth of 15.8% with isolation $>$ 30 dB. However, as described in Chapter 2, it is believed that the maximum practical operating bandwidth for the septum polarizer is less than 25% [1]. Achieving an

even wider bandwidth is quite challenging since there is a trade-off between impedance bandwidth and AR bandwidth in a stepped septum polarizer.

For this reason, a new type of structure is needed to achieve a wide bandwidth $> 25\%$ in the mmWave band, and further to realize high isolation over a bandwidth $> 25\%$.

In recent years, a number of waveguide-based CP antennas being proposed for wideband operation have the potential to operate as wideband dual-CP antennas with extra feeding structures. A compact endfire CP antenna with two symmetrical septa inside the rectangular waveguide [2] shows a 40% overall bandwidth in the V-band. However, its reflection coefficient is not low enough to provide high isolation when it is changed to a dual-CP antenna. Moreover, the two septa inside the waveguide will pose a challenge in fabrication at high frequencies because the septum thickness will decrease as frequency increases. Several new types of CP antenna with hollow waveguide structure without septum have also been proposed over the past few years [3–6]. In [3] and [4], two CP horn antennas based on either a hexagonal or a tapered elliptical waveguide LP-to-CP polarizer achieve an overall bandwidth of 37% and 41.8% in D-band and sub-THz band, respectively. Nevertheless, the reflection coefficients of these CP antennas are only below about -18 dB, which is still too high to realize high isolation when it is changed to dual-CP antennas. A CP horn antenna with cavities as an in-built polarizer in W-band is proposed in [6]. However, its impedance bandwidth is limited to 10% when $|S_{11}|$ is below -15 dB, and the antenna gain is limited within the range of 9.2 - 9.45 dBic.

In this chapter, a novel wideband grooved-wall CP horn antenna is proposed and analyzed for the first time. The operating principle of the grooved-wall CP horn is investigated, and a prototype has been fabricated and verified. The measured results show a bandwidth of 37.8% ranging from 75 GHz to 110 GHz is achieved with $|S_{11}| < -22$ dB and AR < 3.04 dB. The measured gain of this antenna is 16.9 ± 2.7 dBic over the entire working bandwidth. In addition to a wide working bandwidth, with a hollow waveguide structure, this antenna can be scaled up to higher frequencies than those have septum inside. The proposed structure is also simpler than those in [3] and [6]

with much less design parameters required, hence easy for fabrication. This grooved-wall CP horn is also capable of generating dual CP when used together with an OMT. Compared with the dual-CP antenna based on the septum polarizer (such as those we reported in Chapter 3 and Chapter 4), the dual-CP antenna based on the grooved-wall CP horn and OMT proposed in this chapter employs a different waveguide structure to generate dual CP. Without using a septum inside a square waveguide, a pair of grooves is introduced on the inner wall of a horn serving as an inbuilt polarizer, which is capable of generating dual-CP when the horn is connected to an OMT. With an OMT employing a T-shaped waveguide junction, the complete dual-CP antenna has a hollow waveguide structure without any septum inside the waveguide. This septum-free structure can achieve a wider operating bandwidth and is easier for fabrication in the high-frequency band than those based on the septum polarizer. Based on the design of the CP horn demonstrated by experiment, a dual-CP antenna is also presented and verified by full-wave simulations in this chapter. The simulated results show that this dual-CP antenna can achieve reflection coefficient $<$ -15 dB and isolation $>$ 32 dB as well as AR $<$ 3 dB over the frequency range from 82 to 108 GHz (27.4% bandwidth) with a maximum gain up to 17.9 dBic.

The remainder of this chapter is organized as follows. In Section 5.2, the geometry of the proposed grooved-wall CP horn antenna is presented and its working principle is illustrated in Section 5.3. Section 5.4 presents the simulation and measurement results of the proposed CP antenna. After that, this CP antenna's capability of realizing dual-CP is verified by full-wave simulation in Section 5.5. Conclusions are drawn in Section 5.6.

5.2 Antenna Design

The geometry of the proposed grooved-wall CP horn antenna and the front view at the horn aperture are shown in Figure 5.1. The horn consists of a circular waveguide followed by a linear-flared conical circular waveguide with two symmetrical continuous grooves on their walls and is connected to a WR-10 waveguide port by a smooth transition. The

diameters of circular waveguide and conical circular waveguide are d and D, and length of these two parts are l_{cir} and l_{flare}, respectively. The grooves are designed to follow a straight profile from the beginning of the circular waveguide to the aperture of horn with height of h and aligned at 45° with respect to the WR-10 waveguide port. When the WR-10 port is excited with TE_{10} mode, LHCP will be generated through the horn. The overall length of the horn antenna is 32 mm and the aperture diameter is 8.56 mm.

Since the grooves can be considered as the polarizer which is incorporated into the smooth-wall horn antenna, the space for the polarizer and transition section between the polarizer and horn can be saved, thereby achieving compact size. This septum-free structure also has higher power handling capacity and better rigidity than septum-based structure. In comparison with the hollow waveguide structures proposed in [3] and [6], which are comprised of a series of hexagonal and transition waveguides or circular cavities with different dimensions and have more than a dozen of design parameters to optimize, this proposed structure only has 5 parameters and is considered to be much easier for design and fabrication.

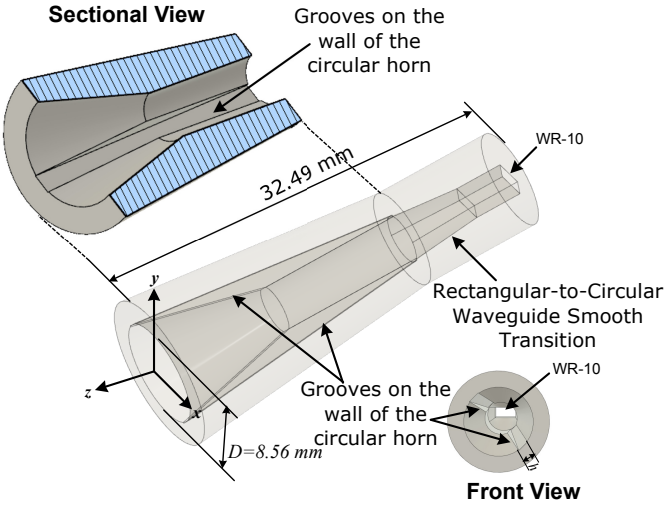

Figure 5.1: Geometry of the grooved-wall CP horn antenna.

5.3 Working Principle and Parametric Study

5.3.1 Mode Decomposition in Grooved-wall Circular Waveguide

The continuous grooves on the wall of horn antenna serve as an integrated polarizer in the horn antenna, which is capable of generating circular polarization wave in the cavity of the horn antenna. The TE_{10} mode excited at the WR-10 waveguide port will firstly be converted into TE_{11} mode when it arrives at the circular waveguide section of the grooved-wall horn, and the direction of the E-field of the TE_{11} mode is oriented at 45° with respect to the pair of grooves. For this reason, the input TE_{11} mode will be divided into two orthogonal degenerate TE_{11} modes with different propagation constants due to the existence of the grooves, as shown in Figure 5.2, and LHCP will be generated if the dimensions of the horn and grooves are designed to give rise to a phase difference of 90° between these two modes at the aperture of the horn antenna.

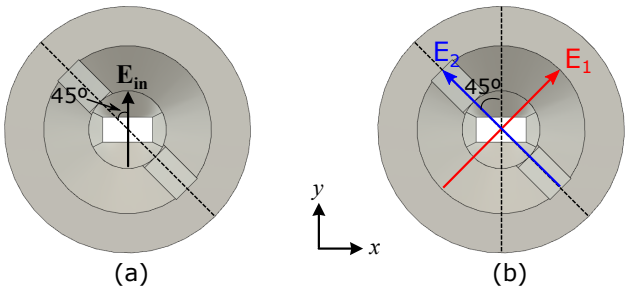

Figure 5.2: (a) Input and (b) output E-field components.

Since the proposed grooved-wall CP horn antenna can be regarded as a concatenation of many discretised grooved-wall circular waveguides with different dimensions, wave propagation characteristics in the grooved-wall circular waveguide is investigated in the following sections to further explain the generation of CP from the input TE_{11} mode and the impact of groove dimensions on the CP performance of the grooved-wall circular waveguide.

5.3.2 Mode Analysis of the Grooved-wall Circular Waveguide

Mode analysis is carried out for the cross section of the grooved-wall circular waveguide using CST Microwave Studio. The cross section geometry of grooved-wall waveguide is shown in the inset of Figure 5.3, where the radius of the circular waveguide (r) is 1.485 mm, depth (dw) and height (h) of the grooves are 0.4 mm and 1 mm respectively.

The result shows two orthogonal propagating modes can exist in the grooved-wall waveguide. Figure 5.3 shows the propagation constants and E-field profiles of these two modes. It can be observed from the figure that the propagation constants of these two degenerate TE_{11} modes are different, which will lead to a phase difference of 90° between them after propagating over a certain distance and thereby generating CP wave.

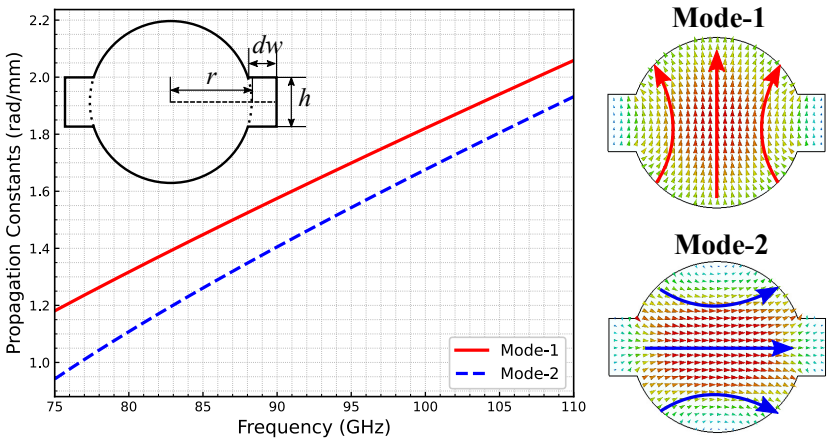

Figure 5.3: Mode analysis for the grooved-wall circular waveguide.

5.3.3 Wave Propagation in the Grooved-wall Circular Waveguide

Based on the mode analysis, a LP-to-CP polarizer based on a grooved-wall circular waveguide with the same cross section dimensions in Section 5.3.2 is used to verify the CP generation effect at 90 GHz. According to the propagation constant difference between mode-1 and mode-2 at 90 GHz obtained from Figure 5.3, the length of the grooves can be derived given phase difference of $\pi/2$. The grooved-wall circular waveguide is then connected to two circular waveguides acting as input and output waveguide respectively, as shown in Figure 5.4. The E-fields along the centre axis of the polarizer are monitored

in the full-wave simulation. The direction of the E-field of the excited TE_{11} mode is deliberately set to be aligned at 45° with respect to the grooves, so that the input TE_{11} mode will be divided into two orthogonal degenerate modes in the grooved-wall section, i.e., mode-1 and mode-2 in Figure 5.3.

The amplitude and phase difference between x and y components of E-fields along the centre axis of the polarizer is shown in Figure 5.4. It can be found that the phase difference between x and y components of the E-fields gradually decreased from 180° owing to the different propagation constants experienced by the two degenerate modes in the grooved-wall circular waveguide, and eventually phase difference of 90° is achieved at the end of the grooved-wall circular waveguide while their amplitudes almost keep the same, which indicates CP wave is generated. The E-field in the complete polarizer shown in the top of Figure 5.4 also presents the transition from a LP wave to a CP wave through the grooved-wall waveguides.

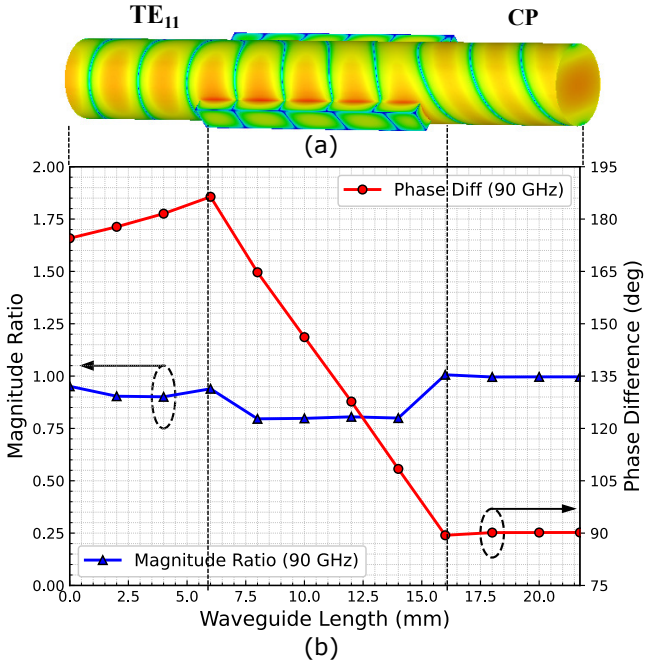

Figure 5.4: (a) The E-field in the polarizer and corresponding (b) Magnitude ratio and phase difference between x and y components of E-fields along the centre axis of the polarizer. Magnitude Ratio is $|E_y|/|E_x|$.

5.3.4 Parametric Study and Analysis

A parametric analysis is carried out on groove depth and height keeping the diameter of grooved-wall circular waveguide constant, in order to find out the impact of these parameters on the CP performance.

The effect of the groove depth (dw) and height (h) on the propagation constant difference ($\Delta\beta$) between the two orthogonal degenerated TE_{11} modes are shown in Figure 5.5 and Figure 5.6, respectively. It can be found that larger dw or h will lead to larger $\Delta\beta$, which means CP can be achieved with shorter waveguide length. However, the result also shows the variation of $\Delta\beta$ with respect to the frequency is larger when larger dw or h is used, which will lead to smaller AR bandwidth. It can also be noted that the increment of $\Delta\beta$ is becoming small as dw or h increases. This indicates the effect of increasing $\Delta\beta$ by increasing dw and/or h is limited when dw/h become large.

The analysis reveals that there is a trade-off between antenna size and AR bandwidth for grooved-wall CP horn antenna design, and proper optimization of the dimensions of horn and grooves is needed to achieve better AR bandwidth and radiation characteristics with compact size.

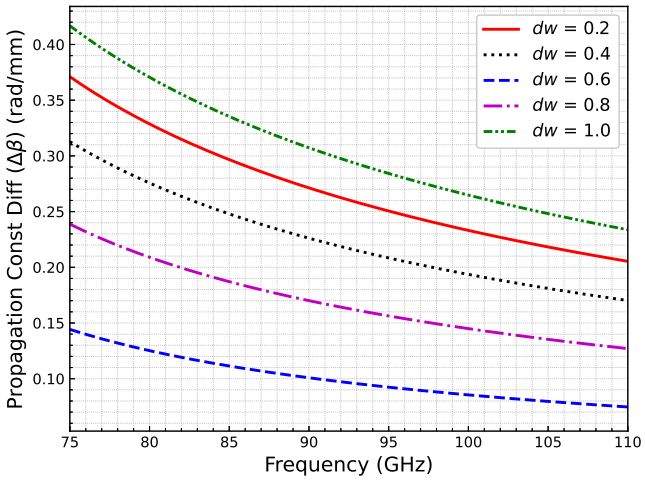

Figure 5.5: Effect of groove depth (dw) on the propagation constant difference ($\Delta\beta$) between the two orthogonal degenerated TE_{11} modes.

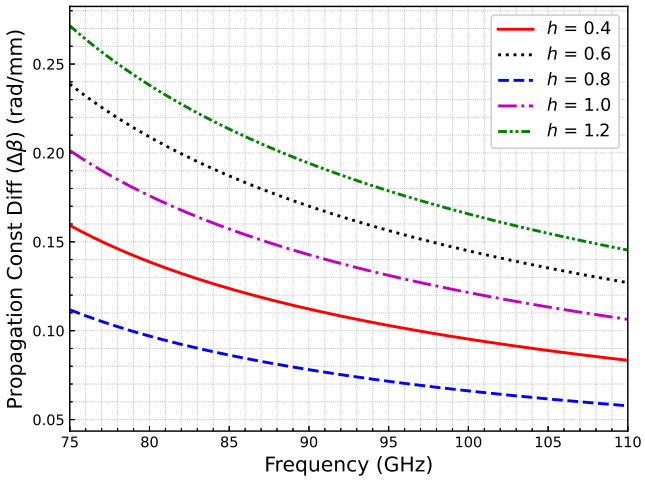

Figure 5.6: Effect of groove height (h) on the propagation constant difference ($\Delta\beta$) between the two orthogonal degenerated TE_{11} modes.

5.4 Prototype and Antenna Performance

5.4.1 Prototype and Fabrication

The dimensions of the grooved-wall CP horn antenna are optimized in the W-band according to the analysis illustrated in Section 5.3, using CST Microwave Studio. Then a prototype working in the W-band is fabricated.

An attractive feature of the proposed horn structure is that, with its compact size, it can be easily fabricated as one piece of brass using wire-cutting Electrical Discharge Machining (EDM) since there is no septum inside the cavity and the grooves are designed to follow a straight profile from the start of the circular waveguide throughout to the aperture of the horn. Fabricating the horn as one piece without splitting it into two halves also avoids the misalignment introduced during assembly that will have a significant adverse impact on the AR, as discussed in [7]. The rectangular-to-circular smooth transition together with a WR-10 UG387/U flange is fabricated separately using wire-cutting EDM as well and welded to the grooved-wall horn. The complete antenna is electroplated with gold for surface smoothness and prevention of oxidation. The fabricated prototype is shown in Figure 5.7.

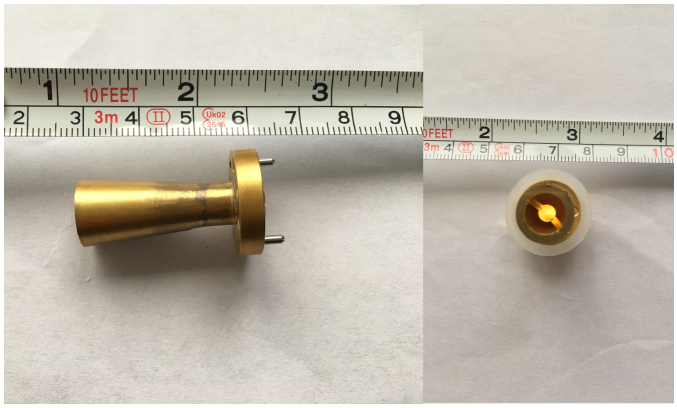

Figure 5.7: Photograph of the prototype of the proposed grooved-wall CP antenna.

5.4.2 Simulated and Measured Results

The scattering parameters of the dual-CP antenna are measured using a Keysight PNA-X network analyzer with an OML WR-10 extension head, and the radiation characteristics are measured in a mmWave compact antenna test range (CATR) at the Antenna Lab of Queen Mary University of London. The photographs of the CATR measurement setup are shown in Figure 5.8.

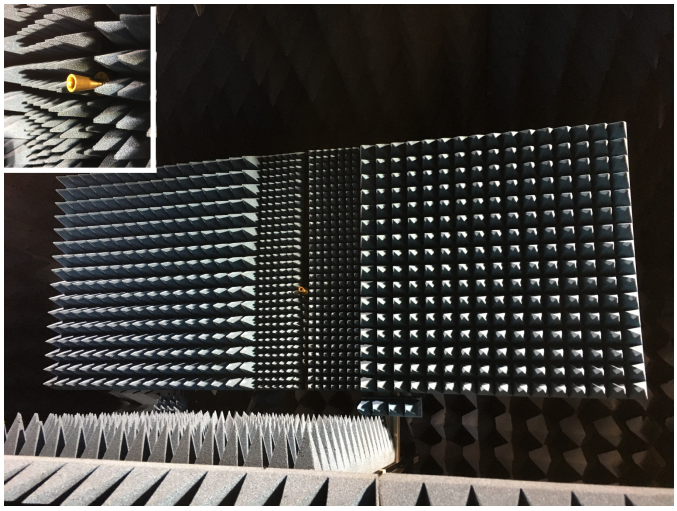

Figure 5.8: Photograph of CATR measurement setup.

The radiation pattern and axial ratio measurement follows the CP measurement method described in Section 2.4. In this measurement, the rotation angle of the reference antenna is set from 0° to 150° with a step of 30° to measure each polarization component

at these angles, which is proved to be sufficient to find the major and minor axes of the polarization ellipse of our antenna.

The measured and simulated reflection coefficient and axial ratio at the boresight are shown in Figure 5.9. The results show that the measured reflection coefficient is below -22 dB, and the axial ratio is lower than 3.04 dB over the entire W-band, which means an overall operating bandwidth of 37.8% is achieved for the proposed grooved-wall CP antenna. It can be seen from the figure that the measured $|S_{11}|$ is close to the simulated result, and the axial ratio agrees well with the simulated result. The discrepancy of $|S_{11}|$ around 75 GHz is probably due to the dimension error introduced in the fabrication.

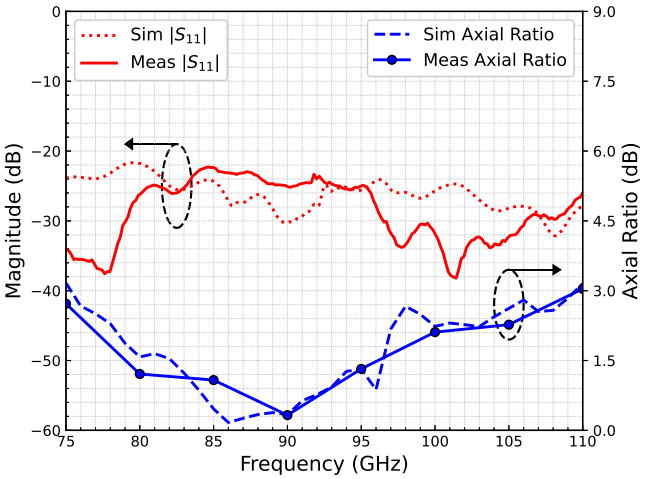

Figure 5.9: Simulated and measured reflection coefficient and axial ratio of the proposed grooved-wall CP antenna.

The normalized measured and simulated polarization patterns [8] of the proposed grooved-wall CP antenna at several frequencies across the W-band are illustrated in Figure 5.10, which are used to calculate the axial ratio shown in Figure 5.9 and reveal the CP characteristics of the proposed CP antenna. The simulated polarization patterns are obtained by monitoring the magnitudes of E-field at boresight in the farfield region with polarization angles ranging from 0° to 350° with a step of 10°. It can be found that the simulation result agrees well with the measured result. The results show that the polarization patterns at frequencies which are in the middle of the working bandwidth

are close to circles, while those at the two ends of the working bandwidth degrade to ellipses hence larger AR. It can also be observed that the major axes of the polarization ellipses deviate from y-axis (0°) at the two ends of the working bandwidth, because the phase difference is shifted away from 90° when the frequency goes towards the low and high ends according to the operating principles of this structure explained in Section 5.3.

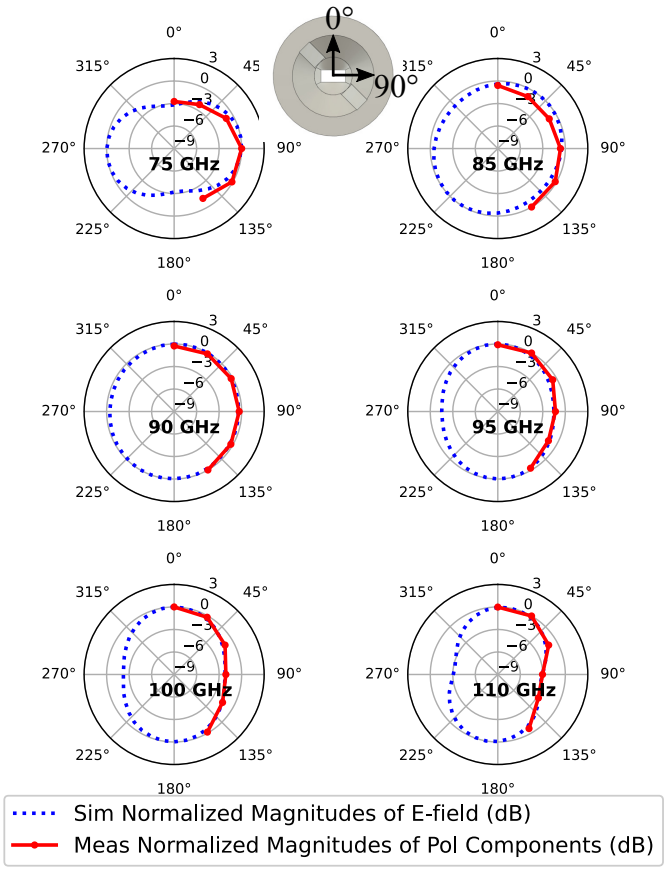

Figure 5.10: Normalized measured and simulated polarization patterns of the proposed grooved-wall CP antenna.

Figure 5.11 depicts the normalized radiation patterns in $yz-$ and $xz-$plane (see Figure 5.1) at 75 GHz, 90 GHz and 110 GHz, respectively. The measured results show that a good rotational symmetry is achieved for the main lobes at all frequencies, which agree with the simulated results. The rotationally symmetric radiation patterns allow this antenna to be used as a primary feed for reflector antennas if high gain is required. The ripples observed in sidelobes of the measured results can be attributed to the thickness

of the absorbers placed on the two sides of the antenna under test and the limitation of the mounting setup.

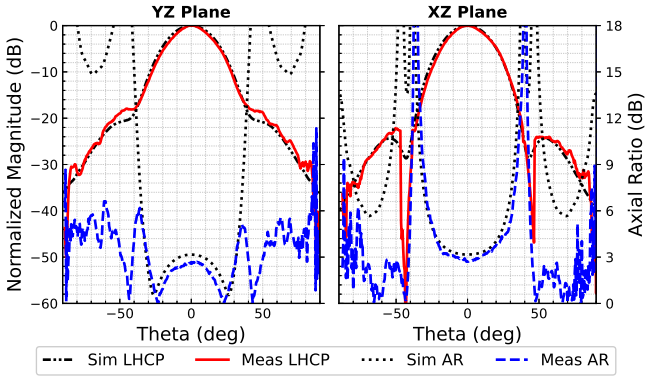

(a)

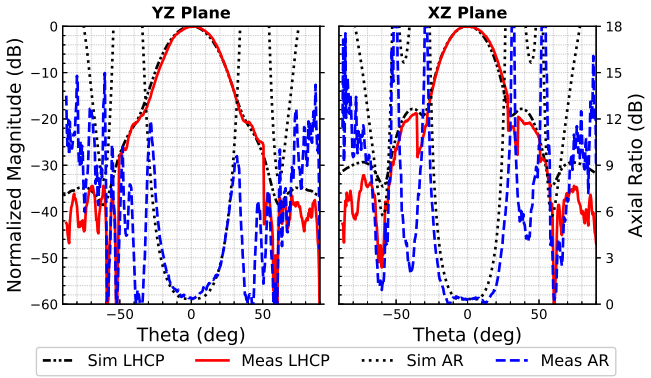

(b)

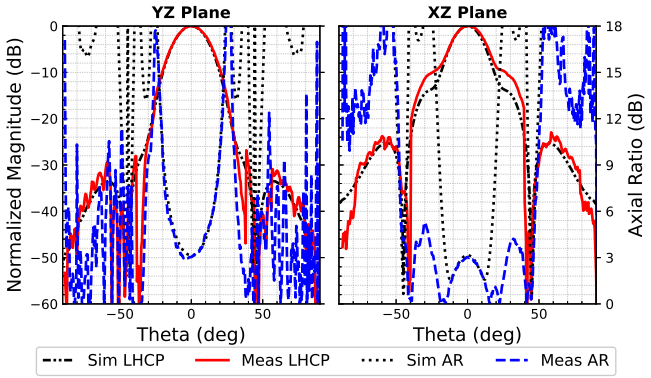

(c)

Figure 5.11: Measured and simulated radiation patterns in $yz-$ and $xz-$plane at (a) 75 GHz, (b) 90 GHz and (c) 110 GHz.

Figure 5.12 presents the measured antenna gain and simulated directivity of co-polar (LHCP) and cross-polar (RHCP) at boresight over the entire working bandwidth. The

result shows antenna gain of co-pol (LHCP) is 16.9 ± 1.7 dBic, and the best cross-polarization isolation is around 34 dB at 90 GHz while the worst case is about 15 dB at the two ends of the working bandwidth. Both results agree well with the simulated ones.

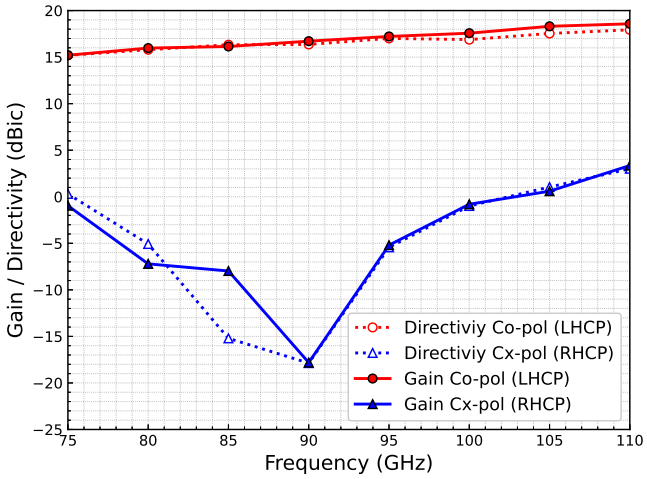

Figure 5.12: Measured antenna gain and simulated directivity of co-polar (LHCP) and cross-polar (RHCP) at over the working bandwidth.

5.5 Dual-CP Antenna Based On the Grooved-Wall CP Horn

After the proposed grooved-wall CP horn is verified both in simulation and measurement showing wideband CP can be achieved, in this section, we are going to demonstrate this grooved-wall horn structure is capable of realizing dual-CP when it is used with an OMT via simulation. The theoretical principle of dual-CP generation for this structure will be illustrated in Chapter 6, which is dedicated to a dual-CP antenna design based on grooved-wall horn.

5.5.1 Antenna Configuration

The structure of the entire dual-CP antenna based on the grooved-wall horn is presented in Figure 5.13, which is comprised of two components. The grooved-wall CP horn proposed in this chapter is connected to an orthomode transducer presented in [9] by a smooth circular-to-square waveguide transformer. The axial port (port 1) and the lat-

eral port (port 2) are both standard WR-10 rectangular waveguide ports. If port 1 is excited, TE_{10} mode will propagate through the OMT and be fed into the grooved-wall horn; when port 2 is excited, TE_{01} mode will be guided through the OMT and fed into the grooved-wall horn.

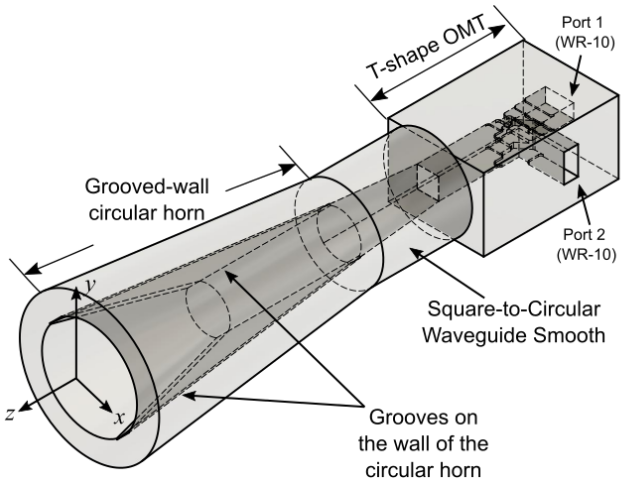

Figure 5.13: Structure of the dual-CP antenna based on the groove-wall CP horn.

5.5.2 Simulation Results

Full-wave simulation of the complete dual-CP antenna shown in Figure 5.13 is carried out using CST Microwave Studio with time-domain solver. The simulation results show that when port 1 is excited, LHCP can be generated; while RHCP can be generated by exciting port 2.

The reflection coefficient and port isolation are shown in Figure 5.14. We aim to achieve a simulated reflection coefficient lower than -15 dB so that a 5 dB performance margin can be left for fabrication errors. It can be found from the figure that the reflection coefficients of both ports are lower than -15 dB from 82 GHz to 110 GHz, and the isolation of both ports are higher than 32 dB over the same frequency range.

Figure 5.15 depicts the simulated AR over the frequency range from 75 GHz to 110 GHz. The simulation result shows that the 3-dB AR bandwidth of both LHCP and RHCP is from 76 GHz to 108 GHz. Thus the overall operating bandwidth with port

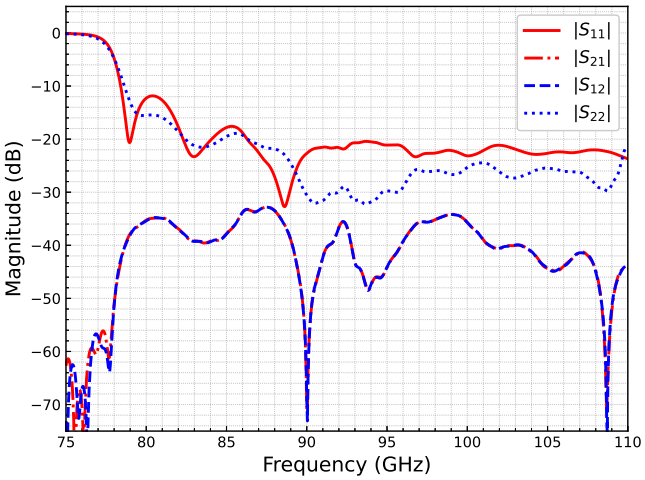

Figure 5.14: Simulated S-parameters of the dual-CP antenna.

isolation > 30 dB and AR < 3 dB is 27.4% (82 - 108 GHz), which is limited both by the impedance bandwidth and 3-dB AR bandwidth. In fact, the impedance bandwidth of the dual-CP antenna is limited by the OMT.

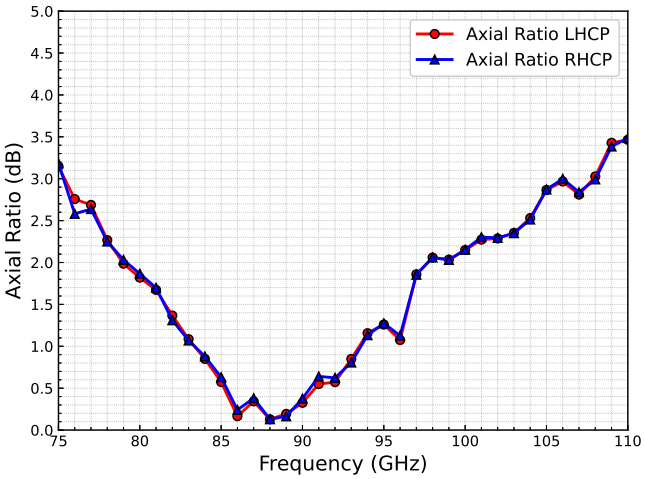

Figure 5.15: Simulated AR of the dual-CP antenna.

The normalized radiation patterns of both LHCP and RHCP in 0°/45°/90° planes at 82, 90, 95 and 108 GHz are presented in Figure 5.16(a) and Figure 5.16(a). It can be found that a good rotational symmetry is achieved for the main lobes at all frequencies.

Figure 5.17 depict the directivity and max SLL of LHCP (port 1 excitation) and

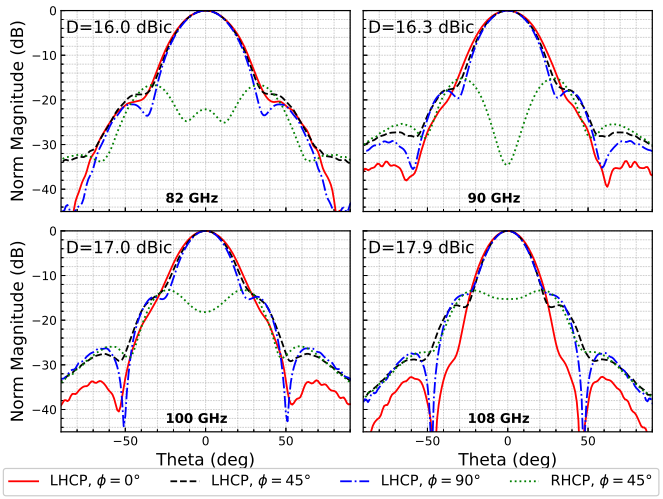

(a)

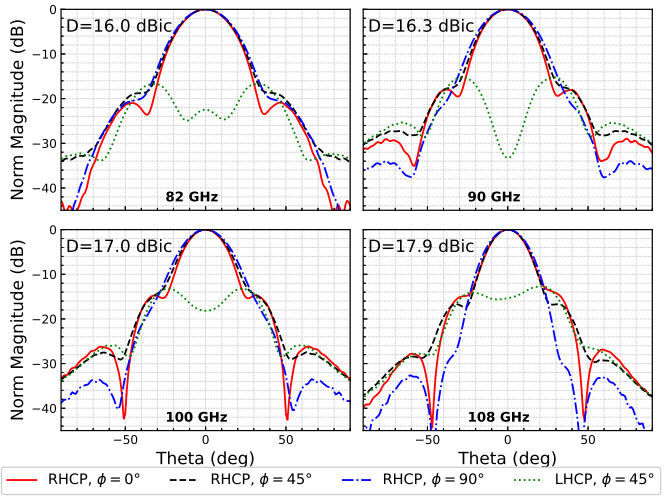

(b)

Figure 5.16: Normalized simulated radiation patterns of (a) LHCP and (b) RHCP.

RHCP (port 2 excitation) over the entire operating bandwidth from 82 to 108 GHz, respectively. The result shows the directivity for both LHCP and RHCP is from 16 dBic to 17.9 dBic over the operating bandwidth. It can also be observed that the SLLs of both LHCP and RHCP are below -14 dB.

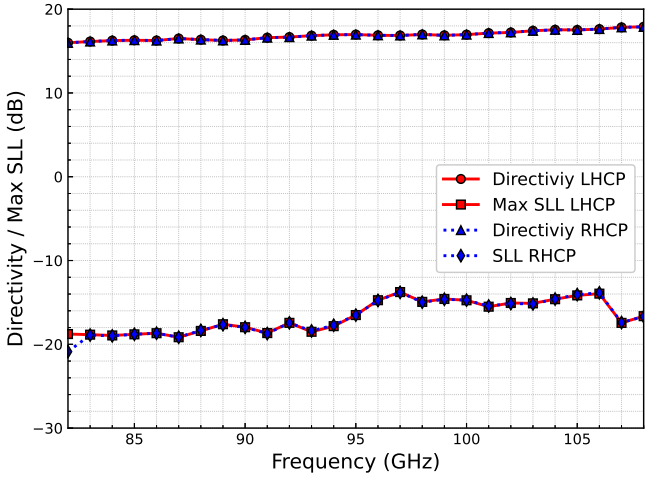

Figure 5.17: Simulated gain and max SLL of the dual-CP antenna.

5.6 Summary

A novel CP horn antenna without any septum or extra polarizer is designed in this chapter, achieving wide impedance bandwidth and 3-dB axial ratio bandwidth with a simple and compact structure. The operating principle of the proposed antenna is also presented with a parametric study. A prototype working in the W-band has been fabricated and experimentally verified. The measured result shows an overall operating bandwidth of 37.8% covering the entire W-band from 75 GHz to 110 GHz with $|S_{11}|$ < -22 dB and AR < 3.04 dB, while the antenna gain is 16.9 ± 1.7 dBic. Moreover, this antenna is expected to have a better power-handling capability and be able to scaled up to even terahertz (THz) band due to its septum-free waveguide structure. A dual-CP antenna based on the proposed grooved-wall CP horn is also designed via full-wave simulations. The simulated results demonstrate the capability of dual-CP generation for the proposed CP horn. According to the simulation results, a reflection coefficient < -15 dB and isolation > 32 dB over the frequency range from 82 to 108 GHz is achieved with AR < 3 dB for the dual-CP antenna. Antenna gain of 16.95 ± 0.95 dBic is observed over the entire operating bandwidth.

References

[1] M. Chen and G. Tsandoulas, "A wide-band square-waveguide array polarizer," *IEEE Transactions on Antennas and Propagation*, vol. 21, no. 3, pp. 389–391, 1973.

[2] X. Cheng, Y. Yao, J. Hirokawa, T. Tomura, T. Yu, J. Yu, and X. Chen, "Analysis and Design of a Wideband Endfire Circularly Polarized Septum Antenna," *IEEE Transactions on Antennas and Propagation*, vol. 66, no. 11, pp. 5783–5793, 2018.

[3] S. Bhardwaj and J. L. Volakis, "Hexagonal Waveguide Based Circularly Polarized Horn Antennas for Sub-mm-Wave/Terahertz Band," *IEEE Transactions on Antennas and Propagation*, vol. 66, no. 7, pp. 3366–3374, 2018.

[4] H. Yu, J. Yu, X. Liu, Y. Yao, and X. Chen, "A Wideband Circularly Polarized Horn Antenna With a Tapered Elliptical Waveguide Polarizer," *IEEE Transactions on Antennas and Propagation*, vol. 67, no. 6, pp. 3695–3703, 2019.

[5] C. Shu, S. Hu, Y. Yao, Y. Alfadhl, and X. Chen, "W-band grooved-wall circularly polarised horn antenna," *IET Microwaves, Antennas Propagation*, vol. 14, no. 11, pp. 1171–1174, 2020.

[6] G. Mishra, S. K. Sharma, and J. S. Chieh, "A Circular Polarized Feed Horn With Inbuilt Polarizer for Offset Reflector Antenna for W-Band CubeSat Applications," *IEEE Transactions on Antennas and Propagation*, vol. 67, no. 3, pp. 1904–1909, 2019.

[7] C. Shu, J. Wang, S. Hu, Y. Yao, J. Yu, Y. Alfadhl, and X. Chen, "A Wideband Dual-Circular-Polarization Horn Antenna for mmWave Wireless Communications," *IEEE Antennas and Wireless Propagation Letters*, vol. 18, no. 9, pp. 1726–1730, 9 2019.

[8] C. A. Balanis, "Polarization Measurements," in *Antenna Theory: Analysis and Design, 4th Edition.* Hoboken, New Jersey: John Wiley & Sons, 2016, ch. 17, p. 1017.

[9] A. Dunning, S. Srikanth, and A. R. Kerr, "A simple orthomode transducer for centimeter to submillimeter wavelengths," in *20th International Symposium on Space Terahertz Technology*, Charlottesville, USA, 2009, pp. 191–193.

Chapter 6

Design of Wideband Dual-Circular-Polarization Antenna with High Isolation Based on the Grooved-Wall Horn Antenna

6.1 Introduction

In Chapter 5, we have designed a wideband CP antenna without any septum or extra polarizer in the W-band by introducing a pair of continuous grooves on the wall through the entire conical horn and achieved a bandwidth of 37.8%. We also demonstrated that this structure has the capability to generate dual-CP with an OMT and the potential to achieve high isolation over wide bandwidth due to continuous-tapered structure. It is worth mentioning that, after we presented this design at IEEE UCMMT in August of 2019 [1] and published a journal paper in June of 2020 [2], another research group

reported a polarizer with grooved structure in August of 2020 [3]. The polarizer reported in [3] applies a single short groove on the wall of the circular waveguide to achieve dual-CP and is connected to an extra conical horn for radiating in the V-band, as shown in Figure 6.1. In comparison with our groove-wall horn design (see Chapter 5), the antenna in [3] shows a simpler and more compact structure with two side-fed ports as well as a mono-groove with an annulus sector cross-section being easy for fabrication. Nevertheless, the short groove structure used in [3] introduces sharp steps on the waveguide wall in the propagation direction of the EM wave, which will degrade the reflection and limit the impedance bandwidth. The measured results in [3] shows that overall impedance bandwidth for both ports is relatively narrow, from 53.71 to 58.1 GHz (6.6%) when $|S_{11}|$ is below -10 dB. The measured port isolation is not revealed, and the simulated port isolation is only 15 dB within the operating bandwidth. By contrast, the groove configuration in our design starts from the beginning of the circular waveguide to the horn's aperture following a straight profile, which shows a much wider impedance bandwidth as reported in Chapter 5.

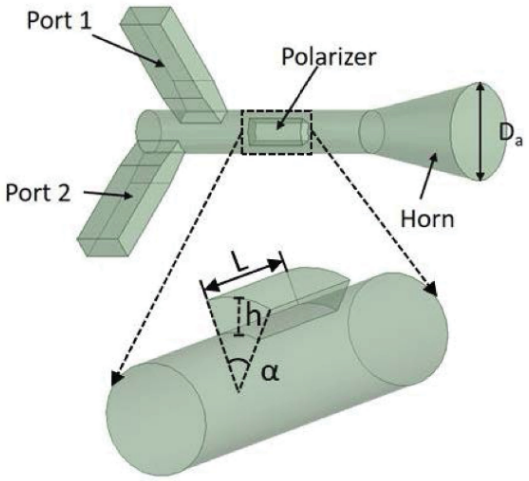

Figure 6.1: Geometry of the dual-CP antenna reported in [3].

In this chapter, a multi-section grooved-wall horn antenna is proposed to generate dual CP with high port isolation when it is used with an orthomode transducer (OMT). Based on our previous work presented in [1, 2] and Chapter 5, we have generalized this

approach and designed a multi-section grooved-wall CP horn by introducing grooves with various widths and depths for each section. Compared with the single-flare configuration in Chapter 5, the multi-section configuration proposed in this chapter will introduce more degrees of freedom for the grooved-wall CP horn design, leading to better overall performance for the entire dual-CP antenna with well-optimized dimensions. Besides wide 3-dB AR bandwidth and rotational symmetric radiation patterns, this CP antenna is also optimized to have low reflection coefficients over a wide bandwidth in order to realize dual-CP with high isolation over a wide bandwidth when it is connected to an OMT. An OMT based on [4] is designed with critical modifications to significantly improve the misalignment tolerance for port isolation and polarization isolation during assembling.

The operating principle of the proposed dual-CP antenna has been analyzed, and a prototype has been fabricated to verify the design in the W-band. The measured results show a port isolation higher than 30 dB and AR $<$ 2.8 dB over a bandwidth of 31.6% from 80 to 110 GHz, while the reflection coefficient is lower than -16 dB. To the best of the authors' knowledge, this is the dual-CP antenna with the highest isolation over widest bandwidth ever reported. Rotationally symmetric radiation patterns over the entire operating bandwidth is also achieved with antenna gain of 19.6 ± 2 dBic. With a high isolation over a wide bandwidth as well as good AR and radiation performance, this dual-CP antenna enables polarization diversity/multiplexing or In-Band Full-Duplex in mmWave wireless communication systems thereby achieving a twofold increase in spectral efficiency.

The remainder of this chapter is organized as follows. An overview of the entire antenna structure is described in Section 6.2. In Section 6.3, the dual-CP generation principles of the proposed antenna is illustrated, and a parametric analysis is performed. Section 6.4 and Section 6.5 presents the design of the multi-section grooved-wall CP horn and the OMT. In Section 6.6 and Section 6.7, simulated and measured results are presented and discussed, followed by conclusions in Section 6.8.

6.2 Antenna Overview

The structure of the entire dual-CP antenna is presented in Figure 6.2, comprising of two components. A multi-section horn with an integrated circular-to-square waveguide transformer is connected to the common port of an orthomode transducer. The horn consists of three conical sections, and a pair of grooves is introduced on the wall of each section. The grooves are aligned at 45° with respect to the x-axis, and the width and depth of the grooves in each section changes linearly. The axial port (port 1) and the lateral port (port 2) are both standard WR-10 rectangular waveguide ports. If port 1 is excited, TE_{10} mode will propagate through the OMT and be fed into the multi-section grooved-wall horn, where LHCP will be generated at the aperture of the horn; when port 2 is excited, TE_{01} mode will be guided through the OMT and fed into the multi-section grooved-wall horn, where RHCP will be generated.

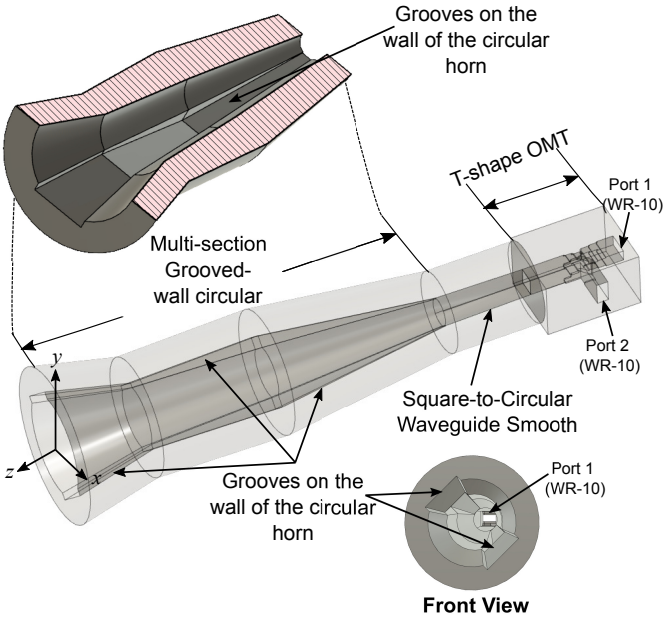

Figure 6.2: Structure of the complete dual-CP antenna.

6.3 Operating Principles

6.3.1 Principle of Dual-CP Generation

When port 1 or port 2 in Figure 6.2 is excited, TE_{10} (v-mode) or TE_{01} (h-mode) will be guided through the OMT to the square aperture of the square-to-circular waveguide transformer. Both modes will be converted to TE_{11} modes when they arrive at the circular waveguide section of the grooved-wall horn, and the direction of the E-field of TE_{11} modes will be oriented at $\pm 45°$ with respect to the pair of grooves, as shown in Figure 6.3. According to the CP generation principles illustrated in Chapter 5, the input TE_{11} mode will then be divided into two orthogonal degenerate TE_{11} modes with different propagation constants as shown in Figure 6.3, and CP can be generated with well-optimized dimensions of the grooved-wall horn.

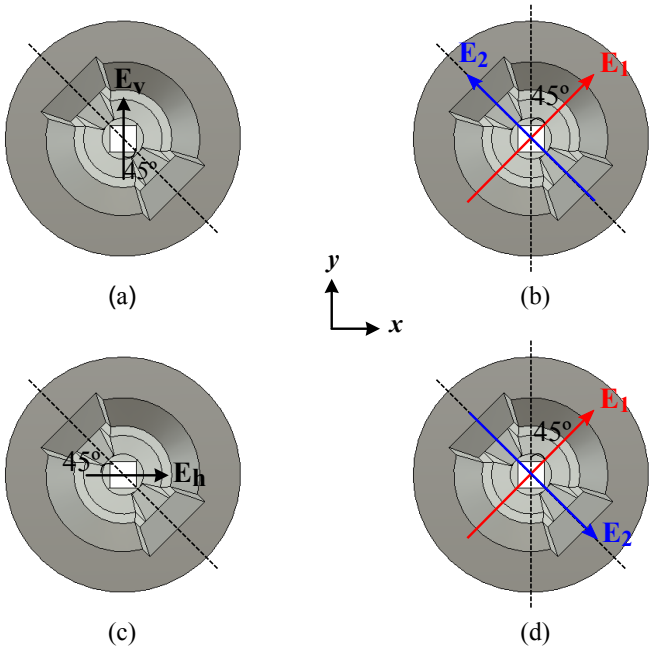

Figure 6.3: Input (a) v-mode and (c) h-mode and two orthogonal degenerated modes for (b)v-mode and (d) h-mode in the grooved-wall CP horn.

In order to illustrate the principle of dual-CP generation, the decomposition of v-mode and h-mode at the cross-section of grooved-wall circular waveguide is shown in Figure 6.4(a) and Figure 6.4(b) respectively, with the coordinates aligned with the direc-

tion of the two orthogonal degenerated modes. It can also be regarded as the front view of the grooved-wall horn aperture, and the input square waveguide port is added in the figure as a reference of the directions of E_v and E_h with respect to the input port of the groove-wall horn.

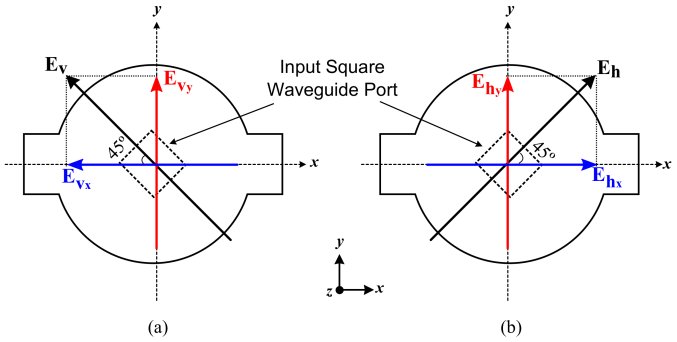

Figure 6.4: The decomposition of (a) v-mode and (b) h-mode at the cross-section of grooved-wall circular waveguide.

The E-field of the v-mode (E_v) can be decomposed into two orthogonal components along $-x$-axis and y-axis owing to the existence of the grooves, as shown in Figure 6.4(a). Let $\phi^0_{v_x}$ and $\phi^0_{v_y}$ denote the initial phases of these two orthogonal components at the start of the grooved-wall circular waveguide respectively, $\beta_{m1}(f)$ and $\beta_{m2}(f)$ denote the propagation constants of the two degenerated modes (mode-1 and mode-2 shown in Figure 5.3) at frequency f respectively. The phase difference between E-fields of the two orthogonal components at frequency f after propagating over a length of l in the grooved-wall circular waveguide when the v-mode is used as the input can be written as

$$\begin{aligned}\Delta\phi_v(f) &= (\phi^0_{v_y} - \beta_{m1}(f)l) - (\phi^0_{v_x} - \beta_{m2}(f)l) \\ &= (\phi^0_{v_y} - \phi^0_{v_x}) - (\beta_{m1}(f) - \beta_{m2}(f))l \\ &= (\phi^0_{v_y} - \phi^0_{v_x}) - \Delta\beta(f)l,\end{aligned} \tag{6.1}$$

where $\Delta\beta(f) = \beta(f)_{m1} - \beta(f)_{m2} > 0$ is the propagation constant difference between mode-1 and mode-2 at frequency f. With given grooved-wall circular waveguide dimensions (r, dw and h), $\Delta\beta(f)$ at a frequency can be obtained by mode analysis, and with a proper waveguide length l, $\Delta\beta(f)l = \pi/2$ can be achieved. Because $\phi^0_{v_y} - \phi^0_{v_x} = \pi$

according to the coordinate system, it can be derived that

$$\begin{aligned}\Delta\phi_v(f) &= (\phi^0_{v_y} - \phi^0_{v_x}) - \Delta\beta(f)l \\ &= \pi - \pi/2 \\ &= \pi/2.\end{aligned} \tag{6.2}$$

This means with a properly designed dimension of the grooved-wall circular waveguide that leads to $\Delta\beta(f)l = \pi/2$, the phase difference between the two orthogonal degenerated modes at the end of the grooved-wall circular waveguide will be $\pi/2$. According to the analysis in our previous work, their E-field magnitudes are close to each other [2]. Consequently, an LHCP wave is generated at the end of the grooved-wall circular waveguide when the grooved-wall circular waveguide is excited with the v-mode (see Figure 6.3).

Similar derivation process can be obtained when the grooved-wall circular waveguide is excited with the h-mode (see Figure 6.3), but with $\phi^0_{h_y} - \phi^0_{h_x} = 0$ according to the coordinate system, as shown in Figure 6.4(b), it can be derived that

$$\begin{aligned}\Delta\phi_h(f) &= (\phi^0_{h_y} - \beta_{m1}(f)l) - (\phi^0_{h_x} - \beta_{m2}(f)l) \\ &= (\phi^0_{h_y} - \phi^0_{h_x}) - (\beta_{m1}(f) - \beta_{m2}(f))l \\ &= (\phi^0_{h_y} - \phi^0_{h_x}) - \Delta\beta(f)l \\ &= 0 - \pi/2 \\ &= -\pi/2.\end{aligned} \tag{6.3}$$

Consequently, an RHCP wave can be generated with the same grooved-wall circular waveguide dimension which leads to $\Delta\beta(f)l = \pi/2$ as that mentioned above, if the h-mode is used as the input.

Hence, it can be concluded that if the dimensions (r, dw, h and l) of the grooved-wall circular waveguide are designed to give rise to a phase difference of $\pi/2$ between the two orthogonal degenerated modes, i.e., mode-1 and mode-2 shown in Figure 5.3, both LHCP and RHCP can be generated by feeding the grooved-wall circular waveguide with

TE_{11} modes which are oriented at $\pm 45^\circ$ with respect to the grooves. For example, v-mode in Figure 6.3 will produce an LHCP wave, while h-mode in Figure 6.3 will produce an RHCP wave. This conclusion is also true for the multi-section grooved-wall horn, because it can be regarded as a concatenation of many discretised grooved-wall circular waveguides with various dimensions. With properly designed cross-section dimensions and length of each section, a phase difference of $\pi/2$ between mode-1 and mode-2 can also be achieved at the aperture of the horn which enables dual-CP generation according to the analysis in this section.

6.3.2 Parametric Study and Analysis

In this section, a parametric study has been performed on the depth and height of groove, as well as the radius of cross-section. Because we are going to design a grooved-wall horn which has various cross-section dimensions, we analyze the dimension of the groove in a relative manner, which is different from that presented in Chapter 5. Given the radius of the grooved-wall waveguide cross-section is $R_{cross-section}$, the depth and height of the grooves is defined as

$$h = h_{min} + h\_ratio \cdot R_{cross-section} \tag{6.4}$$

$$dw = dw\_ratio \cdot R_{cross-section} \tag{6.5}$$

where h_min is the minimum height of the grooves and is set to 0.2 mm in our design.

Figure 6.5 and Figure 6.6 depict the effect of h_ratio and dw_ratio on the propagation constant difference ($\Delta\beta$) between the two orthogonal degenerated TE modes respectively, when $R_{cross-section}$ is kept to 2.4 mm. The results show that, with a fixed $R_{cross-section}$, larger h or dw will result in larger $\Delta\beta$, which means shorter waveguide length will be needed to generate a CP wave. It can be found that the increment of $\Delta\beta$ becomes smaller as h_ratio or dw_ratio increases. This indicates the effect of increasing $\Delta\beta$ by increasing h and/or dw is limited when h and/or dw becomes larger. It can also be observed that groove depth will introduce larger $\Delta\beta$ than groove height with the same size.

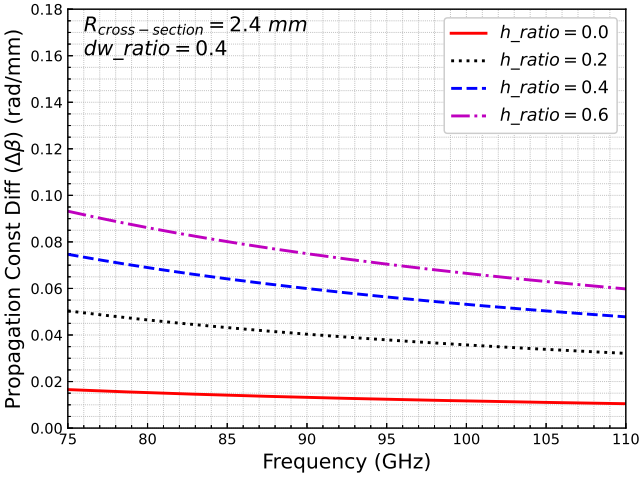

Figure 6.5: Effect of the groove height (h) on the propagation constant difference ($\Delta\beta$) between the two orthogonal TE modes.

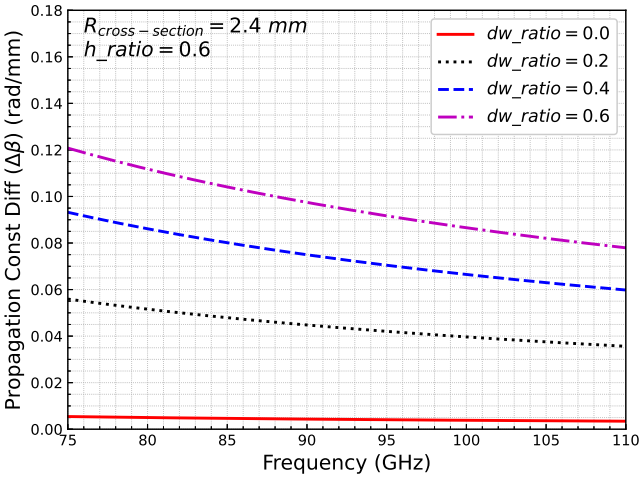

Figure 6.6: Effect of the groove depth (dw) on the propagation constant difference ($\Delta\beta$) between the two orthogonal TE modes.

In Figure 6.7, $\Delta\beta$ with different cross-section radius is shown when *h_ratio* and *dw_ratio* are fixed to 0.6 and 0.4, respectively. It can be found that, with the same groove height ratio and groove depth ratio, the larger waveguide cross-section will lead to smaller $\Delta\beta$, and this impact on $\Delta\beta$ will be larger when the cross-section radius is smaller.

In addition, all the results above show the frequency response of $\Delta\beta$ is not flat over

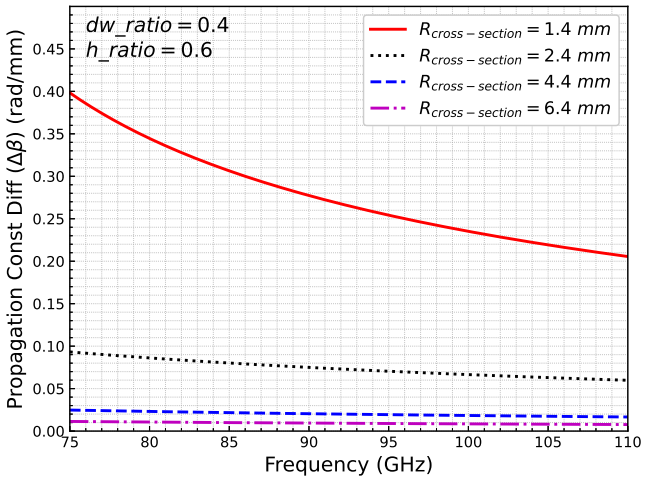

Figure 6.7: Effect of the waveguide cross-section radius ($R_{cross-section}$) on the propagation constant difference ($\Delta\beta$) between the two orthogonal TE modes.

the band. This uneven frequency response will limit the 3-dB AR bandwidth due to the phase error introduced after the two degenerated modes propagate over a certain distance.

Figure 6.8 illustrates the maximum phase error in degree over the expected operating frequency bandwidth from 80 GHz to 110 GHz with the waveguide length that leads to the phase difference of 90° between the two orthogonal degenerated modes at the centre frequency of 95 GHz. The ranges of h_ratio and dw_ratio in this analysis are between 0 and 0.6. The maximum phase error in radian can be expressed as

$$\phi_e^{max} = \underset{f\in F}{max}\{|\Delta\beta(f)l_0 - \pi/2|\}, \quad F = \{f_l \leq f \leq f_r\} \tag{6.6a}$$

$$l_0 = (\pi/2)/\Delta\beta(f_c) \tag{6.6b}$$

where $f_l = 80\ GHz$, $f_r = 110\ GHz$ and $f_c = 90\ GHz$.

It can be found in Figure 6.8 that larger groove height and depth will lead to smaller phase error, and the phase error can be improved more by increasing the groove depth than by increasing the groove height. The reason for this is that, although the frequency

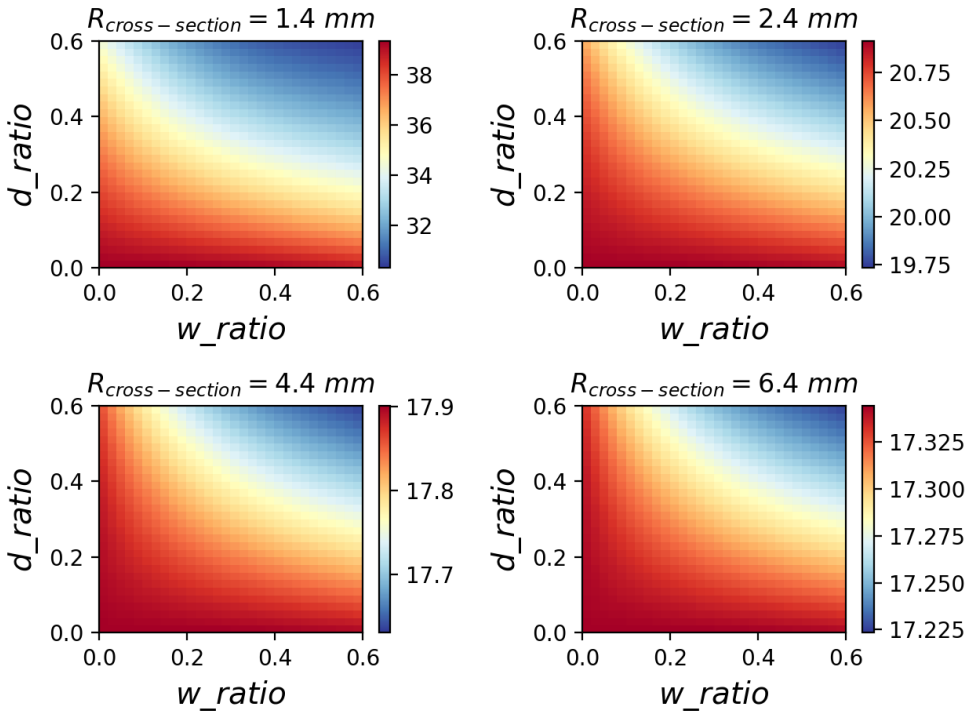

Figure 6.8: Effect of the groove height and depth with different waveguide cross-section radii ($R_{cross-section}$) on the propagation constant difference ($\Delta\beta$) between the two orthogonal TE modes.

response of $\Delta\beta$ is more even when groove height and depth is smaller, as shown in Figure 6.5 and Figure 6.6, the level of $\Delta\beta$ is so low that a much longer waveguide is needed to achieve 90° phase difference at the centre frequency than the length needed when larger groove height and depth are used. Because increasing groove height and depth will significantly increase the level of $\Delta\beta$ hence reducing the required waveguide length l_0 considerably, while the increment of $\Delta\beta(f)$ difference across the bandwidth is not as much as the decrease of l_0, the maximum phase error ϕ_e^{max} can be lower when groove height and/or depth become larger.

On the other hand, the result also shows that larger cross-section radius will result in lower phase error level (see the colour bars next to each subfigure to find the phase error ranges of difference cross-section radius). This means the flatness of the frequency response of $\Delta\beta$ improves significantly, which overcomes the penalty introduced by larger

waveguide length. This is also consistent with the result shown in Figure 6.7.

However, it should be pointed out that larger groove depth will cause narrower impedance bandwidth since larger abrupt change in the waveguide structure is introduced, which implies that there will be a trade-off between impedance bandwidth and 3-dB AR bandwidth.

The analysis in this section reveals that grooved-wall circular waveguide with mixed cross-section radii and large groove heights should be designed to achieve better overall bandwidth within a reasonable waveguide length, which proves the feasibility to design a wideband multi-section grooved-wall CP horn with waveguide flaring.

6.4 Multi-section Grooved-wall CP Horn Design

6.4.1 Geometry Design

The geometry of a grooved-wall CP horn with three linearly flared sections is presented in Figure 6.9. The number of sections could be larger, and the profile of the horn could even follow an arbitrary spline. This multi-section grooved-wall horn can be considered as a concatenation of discrete grooved-wall circular waveguides with variable cross-section dimensions and small discretization step. According to the previous section, a CP wave can be achieved at the aperture of this horn with well optimized dimensions.

In the design of the N-section grooved-wall CP horn, dimensions of the $N+1$ cross-sections $(S_0, ..., S_N)$ will be decided in the first place; then all cross-sections will be connected sequentially with linear transition. The design methodology of the N-section grooved-wall CP horn is illustrated as follows. In our case, N is 3, as shown in Figure 6.9.

1. Several pre-defined design parameters listed in Table 6-A should be set according to the dimension requirement of the horn, which describes the searching space for the optimization of horn geometry. In addition, R_i^{min} should be set considering the cut-off frequency of the TE_{11} mode in the circular waveguide, and R_o^{max} can

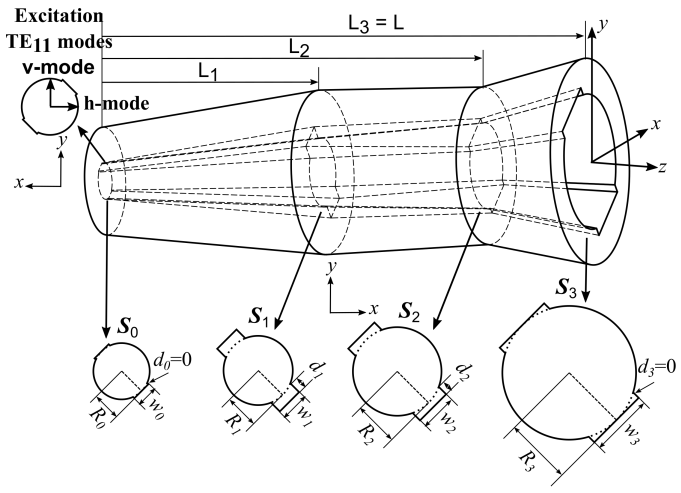

Figure 6.9: Geometry of the multi-section grooved-wall CP horn.

be selected with the consideration of antenna gain. The values of these parameters in our design are also given in Table 6-A.

2. Determine the radius of the input circular waveguide R_i, according to

$$R_i = (R_i^{max} - R_i^{min}) \cdot r_i + R_i^{min} \qquad (0 \le r_i \le 1) \tag{6.7}$$

3. Determine the radius of the horn aperture R_o as

$$R_o = (R_o^{max} - R_i) \cdot r_o + R_i \qquad (0 \le r_o \le 1) \tag{6.8}$$

4. Determine the length of the horn as

$$L = (L_{max} - L_{min}) \cdot l + L_{min} \qquad (0 \le l \le 1) \tag{6.9}$$

5. Determine the length of each section. Let L_n represents the distance between cross-section S_n and S_0, and $L_N = L$, as shown in Figure 6.9. L_n is written as

$$L_n = L_{n+1} \cdot l_n \qquad (0 \le l_n \le 1,\ n = N-1, ..., 1) \tag{6.10}$$

6. Determine the radius of each cross-section. Let R_n denotes the radius of each cross-section as shown in Figure 6.9, and $R_0 = R_i$, $R_N = R_o$. R_n is given by

$$R_n = (R_{n+1} - R_i) \cdot r_n + R_i \qquad (0 \leq r_n \leq 1,\ n = N-1, ..., 1) \tag{6.11}$$

7. Determine the groove depth of each cross-section. In our design, the groove depth of the first cross-section is set to 0 in order to minimize the discontinuity between it and the input circular waveguide or the square-to-circular waveguide transformer. The groove depth of the last cross-section is also set to 0 so that the aperture will be close to a circle where the amplitudes of the two orthogonal TE_{11} modes will be more balanced, as shown in Section 5.3.3. The groove depth of cross-sections is given by

$$dw_n = \begin{cases} R_n \cdot dw\_ratio_n & \text{if } n = 1, ..., N-1, \\ 0 & \text{if } n = 0, N. \end{cases} \tag{6.12}$$

   where $0 \leq dw\_ratio_n \leq 1$.

8. Determine the groove height of each cross-section. The groove height of each cross-section is designed to be no larger than that of its following cross-section. We find this constraint will lead to better reflection coefficients, thereby allowing the optimization to converge faster. For this reason, the groove height of each cross-section can be written as

$$h_n = \begin{cases} min(h_{min} + R_n \cdot h\_ratio_n,\ h_{n+1}) & \text{if } n = N-1, ..., 0, \\ h_{min} + R_n \cdot h\_ratio_n & \text{if } n = N. \end{cases} \tag{6.13}$$

   where $0 \leq h\_ratio_n \leq 1$. h_{min} is the minimum height, which is used for the ease of fabrication and set to 0.2 mm in our design.

All design parameters that will be optimized are summarized in Table 6-B with their upper and lower boundaries. The initial values of these parameters should be

set as the start point of the optimization, and the optimal values will be determined by the optimization. By following this approach, the geometries generated during the optimization will be physically feasible to fabricate. It is also worth noting that, by using this approach, the values of all geometric variables in optimization will fall into the range between 0 and 1, which is desirable for the optimization algorithm to work effectively.

Table 6-A: Pre-defined design parameters for the multi-secton grooved-wall CP horn.

Parameter	Value	Description
R_i^{min}	1.1	Minimum radius of the input circular waveguide
R_i^{max}	1.6	Maximum radius of the input circular waveguide
R_o^{max}	6.32 ($2\lambda_c$)	Maximum radius of the horn aperture
L_{min}	10	Minimum length of the horn
L_{max}	50	Maximum length of the horn
N	3	Number of sections of the horn

Table 6-B: Optimization parameters for the multi-secton grooved-wall CP horn.

Parameter	Min.	Max.	Description
r_i	0	1	ratio used to determine the radius of the first cross-section (input circular waveguide).
r_o	0	1	ratio used to determine the horn aperture.
l	0	1	ratio used to determine the length of the horn.
l_n	0	1	ratio used to determine the length of each cross-section. ($n = N-1, \ldots, 1$)
r_n	0	1	ratio used to determine the radius of each cross-section. ($n = N-1, \ldots, 1$)

6.4.2 Geometry Optimization using CMA-ES

The geometry of the grooved-wall multi-section horn is optimized using the Covariance Matrix Adaptation Evolution Strategy (CMA-ES) algorithm, which is proved to be promising in optimizing complicated EM devices in a self-adaptive way [5], as described in Section 2.3.1. We have developed a Python software to launch and control CST Microwave Studio full-wave simulations and analyze the result data exported from CST simulation automatically. A Python implementation of CMA-ES [6] is integrated into this software, so that the complete software is able to perform automatic CMA-ES opti-

mization with full-wave simulations. Each set of geometric parameters generated by CMA-ES will be used to update the model of the grooved-wall multi-section horn in CST Microwave Studio before each simulation, and the reflection coefficient and radiation patterns over the operating bandwidth will be evaluated by the full-wave simulation. A cost function described below will then be calculated based on the exported simulation results, and CMA-ES will try to minimize the value of the cost function to find the optimal design after a sufficient number of iterations.

Since we aim to achieve low reflection coefficients, AR $<$ 3 dB as well as good radiation patterns with rotational symmetry and a low side-lobe level (SLL) over the entire operating bandwidth, a cost function is defined including multiple objectives. The overall cost function is written as

$$F = R_{vv} + R_{hv} + w_P P + w_S S + A \tag{6.14}$$

where R_{vv} is the objective function for evaluating the reflection in v-mode when input port is excited by v-mode which will affect the reflection coefficient of the complete dual-CP antenna, and R_{hv} is the objective function for evaluating the reflection in h-mode when input port is excited by v-mode which will affect the isolation of the complete dual-CP antenna. The v and h-mode are shown in Figure 6.9. P is the objective function for evaluating rotational symmetry of the radiation pattern, S is the objective function for evaluating SLL. w_P and w_S are the weighting factor for P and S, respectively. A is the objective function for evaluating AR.

The objective function for both R_{vv} and R_{hv} is written as

$$R_i = w_{R_{mae}} R^i_{mae} + w_{R_{max}} R^i_{max}, \quad i \in \{vv, hv\} \tag{6.15}$$

where $w_{R_{mae}}$ and $w_{R_{max}}$ are the weighting factors, while R^i_{mae} and R^i_{max} are used to evaluate how close the reflection coefficient is to the target level in terms of average level and the maximum level respectively, as expressed below. "mae" here is the abbreviation

for mean absolute error.

$$R^i_{mae} = \frac{\sum_{n=1}^{N} max(r^i(f_n) - r_{target},\ 0)/N}{\alpha|r_{target}|} \tag{6.16a}$$

$$R^i_{max} = \frac{max(r^i_{max} - r_{target},\ 0)}{\alpha|r_{target}|} \tag{6.16b}$$

where f_n is a frequency sample of N samples over the entire operating bandwidth, $r^i(f_n)$ and r_{target} are the reflection coefficient at f_n and the target reflection coefficient in dB , respectively. $r^i_{max} = max\{r^i(f_n) \mid 1 \leq n \leq N\}$ is the maximum reflection coefficient over the entire operating bandwidth. Additionally, a scale factor of $\alpha|r_{target}|$ is used to scale the mean absolute difference between the simulated result of the current model and the target reflection coefficient, so that the value of the objective function represents the relative difference rather than absolute difference. A weighting factor α is used to adjust the scale factor in an effort to keep the value of this objective function at the same level as those of other objective functions.

The objective function for evaluating the rotational symmetry of the radiation pattern P is expressed as

$$P = \frac{\sum_{m=1}^{M} P(f_m)}{M} \tag{6.17}$$

where f_m is a frequency sample for farfield calculation, and farfield will be calculated at M frequency samples across the entire operating bandwidth. In our case, $f_m = (80 + 10m)\ GHz,\ m = 0, ..., 3$. $P(f_m)$ in equation (6.17) is the objective function at a given frequency, which is given by

$$P(f_m) = \sum_{c \in C} P^c(f_m), \qquad C = \{0, 45, 90\} \tag{6.18}$$

where $P^c(f_m)$ is calculated using the normalized radiation pattern in c-degree plane at

frequency f_m, which is defined as

$$P^c(fm) = \frac{\sum_{j=1}^{J} \beta(\theta_j)(p^c_{fm}(\theta_j) - \overline{p}_{fm}(\theta_j))^2}{J}, \qquad -\theta_{taper} \le \theta_j \le \theta_{taper} \tag{6.19}$$

where $p^c_{f_m}(\theta_j)$ is the power level in dB at a given azimuth angle sample θ_j in the c-degree plane of the normalized radiation pattern at frequency f_m. Only the beamwidth within a -12-dB taper ranging from $-\theta_{taper}$ to θ_{taper} is optimized to achieve rotational symmetry because beamwidth within -10 - -12 dB taper is usually used to illuminate the reflector if the horn is used as the primary feed to the reflector antenna. So the taper angle θ_{taper} will be obtained firstly by finding the widest -12-dB taper angle among $0°/45°/90°$ planes of the normalized radiation pattern at each frequency, and then $P^c(f_m)$ will be calculated within the azimuth angle range $-\theta_{taper} \le \theta \le \theta_{taper}$, and the total number of θ samples in this range is denoted as J. In equation (6.19), $\overline{p}_{f_m}(\theta_j)$ is the average power level of all cut planes at θ_j (within -12-dB taper angle) of the normalized radiation pattern at frequency f_m, and β_j is a θ dependent weighting factor, which are written as

$$\overline{p}_{fm}(\theta_j) = \frac{\sum_{c \in C} p^c_{fm}(\theta_j)}{3}, \qquad C = \{0, 45, 90\}, \quad -\theta_{taper} \le \theta_j \le \theta_{taper} \tag{6.20}$$

$$\beta(\theta_j) = 10^{-(|\theta_j|/\theta_{taper})}, \qquad -\theta_{taper} \le \theta_j \le \theta_{taper} \tag{6.21}$$

The objective function for evaluating the SLL of the radiation pattern is

$$S = \frac{\sum_{m=1}^{M} S(f_m)}{M} \tag{6.22}$$

which is calculated using the same farfield radiation patterns at frequency samples described in equation (6.17), and the object function at each frequency sample is defined as

$$S(f_m) = \frac{max(s_{max}(f_m) - s_{target},\ 0)}{\alpha |s_{target}|} \tag{6.23}$$

where $s_{max}(f_m)$ is the highest SLL among 0°/45°/90° planes of the normalized radiation pattern at f_m, and s_{target} is the target SLL. The scale factor of $\alpha|r_{target}|$ is also applied, as explained in equation (6.16).

The objective function for evaluating AR over the operating bandwidth in equation (6.14) is written as

$$A = w_{A_{mae}} \frac{\sum_{m=1}^{M} A_{mae}(f_m)}{M} + w_{A_{max}} \frac{\sum_{m=1}^{M} A_{max}(f_m)}{M} \tag{6.24}$$

where $A_{mae}(f_m)$ and $A_{max}(f_m)$ are used to evaluating the average and maximum AR level over the beamwidth within $[-\theta_{taper},\ \theta_{taper}]$ at a given frequency sample f_m , respectively, which are defined as

$$A_{mae}(f_m) = \frac{\sum_{j=1}^{J} max(a_{f_m}^{max}(\theta_j) - a_{target},\ 0)/N}{a_{target}}, \quad -\theta_{taper} \le \theta_j \le \theta_{taper} \tag{6.25a}$$

$$A_{max}(f_m) = \frac{max(a_{f_m}^{max} - a_{target},\ 0)}{a_{target}} \tag{6.25b}$$

where a_{target} is the target AR, $a_{f_m}^{max}(\theta_j)$ is the largest AR at θ_j among 0°/45°/90° planes of the normalized radiation pattern at frequency f_m, and $a_{f_m}^{max}$ is the maximum AR within the beamwidth between $-\theta_{taper}$ and θ_{taper} among 0°/45°/90° planes of the normalized radiation pattern at frequency f_m, which can be written as

$$a_{f_m}^{max}(\theta_j) = \underset{c \in C}{max}\{a_{f_m}^{c}(\theta_j)\}, \quad C = \{0, 45, 90\} \tag{6.26a}$$

$$a_{f_m}^{max} = \underset{j}{max}\{a_{f_m}^{max}(\theta_j) \mid 1 \le j \le J\} \tag{6.26b}$$

Since it is quite challenging to achieve 5 objectives at the same time owing to the trade-off among these characteristics, the parameters of the optimization cost functions should be set carefully and may need to be tuned according to the initial optimization results. The parameters of the cost functions we used in the optimization are listed in

Table 6-C, and the optimized dimensions are shown in Table 6-D.

Table 6-C: Parameters of the cost functions for the optimization.

Parameters	$w_{R_{mae}}$	$w_{R_{max}}$	$w_{A_{mae}}$	$w_{A_{max}}$	w_P
Values	1	1	1	1	1
Parameters	w_S	r_{target}	s_{target}	a_{target}	α
Values	1	-43 dB	-30 dB	1.5 dB	0.1

Table 6-D: The optimized dimensions of the multi-section grooved-wall horn.

Parameters	L_0	L_1	L_2	L_3
Values (mm)	0	19.775	34.659	44.075
Parameters	$R_0(R_i)$	R_1	R_2	$R_3(R_o)$
Values (mm)	1.531	2.914	3.618	5.688
Parameters	dw_0	dw_1	dw_2	dw_3
Values (mm)	0	1	0	0
Parameters	h_0	h_1	h_2	h_3
Values (mm)	1.07	2.58	3.706	5.715

6.4.3 Simulation results of the optimized multi-section grooved-wall CP horn

The simulated reflection coefficients and the AR of the optimized multi-section grooved-wall CP horn are shown in Figure 6.10, where $|S1(v), 1(v)|$ is the reflection in v-mode (see Figure 6.9) when input port is excited by v-mode and $|S1(h), 1(v)|$ is the reflection in h-mode (see Figure 6.9) when input port is excited by v-mode, as explained in Section 6.4.2. It can be found that $|S1(v), 1(v)| <$ -42 dB and $|S1(h), 1(v)| <$ -35 dB is achieved over the desired operating bandwidth from 80 to 110 GHz. The AR is below 2.6 dB over the same bandwidth.

Figure 6.11 depicts the variation of the phase and magnitude difference between the two orthogonal components of the LHCP wave (generated when the input port is excited by v-mode) with respect to the frequency. The result shows that the magnitudes of the two orthogonal components are very close to each other, and the phase difference is $90° \pm 15°$ within the frequency range of 80 - 110 GHz. The result for RHCP corresponding

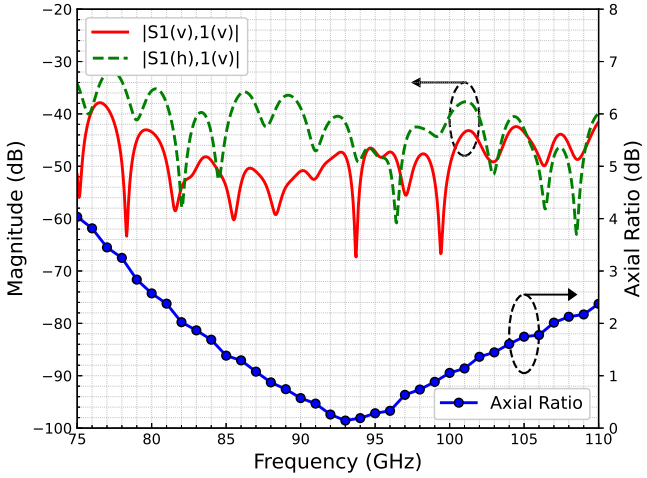

Figure 6.10: Simulated S-parameters and AR of the optimized multi-section grooved-wall CP horn.

to the excitation with h-mode at the input port is the same due to the symmetry of the structure, except that the phase difference has the different sign.

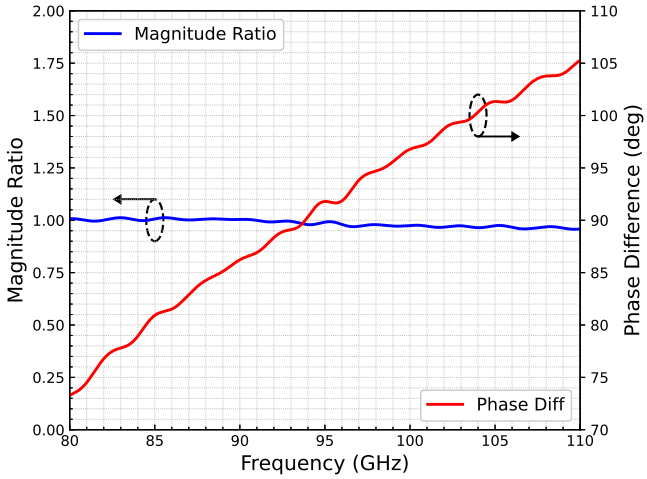

Figure 6.11: Simulated magnitude and phase difference between x and y components of the LHCP wave generated when the input port of the optimized multi-section grooved wall horn is excited by v-mode. Magitude difference is $|E_y|/|E_x|$.

The radiation patterns at 80/95/110 GHz are shown in Figure 6.12. It can be observed that rotational symmetry for radiation patterns is achieved within a 12-dB taper angle at all frequencies. It can also be found that SLLs are all below -30 dB.

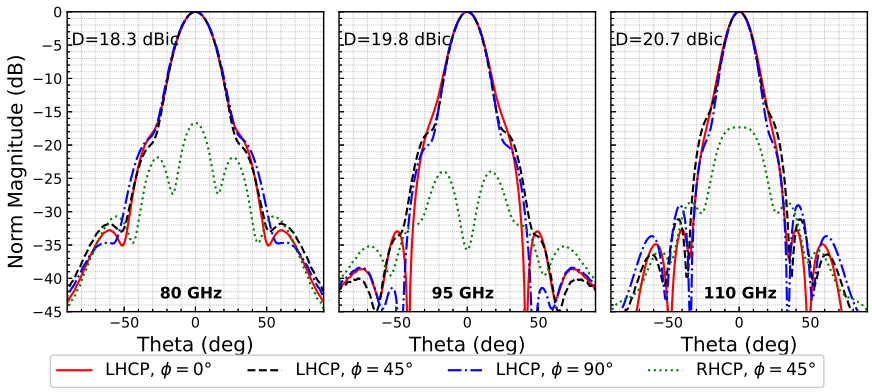

Figure 6.12: Simulated radiation patterns at 80/95/110 GHz of the optimized multi-section grooved wall CP horn

6.5 Orthomode Transducer Design

6.5.1 OMT Type Selection

As described in Section 6.3.1, if the input port of the grooved-wall CP horn is excited by TE_{11} mode which is aligned at $+45°$ or $-45°$ with respect to the grooves, LHCP or RHCP can be generated. Consequently, the grooved-wall CP horn can be connected to an orthomode transducer (OMT) to realize dual-CP.

An OMT is a passive device which is used to combine or separate two orthogonal polarizations within the same frequency range. In general, an OMT consists of one common port and two single-mode ports. Two fundamental modes can propagate in the common port, which act as the two orthogonal polarizations (vertical and horizontal polarizations). Each of the other two ports is coupled to one of the fundamental modes in the common port.

Several types of wideband OMT have been proposed in the mmWave band. Some designs based on the twofold symmetric junction proposed by Bøifot [7], which uses a thin septum and capacitive compensation pins in the waveguide, have been demonstrated in the W-band [8, 9]. Nevertheless, the small dimensions of the septum and pins pose a significant challenge for a reliable and cost-effective fabrication and assembly of this type of OMT.

Another widely investigated type of OMT is based on a turnstile junction. Several prototypes of this OMT have been demonstrated to be able to achieve very good port isolation over a wide bandwidth in the K-band [10], 31-45 GHz band [11], and the W-band [12]. Although neither the pins nor the septum is required in this type of OMT, a metallic stub located at the centre of the turnstile junction is needed as a matching element, and this device will have to be split into 3 or 4 blocks in fabrication, which means it is susceptible to misalignment errors.

A full-waveguide OMT using symmetric dual-side backward coupler is proposed in the W-band with wide operating bandwidth [13]. Although this is a full-waveguide design without using any critical elements inside the waveguide, such as septum, cylinders or pyramids in aforementioned types, one of its output needs to be perpendicular to the waveguide split plane, which is still complicated for fabrication.

Besides those OMTs which employ symmetric structures, asymmetric full-waveguide OMTs with more compact size are also proposed for the ease of fabrication, which can also achieve proper operating bandwidth with good matching isolation level. In [4] a simple asymmetric OMT is proposed and demonstrated in the W-band, which uses T-shaped waveguide junction with mitred bend to split two polarizations. This design has also been scaled up to over 600 GHz, demonstrated to be able to achieve proper performance with conventional CNC milling even at such high frequencies [14, 15].

In order to demonstrate that the wideband dual-CP antenna with high isolation can be realized by using grooved-wall CP horn with low reflection we designed in this chapter, a wideband OMT with high isolation is required as explained in Section 6.3.1. Although the symmetric OMTs such as [11] and [13] could be a better choice as they offer wider bandwidth and better matching and isolation level, their structures are complicated for fabrication, which also limits their capability to scale up to even higher frequencies. Since we aim to demonstrate the dual-CP capability of our grooved-wall CP horn in a cost-effective way and show its potential to be scaled up to higher frequencies, the asymmetric OMT in [4] was chosen.

6.5.2 OMT Design

The geometry of the OMT we used in this paper is shown in Figure 6.13. The vertical polarization in the common port (port 3) is guided to the v-port (port 1) which is in line with the common port, while the horizontal polarization is extracted to the h-port (port 2) by using a T-shaped waveguide. This design is based on the designs presented in [4, 14], but with a critical modification that can resolve a major issue of this type of OMT.

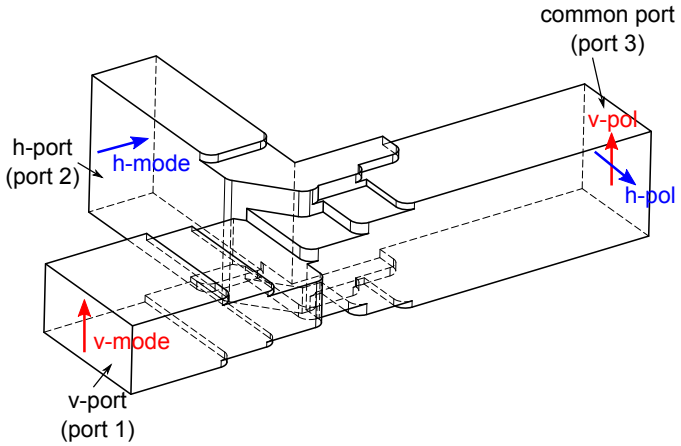

Figure 6.13: Schematic of the asymmetric OMT used in this paper.

In [4] and [14], the OMTs are split horizontally into two block halves in the middle of the common port in fabrication, as shown in Figure 6.14(a). However, it is noted in [4, 14] that the polarization isolation is very sensitive to the misalignment between the upper and lower block halves, and the reason is explained in [4]. According to the analysis in [4], the polarization isolation will deteriorate to 22 dB when the misalignment is $7\mu m$ in W-band.

In order to avoid degradation of the cross-polarization level caused by this misalignment error and achieve high polarization and port isolation without the stringent requirement of misalignment error for assembling, we modified the OMT design in [4] so that the stepped waveguide transformer to the v-port is aligned with the T-junction waveguide on the side of the h-port arm, which is illustrated in Figure 6.14(b). This modification allows the OMT to be split on the aligned side of the axial part of the OMT, which pre-

vents the cross-section of the axial waveguide to the common port from being changed if there is a misalignment between two splitting blocks during assembling, as shown in Figure 6.14(b).

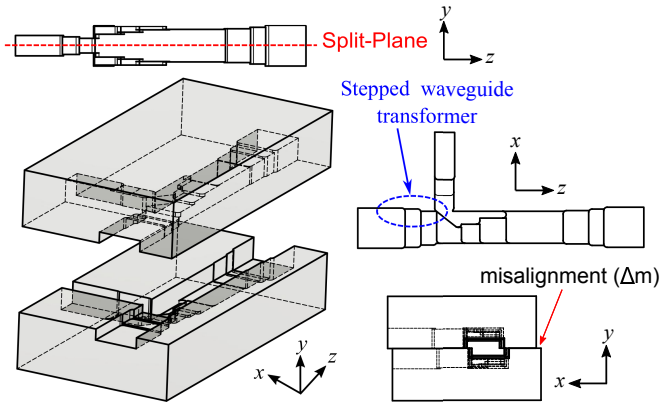

(a) Horizontal-split blocks in [4].

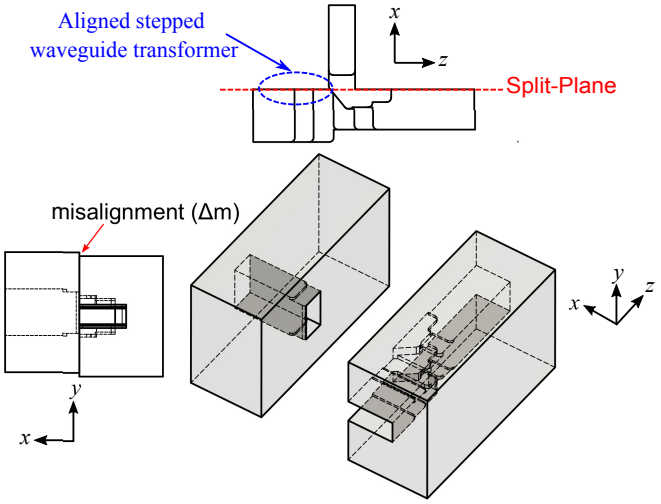

(b) Vertical-split blocks propsed in this paper.

Figure 6.14: OMT split-block design (a) in [4] and (b) proposed in this paper.

The OMT design is optimized using CST Microwave Studio to cover the frequency range from 80 - 110 GHz with expected polarization and port isolation larger than 50 dB. The number of waveguide steps is also reduced for the ease of fabrication in comparison with that in [4] while still maintaining a reflection coefficient lower than -20 dB. The optimized dimensions of the OMT are presented in Figure 6.15.

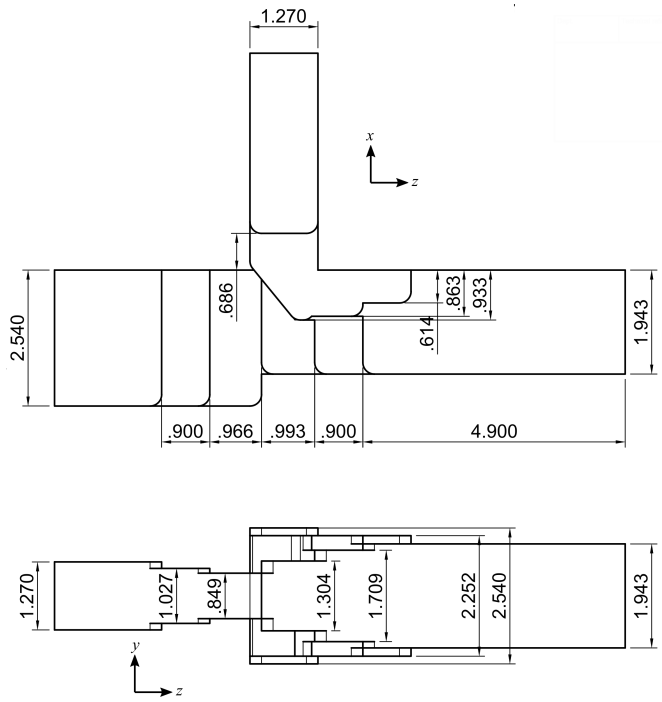

Figure 6.15: Dimensions of the optimized OMT.

6.5.3 OMT Simulation Results

The full-wave simulation of the proposed OMT is carried out using CST Microwave Studio. The reflection coefficients, port isolations and polarization isolations of the proposed OMT are shown in Figure 6.16 to Figure 6.18. The impact on these characteristics caused by the misalignment shown in Figure 6.14(b) is also presented. In order to demonstrate the improvement for misalignment tolerance resulted from the modification we introduced in this paper, horizontal split-block design in [4] (see Figure 6.14(a)) is also applied to this OMT, and the results are compared with those when vertical split-block design we proposed is applied.

It can be observed from Figure 6.16 that the reflection coefficients for both port 1 and 2 are below 20 dB, and there is no noticeable impact on the reflection coefficients for both port 1 and port 2 if the misalignment is within 40 μm when the splitting approach we proposed is applied. On the other hand, the reflection coefficient at two ends of the operating bandwidth deteriorates when horizontal splitting is applied, and

the misalignment reaches 40 μm.

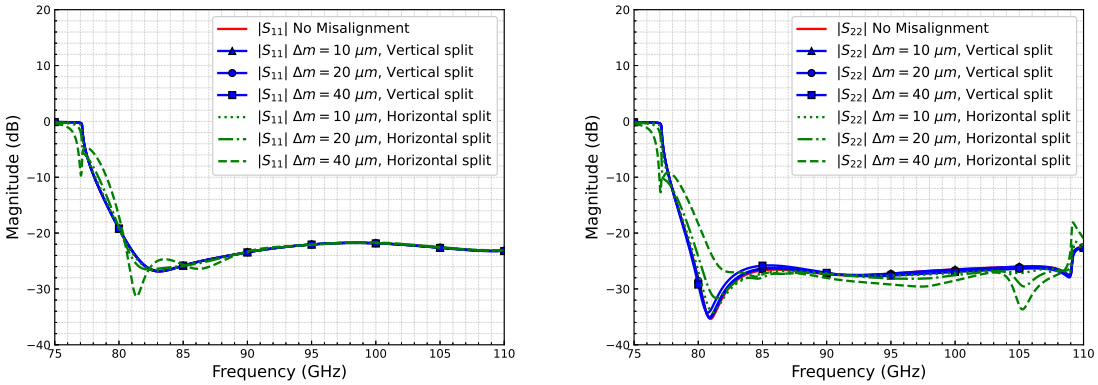

(a) (b)

Figure 6.16: Reflection coefficients for (a) port 1 and (b) port 2.

In Figure 6.17, it can be seen that the port isolation is lower than 60 dB for both port 1 and port 2, and will decrease as the misalignment between two vertical-split blocks increases, but can still be kept higher than 40 dB from 80 GHz to 110 GHz if the misalignment is smaller than 40 μm. However, when the misalignment increases to 40 μm, the port isolation level will decrease to 25 dB at 80 GHz if the proposed OMT is horizontally split into two block halves.

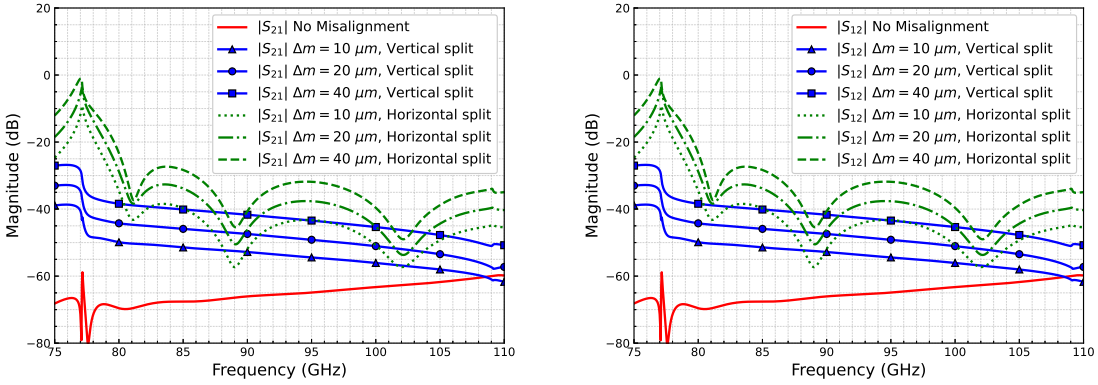

(a) (b)

Figure 6.17: Port isolation when (a) port 1 is excited and when (a) port 2 is excited.

Figure 6.18 depicts the polarization isolation level for vertical and horizontal polarization, where $|S3(h), 1(v)|$ denotes the cross-polarization (horizontal polarization) level

at port 3 when port 1 is excited, and $|S3(v), 1(h)|$ denotes the cross-polarization (vertical polarization) level at port 3 when port 2 is excited. It can be found that the polarization isolation > 50 dB is achieved. Significant degradation of polarization can be observed if the OMT is horizontally split, the polarization isolation decreases to 20 dB at the lower end of the expected operating bandwidth even with only 10 μm misalignment, which is also consistent with the analysis result presented in [4]. By contrast, the polarization isolation can still be kept above 35 dB even if the misalignment increases up to 40 μm when the OMT is vertically split as we proposed.

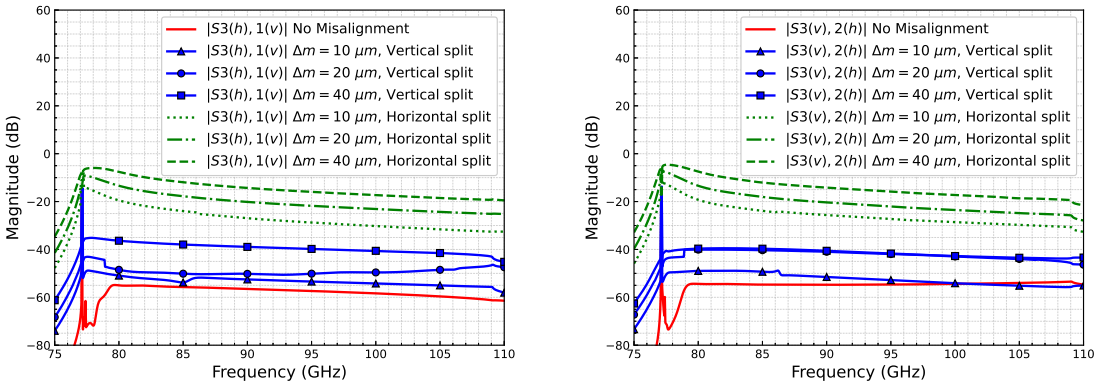

(a) (b)

Figure 6.18: Polarization isolation for (a) vertical polarization (when port 1 is excited) and (b) horizontal polarization (when port 2 is excited).

In conclusion, the simulated results show that, by using our design, a significant improvement in port isolation and polarization isolation can be achieved when there is a misalignment between 2 split blocks during assembling.

6.6 Full-Wave Simulation and Fabrication Considerations of the Complete Dual-CP Antenna

Full-wave simulation of the complete dual-CP antenna shown in Figure 6.2 is performed using CST Microwave Studio taking the possible misalignment errors during assembling into account.

The OMT is split into two blocks, as illustrated in Figure 6.14(b). The multi-section grooved-wall horn and the square-to-circular waveguide transformer are fabricated as one piece rather than two split-block halves. Fabricating as two split-block halves will be more cost-effective, but the misalignment of two halves during assembling will significantly affect the AR as discussed in [16]. The horn with the square-to-circular waveguide transformer is then assembled with the OMT via UG387 flanges, as shown in Figure 6.19. Both components are fabricated using Electrical Discharge Machining (EDM).

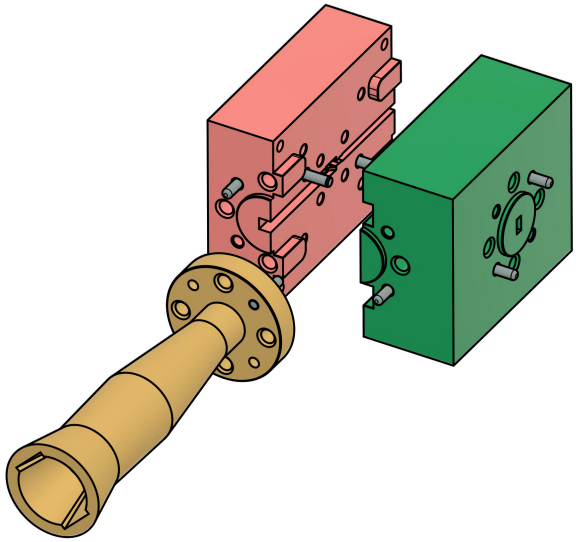

Figure 6.19: Mechanical design and assembly of the dual-CP antenna.

A misalignment error between the two blocks of the OMT (Δm) shown in Figure 6.14(b) is deliberately introduced in the simulation of the complete dual-CP antenna. The results in Figure 6.20 show that the reflection coefficients lower than -18 dB and the port isolation higher than 34 dB for port 1 (v-port) and port 2 (h-port) can be achieved over the frequency range from 80 GHz to 110 GHz, while the ARs of LHCP and RHCP are lower than 2.6 dB over the same frequency range. It can also be found that the performance will not be affected too much when Δm is within 40 μm.

Figure 6.21 shows the simulation results of the complete dual-CP antenna when a flange misalignment between the horn and the OMT is introduced in the simulation. It

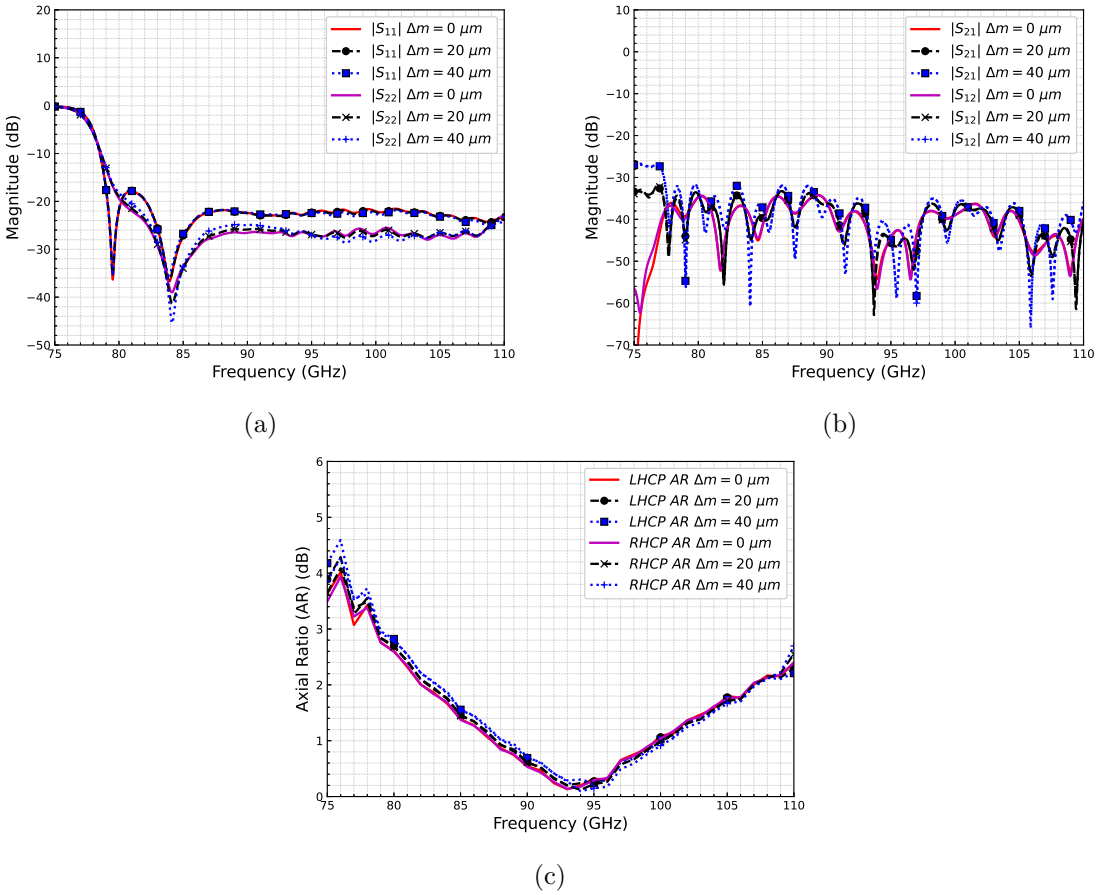

Figure 6.20: Simulated (a) reflection coefficient, (b) port isolation and (c) AR of the complete dual-CP antenna with a misalignment error between the two blocks of the OMT.

can be found in Figure 6.21(a) that the misalignment will cause more fluctuation to the reflection coefficients, and the reflection coefficients of two ports can go up to -12 dB when the misalignment reaches 150 μm. The result in Figure 6.21(b) shows that the impact of misalignment on port isolation. It can be observed that the port isolation degrades as the misalignment increases, especially at the higher end of the frequency band. The port isolation is still acceptable when the misalignment is smaller the 75 μm since it is still higher than 30 dB in most of the desired operating bandwidth. However, the port isolation at will degrade to be higher than 30 dB in the frequency range higher than 105 GHz if the misalignment increases to 150 μm. According to Figure 6.21(c), the flange misalignment will reduce the 3-dB AR bandwidth, but the AR can still be

kept below 3-dB even when the flange misalignment increases to 150 μm. Overall, it can be found that the flange misalignment has little impact on the performance if it can be kept below 75 μm. However, the operating bandwidth with port isolation higher than 30 dB will be reduced because of the degradation of the port isolation when the flange misalignment increases to 150 μm.

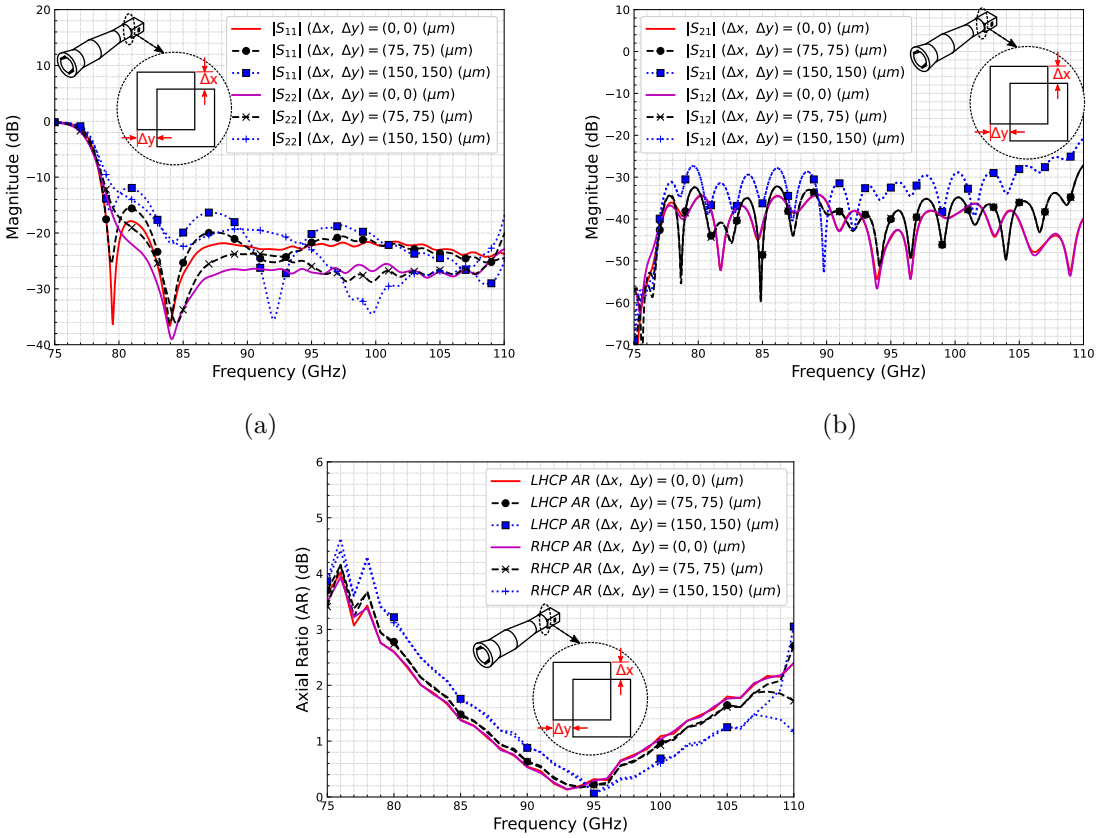

Figure 6.21: Simulated (a) reflection coefficient, (b) port isolation and (c) AR of the complete dual-CP antenna with a flange misalignment between the horn and the OMT.

The simulation result of the complete dual-CP antenna when there is a rotating misalignment between the flanges of the horn and the OMT is shown in Figure 6.22, i.e., when the grooves are not aligned at 45° with respect to the vertical and horizontal polarization in the common port of the OMT. It can be seen in Figure 6.22(a) and Figure 6.22(b) that there is little impact on the reflection coefficient and isolation if

the rotating misalignment is within 6°. However, it can be observed in Figure 6.22(c) that the AR degrades and the 3-dB AR bandwidth becomes narrower as the rotating misalignment increases. According to the simulation result in Figure 6.22(c) the 3-dB AR bandwidth will not be able to cover the frequency range from 80 - 110 GHz if the rotating misalignment is larger than 6°.

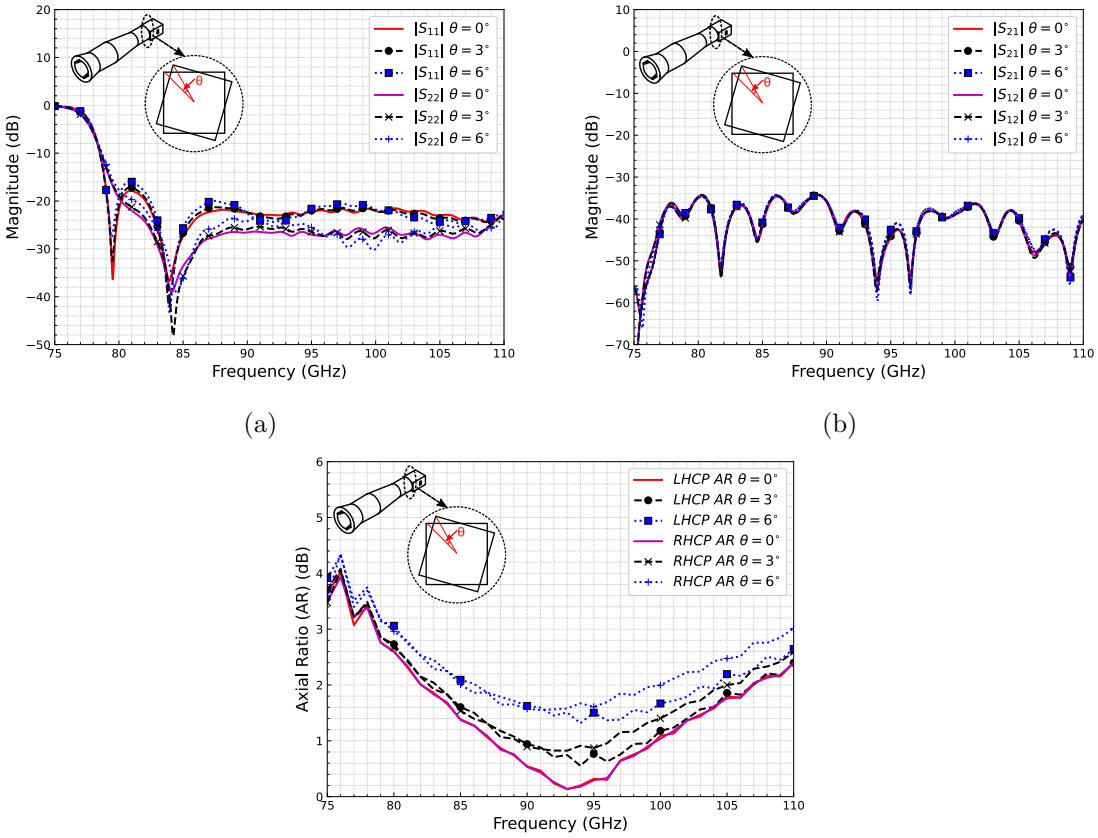

Figure 6.22: Simulated (a) reflection coefficient, (b) port isolation and (c) AR of the complete dual-CP antenna with rotating misalignment between the flanges of the horn and the OMT.

6.7 Measurement and Discussion

6.7.1 Simulated and Measured Results

A prototype of the proposed dual-CP antenna working in the W-band is fabricated, and a photograph of the prototype is shown in Figure 6.23. The multi-section grooved-wall

horn is fabricated as one piece using spark erosion, and the two splitting blocks of the OMT is fabricated using spark erosion and CNC milling.

Figure 6.23: Photograph of the prototype of the proposed dual-CP antenna.

The scattering parameters measurement of the dual-CP antenna are performed using a Keysight PNA-X network analyzer with two OML WR-10 extension heads, as shown in Figure 6.24. The measured and simulated reflection coefficients and port isolation of the dual-CP antenna are shown in Figure 6.25. It can be found from Figure 6.25(a) that the reflection coefficients of both port 1 and port 2 are below -20 dB over most of the frequency range from 80 GHz to 110 GHz, they only deteriorate to -16 dB around 82.5 GHz, and the measured results are close to the simulated ones. According to Figure 6.25(b), measured $|S_{21}|$ and $|S_{12}|$ are both lower than -32.5 dB over the frequency range from 80 GHz to 110 GHz, which agrees well with the simulated results. Therefore, port isolation higher than 32.5 dB is achieved over a bandwidth of 31.6%.

The radiation characteristics are measured using a mmWave Compact Antenna Test Range (CATR) in the Antenna Lab at Queen Mary University of London. The photograph of the CATR measurement setup for the proposed dual-CP antenna is shown in

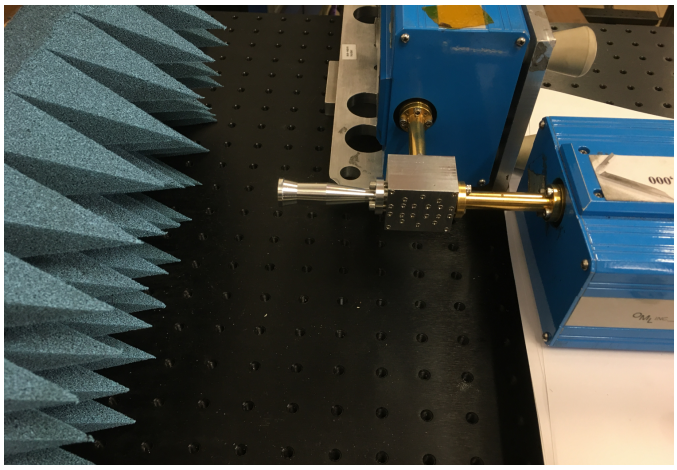

Figure 6.24: Photograph of S-parameter measurement setup.

Figure 6.26. The radiation pattern and axial ratio measurement follows the CP measurement method described in Section 2.4. In this measurement, the rotation angle of the reference antenna is set from 0° to 150° with a step of 30° to measure each polarization component at these angles, which is proved to be sufficient to find the major and minor axes of the polarization ellipse of this antenna.

The normalized measured polarization patterns [17] of the proposed dual-CP antenna at several frequencies across the expected operating bandwidth from 80 GHz to 110 GHz are illustrated in Figure 6.27, which reveals the CP characteristics of the proposed dual-CP antenna. The coordinate system in Figure 6.27 follows that in Figure 6.2. As can be seen from the figure, the polarization patterns at the middle frequencies are closer to circles than those at the edge frequencies, which implies good AR is achieved in the middle of the expected working bandwidth, and AR deteriorates at the two ends of the expected working bandwidth. It can also be observed that the major axes of the polarization ellipses deviate from $x-$ and $y-$axis (0° and 90°), which means the phase difference shifts away from 90° when the frequency goes towards the low and high ends of the operating bandwidth and is consistent with the simulated result shown in Figure 6.11.

Figure 6.28 depicts the measured AR derived from the aforementioned measuring

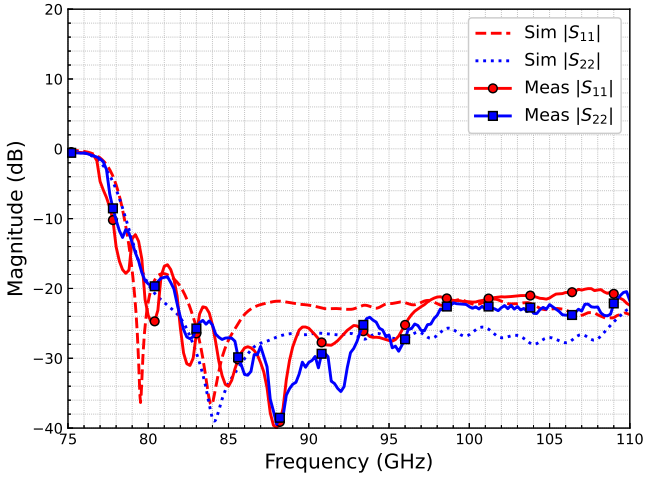

(a)

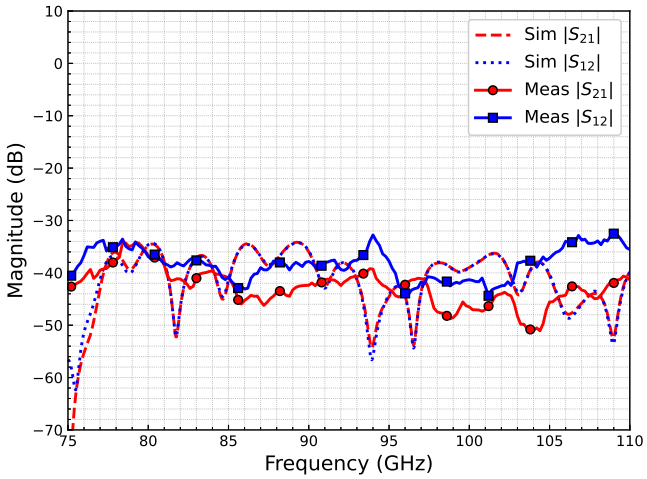

(b)

Figure 6.25: Measured and simulated (a) Reflection coefficient and (b) Isolation of the proposed dual-CP antenna.

approach and the polarization patterns. The result shows that the measured AR of both LHCP and RHCP are below 2.8 dB from 80 GHz to 110 GHz. It can also be observed that the measured AR slightly shifts left from the simulated AR. This small discrepancy is probably due to the fabrication error of groove dimensions which will cause the phase difference between the two orthogonal components of the generated CP wave to deviate from that in design.

Taking the impedance and AR performance into account, the overall operating band-

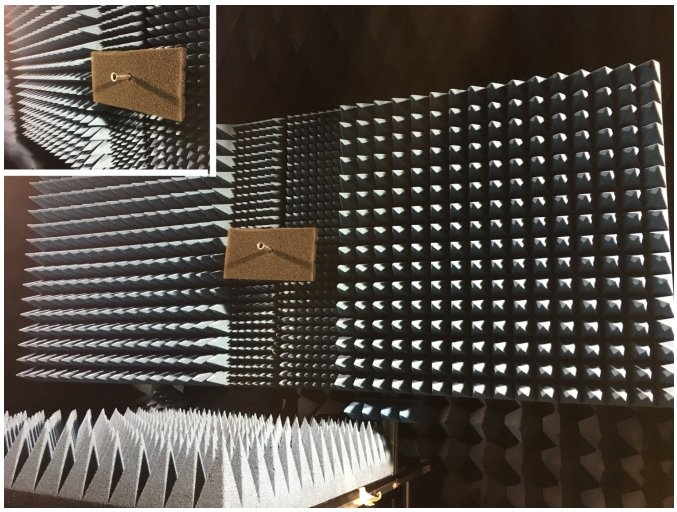

Figure 6.26: Photograph of CATR measurement setup.

width of 31.6% (80 - 110 GHz) is achieved for the proposed dual-CP antenna with port isolation > 32.5 dB and AR < 2.8 dB. In fact, the overall operating bandwidth is limited by the reflection coefficient of the OMT.

The normalized measured and simulated radiation patterns of LHCP and RHCP within $\pm 60^{\circ}$ in the $yz-$ and $xz-$plane (see Figure 6.2) at 80 GHz, 95 GHz and 110 GHz are presented in Figure 6.29 and Figure 6.30. AR with respect to θ is also shown in the figures. The measured radiation patterns agree well with the simulated ones. It can be found that a good rotational symmetry is achieved for the main lobes at all frequencies, allowing this dual-CP antenna to be used as a feed to a reflector antennas if higher gain is required. Sidelobe level (SLL) lower than -30 dB is also observed.

Figure 6.31(a) and Figure 6.31(b) show the measured gain and simulated directivity of co-polar and cross-polar at boresight over the entire operating bandwidth for LHCP (port 1 excitation) and RHCP (port 2 excitation), respectively. The result shows that the co-polar gain of LHCP is from 17.6 dBic to 21.6 dBic, and the co-polar gain of RHCP is from 17.9 dBic to 21.6 dBic. It can also be derived from the figure that the best cross-polarization discrimination (XPD) is around 34 dB, while the worst case is about 17 dB for RHCP within the operating bandwidth. All the results agree well with

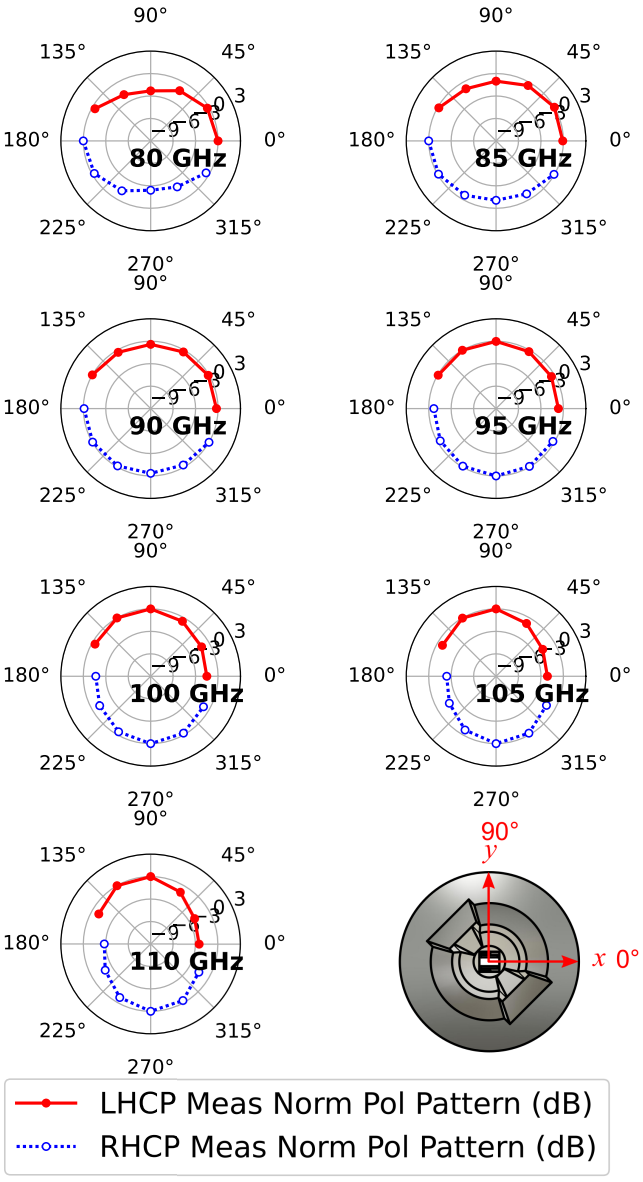

Figure 6.27: Measured polarization patterns of the proposed dual-CP antenna at several frequencies within the frequency range from 80 to 110 GHz.

the simulated ones.

6.7.2 Comparison and Discussion

The performance of other reported dual-CP antennas based on waveguide structures are summarized in Table 6-E in comparison with the results of the dual-CP antenna

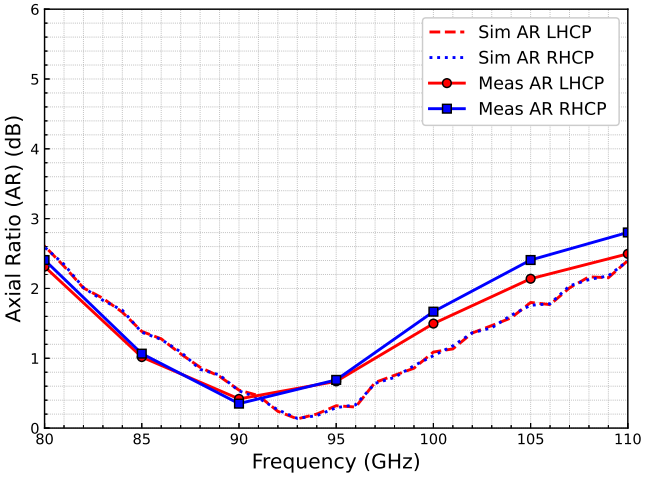

Figure 6.28: Measured and simulated AR of the proposed dual-CP antenna over the frequency range from 80 to 110 GHz.

proposed in this work. The overall bandwidth in the table describes the overlapped bandwidth for the impedance and AR. It can be found that our design shows the highest isolation over the widest bandwidth among all dual-CP antennas ever reported both in microwave and mmWave band. In comparison with the design presented in [3] consisting of a mono-groove polarizer and a horn, our design shows significantly higher isolation over a wider bandwidth with lower reflection coefficient and similar AR, as well as higher gain. When compared with the designs based on the septum polarizer and horn, our design with a septum-free structure not only has higher isolation over wider bandwidth, but also can be scaled up to THz band. Furthermore, this new type of dual-CP antenna still has a great potential for better performance if more sections are introduced to form a more complex profile, because it can inherit the superior radiation performance like rotationally symmetric radiation patterns and low SLL from well-investigated profiled smooth-wall horn.

6.8 Summary

In this chapter, a new type of dual-CP antenna is presented, which is based on a multiple-section grooved-wall CP antenna we proposed and an OMT. The multiple-

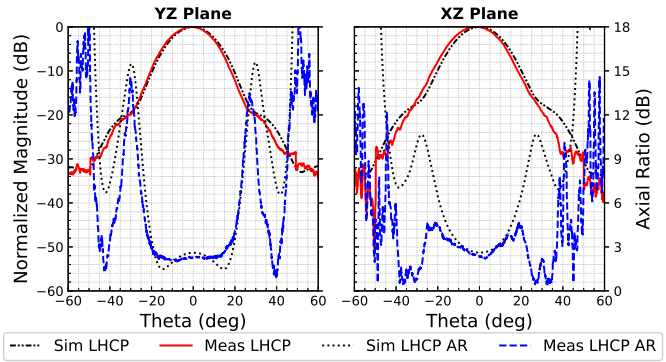

(a)

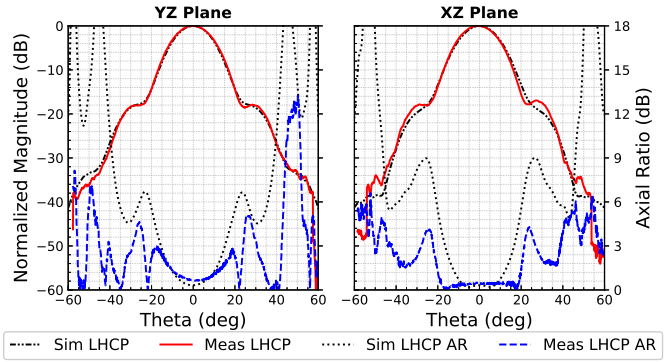

(b)

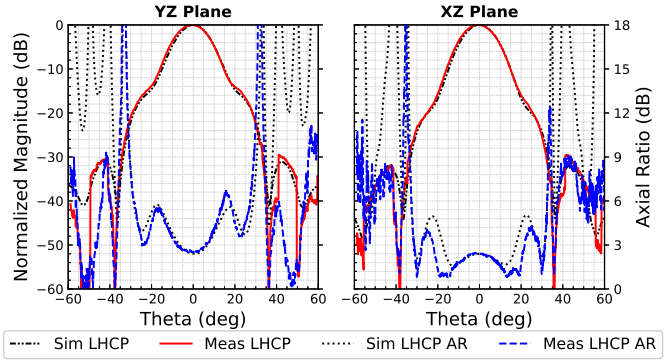

(c)

Figure 6.29: Normalized measured and simulated LHCP (port 1 excited) radiation patterns of the proposed dual-CP antenna at (a) 80 GHz, (b) 95 GHz and (c) 110 GHz.

section grooved-wall CP antenna consisting of multiple conical sections has a pair of grooves with variable depth and height on the walls of each section, which serves as an inbuilt polarizer to generate CP. This CP antenna is demonstrated to be able to generate dual-CP with an OMT. The operating principle and design method of the dual-CP

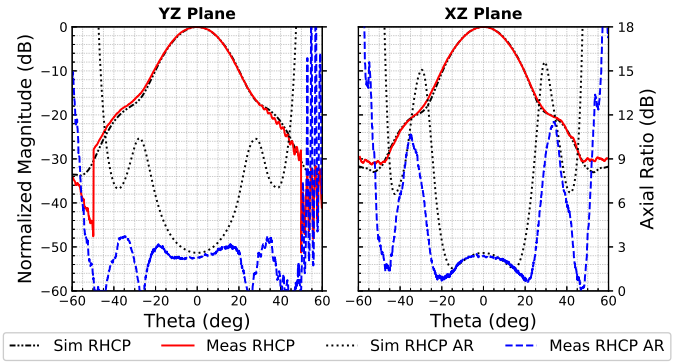

(a)

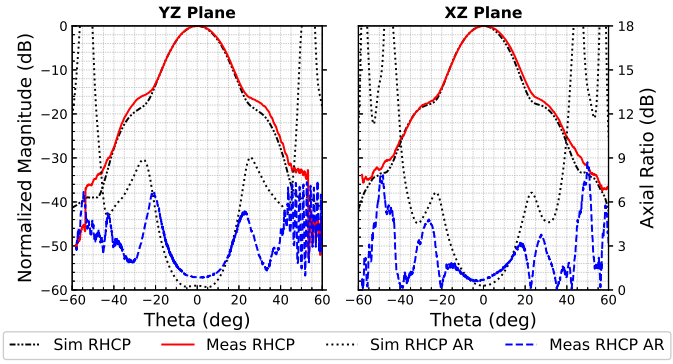

(b)

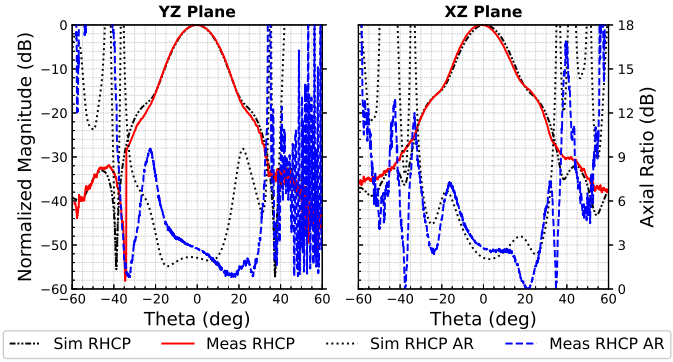

(c)

Figure 6.30: Normalized measured and simulated RHCP (port 2 excited) radiation patterns of the proposed dual-CP antenna at (a) 80 GHz, (b) 95 GHz and (c) 110 GHz.

antenna are illustrated. A prototype of the proposed dual-CP antenna working in the W-band is fabricated and verified by experimental measurement. The measured results show that a 31.6% bandwidth ranging from 80 to 110 GHz is achieved with reflection coefficient $<$ -20 dB and port isolation $>$ 32.5 dB as well as AR $<$ 2.8 dB for both

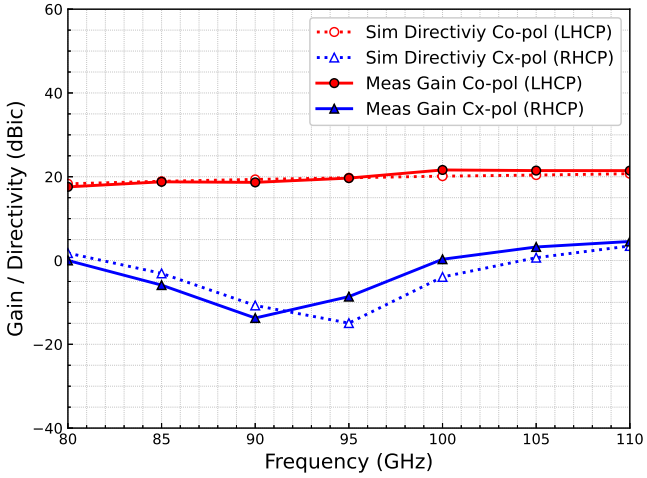

(a)

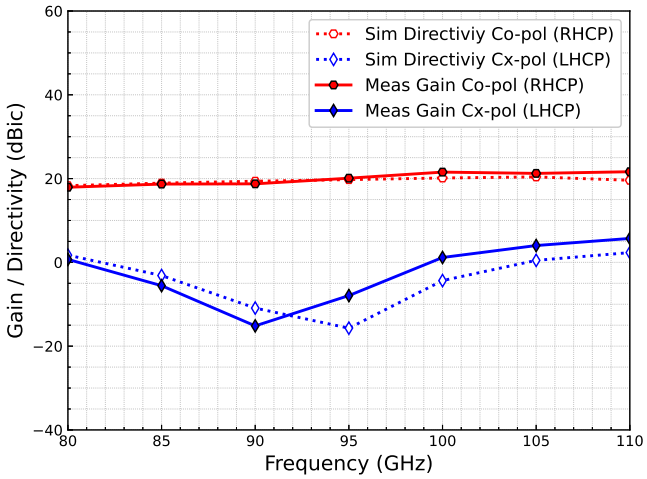

(b)

Figure 6.31: Measured gain and simulated directivity of of co-polar and cross-polar at boresight over the entire operating bandwidth for (a) LHCP (port 1 excitation) and (b) RHCP (port 2 excitation).

LHCP and RHCP. A high gain of 19.6 ± 2 dBic is realized for both LHCP and RHCP over the entire operating bandwidth. Rotationally symmetric radiation patterns are also observed with the SLL lower than -30 dB. To the best of authors' knowledge, this is the dual-CP antenna with the highest isolation over widest bandwidth ever reported among all dual-CP antennas. Furthermore, with a septum-free structure, this type of dual-CP antenna has the potential to be scaled up to even THz band.

Table 6-E: Comparison with other dual-CP antennas based on waveguide structures.

Ref	Frequency (GHz)	Type	Reflection Coefficient (dB)	Isolation (dB)	AR (dB)	Overall Band-width	Max Gain (dBic)	Year
[18]	1.27 - 1.32	Waveguide septum polarizer + Horn	<-25	>30	<1*	3.9%	-	2011
[19]	1.57542	Waveguide septum polarizer + Horn	<-29.3	>23	<0.023	1.0%	16.2	2016
[20]	8 - 8.5	Waveguide septum polarizer array	<-15	>20	<0.7	13.0%	8	2009
[21]	28.5 - 31.2	Waveguide septum polarizer + Horn	<-25	>27	<0.7	9.0%	-	2018
[22]	27.6 - 32.4	Waveguide array + Septum polarizer	<-10	>13	<3	16.0%	32.8	2017
[3]	53.71 - 58.1	Horn + Mono-Groove Polarizer	<-10	>15*	<2.2	7.9%	12	2020
[23]	213 - 237	Waveguide septum polarizer + Horn	<-21	>30	<1.5	10.0%	22**	2013
This work	80 - 110	Multi-section grooved-wall CP horn + OMT	<-20	>32.5	<2.8	31.6%	21.6	2020

* Simulated results.
** Simulated results of the linearly-polarized horn.

References

[1] C. Shu, S. Hu, Y. Yao, and X. Chen, "A W-band Compact Circularly Polarized Horn Antenna," in *2019 12th UK-Europe-China Workshop on Millimetre Waves and Terahertz Technologies (UCMMT)*, 2019.

[2] C. Shu, S. Hu, Y. Yao, Y. Alfadhl, and X. Chen, "W-band grooved-wall circularly polarised horn antenna," *IET Microwaves, Antennas Propagation*, vol. 14, no. 11, pp. 1171–1174, 2020.

[3] N. Luo, X. Yu, G. Mishra, and S. K. Sharma, "A Millimeter-Wave (V-Band) Dual-Circular-Polarized Horn Antenna Based on an Inbuilt Monogroove Polarizer," *IEEE Antennas and Wireless Propagation Letters*, vol. 19, no. 11, pp. 1933–1937, 2020.

[4] A. Dunning, S. Srikanth, and A. R. Kerr, "A simple orthomode transducer for centimeter to submillimeter wavelengths," in *20th International Symposium on Space Terahertz Technology*, Charlottesville, USA, 2009, pp. 191–193.

[5] M. D. Gregory, Z. Bayraktar, and D. H. Werner, "Fast Optimization of Electro-

magnetic Design Problems Using the Covariance Matrix Adaptation Evolutionary Strategy," *IEEE Transactions on Antennas and Propagation*, vol. 59, no. 4, pp. 1275–1285, 2011.

[6] Y. A. Nikolaus Hansen and P. Baudis, "pycma version 2.7.0," 2019. [Online]. Available: https://github.com/CMA-ES/pycma

[7] A. M. Boifot, E. Lier, and T. Schaug-Pettersen, "Simple and broadband orthomode transducer (antenna feed)," *IEE Proceedings H - Microwaves, Antennas and Propagation*, vol. 137, no. 6, pp. 396–400, 1990.

[8] G. Narayanan and N. Erickson, "Full-waveguide band orthomode transducer for the 3 mm and 1 mm bands," in *Proceedings of the 14th International Symposium on Space Terahertz Technology*, 2003, pp. 508–512.

[9] E. J. Wollack and W. Grammer, "Symmetric waveguide orthomode junctions," in *Proceedings of the 14th International Symposium on Space TeraHertz Technology*, 2003, pp. 169–176.

[10] A. Navarrini and R. L. Plambeck, "A turnstile junction waveguide orthomode transducer," *IEEE Transactions on Microwave Theory and Techniques*, vol. 54, no. 1, pp. 272–277, 2006.

[11] D. Dousset, S. Claude, and K. Wu, "A Compact High-Performance Orthomode Transducer for the Atacama Large Millimeter Array (ALMA) Band 1 (31–45 GHz)," *IEEE Access*, vol. 1, pp. 480–487, 2013.

[12] G. Pisano, L. Pietranera, K. Isaak, L. Piccirillo, B. Johnson, B. Maffei, and S. Melhuish, "A Broadband WR10 Turnstile Junction Orthomode Transducer," *IEEE Microwave and Wireless Components Letters*, vol. 17, no. 4, pp. 286–288, 2007.

[13] A. Navarrini and R. Nesti, "Symmetric Reverse-Coupling Waveguide Orthomode Transducer for the 3-mm Band," *IEEE Transactions on Microwave Theory and Techniques*, vol. 57, no. 1, pp. 80–88, 2009.

[14] T. J. Reck and G. Chattopadhyay, "A 600 GHz Asymmetrical Orthogonal Mode Transducer," *IEEE Microwave and Wireless Components Letters*, vol. 23, no. 11, pp. 569–571, 2013.

[15] C. A. Leal-Sevillano, K. B. Cooper, E. Decrossas, R. J. Dengler, J. A. Ruiz-Cruz,

J. R. Montejo-Garai, G. Chattopadhyay, and J. M. Rebollar, "Compact Duplexing for a 680-GHz Radar Using a Waveguide Orthomode Transducer," *IEEE Transactions on Microwave Theory and Techniques*, vol. 62, no. 11, pp. 2833–2842, 2014.

[16] C. Shu, J. Wang, S. Hu, Y. Yao, J. Yu, Y. Alfadhl, and X. Chen, "A Wideband Dual-Circular-Polarization Horn Antenna for mmWave Wireless Communications," *IEEE Antennas and Wireless Propagation Letters*, vol. 18, no. 9, pp. 1726–1730, 9 2019.

[17] C. A. Balanis, "Polarization Measurements," in *Antenna Theory: Analysis and Design, 4th Edition.* Hoboken, New Jersey: John Wiley & Sons, 2016, ch. 17, p. 1017.

[18] M. J. Franco, "A High-Performance Dual-Mode Feed Horn for Parabolic Reflectors with a Stepped-Septum Polarizer in a Circular Waveguide [Antenna Designer's Notebook]," *IEEE Antennas and Propagation Magazine*, vol. 53, no. 3, pp. 142–146, 2011.

[19] M. Mrnka, M. Pavlovic, and Z. Raida, "Antenna Range Illuminator Based on a Septum Polarizer and a Dual-Mode Horn [Measurements Corner]," *IEEE Antennas and Propagation Magazine*, vol. 58, no. 4, pp. 82–86, 2016.

[20] C. Kumar, V. V. Srinivasan, V. K. Lakshmeesha, and S. Pal, "Novel Dual Circularly Polarized Radiating Element for Spherical Phased-Array Application," *IEEE Antennas and Wireless Propagation Letters*, vol. 8, pp. 826–829, 2009.

[21] G. Addamo, O. A. Peverini, D. Manfredi, F. Calignano, F. Paonessa, G. Virone, R. Tascone, and G. Dassano, "Additive Manufacturing of Ka-Band Dual-Polarization Waveguide Components," *IEEE Transactions on Microwave Theory and Techniques*, vol. 66, no. 8, pp. 3589–3596, 2018.

[22] J. Wu, Y. J. Cheng, H. B. Wang, Y. C. Zhong, D. Ma, and Y. Fan, "A Wideband Dual Circularly Polarized Full-Corporate Waveguide Array Antenna Fed by Triple-Resonant Cavities," *IEEE Transactions on Antennas and Propagation*, vol. 65, no. 4, pp. 2135–2139, 4 2017.

[23] C. A. Leal-Sevillano, K. B. Cooper, J. A. Ruiz-Cruz, J. R. Montejo-Garai, and J. M. Rebollar, "A 225 GHz Circular Polarization Waveguide Duplexer Based on a

Septum Orthomode Transducer Polarizer," *IEEE Transactions on Terahertz Science and Technology*, vol. 3, no. 5, pp. 574–583, 2013.

Chapter 7

Conclusion and Future Work

7.1 Conclusion

Millimetre-wave (mmWave) wireless communications is considered as a promising technology that can provide ultra-high data rate beyond 5G. This research aims to design wideband dual-circular-polarization (dual-CP) antennas which enable wireless links with high reliability and capacity in the mmWave band, and four dual-CP antennas are presented in this thesis.

Firstly, a dual-CP antenna based on a stepped septum polarizer is designed in simulation and verified in experiment by applying a smooth-wall horn with an optimized profile to achieve a wide bandwidth of 20.9% with isolation $>$ 20 dB in the W-band.

Secondly, to further improve the performance of the dual-CP antenna based on the conventional stepped septum polarizer, a grooved-wall septum polarizer is proposed for the first time with a 2-step design method. A dual-CP antenna is designed based on this grooved-wall septum polarizer and demonstrated in experiment to achieve a high isolation $>$ 30 dB over a bandwidth of 15.8% in the W-band.

Thirdly, in order to break the limitation of bandwidth and isolation for the dual-CP

antenna, a novel grooved-wall CP horn antenna is proposed with a septum-free structure, which is capable of generating dual CP when it is used together with an Orthomode Transducer (OMT). This structure is firstly applied on a simple and compact conical horn achieving a wide bandwidth in the W-band, and demonstrated to realize dual-CP with wide bandwidth and high isolation when used with an OMT.

Fourthly, this grooved-wall approach is generalized to design a multi-section CP horn antenna with a low reflection coefficient over a wide bandwidth in the W-band. This horn antenna together with an improved OMT is experimentally verified to be capable of generating dual-CP with high isolation of 32.5 dB over a wide bandwidth of 31.6%. To the authors' best knowledge, this result shows the highest isolation over a widest bandwidth among all types of dual-CP antennas ever reported. Moreover, this new type of CP/dual-CP antenna still has a great potential for further performance improvement in terms of not only bandwidth and isolation but also radiation characteristics, when a more complex profile is adopted. Additionally, with the septum-free structure, this new type of CP/dual-CP antenna can be easily scaled up to terahertz (THz) band.

The main features of the antenna presented in this thesis are summarized in Table 7-A.

Table 7-A: Antennas proposed in this thesis and their main features.

Chapter	Frequency (GHz)	Type	Reflection Coefficient (dB)	Isolation (dB)	AR (dB)	Overall Band-width	Max Gain (dBic)	Pol
3	76.8 - 94.7	Septum polarizer + Horn	<-15	>20	<5.8	20.9%	20.3	dual-CP
4	93 - 109	Grooved-wall septum polarizer + Horn	<-17	>30	<3	15.8%	25.6	dual-CP
5	75 - 110	Grooved-wall CP horn	<-22	N/A	<3.04	37.8%	18.6	CP
5	82 - 108	Grooved-wall CP horn + OMT	<-15*	>32*	<3*	27.4%*	17.9*	dual-CP
6	80 - 110	Multi-section grooved-wall CP horn + OMT	<-20	>32.5	<2.8	31.6%	21.6	dual-CP

* Full-wave simulated results.

Finally, a design/optimization method for complex EM devices is proposed based on inverse modelling using deep neural networks (DNNs) and CMA-ES algorithms. This method is suitable for generating new designs for complex EM devices with many design parameters and multiple objectives at a reduced computational cost based on existing design data. This method has also been verified in a design of a W-band septum polarizer, achieving a high isolation $>$ 40 dB over 15.8% bandwidth.

7.2 Future Work

In order to design dual CP antennas with even better performance in the millimetre-wave and THz bands, further work is identified in the following aspects.

7.2.1 Further Optimization of the Dual-CP Antenna based on the Multi-Section Grooved-Wall CP Horn

The dual-CP antenna based on the multi-section grooved-wall CP horn is a new type of dual-CP antenna just been proposed, so it still has a potential for even wider operating bandwidth $>$ 40% with isolation $>$ 30 dB or operating bandwidth $>$ 30% with even higher isolation $>$ 40 dB, if more sections are used to form a more complex profile. Specifically, 4 or more sections can be used to introduce more degrees of freedom for the design of the multi-section grooved-wall CP horn by following the design method elaborated in Section 6.4 with N set to 4 or more. The values of the design parameters listed in Table 6-A should also be set accordingly, such as a long L_{max}. Moreover, it is worth attempting to apply and optimize spline-profiles, such as that proposed in [1], to the grooved-wall CP horn to achieve superior performance. As this grooved-wall CP horn structure has an advantage that it can inherit the superior radiation performance from well-investigated smooth-wall horn, so better radiation performance such as rotational symmetry and low SLL of the radiation patterns can be further optimized.

7.2.2 Design of a Wideband Orthomode Transducer (OMT)

The operating bandwidth of the dual-CP antenna based on the multi-section grooved-wall horn is limited by the bandwidth of the OMT we used. The OMT proposed in [2] with a bandwidth of 36.8% could be scaled up to W-band to be used with the multi-section/profiled grooved-wall CP horn to realize dual-CP antenna with wider operating bandwidth and higher isolation than that of the dual-CP antennas proposed in this thesis. Additionally, because the common port of the OMT proposed in [2] is a circular waveguide, no square-to-circular waveguide transition section will be needed between the OMT and the grooved-wall CP horn. By removing the square-to-circular waveguide transition section, this configuration will not only reduce the length of the entire dual-CP antenna but also avoid the limitation on bandwidth introduced by the square-to-circular waveguide transition. However, a metallic stub is located at the centre of the turnstile junction inside the OMT acting as a matching element, which prevent this OMT from being fabricated in the THz band. If the multi-section/profiled grooved-wall CP horn antenna can be optimized to achieve bandwidth larger than 36.8%, a new type of OMT may need to be designed to match the wide bandwidth and realize a dual-CP antenna with bandwidth larger than 36.8%.

7.2.3 Optimization of the Multi-Section Grooved-Wall CP Horn with Deep-Learning-Based Inverse Modelling

The optimization of the multi-section grooved-wall CP horn described in Section 6.4 took about 30 days to obtain the design that met the requirement. If further optimization to achieve better performance is needed, for example, to achieve lower reflection coefficients over a wider bandwidth and wider 3-dB AR bandwidth, the optimization will have to start all over again with new targets set in the cost functions. Moreover, this optimization probably will take more time because it aims to achieve a design with better performance. To reduce the computational cost, it is worth trying to apply the deep-learning-based inverse modelling with CMA-ES we proposed in Section 2.3.2 to the optimization of a grooved-wall CP horn with better performance than that we proposed in Chapter 6.

The historical data samples saved during the optimization of the grooved-wall CP horn in Chapter 6 can be used to train the DNNs model following the method elaborated in Section 2.3.2.1. The challenge lies in the fact that the number of samples from previous optimization is limited because the full-wave simulation of the multi-section grooved-wall CP horn is time-consuming. For this reason, DNNs with relatively small sizes may be used in training. Despite this challenge, the deep-learning-based inverse modelling with CMA-ES can still be used as a tentative method to obtain the approximate performance potential of the grooved-wall CP horn antenna, which will benefit.

References

[1] C. Granet, G. L. James, R. Bolton, and G. Moorey, "A smooth-walled spline-profile horn as an alternative to the corrugated horn for wide band millimeter-wave applications," *IEEE Transactions on Antennas and Propagation*, vol. 52, no. 3, pp. 848–854, 2004.

[2] D. Dousset, S. Claude, and K. Wu, "A Compact High-Performance Orthomode Transducer for the Atacama Large Millimeter Array (ALMA) Band 1 (31–45 GHz)," *IEEE Access*, vol. 1, pp. 480–487, 2013.

Appendix A

Author's Publications

Journal papers

1. **C. Shu**, J. Wang, S. Hu, Y. Yao, J. Yu, Y. Alfadhl and X. Chen, "A Wideband Dual-Circular-Polarization Horn Antenna for mmWave Wireless Communications," *IEEE Antennas and Wireless Propagation Letters*, vol. 18, no. 9, pp. 1726–1730, 9 2019.

2. **C. Shu**, S. Hu, Y. Yao, Y. Alfadhl and X. Chen, "W-band grooved-wall circularly polarised horn antenna," *IET Microwaves, Antennas Propagation*, vol. 14, no. 11, pp. 1171–1174, 2020.

3. **C. Shu**, S. Hu, Y. Yao, Y. Alfadhl and X. Chen, "Wideband Dual-Circular-Polarization Antenna with High Isolation Based on the Grooved-wall Septum Polarizer for Millimeter-Wave Applications," *IEEE Antennas and Wireless Propagation Letters*, to be submitted.

4. **C. Shu**, S. Hu, Y. Yao, Y. Alfadhl and X. Chen, "Wideband Dual-Circular-Polarization Antenna with High Isolation Based on the Grooved-wall horn for Millimeter-Wave Applications," *IEEE Transactions on Antennas and Propagation*, submitted.

Conference papers

1. **C. Shu**, S. Hu, Y. Yao, and X. Chen, "Deep-Learning-based Inverse Modelling with CMA-ES as Applied to the Design of A Wideband High-isolation Septum Polarizer," *2020 IEEE International Symposium on Antennas and Propagation and North American Radio Science Meeting (AP-S/URSI)*, pp. 2001-2002, 2020.

2. **C. Shu**, S. Hu, Y. Yao, and X. Chen, "A High-Gain Antenna with Dual Circular Polarization for W-band mmWave Wireless Communications," *2019 Computing, Communications and IoT Applications (ComComAp)*, pp. 29-32, 2019.

3. **C. Shu**, S. Hu, Y. Yao, and X. Chen, "A W-band Compact Circularly Polarized Horn Antenna," *2019 12th UK-Europe-China Workshop on Millimeter Waves and Terahertz Technologies (UCMMT)*, pp. 1-2, 2019.

4. **C. Shu**, J. Wang, S. Hu, J. Shen, Y. Yao, and X. Chen, "A Dual Circular-Polarized Antenna for mmWave Wireless Communications," *2019 13th European Conference on Antennas and Propagation (EuCAP)*, pp. 1-3, 2019.

5. **C. Shu**, S. Hu, Y. Yao, and X. Chen, "A High-gain Antenna with Polarization-Division Multiplexing for Terahertz Wireless Communications," *2018 43rd International Conference on Infrared, Millimeter, and Terahertz Waves (IRMMW-THz)*, pp. 1-2, 2018.

6. **C. Shu**, S. Hu, Y. Yao, and X. Chen, "A W-band Antenna with Dual Circular Polarization for mmWave Wireless Communications," *2018 11th UK-Europe-China Workshop on Millimeter Waves and Terahertz Technologies (UCMMT)*, vol 1, pp. 1-3, 2018.

7. **C. Shu**, S. Hu, Y. Yao, and X. Chen, "High-gain reflector antenna with beam steering for terahertz wireless communications," *2017 10th UK-Europe-China Workshop on Millimetre Waves and Terahertz Technologies (UCMMT)*, pp. 1-4, 2017.